Competing α-effects in the Solar Dynamo

Laura Cole

Thesis submitted for the degree of
Doctor of Philosophy

School of Mathematics & Statistics
Newcastle University
Newcastle upon Tyne
United Kingdom

November 2016

For my parents Eileen and John Gray.

Acknowledgements

Firstly, I would like to thank my supervisor Paul Bushby for his support and guidance during my time as a PhD student. I have thoroughly enjoyed our weekly research meetings and I feel very privileged to have worked with such a superb mathematician.

Particular thanks goes to George Stagg who has helped me with several computing and programming issues as well as Nina Wilkinson, Holly Ainsworth and Ged Cowburn for making my time here so enjoyable. I am also grateful to David Cushing for sharing his extraordinary perspective on life and to Helen Green for helping me put things into perspective.

I am eternally grateful to my family. Their love and support has made me the person that I am today and they are the reason that I have been able to write this thesis. Special thanks must go to my grandparents who always encouraged me throughout my school life to achieve my very best. Mam and Dad, words cannot describe how proud I am of you, I can only hope that you are equally proud of me. Michael, you have been there from the very beginning, thank you for sharing this experience with me and supporting me every step of the way. Ellie and James, you will never know how much I love you, thank you for making my life complete.

Abstract

The large-scale magnetic field in the Sun varies with a period of approximately 22 years, although the amplitude of the cycle is subject to long-term modulation with recurrent phases of significantly reduced magnetic activity. It is believed that a hydromagnetic dynamo is responsible for producing this large-scale field, although this dynamo process is not well understood. Any dynamo that is responsible for the generation and maintenance of a large scale magnetic field requires mechanisms that are able to convert poloidal field lines into toroidal field lines and vice versa. Differential rotation is widely accepted to generate toroidal field however the converse process that is required for poloidal field regeneration is still a topic of some debate. This thesis aims to investigate how competing mechanisms for poloidal field regeneration (namely a time delayed Babcock-Leighton surface α-effect and an interface-type α-effect) interact with each other, leading to the modulation of the dynamo wave.

Initially, the study completed by Jouve *et al.* (2010) is expanded upon to include both sources for poloidal field regeneration. This requires solving the standard $\alpha\omega$ dynamo equations in one spatial dimension, including source terms corresponding to both competing α-effects in the evolution equation for the poloidal field. In addition to solving the one-dimensional PDEs directly, using numerical techniques, a local approximation is used to reduce the governing equations to a set of coupled ODEs, which are studied using a combination of analytical and numerical methods. In the ODE model, it is straightforward to find parameters such that a series of bifurcations can be identified as the time delay is increased, with the dynamo transitioning from periodic states to chaotic states via multiply periodic solutions. Similar transitions can be observed in the full model, with the chaotically modulated solutions exhibiting solar-like behaviour. Further refinements to this model produce similar results albeit in a smaller region of parameter space.

In order to impose more realistic physical properties of the system, the $\alpha\omega$ dynamo equations with both mechanisms for poloidal field regeneration are then solved numerically in two spatial dimensions. Upon retaining a parametrised time delayed field, the 2D code is able to produce modulation that is similar to that found in the 1D system. Removing the parametrised time delayed field, a shallow flow is imposed and the equations are solved in full. Modulation is found when the relative strength of the competing α-effects are varied and it is also apparent that the parity of the dynamo wave is dependent upon the strength of the meridional flow.

Contents

List of Figures

List of Tables

Part I

Introduction

Chapter 1

Observations

The Sun is our nearest star. Located at the centre of the solar system, it has a mass of 1.9891×10^{30}kg and a radius of 6.957×10^{8}m. Due to its close proximity to the Earth, we are able to make detailed observations which give us some understanding of its large-scale magnetic field. It is believed that the magnetic activity within the Sun is generated and maintained by a dynamo and it is the purpose of this thesis to describe a series of dynamo models that can be used to reproduce the observations that we see from the Sun. Before doing so, it is important to summarise some of the key features of the solar interior as well as relevant observations of the Sun's magnetic field.

1.1 Solar Structure

The Sun is not a homogeneous body, rather the structure changes from the surface to the core, shown here in Figure 1.1. The core is the most dense part of the Sun and is the location at which nuclear fusion compresses hydrogen nuclei together to form helium releasing thermal energy in the process. This energy is then transported diffusively through the Sun's radiative zone to the convection zone, (see, for example, Weiss & Tobias, 2000). Once energy reaches the Sun's convection zone it is then transferred to the solar surface by turbulent motions which can be seen at the surface (photosphere). The Sun's core and the radiative zone are believed to rotate almost as a solid body. However there is extensive evidence to suggest that the convective zone rotates differentially, (see, for example, Stix, 2002). Due to this change in behaviour, the point at which the convective zone and the radiative zone meet is matched by a thin shear region called the tachocline. Section 1.3 gives more detail about how the composition of our Sun is crucial when generating and maintaining a hydromagnetic dynamo.

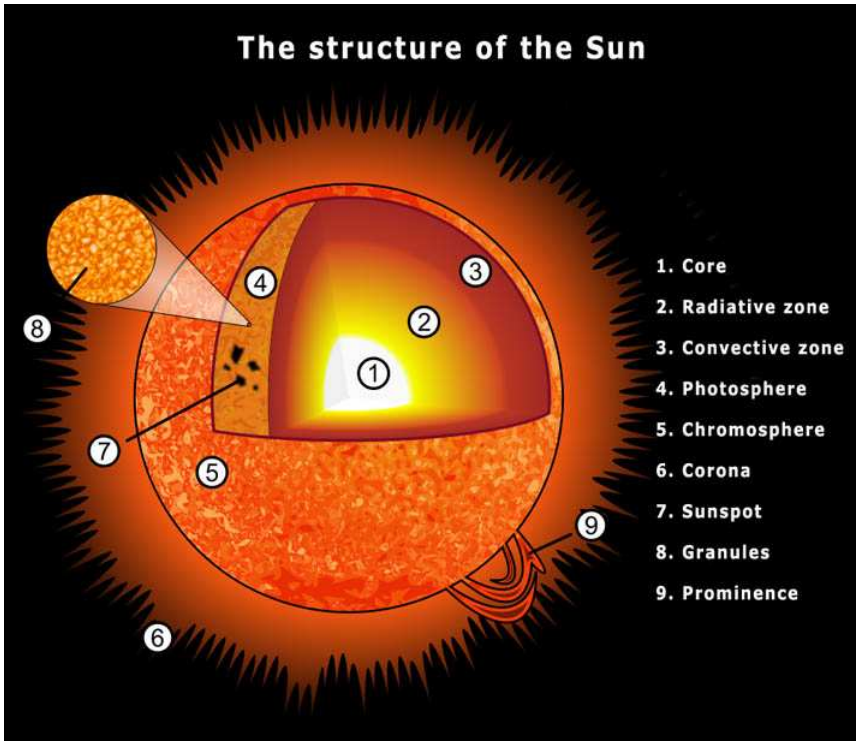

Figure 1.1: The internal structure of The Sun. This image is taken from `http://www.holoscience.com/wp/wp-content/uploads/2012/04/The-structure-of-the-Sun.jpg`

1.2 Solar Magnetism

This section aims to give a detailed description of our current beliefs about the Sun's magnetic field. Much of the information that we have about solar magnetism is gained through the study of sunspots. Sunspots are patches on the surface of the sun that appear darker than their surroundings. They are not identical, rather they vary in size (from 1500km up to 80,000 km), position and strength; see for example Thomas & Weiss (1992). For reasons that shall be discussed later, the temperatures of these sunspots are cooler than surrounding areas (4000 ° Kelvin as opposed to 6000 ° Kelvin) and thus they appear noticeably darker. A comprehensive review of historical sunspot observations is included in this section along with why they are considered to be important when understanding large-scale solar magnetism.

1.2.1 Sunspots

The first recorded instance of a sunspot was by Theophrastus, a student of Aristotle, in the fourth century BC (Bhatnagar & Livingston, 2005). The theories of Aristotle, who believed the Sun to be a perfectly unblemished sphere, were seldom questioned and the presence of such a spot on the Sun's surface was considered to be highly unlikely.

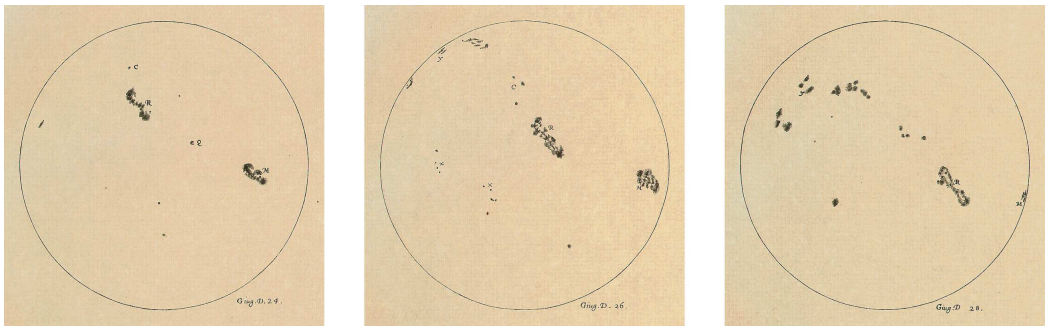

Figure 1.2: Three of Galileo's sunspot drawings. This image is taken from `http://galileo.rice.edu/sci/observations/sunspot_drawings.html`

Theophrastus' observation was widely disregarded and it was not until the work of Galileo in the early 17th century that his observation was accepted as the first recorded occurrence of a sunspot (Hanslmeier, 2002). While there were some systematic sunspot observations by the Chinese from around the year 23 B.C. their records were not translated into a European language until 1873 (Giovanelli, 1984).

The most significant development for western astronomers in their understanding of sunspots was the invention of the telescope in 1608. Although not conceived by Galileo, his improvements upon the original design allowed him to undertake a sustained observation of sunspot behaviour during which he systematically recorded in a series of sunspot drawings from 2nd June until 18th July 1613, three of which are included here as Figure 1.2. From his observations Galileo directly challenged the teachings of Aristotle, which had been accepted for two thousand years, deducing that sunspots occurred on the surface of the Sun. Galileo was the first person to suggest that there was a pattern to the position of the sunspots, believing that they formed in two narrow belts extending 30 degrees on either side of the equator.

While Galileo's study was by far the greatest of his time, there were also other astronomers who used the telescope to study sunspots, notably Goldsmid, Harriot, Kepler and Scheiner, with varied success (North, 1974). In 1609 Johannes Kepler, who is probably best known for his laws on planetary motion, was interested in observing a transit of the planet Mercury across the Sun. Through his telescope he observed a black spot that travelled across the Sun's surface and since this coincided with his predictions, he incorrectly attributed this to a transit of Mercury. This was in fact the first recorded observation of a sunspot through a telescope (Caspar & Hellman, 1993).

The observations of sunspots by Christopher Scheiner from 1625 to 1627, offered the first suggestion of solar differential rotation, that is to say that sunspots occurring near the equator moved across the solar disk more rapidly than those located at higher latitudes. Published in a volume called Rosa Ursina sive Sol, Scheiner promoted the idea that sunspots on either side of the equator at higher latitudes had longer periods of revolution

than those near the equator (Bhatnagar & Livingston, 2005).

It was not until 1843 that we gained any insight into the cyclic pattern of the frequency of sunspots. The German astronomer Heinrich Schwabe, like Kepler over two hundred years earlier, was interested in Mercury's transit of the Sun and through his observations he noticed that the number of sunspots reached a maximum approximately every eleven years. He published his data in a short article called "Solar Observations During 1843", however little attention was paid to this and it was not until 1851 when another German astronomer Alexander von Humboldt republished this data in his own book Kosmos, that Schwabe's work was fully appreciated (Goedbloed & Poedts, 2004).

Further characteristics of the solar cycle were investigated by the English amateur astronomer Richard Carrington. Starting in 1853, he intended to carry out a complete study and recording of an eleven year cycle. Unfortunately he didn't make complete records for this whole cycle. However over the eight years that he did undertake this study, not only did he reinforce the idea of solar differential rotation, but he also deduced that the typical latitudes of the sunspots decreased from the beginning of the cycle to the end (Balogh & Thompson, 2009).

In 1904, Edward Maunder became the first person to display the characteristics of the solar cycle in the form of an image, shown here in Figure 1.3. He worked at the Royal Observatory in Greenwich and participated in measuring and photographing sunspots. The time series shows that at the beginning of each cycle, sunspots tend to be found at mid-latitudes, with zones of emergence drifting towards the equator as the cycle progresses. Further observations of sunspots can be seen in the butterfly diagram, see Figure 1.4, where the sunspot number is plotted as a function of latitude and time. The figure shows that the emergence of sunspots vary on a cycle of approximately 11 years and that their appearance is confined to a region between $\approx \pm 30^{\circ}$ in latitude with sunspot emergence regions migrating equatorwards as the cycle progresses. The solar cycle is not strictly periodic. In particular, the peak amplitude (measured, for example, by the sunspot coverage) varies from one cycle to the next, shown here in Figure 1.5.

The most significant development that is relevant to this study was made by George Ellery Hale in 1908. Using the spectroheliograph which he invented, shown here in Figure 1.6, he observed the Zeeman splitting of spectral lines and in doing so he became the first person to link the Sun's magnetic field to sunspots (Hoyt & Schatten, 1996). Hale found that sunspots occurred at points where the magnetic field of the Sun was strong, usually between 2500 to 3000 Gauss. It is worth noting that these magnetic fields tend to inhibit convection, which explains why these regions are cooler (and hence darker) than their non-magnetic surroundings.

Hale's law (Hale *et al.*, 1919) states that strong magnetic regions on either side of the equator consist of pairs of sunspots that always lead (with respect to the East-West

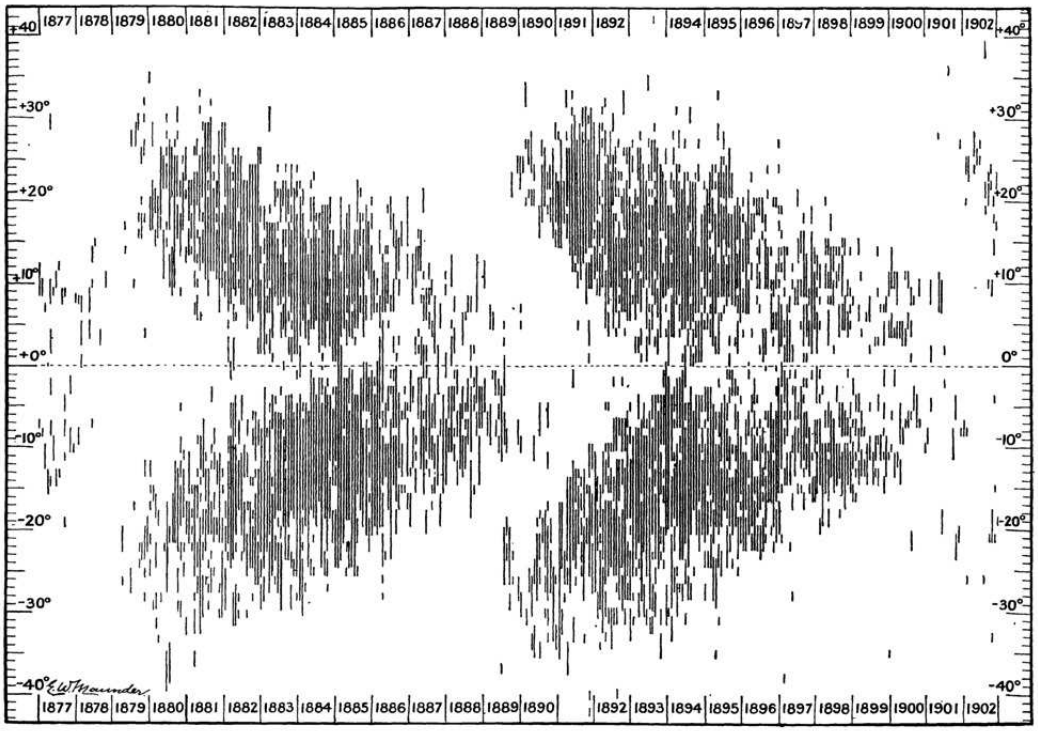

FIG. 8.—DISTRIBUTION OF SPOT-CENTRES IN LATITUDE, ROTATION BY ROTATION, 1877–1902.

Figure 1.3: Maunder's butterfly diagram. (Maunder, 1904)

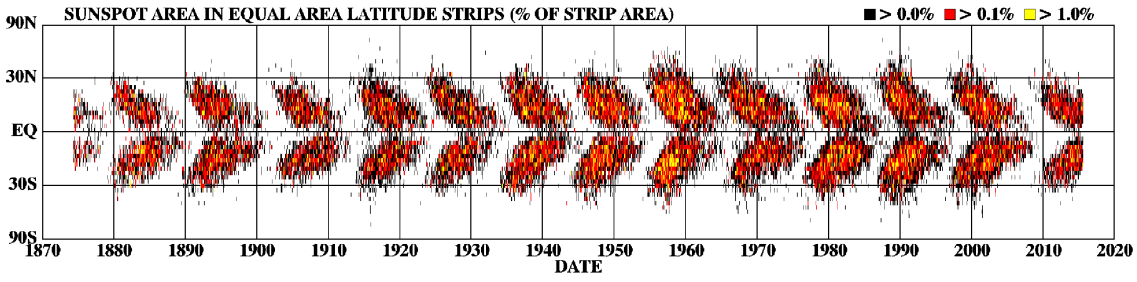

Figure 1.4: The butterfly diagram: Time is plotted on the horizontal axis and latitude on the vertical axis. It is clear that as the cycle progresses sunspot emergence regions migrate towards the equator. Note that the magnetic activity is not consistent and that it varies in magnitude from cycle to cycle. This image is constantly updated by NASA. (Hathaway, 2015*a*).

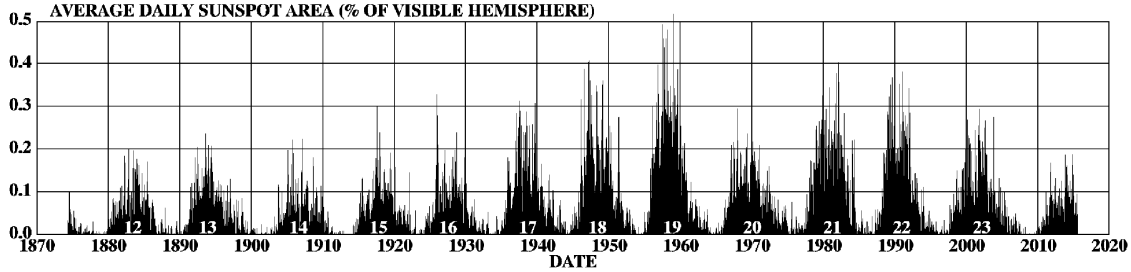

Figure 1.5: Sunspot area: Time is plotted on the horizontal axis and the average daily sunspot area (%) of the visible hemisphere is plotted on the vertical axis. It is clear that the behaviour of each cycle is different, with the number of sunspots varying from one cycle to the next. (Hathaway, 2015*a*).

Figure 1.6: The spectroheliograph that Hale used in 1908. This image is taken from `http://www.lib.uchicago.edu/e/spcl/centcat/fac/facch04_01.html`

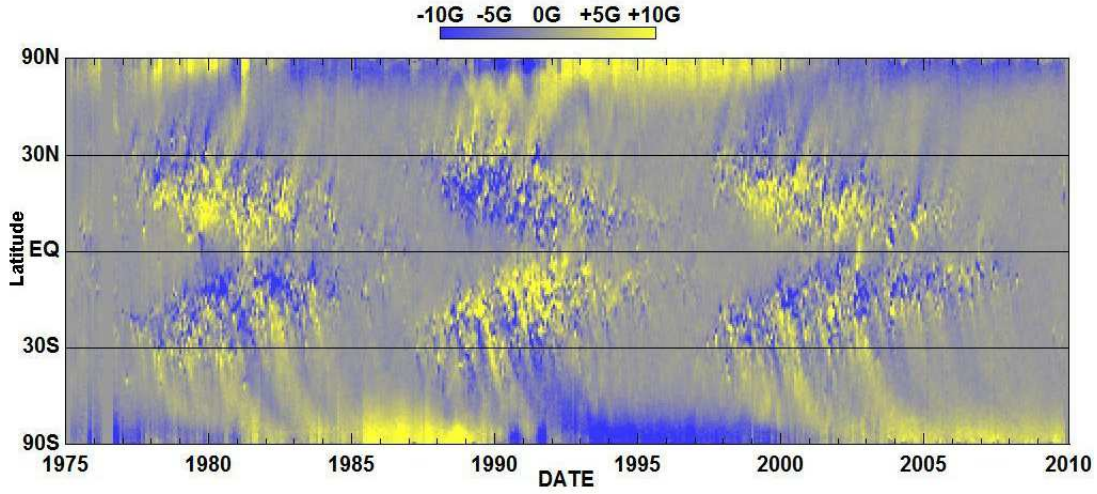

Figure 1.7: The magnetic butterfly diagram: Note the reversal of the polarity at the end of each solar cycle. (Hathaway, 2015*b*).

direction) with the same polarity. That is to say that if a pair of sunspots in the Northern hemisphere had a leading sunspot of positive polarity, the rest of the sunspots in the Northern hemisphere would also lead with a sunspot of positive polarity. In addition he stated that the magnetic polarity between a pair of sunspots was opposite, that is to say that each sunspot pair consists of a sunspot that is of positive polarity and another sunspot that is of negative polarity. Hale's law also tells us about the parity and polarity reversal of the sunspot pairs: if the sunspots in the Northern hemisphere lead with positive polarity then the sunspots in the Southern hemisphere lead with negative polarity, with the polarity of the sunspot pair flipping from one cycle to the next. His observations show that the underlying large-scale (predominantly azimuthal) magnetic field has a magnetic period of approximately 22 years. This behaviour can be seen in the magnetic butterfly diagram in Figure 1.7, an image which is constantly updated by NASA.

Another indicator of the cyclic frequency of sunspots is the 'sunspot number'. This is calculated by multiplying the number of sunspots by ten times the number of sunspot groups (Hathaway, 2015*c*). Since the average sunspot group contains ten sunspots, this gives an average number of sunspots for that day and the result is plotted on a graph, given here in Figures 1.8 and 1.5.

It is clear from these historical observations that the solar cycle is not strictly periodic. In particular, the peak amplitude (measured, for example, by the sunspot coverage) varies from one cycle to the next and the cycle period varies roughly between 9 and 13 years. Vizoso & Ballester (1990) and Carbonell *et al.* (1993) both studied the yearly averaged sunspot numbers and provide evidence to suggest that there is an asymmetry in their location between the Sun's northern and southern hemisphere. Although this modulation does

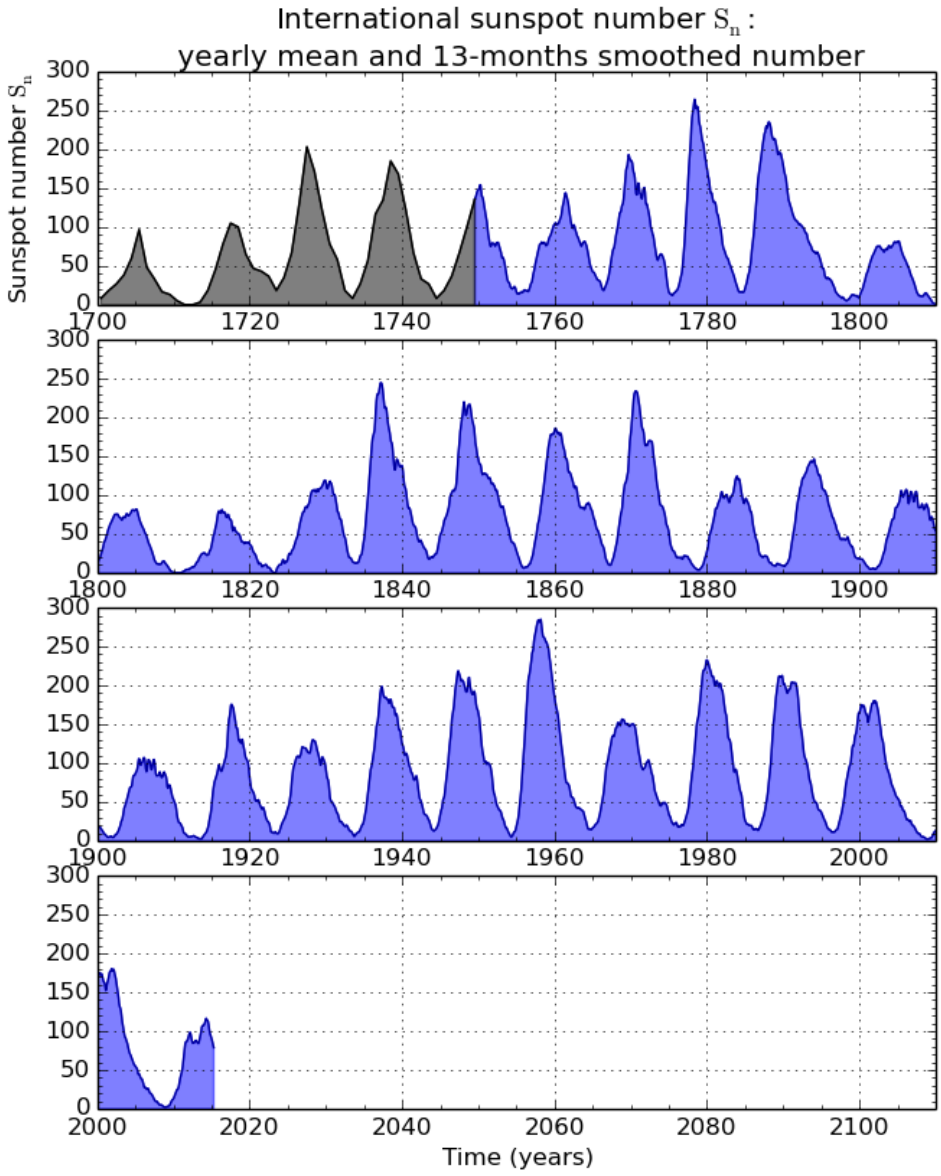

Figure 1.8: Sunspot number: The black part of the plot shows the yearly mean sunspot number up to 1749. The blue part of the plot shows a 13-month smoothed sunspot number from 1749 up to the present day. The time series shows cyclic behaviour with a period of around 11 years. This image is taken from `http://sidc.oma.be/silso/yearlyssnplot`

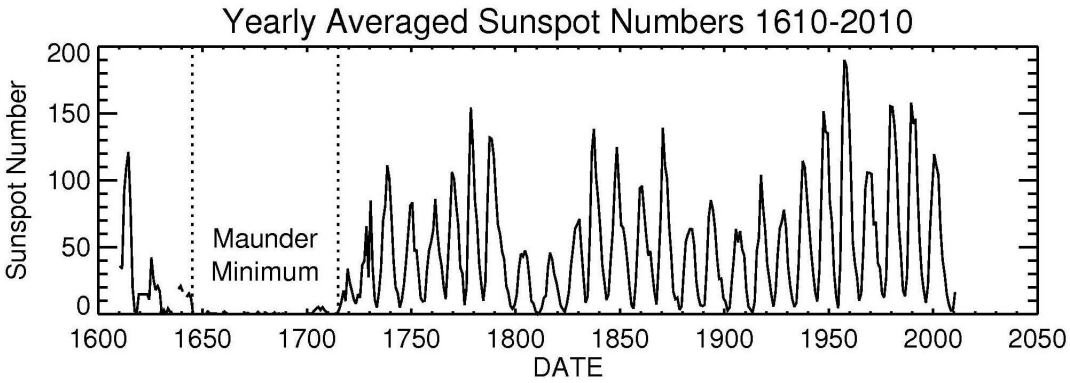

Figure 1.9: Time series plot of the sunspot number showing the Maunder Minimum characterised by a prolonged period of significantly reduced magnetic activity with the Sun. This image is taken from `http://science.nasa.gov/media/medialibrary/2008/07/11/11jul_solarcycleupdate_resources/ssn_yearlyNew2.jpg`

not usually disrupt the cycle, more extreme episodes of modulation have been recorded. The most dramatic modulation episode was a period of significantly reduced sunspot activity between 1645 and 1715 (see Figure 1.9), known as the Maunder minimum, (see, for example, Eddy, 1976; Ribes & Nesme-Ribes, 1993; Hoyt & Schatten, 1996). It is also evident that the long term modulation of the cycle appears to vary with a time scale of 80 years (see, for example, Hartmann, 1971; Gleissberg, 1939, 1971; Henkel, 1972). This 80 year period is established through studying the maximum value of the sunspot number and calculating a moving average over three or four consecutive solar cycles.

Sunspot records are not the only indicators of modulation. Due to the fact that the Sun's strong magnetic field protects the Earth from cosmic rays, the abundance of certain isotopes in the Earth's atmosphere is known to be anti-correlated with the solar cycle. Therefore by analysing Beryllium-10 deposits in ice cores, (Delaygue & Bard, 2011; Raisbeck & Yiou, 1988; Beer *et al.*, 1988, 1991) and Carbon-14 levels in tree rings, (Muscheler *et al.*, 2007; Stuiver & Braziunas, 1988) it is possible to deduce the history of the solar cycle. Such studies have indicated that cyclic activity did persist throughout the Maunder Minimum but at a significantly reduced level (Beer *et al.*, 1998). Furthermore it is clear that the Maunder Minimum is not exceptional – the solar cycle has often been interrupted by recurrent "Grand Minimum" phases of significantly reduced magnetic activity.

1.2.2 The large-scale internal magnetic field

Having reviewed the observational aspects of the sunspot cycle, it is useful at this stage to summarise what these observations imply about large-scale solar magnetism. At the solar photosphere, sunspot-bearing active regions are formed when loops of magnetic flux rise to the surface from the base of the convection zone due to the action of magnetic buoyancy

(Parker, 1955*b*). Given the systematic properties of the solar cycle (see, for example Stix, 2002; Charbonneau, 2005; Jones *et al.*, 2010, for further details), we can therefore deduce that there is an internal large-scale magnetic field that has certain specific properties. In particular:

- The underlying magnetic field that generates sunspots has a strong azimuthal component
- The magnetic field is confined to a region at low latitudes ($\pm 30^\circ$)
- The large-scale azimuthal field is antisymmetric about the equator and reverses sign at the end of each sunspot cycle
- The appearance of sunspots are modulated in time
- Sunspot emergence groups migrate equatorwards

1.2.3 Radial field at the solar surface

The large-scale azimuthal field is responsible for the production of sunspots on the solar surface; however it is also important to consider the radial component of the magnetic field and how it evolves over time. Over the course of the solar cycle, the radial component of the magnetic field has been observed to migrate polewards at the solar surface (see, for example, Bumba & Howard, 1965; Howard & Labonte, 1981; Makarov *et al.*, 1983; Makarov & Sivaraman, 1989; Wang *et al.*, 1989*a*,*b*). Butterfly diagrams, which are concerned with the strong large-scale azimuthal field at the base of the convection zone, are constructed through plotting the observed sunspot number as a function of latitude and time. Similar "reverse butterfly diagrams" can be produced through plotting the radial field strength at the solar surface as a function of latitude and time. Such plots show that the radial magnetic field at the solar surface migrates polewards, (see, for example, Wang *et al.*, 1989*a*; Dikpati & Choudhuri, 1994, 1995). Furthermore, as shown by Babcock (1959), the radial field at the solar surface reverses at sunspot maximum, which implies that there is a phase shift between the radial field at the solar surface and the large-scale azimuthal field at the base of the convection zone.

1.3 Flows in the solar interior

Large-scale flows transport magnetic flux around the solar interior. Crucial components of the solar dynamo can be explained by studying the Sun's global scale flows such as differential rotation and meridional circulation. These large-scale flows are also important

when describing the evolution of active regions throughout each solar cycle (see, for example, Haber *et al.*, 2002*a*; Gizon *et al.*, 2001). This section aims to describe in detail the most important velocity fields that are present within the Sun and their relevance when constructing a suitable dynamo model that can describe its magnetic activity.

1.3.1 Differential Rotation

It has been accepted since the studies of Scheiner in 1625-1627 and by Carrington in 1853 that the sun rotates more rapidly at the equator than it does at the poles (see, for example, Bhatnagar & Livingston, 2005; Balogh & Thompson, 2009). The solar rotation rate can be measured by direct Doppler velocity measurements (Howard & Labonte, 1980), or by heliosisemology which allows us to probe the solar interior (see, for example, Giles, 1999; Schou *et al.*, 1998). The resulting angular velocity is shown here in Figure 1.10.

We see that this angular velocity is strongly dependent upon latitude with surface regions near the equator rotating more rapidly than at the poles. What is also apparent is that the latitudinal dependence of the differential rotation profile also extends down through the convection zone (see, for example, Harvey *et al.*, 1986; Thompson *et al.*, 1996; Dziembowski *et al.*, 1989), until there is a sharp change in the angular velocity at the base of the convection zone (located, approximately, at 0.7 times the solar radius). For regions that lie below this radius, the Sun essentially rotates as a solid body. It is important to note that there are limitations to the data as the heliosisemological results are not well defined as we approach the centre of the Sun, or as we approach the poles and therefore the angular velocity has not been measured reliably in these regions.

Coupling the radiative interior of the Sun, which is rotating as a solid body, to the differentially rotating convection zone is a region that is commonly known as the tachocline (see, for example, Hughes *et al.*, 1998). First defined by Spiegel & Zahn (1992), the tachocline is a very thin boundary layer of approximately $0.05R_{\odot}$ to $0.09R_{\odot}$ in width (Zhao *et al.*, 2009) and is characterised by having very strong radial gradients in the velocity profile at this fixed radius. Due to the physical properties of the tachocline, it is widely believed that it is the location where the solar dynamo operates. Differential rotation also plays a crucial role in the dynamo process by converting the radial field into the large-scale azimuthal field and is an essential ingredient of our dynamo model, the details of which are given in Chapter 2.

First described by Howard & Labonte (1980) and then further studied by others including Snodgrass & Howard (1985), Howe *et al.* (2000) and Zhao & Kosovichev (2004), torsional oscillations are bands of zonal flows (with an average speed of $\approx 3ms^{-1}$) that are superimposed upon the mean differential rotation. The average speed of these torsional oscillations is very small compared to a differential rotation velocity profile of $\approx 170ms^{-1}$. Shown here in Figure 1.11, these alternating zones of faster and slower rotation are gen-

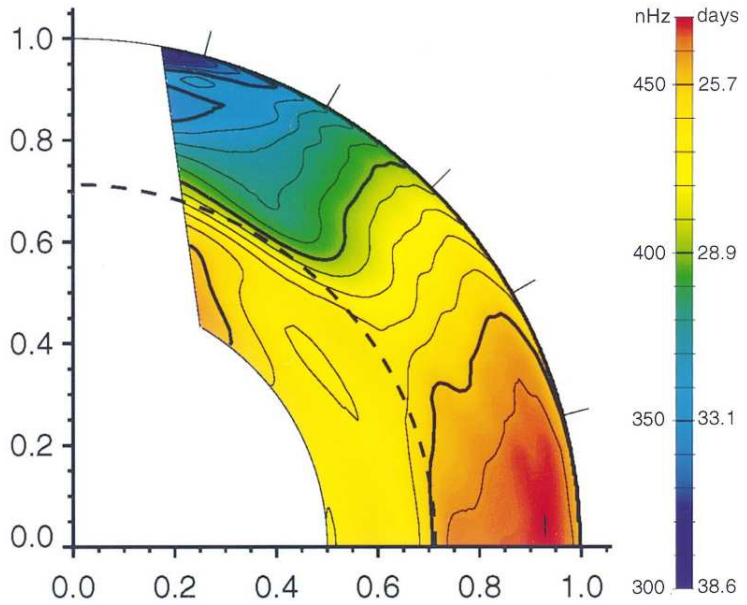

Figure 1.10: Local rotation period (frequency) in days(nHz). Red contours indicate faster rotating areas and blue contours correspond to slower rotating areas. Note the differential rotation profile extends down through the convection zone to a region that is approximately $0.7R_{\odot}$. Here, the x and y axes have been scaled such that 1.0 represents the solar radius and 0.0 represents the core. This image is adapted from Schou *et al.* (1998).

erated with a period of approximately 22 years, (see, for example, Zhao & Kosovichev, 2004). Each cycle includes the generation of faster and slower rotational bands in each hemisphere which move towards the equator at low latitudes and towards the poles at higher latitudes (Vorontsov *et al.*, 2002). It is always the case that the faster rotational bands that move towards the equator are found on the equatorial side of the solar activity belts. These torsional oscillations have also been observed below the Sun's photosphere through the use of heliosisemology. It was shown by Howe *et al.* (2000) that these rotational bands extend to a depth of $\approx 0.92R_{\odot}$. However Vorontsov *et al.* (2002) have suggested that although the low latitude branch that migrates towards the equator is limited to a depth of approximately 10% of the solar radius, the high latitude branch (which develops at around 60° latitude) may extend through the entire convection zone until it reaches the solar tachocline at approximately $0.7R_{\odot}$.

1.3.2 A Meridional Flow

Doppler velocity measurements are able to directly measure the flows at the solar photosphere. Duvall (1979) used this technique to measure a poleward meridional flow with a constant velocity of $20ms^{-1}$ between the latitudes of 10° and 50°. This result was later confirmed by various authors including Hathaway *et al.* (1996), Howard & Labonte (1981) and Ulrich *et al.* (1988). Giles *et al.* (1997) identified a poleward meridional flow with the

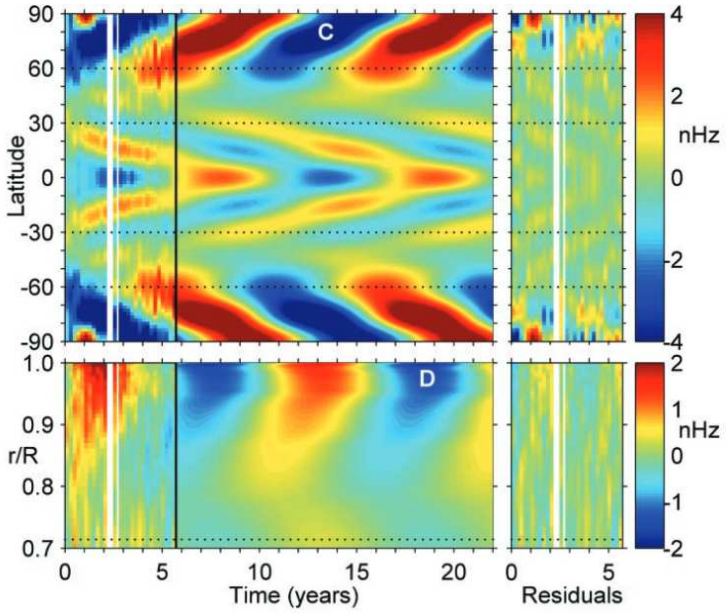

Figure 1.11: The top part of the figure shows the variation in rotation as a function of time and latitude at a fixed radius of $0.98R_{\odot}$. It is clear to see that there are four zones of faster rotation, two in each hemisphere. There is a poleward branch beginning at around $\pm 60°$ latitude and an equatorward branch that is confined to latitudes below $\pm 30°$. The bottom part of the figure also displays the variation in rotation but now it is given as a function of depth and time at a fixed latitude of 20°. This image is taken from Vorontsov *et al.* (2002).

same maximum velocity by using heliosisemology. This meridional flow has been measured to be more than an order of magnitude smaller than that of other flows on the surface of the Sun. For example, representative velocities of the corresponding phenomena are given by; differential rotation $\approx 170ms^{-1}$, granulation $\approx 3000ms^{-1}$ and supergranulation $\approx 170ms^{-1}$ (Hathaway & Rightmire, 2010). Therefore the meridional flow has proven problematic to measure.

Figure 1.12 shows the mean meridional flow profile at the solar surface measured over 167 solar rotations. We see that in each hemisphere the flow is in opposite directions and always moves towards the poles. At the solar equator the meridional flow is zero, then as the flow moves polewards it increases in speed until it reaches a maximum velocity of approximately $15ms^{-1}$ somewhere between a latitude of $\pm 40°$ and $\pm 50°$. After it reaches this maximum the flow decelerates until it approaches zero as it nears the poles.

This meridional flow may be crucial in the transportation of magnetic flux within the solar interior (Wang *et al.*, 1989*b*). Although we see a poleward flow at the solar surface a returning flow must exist due to mass conservation ($\nabla \cdot (\rho \mathbf{u}) = 0$). Dikpati & Gilman (2009) argued that the equatorward meridional flow is the primary mechanism for transporting magnetic flux from the polar area back down to lower latitudes near the equator. Although this mechanism may be very important, the exact location of the equatorward meridional

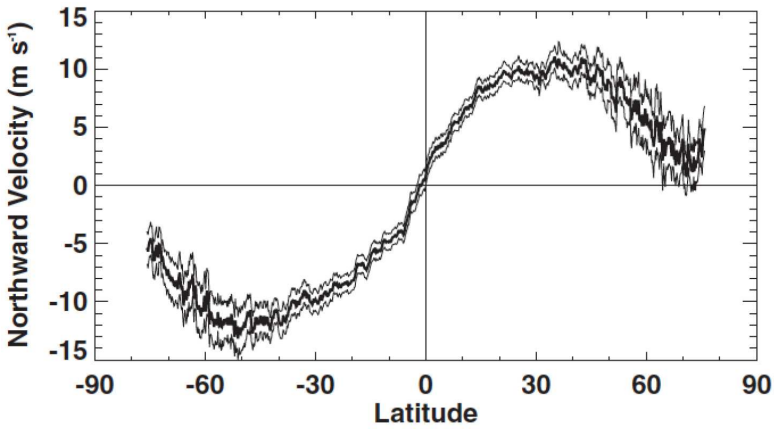

Figure 1.12: The mean meridional flow profile at the solar surface measured over 167 rotations. The flow vanishes at the equator and is in opposite directions in each hemisphere. This image is taken from Hathaway & Rightmire (2010).

flow remains unclear.

In fact, very little *is* certain about the meridional flow in the solar interior. Giles *et al.* (1997) concluded that the poleward flow penetrated into the convection zone to a radius of at least $0.96R_{\odot}$. Other studies have also concluded that the surface meridional flow penetrates into the Sun's shallow interior (i.e. deeper than $r = 0.96$) (see, for example, Haber *et al.*, 2002*b*; Bogart & Basu, 2004; Zhao & Kosovichev, 2004; Zhao *et al.*, 2012). Schou *et al.* (1998) and Braun & Fan (1998) have suggested that a poleward flow exists down to a radius of $\approx 0.85R_{\odot}$ although due to the difficulties in measuring the meridional flow within the solar interior, this result is far from conclusive.

The same uncertainty surrounds the returning equatorward flow. One popular theory is that this occurs near the base of the convection zone at approximately $0.7R_{\odot}$, shown here in Figure 1.13 (see, for example, Giles, 1999). Many flux transport dynamo models have used a single cell meridional circulation with an equatorward flow that is located just above the base of the convection zone (tachocline), (see, for example, Dikpati & Charbonneau, 1999) or indeed a returning flow that is located at a radius that lies in an offshoot region just below the base of the convection zone (Nandy & Choudhuri, 2002).

A more recent study by Hathaway (2012), that was based upon tracking the advection of supergranules, suggests that the Sun's poleward meridional flow is confined to a shallow region in the surface shear layer and the Sun's returning equatorward flow is located at a depth very close to this. Although this result is in contrast to previously published work it is supported by further studies (Zhao *et al.*, 2013; Sivaraman *et al.*, 2010) who have also concluded that the returning equatorward flow is located at a shallow depth.

More recently it has been suggested by Zhao *et al.* (2013) that the flow is made up of a double-cell meridional circulation with one cell operating poleward at the surface with the

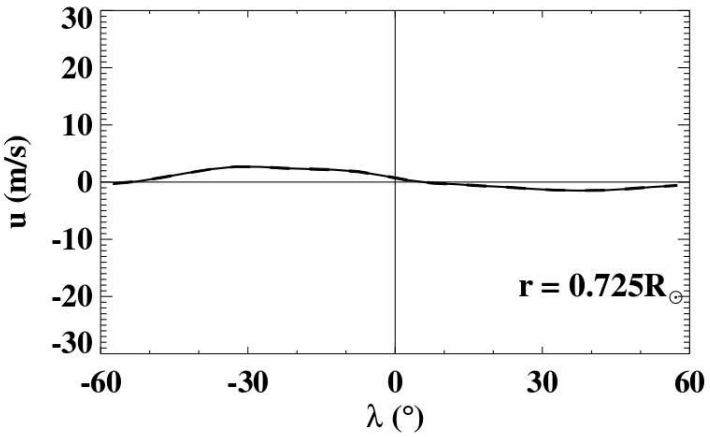

Figure 1.13: Meridional flow at a fixed radius of $0.725R_{\odot}$. This figure shows the presence of a returning equatorward meridional flow, taken from Giles (1999). Crucially, the flow is of the opposite direction to the flow that is present on the Sun's surface. This result isn't conclusive due to the difficulties in measuring the meridional flow within the solar interior.

corresponding equatorward flow between $0.82R_{\odot}$ and $0.91R_{\odot}$ and an additional poleward flow at approximately $0.82R_{\odot}$ indicating the presence of another meridional circulation cell located below the shallower one, shown here in figures 1.14 and 1.15. This would support the study of Hathaway (2012) who concluded that the returning equatorward flow is located at a shallow depth without probing further into the solar interior.

Due to the uncertainty of the exact location of the returning equatorward flow there are no strong constraints on dynamo models which can choose to impose either form of meridional circulation with flows that close near the base of the convection zone or at a shallow depth.

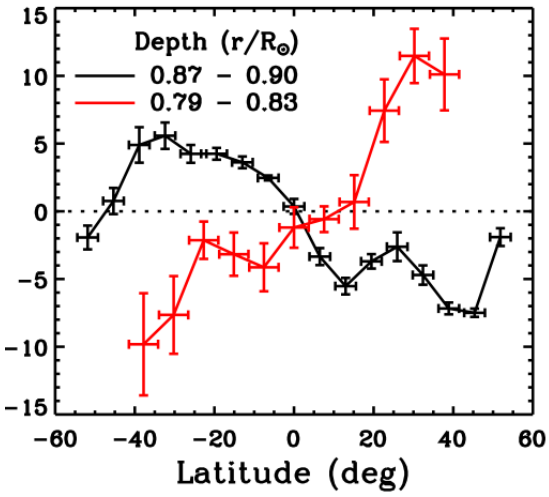

Figure 1.14: Meridional flow measured at two fixed radii. The black line corresponds to a radius of $0.87R_\odot - 0.90R_\odot$ and the red line to a radius of $0.79R_\odot - 0.83R_\odot$. Here the equatorward meridional flow is present at $0.87R_\odot$ with an additional poleward flow at $0.79R_\odot$. This image is taken from Zhao *et al.* (2013).

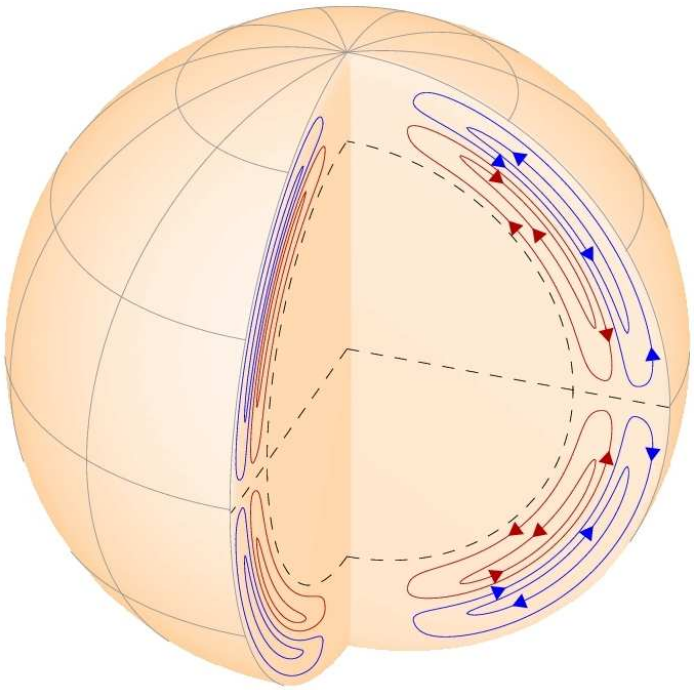

Figure 1.15: Double cell meridional circulation. Note the poleward direction of the flow at the surface and the presence of a second meridional cell. This image is taken from Zhao *et al.* (2013).

Chapter 2

Dynamo Theory

2.1 Governing Equations

2.1.1 Maxwell's Equations

The equations describing an electric field and magnetic field present in a conducting fluid are given by Maxwell's Equations and are as follows:

$$\nabla \cdot \mathbf{E} = \frac{\rho_c}{\epsilon_0}, \tag{2.1}$$

$$\nabla \cdot \mathbf{B} = 0, \tag{2.2}$$

$$\nabla \times \mathbf{E} = -\frac{\partial \mathbf{B}}{\partial t}, \tag{2.3}$$

$$\nabla \times \mathbf{B} = \mu_0 \mathbf{J} + \epsilon_0 \mu_0 \frac{\partial \mathbf{E}}{\partial t}, \tag{2.4}$$

where $\mathbf{E}$ is the electric field, $\mathbf{B}$ is the magnetic field, $\mathbf{J}$ is the current density, ρ_c is the charge density, ϵ_0 is the permittivity and μ_0 is the permeability of free space.

2.1.2 Ohm's Law

Ohm's law in a moving medium states that:

$$\mathbf{J} = \sigma \mathbf{E} + \sigma(\mathbf{U} \times \mathbf{B}) \tag{2.5}$$

where σ is the conductivity of the medium. The first term on the right hand side of Equation (2.5) is the current generated by the electric field acting upon the fluid when it is at rest. The second term in Equation (2.5) is an additional electric current generated by a fluid moving with velocity $\mathbf{U}$ in the presence of a magnetic field $\mathbf{B}$.

2.1.3 The Induction Equation

Maxwell's equations and Ohm's law can be used to generate the induction equation, the governing equation for the evolution of a magnetic field within an electrically conducting medium. Considering the dimensions of Equation (2.3), leads to the following result:

$$|\nabla \times \mathbf{E}| = \left|-\frac{\partial \mathbf{B}}{\partial t}\right|, \qquad \Longrightarrow \frac{E}{L} \sim \frac{B}{T}, \qquad \Longrightarrow \frac{E}{B} \sim \frac{L}{T} \sim U$$

where E is a typical strength of the electric field, B is a typical strength of the magnetic field, T is a typical time scale, L is a typical length scale and U is a typical fluid speed. Using the same technique on Equation (2.4) leads to an interesting result:

$$\frac{|\mu_0 \epsilon_0 \partial \mathbf{E}/\partial t|}{|\nabla \times \mathbf{B}|} \sim \frac{\mu_0 \epsilon_0 L E}{BT} \sim \frac{U^2}{c^2}$$

where $c^2 = 1/\mu_0\epsilon_0$. This means that for speeds much smaller than the speed of light, U^2/c^2 is small thus it is possible to neglect $\mu_0\epsilon_0\partial\mathbf{E}/\partial t$ in Equation (2.4). The simplified version of this equation is therefore:

$$\nabla \times \mathbf{B} = \mu_0 \mathbf{J}. \tag{2.6}$$

which is Ampère's Law. In order to derive the induction equation, Ohm's law is used to replace $\mathbf{J}$ in Equation (2.6):

$$\eta \nabla \times \mathbf{B} = \mathbf{E} + (\mathbf{U} \times \mathbf{B}), \tag{2.7}$$

where $\eta = 1/\mu_0\sigma$, the magnetic diffusivity. Next, take the curl of Equation (2.7):

$$\nabla \times (\eta \nabla \times \mathbf{B}) = \nabla \times [\mathbf{E} + (\mathbf{U} \times \mathbf{B})]. \tag{2.8}$$

The Maxwell-Faraday equation, given here in Equation (2.3) can be used to change Equation (2.8) into a time evolution equation for $\mathbf{B}$. The governing equation is thus given by:

$$\frac{\partial \mathbf{B}}{\partial t} = \nabla \times (\mathbf{U} \times \mathbf{B}) - \nabla \times (\eta \nabla \times \mathbf{B}). \tag{2.9}$$

Also, the more specific case is considered when η is assumed to be constant. To proceed, the following well known vector identity is used:

$$\nabla \times (\nabla \times \mathbf{A}) = \nabla(\nabla \cdot \mathbf{A}) - \nabla^2 \mathbf{A},$$

and the induction equation becomes:

$$\frac{\partial \mathbf{B}}{\partial t} = \nabla \times (\mathbf{U} \times \mathbf{B}) + \eta \nabla (\nabla \cdot \mathbf{B}) - \eta \nabla^2 \mathbf{B}. \tag{2.10}$$

It is possible to make use of Gauss' law for magnetism, Equation (2.2), which requires that the divergence of the magnetic field $\mathbf{B}$ is zero. This further simplifies the right hand side of Equation (2.10):

$$\frac{\partial \mathbf{B}}{\partial t} = \nabla \times (\mathbf{U} \times \mathbf{B}) + \eta \nabla^2 \mathbf{B}. \tag{2.11}$$

The first term on the right hand side of the induction equation is a source term which generates magnetic field due to the effects of advection by the fluid flow. The second term is a diffusive term which leads to the decay of the magnetic field. In order to maintain a dynamo, the diffusion term has to be smaller in magnitude than the advective term or the magnetic field will simply decay.

2.1.4 The Magnetic Reynolds Number

The Magnetic Reynolds number, R_m, is introduced when considering the ratio of the advective term to the diffusive term in the induction equation.

$$\frac{|\nabla \times (\mathbf{U} \times \mathbf{B})|}{\eta |\nabla^2 \mathbf{B}|} \sim \frac{UL}{\eta} = R_m.$$

The diffusive limit In the diffusive limit, the diffusion term dominates since $R_m \ll 1$ and the induction equation becomes:

$$\frac{\partial \mathbf{B}}{\partial t} = \eta \nabla^2 \mathbf{B},$$

which is well known in applied mathematics as the vector diffusion equation. It is possible to use dimensional analysis to estimate the time scale over which the magnetic field will decay. Again, the assumptions are made such that B is a typical value of the magnetic field and L is a typical length scale. A new parameter is introduced τ_η, known as the magnetic diffusion time scale and is used to estimate the time it takes for the magnetic field to decay. The dimensional analysis yields:

$$\tau_\eta \sim \frac{L^2}{\eta}.$$

The diffusion time for the Earth is calculated to be 3×10^5 years, (see, for example, Choudhuri, 1998). The Earth's magnetic field is known to have existed for approximately 3×10^9 years which is longer than the diffusive timescale τ_η and so it is clear that in the case of the Earth, the induction term $\nabla \times (\mathbf{U} \times \mathbf{B})$ must be efficient enough to counteract the diffusive term.

The same reasoning can also be applied to the Sun. The diffusion time for the Sun's magnetic field is calculated to be 10^{11} years and although this decay time is large the Sun's magnetic field is known to oscillate with a period of approximately 11 years. This requires a mechanism that is able to make the magnetic field oscillatory and so a hydromagnetic dynamo is certainly plausible, (see, for example, Choudhuri, 1998).

The perfectly conducting limit In the perfectly conducting limit, the advection term dominates since $R_m \gg 1$ and the induction equation becomes:

$$\frac{\partial \mathbf{B}}{\partial t} = \nabla \times (\mathbf{U} \times \mathbf{B}).$$

Alfvén's theorem states that in a perfectly conducting fluid, the magnetic field lines move as if they were "frozen in" to the fluid (Alfvén, 1942). It has already been established that the advection term in the induction equation needs to be present in order to protect against a decaying magnetic field and in most astrophysical systems, $R_m \gg 1$, therefore this "frozen in" approximation is usually valid.

2.2 Dynamo Basics

A dynamo is a self-sustaining process that is able to convert kinetic energy into magnetic energy. This process is a closed loop which requires no external components in order to generate and maintain a magnetic field. The idea is essentially that the motion of an electrically conducting fluid through a magnetic field will induce a current. This current will in turn generate more magnetic field through Ampère's law, Equation (2.6), giving a closed process.

2.2.1 Kinematic and Non-Linear Dynamos

The induction equation, Equation (2.11), requires that in order for dynamo action to occur, the advective term must be larger than the diffusive term ensuring that the magnetic field will not decay. This means that the velocity field $\mathbf{U}$ must be strong enough to be able to maintain a magnetic field working against dissipative effects. The Navier-Stokes equations describe how a velocity field evolves in an electrically conducting fluid:

$$\rho \left(\frac{\partial \mathbf{U}}{\partial t} + (\mathbf{U} \cdot \nabla) \mathbf{U} \right) = -\nabla p + \rho \nu \nabla^2 \mathbf{U} - 2\boldsymbol{\Omega} \times \mathbf{U} + \mathbf{J} \times \mathbf{B}. \tag{2.12}$$

The Lorentz force $\mathbf{J} \times \mathbf{B}$ can be rewritten using Maxwell's Equations as $(1/\mu_0)(\nabla \times \mathbf{B}) \times \mathbf{B}$ hence the Navier-Stokes equation is non-linear in $\mathbf{B}$ when the fluid is electrically conducting.

Traditionally, dynamos are divided into two categories, namely kinematic dynamos and non-linear dynamos. The difference between these models is how the velocity field **U** is chosen. In kinematic dynamos, **U** is prescribed and can be chosen to represent observations which means that the Navier-Stokes equation doesn't need to be solved alongside the induction equation. In non-linear dynamos, the Navier-Stokes equations are solved together with the induction equation to find **U**. As shown in Equation (2.12), the Navier-Stokes Equation is non-linear in **B**, which greatly increases the complexity of the problem.

2.2.2 Antidynamo theorems

Through considering simple setups of the magnetic and velocity fields in a kinematic dynamo problem, it is possible to show that certain criteria have to be met in order to generate valid solutions. Cowling (1934) considered an axisymmetric magnetic field and imposed a velocity field that is also symmetric about the same axis. Under these circumstances it is possible to show that a steady axisymmetric flow cannot sustain a steady axisymmetric magnetic field. The proof of this theorem has been omitted for brevity but the details can be found in Moffatt (1978) or Choudhuri (1998). Another constraint was introduced by Zel'dovich (1957) who crucially concluded that a 2D incompressible flow (in which $U_z = 0$ in cartesian co-ordinates) cannot maintain a magnetic field.

2.2.3 Large-Scale and Small-Scale Dynamos

As discussed in Section 2.1.3, any dynamo must include a flow (to advect the magnetic field) or the field will simply decay. It is the velocity field that determines whether the generated dynamo action is classed as either small-scale or large-scale. A small-scale dynamo generates magnetic field at scales that is comparable to the velocity field or smaller whereas large-scale dynamos generate magnetic field at scales much larger than that of the velocity field (see, for example, Brandenburg *et al.*, 2012). It is believed that the Sun contains both large-scale and small-scale dynamos.

2.3 The dynamo process

2.3.1 Poloidal and toroidal fields

Before discussing the details of the components which combine to create a dynamo, it is necessary to define some of the terminology that is used. Throughout this thesis, poloidal field lines lie in the meridional plane (at least in axisymmetric geometry) whereas toroidal field lines are aligned to the azimuthal direction.

A dynamo process can be thought of as a closed loop which means that no external components are required to generate and maintain the magnetic field. Since this is the

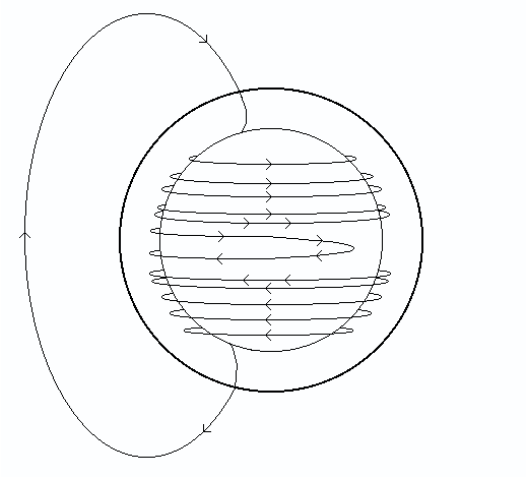

Figure 2.1: The omega-effect is caused by differential rotation. The Sun rotates faster at the equator than it does at the poles thus magnetic flux is stretched and wound around itself at the equator of the Sun resulting in the generation of toroidal field lines. Taken from Hathaway (2016).

case, a dynamo can be thought of as a cyclic process that converts poloidal field into toroidal field and vice versa. The remaining material in this section aims to describe the physical processes that are responsible for poloidal and toroidal field regeneration.

2.3.2 The ω effect

It was Bullard & Gellman (1954) who first stated that differential rotation was responsible for generating toroidal field from poloidal field. This differential rotation is caused by the fact that the Sun rotates significantly faster at the equator than it does at the poles resulting in poloidal field lines stretching out and effectively becoming wrapped around the Sun's rotational axis. Section 1.3.1 details the physical characteristics of the Sun that overwhelmingly supports this theory. It is widely accepted that differential rotation is responsible for the regeneration of toroidal field lines, meaning that this is a key component of the dynamo process, and without this mechanism, the dynamo loop would not be completed. A schematic diagram of the ω-effect is shown here in Figure 2.1.

2.3.3 The α effect

By necessity, a process is needed to convert toroidal magnetic field lines back into poloidal magnetic field lines. A process known as the α-effect is commonly invoked to complete this part of the dynamo loop and was first introduced in heuristic form by Parker (1955*a*). More elaborate forms have since been devised and a discussion of which is included here in Section 2.5. Parker's proposal was based upon the idea that the poloidal field is regenerated by cyclonic turbulence. This α-effect makes use of the fact that convection within the Sun's

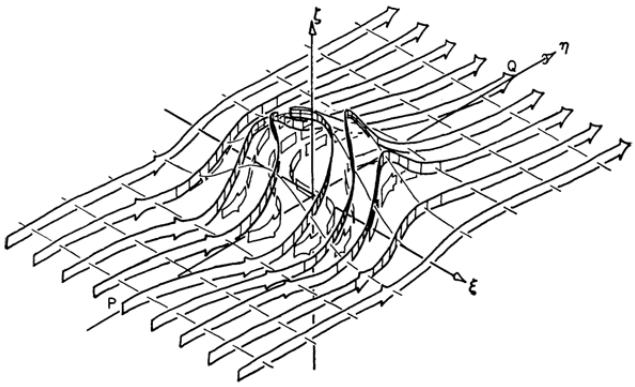

Figure 2.2: α-effect showing generation of poloidal field lines from toroidal field lines. As cyclonic turbulence pushes the toroidal field radially outwards they also become twisted in the poloidal direction. Taken from Parker (1955*a*).

interior will cause the toroidal field lines to be stretched upwards towards the surface. During this process, they also twist (due to the action of the Coriolis force) such that the resulting field line is momentarily acting in the poloidal direction. This in turn causes a current to be generated in the poloidal direction. Although the currents generated are small compared to the currents operating in the toroidal direction, if an average is taken over several of these turbulent events, generation of poloidal field lines will occur. The twisting of the toroidal field lines is shown here in Figure 2.2.

2.3.4 Parker's dynamo model

Parker (1955*a*) used these ideas to construct a simple illustrative dynamo model. The need for both α and ω effects becomes clear upon studying the induction equation (2.11). Working in cartesian geometry and in the Northern hemisphere, it is assumed that the x-axis is equatorwards, the y-axis is in the azimuthal direction and the z-axis points radially outwards. This corresponds as x acting as co-latitude to θ. In order to simplify the problem, it is assumed that A and B are both functions of x and t only. The standard poloidal/toroidal decomposition is used, the velocity profile is taken to represent a uniform shear and the magnetic diffusivity is taken to be constant:

$$\begin{aligned}\mathbf{B} &= B\hat{\mathbf{y}} + \nabla \times A\hat{\mathbf{y}},\\ \mathbf{u} &= \Omega_0 z\hat{\mathbf{y}},\\ \eta &= const,\end{aligned}$$

where A is the magnetic vector potential corresponding to the poloidal field, B is the

magnetic field operating in the toroidal direction and Ω_0 is constant.

Substituting these equations into the mean field induction equation yields the following set of coupled PDEs:

$$\frac{\partial A}{\partial t} = \eta \frac{\partial^2 A}{\partial x^2}, \tag{2.13}$$

$$\frac{\partial B}{\partial t} = \Omega_0 \frac{\partial A}{\partial x} + \eta \frac{\partial^2 B}{\partial x^2}. \tag{2.14}$$

It is clear that Equation (2.13) is simply a diffusion equation that contains no advective term. This means that A will eventually decay and the source term in Equation (2.14) will also vanish leading to the decay of the poloidal field. This clearly demonstrates the need for an α-effect to complete the dynamo loop and allow poloidal and toroidal field to be generated from one another. Parker (1955*a*) modified the governing equations to include an α-effect that would appear in the evolution equation for the toroidal field:

$$\frac{\partial A}{\partial t} = \alpha B + \eta \frac{\partial^2 A}{\partial x^2},$$
$$\frac{\partial B}{\partial t} = \Omega_0 \frac{\partial A}{\partial x} + \eta \frac{\partial^2 B}{\partial x^2}.$$

We can look for wave-like solutions of the form:

$$(A, B) = (A_0, B_0) \exp[i(kx + \omega t)],$$

where k is the wave number, ω is the frequency of the wave and both A_0 and B_0 are constants. Taking $k > 0$ without loss of generality leads to the following set of simultaneous equations:

$$A_0(i\omega + \eta k^2) - \alpha B_0 = 0,$$
$$ik\Omega_0 A_0 - (i\omega + \eta k^2) B_0 = 0,$$

meaning that as x is increased, the dynamo wave would propagate equatorwards. The equations are solved by rewriting them in matrix form, the solution of which is only non-trivial when the determinant of the matrix is zero. The following characteristic equation is generated:

$$k\Omega_0 \alpha i - (i\omega + \eta k^2)^2 = 0.$$

Solving this equation for $i\omega$ will determine the frequency of the resulting dynamo wave.

After some algebra, it can be shown that:

$$i\omega = \pm\sqrt{\left|\frac{\alpha\Omega_0 k}{2}\right|} - \eta k^2 \pm i\sqrt{\left|\frac{\alpha\Omega_0 k}{2}\right|}$$

where the modulus signs have been introduced to ensure that the expression under the square root remains positive and no imaginary part is introduced into the growth rate. It is important to note that the $\pm$ sign must have the same sign as the product of $\alpha\Omega_0$. Therefore the solutions for A and B are given by:

$$(A, B) = (A_0, B_0)\exp\left[ikx + \left(-\eta k^2 \pm \sqrt{\left|\frac{\alpha\Omega_0 k}{2}\right|} \pm i\sqrt{\left|\frac{\alpha\Omega_0 k}{2}\right|}\right)t\right].$$

For non-decaying solutions it is required that the real part of the growth rate is non-zero, i.e.:

$$-\eta k^2 \pm \sqrt{\left|\frac{\alpha\Omega_0 k}{2}\right|} > 0. \tag{2.15}$$

It is clear that the solution associated with the negative square root leads to decaying solutions and so this can be ignored. Rearranging this expression introduces a critical dynamo number (D_c) which much be exceeded if the resulting dynamo wave is to grow with time:

$$D_c = \left|\frac{\alpha\Omega_0}{\eta^2 k^3}\right| > 2.$$

Studying the imaginary part of the growth rate also leads to a satisfying conclusion:

$$\Im(i\omega) = \pm\sqrt{\left|\frac{\alpha\Omega_0 k}{2}\right|},$$

where the $\pm$ sign must have the same sign as the product of $\alpha\Omega_0$. For $\alpha\Omega_0$ greater than zero, $\Im(i\omega)$ remains positive resulting in a dynamo wave propagating in the negative x direction. However, if $\alpha\Omega_0$ is less than zero, $\Im(i\omega)$ is negative meaning that the dynamo wave propagates in the positive x direction.

It is clear that the product of the α and Ω_0 terms are important when considering the dynamo solution. Not only does this product have to be large enough to generate non-decaying solutions but the sign of the product controls the direction in which the wave travels.

2.4 Mean Field Theory

Parker's dynamo is based primarily upon physical intuition, however it is possible to derive a similar set of equations using mean-field dynamo theory.

Introduced by Steenbeck *et al.* (1966), mean-field theory describes how small-scale turbulent flows affect the generation and maintenance of large-scale magnetic fields. The primary way that this is achieved is through splitting the magnetic field $\mathbf{B}$ and the velocity field $\mathbf{U}$ into their mean (denoted by subscript zero) and fluctuating part (denoted by lower case letters). An important part of the theory is that the length scales over which the mean and fluctuating parts differ must be significant, i.e. if the mean part varies over a length scale L and the fluctuating part varies over a length scale l then it is necessary for $L \gg l$ in order for mean field theory to be valid. The Reynolds averaging rules are applied and the assumption is also made that the average value of the fluctuating part is zero, i.e.:

$$\begin{aligned} \mathbf{B} = \mathbf{B_0} + \mathbf{b}, \quad \langle \mathbf{b} \rangle = 0, \quad &\implies \langle \mathbf{B} \rangle = \langle \mathbf{B_0} \rangle = \mathbf{B_0}, \\ \mathbf{U} = \mathbf{U_0} + \mathbf{u}, \quad \langle \mathbf{u} \rangle = 0, \quad &\implies \langle \mathbf{U} \rangle = \langle \mathbf{U_0} \rangle = \mathbf{U_0}, \end{aligned}$$

where $< . >$ denotes an ensemble average. Substituting these quantities into the induction equation leads to the averaged induction equation:

$$\frac{\partial \mathbf{B_0}}{\partial t} = \nabla \times (\mathbf{U_0} \times \mathbf{B_0}) + \nabla \times \boldsymbol{\mathcal{E}} + \eta \nabla^2 \mathbf{B_0} \tag{2.16}$$

where $\mathcal{E} = \langle \mathbf{u} \times \mathbf{b} \rangle$, is known as the mean electromotive force and is the product of the random fluctuations of the field and flow. The fluctuating part of the induction equation can be obtained by subtracting Equation (2.16) from the mean field induction equation:

$$\frac{\partial \mathbf{b}}{\partial t} = \nabla \times (\mathbf{U_0} \times \mathbf{b}) + \nabla \times (\mathbf{u} \times \mathbf{B_0}) + \nabla \times \mathbf{G} + \eta \nabla^2 \mathbf{b} \tag{2.17}$$

where $\mathbf{G} = \mathbf{u} \times \mathbf{b} - \langle \mathbf{u} \times \mathbf{b} \rangle$. The aim now is to find a way of expressing $\mathcal{E}$ in terms of $\mathbf{U_0}$ and $\mathbf{B_0}$ so the system can be solved for $\mathbf{B}$.

By examining Equation (2.17) it is apparent that $\mathbf{b}$ is linearly related to $\mathbf{B_0}$; therefore it follows that $\mathcal{E}$ is also linearly related to $\mathbf{B_0}$. Thus it is acceptable to express $\mathcal{E}$ as a rapidly converging series of the form:

$$\mathcal{E}_i = \alpha_{ij} B_{0j} + \beta_{ijk} \frac{\partial B_{0j}}{\partial x_k} + \gamma_{ijkl} \frac{\partial^2 B_{0j}}{\partial x_k \partial x_l} + \ldots,$$

where the coefficients $\alpha_{ij}, \beta ijk, \ldots$ are pseudo-tensors because $\mathcal{E}$ is a polar vector whose

components change sign when switching between a right-handed and left-handed coordinate system and $\mathbf{B_0}$ is an axial vector whose components remain unchanged with the same transformation (Moffatt, 1978).

The leading term in the series expansion for $\mathcal{E}$ is given by:

$$\mathcal{E}_i^{(0)} = \alpha_{ij} B_{0j}.$$

For simplicity only the special case is considered when $\mathbf{u}$ is isotropic, i.e.

$$\alpha_{ij} = \alpha \delta_{ij},$$

where δ_{ij} is the Kronecker delta symbol. The second term in the series expansion for $\mathcal{E}$ is given by:

$$\mathcal{E}_i^{(1)} = \beta_{ijk} \frac{\partial B_{0j}}{\partial x_k}.$$

Again, only the simplest case is considered when $\mathbf{u}$ is isotropic, i.e.

$$\beta_{ijk} = \beta \epsilon_{ijk},$$

where ϵ_{ijk} is the Levi-Civita symbol. Therefore, a truncated expression for $\mathcal{E}_i$ is given by:

$$\mathcal{E} = \alpha \mathbf{B} - [\beta(\nabla \times \mathbf{B_0})] + \ldots$$

Substituting this truncated expression into Equation (2.16) leads to the following form of the mean-field induction equation:

$$\frac{\partial \mathbf{B_0}}{\partial t} = \nabla \times (\mathbf{U_0} \times \mathbf{B_0}) + \nabla \times [\alpha \mathbf{B_0} - \beta(\nabla \times \mathbf{B_0})] + \eta \nabla^2 \mathbf{B_0}.$$

Assuming β to be constant allows a well known vector identity to be used and the final form of the mean-field induction equation is derived:

$$\frac{\partial \mathbf{B_0}}{\partial t} = \nabla \times (\mathbf{U_0} \times \mathbf{B_0}) + \nabla \times (\alpha \mathbf{B_0}) + \eta_t \nabla^2 \mathbf{B_0},$$

where $\eta_t = \eta + \beta$.

Under these assumptions, it is clear that α can be a mechanism through which poloidal field can be generated. Considering β to be a positive constant shows that it contributes to the value of the effective diffusivity, leading to the conclusion that the turbulent motions also enhance the dissipation of magnetic fields.

The calculations of α and β are non-trivial. However expressions can be derived by studying the fluctuating part of the induction equation. Considering the case when $\mathbf{U_0} = \mathbf{0}$, leads to the simplification of Equation (2.17) since a term on the right hand side

vanishes. The equation is still extremely complex due to the presence of $\nabla \times \mathbf{G}$ and so the first order smoothing approximation is often used to simplify such an analysis.

The following equation shows the orders of magnitude for each term in the fluctuating part of the induction equation under the assumption that the mean flow is zero:

$$\frac{\partial \mathbf{b}}{\partial t} = \nabla \times (\mathbf{u} \times \mathbf{B_0}) + \quad \nabla \times \mathbf{G} \quad + \quad \eta \nabla^2 \mathbf{b}$$

$$O\left(\frac{b_0}{t}\right) = \quad O\left(\frac{b_0 u_0}{l_0}\right) \quad + \quad O\left(\frac{u_0 b_0}{l_0}\right) \quad + \quad O\left(\frac{\eta b_0}{l_0^2}\right)$$

where b_0 is a typical value of the magnetic field $\mathbf{b_0}$, u_0 is a typical value of the velocity field $\mathbf{u_0}$, l_0 is a typical length scale and t_0 is a typical value of the time scale t. There are two distinct situations that must be considered; the first is appropriate for conventional turbulence, $u_0 t_0 / l_0 = O(1)$, and the second is for random waves, $u_0 t_0 / l_0 \ll 1$. In the case of random wave turbulence dimensional analysis shows that $|\nabla \times \mathbf{G}| \ll |\partial \mathbf{B}/\partial t|$ and Equation (2.17) can be approximated by:

$$\frac{\partial \mathbf{b}}{\partial t} = \nabla \times (\mathbf{u} \times \mathbf{B_0}) + \eta_t \nabla^2 \mathbf{b}. \tag{2.18}$$

In the other case when conventional turbulence is considered, then $|\nabla \times \mathbf{G}|$ and $|\partial \mathbf{B}/\partial t|$ are of the same magnitude and neither can be neglected. However, a further simplification can be made through the introduction of the magnetic Reynolds number:

$$R_m = \frac{u_0 l_0}{\eta}.$$

If the magnetic Reynolds number is small, then both $|\nabla \times \mathbf{G}|$ and $|\partial \mathbf{B}/\partial t|$ is small compared to $|\eta \nabla^2 \mathbf{b}|$ and Equation (2.17) can be approximated by:

$$0 = \nabla \times (\mathbf{u} \times \mathbf{B_0}) + \eta_t \nabla^2 \mathbf{b}. \tag{2.19}$$

Although the assumptions made when deriving Equations (2.18) and (2.19) are different, both equations describe similar behaviour: the fluctuating part of the magnetic field $\mathbf{B}$ is generated through interactions between the mean field $\mathbf{B_0}$ and the fluctuating part of $\mathbf{U}$. In the case when $R_m \ll 1$ then the solution of Equation (2.18) will be an approximate solution to Equation (2.19). It is possible to solve Equation (2.18) for α through the use of Fourier transform techniques, see Moffatt (1978). The result shows that it is possible to derive an expression that relates α to the helicity of the velocity field. However, it is important to note that outside the first order smoothing approximation, (i.e. at high R_m, which is usually the case in astrophysical bodies) it is not possible to connect α directly

to the helicity of the flow, (see, for example, Cattaneo & Hughes, 2009).

2.5 Solar dynamo models

There are many things that are clear about the solar dynamo. Differential rotation is responsible for generating toroidal field lines from poloidal field lines (Bullard & Gellman, 1954). It is also thought that differential rotation in the tachocline leads to strong toroidal field at the base of the convection zone. Due to this property (and also because of strong turbulent pumping in the region) the tachocline is is the preferred location for flux storage (see, for example, Tobias, 2005).

However, what cannot be agreed upon is the nature of the α-effect (the process that is responsible for converting toroidal field lines back into poloidal field lines) and this is a topic of some debate. One such representation is the interface type α-effect, first described by Parker (1955*a*), as is described in Section 2.3.3. Another representation is from a Babcock-Leighton source term.

Interface dynamo models The challenge with this representation of the α-effect lies in describing a viable location where the α and ω-effects can be coupled. Strong toroidal fields will tend to inhibit (or quench) the operation of the α-effect, so interface dynamo models are usually constructed in such a way that Parker's α-effect due to cyclonic turbulence is restricted to the region just above the base of the convection zone, whilst the ω-effect (that was first introduced by Bullard & Gellman (1954)), operates just below the interface. The two layers are coupled by the effects of magnetic diffusion, as well as magnetic buoyancy and turbulent pumping, see for example (Tobias *et al.*, 2001). Importantly this means that the poloidal field is never strong in the region where the α-effect is located and thus the strong poloidal field does not suppress the α-effect, allowing the poloidal field to be regenerated. Parker (1993) described an interface dynamo model which was able to couple an α-effect operating in the convection zone with the differential rotation located at the base of the convection zone. These two effects were coupled through making use of a depth-dependent diffusion profile which had previously been studied by Ivanova & Ruzmaikin (1976). Interface dynamo models have proved very attractive and even with strong α-quenching, it has been shown that an interface dynamo of this type can operate efficiently, Charbonneau & MacGregor (see, for example, 1996).

Babcock-Leighton dynamo models In Babcock-Leighton dynamo models, the poloidal field is regenerated at the solar surface through the decay of active regions (which tend to emerge with a systematic tilt with respect to the azimuthal direction due to Joy's law), shown here in Figure 2.3. A toroidal field strength in excess of a few tens of kilogauss is re-

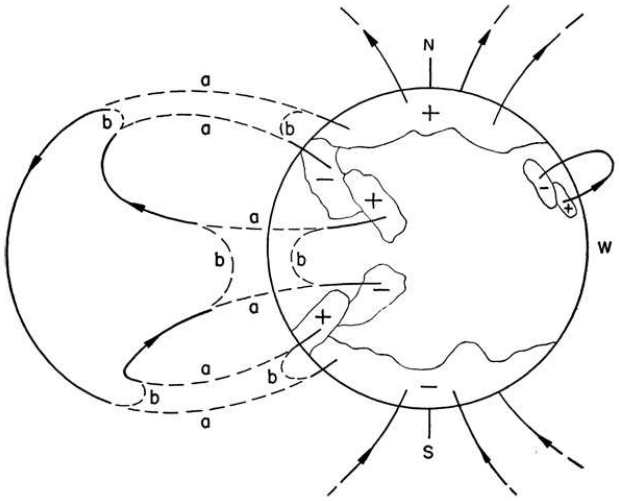

Figure 2.3: Babcock Leighton mechanism of poloidal field generated due to the decay of active regions. Taken from Babcock (1961)

quired for bipolar active regions to emerge with a systematic tilt compatible with Joy's law (see, for example, D'Silva, 1993; Caligari *et al.*, 1995; Fisher *et al.*, 1995). First proposed by Babcock (1961) and Leighton (1964), these models have also been elaborated upon by Wang *et al.* (1991), Wang & Sheeley (1991), Wang *et al.* (1991), Choudhuri *et al.* (1995), Durney (1995), Durney (1996), Durney (1997), and Dikpati & Charbonneau (1999).

This surface α-effect can only contribute to the dynamo if there is some mechanism that is capable of transporting the resultant poloidal field to the tachocline. This could be achieved by diffusion or by pumping, but meridional flows could also play an important role in this respect. A polewards meridional flow is observed at the solar surface (see, for example, Hathaway & Rightmire, 2010) and, by mass conservation arguments, there must be a returning circulatory flow somewhere within the solar interior. A single-cell meridional circulation, with an equatorial flow at the base of the convection zone would couple the surface layers to the tachocline in an effective way, thus completing the dynamo loop. Sheeley *et al.* (1987) and Wang *et al.* (1991) have added such a poleward meridional circulation at the solar surface to the Babcock-Leighton model first described by Babcock (1961) and Leighton (1964) with the result that meridional flows are very likely to play a fundamental part in the dynamo process.

In the earliest representation of Babcock-Leighton dynamo models, the only way in which the magnetic flux was transported to the tachocline was through diffusion, (Leighton, 1964, 1969). However in subsequent models, a meridional flow was included as a flux transport mechanism from the solar surface to the base of the convection zone (see, for example, Choudhuri *et al.*, 1995; Durney, 1995, 1996, 1997; Nandy & Choudhuri, 2001). Through the inclusion of a meridional flow, these models were able to reproduce

butterfly diagrams with a phase shift of approximately $\pi/2$ radians between the maximum of the toroidal field at the base of the convection zone and the reversal of the radial field at the solar surface. The Babcock-Leighton dynamo is only able to operate if there is sufficient magnetic flux transported to the solar surface through the decay of bipolar magnetic regions. This requires the magnetic flux tubes to be of sufficient strength and quantity in order to deposit magnetic flux on the solar surface. This has been seen as a problem by some (see, for example, Layzer *et al.*, 1979), however it is an attractive feature when considering the mechanisms through which grand minima are produced. An advantage of the Babcock-Leighton mechanism is that a strong toroidal field is *required* at the base of the convection zone in order for magnetic flux tubes of sufficient strength to rise to the solar surface. This is in direct contrast to the interface dynamo models where strong toroidal fields tend to inhibit the interface α-effect.

More details of further studies concerning Babcock-Leighton dynamo models are given in Section 6.1.

2.6 Modulating the Solar Dynamo

As I have already described in Chapter 1, the solar cycle is modulated in time. A complete model of the solar dynamo must be able to explain the observed modulation as well as the 22 year magnetic cycle, and the following sections aim to describe a range of deterministic or stochastic models which are able to capture this behaviour.

2.6.1 Stochastic

The solar convection zone is highly turbulent meaning that there is a strong likelihood that the physical process that combine to create the solar dynamo will contain some form of (effectively) random fluctuations. It has been shown that it is possible to induce modulation by introducing stochastic effects into Babcock-Leighton models (see, for example, Charbonneau & Dikpati, 2000; Bushby & Tobias, 2007), as well as into models of interface type (Ossendrijver, 2000).

Indeed, stochastic fluctuations in the interface α-effect have proven successful when trying to reproduce modulated solutions. Moss *et al.* (1992) showed that through including a stochastic fluctuation to the interface type α-effect, the resulting solar cycle behaviour showed variations in both space and time. Hoyng (1993) considered a similar model utilising an α-effect which included stochastic fluctuations as a function of time and a key result from the study was the relationship between the phase and amplitude of the magnetic cycle. They found that stronger magnetic cycles of greater amplitude lasted for shorter periods of time, whereas weaker magnetic cycles lasted for longer periods of time. This phenomenon is well known in solar physics as the Waldmeier effect, (see, for

example, Karak & Choudhuri, 2010). Ossendrijver *et al.* (1996) expanded upon the model described by Hoyng (1993) and included stochastic fluctuations to α that were both a function of latitude and time. Their results were also able to produce the anticorrelation between the solar cycle phase and amplitude already described by Hoyng (1993). They also found asymmetry in the amount of magnetic flux within each hemisphere. As described by Vizoso & Ballester (1990) and Carbonell *et al.* (1993) solar observations have shown that this asymmetry usually peaks during a cycle minimum and the study by Ossendrijver *et al.* (1996) was able to reproduce this feature.

It is not only interface dynamo models that are successful in reproducing modulation due to stochastic effects. Charbonneau & Dikpati (2000) chose to look at a Babcock-Leighton dynamo model with large-amplitude stochastic fluctuations in either or both of the meridional flow or poloidal field source term. When the only fluctuating component of the model was built into the meridional circulation, modulated cycles are found and the results indicate that cycles of greater amplitude lead to longer cycles, which is in direct disagreement with solar observations. However when the model is adapted to include a statistically steady meridional flow and a stochastically fluctuating poloidal field source term, modulation is again present and the results can reproduce the observed anticorrelation between the solar cycle phase and amplitude. The authors also show that for a given set of parameters, fluctuations in both the meridional circulation and poloidal source term can reproduce the anticorrelation between the solar cycle phase and amplitude. The model is able to induce short term modulation of the solar cycle however it proves difficult to produce long periods of reduced magnetic activity.

2.6.2 Deterministic

Fully deterministic models (with no random elements) can also produce modulated dynamo waves. Weiss *et al.* (1984) and Jones *et al.* (1985) considered a simple system in which the dynamo was modelled using a set of coupled ordinary differential equations, which included the nonlinear interactions between the magnetic field and the flow. They found that it was possible to generate quasiperiodic and chaotically-modulated solutions in addition to standard periodic dynamo waves.

More recent studies have shown that the full mean-field equations also exhibit significant modulation when dynamical nonlinearities are included in the governing equations. Kitchatinov *et al.* (1994) and Brandenburg *et al.* (1989) introduced nonlinearities into the governing equations and were able to show that the magnetic energy was modulated on a timescale that was significantly longer than the period of the dynamo wave. These models, however, rely upon the interactions between quadrupolar and dipolar parities which is not consistent with observations of the Sun's overwhelmingly dipolar magnetic field exhibiting amplitude modulation.

Tobias (1996) demonstrated that it is possible to induce significant modulation of the magnetic cycle through including a velocity perturbation acting in the toroidal direction that is dependent upon the large-scale Lorentz force. This leads to the introduction of a magnetic Prandtl number τ and the results show that as τ becomes small, the amplitude of the magnetic cycle is significantly modulated. Although the governing equations are solved in 2 dimensions, only one hemisphere is contained in the computational domain and the boundary conditions are selected such that the solution must be dipolar in nature. Tobias (1997) solved the same governing equations in both hemispheres and concluded that solutions of dipolar symmetry were still able to generate modulation when the dynamo was free to choose its preferred parity. The suppositions of Tobias (1996) and Tobias (1997) are confirmed by Brooke *et al.* (2002) who deduced that the modulation occurs on a timescale that is related to the magnetic Prandtl number through a simple power law relationship.

The back reaction of the Lorentz force upon the magnetic field has also been studied by Bushby (2006). The conclusion supported previous work by confirming that when the magnetic Prandtl number is small, episodes of significantly reduced magnetic activity were present within the system. A further conclusion of this paper was that even when the solution is chaotically modulated, it is possible to find migrating bands of zonal flows at high and low latitudes that oscillate in time. These solar-like zonal flows were not able to be demonstrated by Brooke *et al.* (2002).

It is also possible to show that time delays can be responsible for modulating the dynamo wave. Yoshimura (1978) demonstrated that modulation can arise if explicit time delays are built into the nonlinear terms in a simple system of model dynamo equations. One way this is done is through considering the delay instigated through the action of the velocity field upon the magnetic field. When new magnetic flux is formed, the velocity field cannot adjust instantaneously to this change and a time delay will be introduced into the system. This model was particularly successful in reproducing solutions with long term modulation that are characterised by periods of reduced activity occurring every $50 - 80$ years.

It has already been established by Dikpati & Charbonneau (1999), Charbonneau & Dikpati (2000) and Hathaway *et al.* (2003) that the meridional flow is responsible for setting the sunspot cycle period (this is intuitive since the Babcock-Leighton dynamo model relies upon the meridional flow to complete the dynamo loop). However, the process of transporting magnetic flux from the solar surface to the base of the convection zone is not instantaneous and will introduce a time delay that is comparable to the cycle period. It is this time delay that Charbonneau *et al.* (2005) introduced into the Babcock-Leighton dynamo model that was described by Dikpati & Charbonneau (1999) and they were able to show that as the dynamo number is increased, the solution goes through a sequence of

period-doubling bifurcations until the solution eventually becomes strongly modulated.

It is not only Babcock-Leighton dynamo models that include this time delay. In fact, any dynamo model where the α and ω effects are spatially separated will, by necessity, introduce a time delay due to the fact that magnetic flux cannot be transported instantaneously between these two regions. It is exactly this setup that is described by Wilmot-Smith *et al.* (2006) who found that this time delay can lead to modulation with the most strongly modulated solutions found in the regime where the time delay is much larger than the diffusive timescale.

Many studies have concentrated upon examining the rise time of toroidal flux tubes from the base of the convection zone up into the solar surface (see, for example, D'Silva & Choudhuri, 1993; Fan *et al.*, 1994; Caligari *et al.*, 1995; Jouve & Brun, 2009) with the conclusion that the initial strength of the magnetic field at the base of the convection zone is a key factor in the time evolution of the flux tube. Jouve *et al.* (2010) expanded upon the results of these studies to formulate a two-dimensional dynamo model that included a Babcock-Leighton source term that was dependent upon the time delay generated by the rise time of the flux tubes from the base of the convection zone to the solar surface. The study was successful; they were able to demonstrate the existence of modulated cycles. They then went on to consider a simpler one-dimensional dynamo model in which the surface α-effect term was represented by the inclusion of a time-delayed toroidal field (with a parameterised time delay that was dependent upon the magnetic field strength). They were able to demonstrate the existence of a sequence of bifurcations from periodic to chaotically modulated solutions as the time delay parameter was increased.

2.7 Competing alpha-effects

Given the uncertainty of the mechanism that is responsible for the regeneration of the poloidal field, it is acceptable to consider the scenario in which both a surface α-effect and interface α-effect are operating within the solar dynamo. Because these two processes remain spatially separated, it is interesting to investigate the competition (interaction) between these two mechanisms and their effect on the time evolution of the toroidal field with the ultimate aim to identify (if possible) which is the dominant source term.

Previous studies have investigated systems with competing α-effects. Dikpati & Gilman (2001) introduced both sources of poloidal field regeneration into a model that solved the $\alpha\omega$ dynamo equations in 2D spherical geometry. They show that when the relative strengths of the source terms are equal, a mixed mode solution is found. When either α-effect is taken to be 5 times larger than the other, it is found that the cycle period is governed by the α-effect of greater magnitude. The paper also details how the magnitudes of these competing α-effects can be chosen such that they no longer work to enhance the

dynamo and indeed they can be combined such that they interact destructively to kill the dynamo. It is important to note that the paper cannot determine which α-effect is the dominant source of poloidal field regeneration; however the point is made that it is likely that both α-effects are present within the Sun but that only the interface α-effect can be responsible for restarting the dynamo after a period of grand minima due to the fact that a Babcock-Leighton source term relies upon the decay of active regions at the solar surface.

Mason *et al.* (2002) provide strong evidence to suggest that the interface type α-effect is the preferred method for poloidal field regeneration through demonstrating that even when the surface α-effect is several orders of magnitude stronger than the interface α-effect, the region near the tachocline remains the preferred location for the regeneration of the poloidal field. The study is constructed by considering a cartesian system with an interface type α-effect at the tachocline and an additional (local) surface α-effect which are both represented by using delta functions. It is important to note that the system is studied with no meridional flow meaning that the only way in which magnetic flux can be transported from the solar surface to the tachocline (the region where the dynamo is believed to operate) is through the effects of diffusion. A meridional flow would certainly enhance the effects of a surface α-effect; however it would also transport poloidal flux that is generated by cyclonic turbulence in the convection zone further enhancing the dynamo from a non-surface α-effect. Mann & Proctor (2009) extended this model by including the effects of a meridional flow and a non-local surface alpha effect. The conclusion is made that the inclusion of both of these factors significantly affect the potency of the surface alpha-effect. Firstly, it is found that a non-local surface source term is more efficient than a local surface source term meaning that the deep-seated α-effect would need to be significantly stronger if it is to remain the dominant source of poloidal field regeneration. Secondly, after introducing a meridional flow into the model, the results indicate that the deep-seated α-effect becomes less efficient as the speed of the meridional flow increases. By increasing the meridional flow, the toroidal flux that is generated by the deep-seated α-effect spends less time in the tachocline hence reducing its effectiveness.

It is fair to say that there is no consensus as to which source term is the dominant mechanism for poloidal field regeneration. What is clear however is that a Babcock-Leighton surface source term (which is dependent upon the toroidal field at the base of the convection zone to deposit toroidal flux at the solar surface in the form of sunspots) would be unable to restart the solar dynamo after a period of grand minima. It is therefore likely that both α-effects are present within the Sun with the interface type alpha effect (which arises through the action of cyclonic turbulence in the solar convection zone) responsible for restarting the dynamo after a period of reduced magnetic activity (Charbonneau *et al.*, 2004).

Part II

Competing α-effects in Cartesian Geometry

Chapter 3

Competing α-effects

The aim of this chapter is to investigate the competition between two different α-effects, motivated by likely competition between a deep-seated (interface) α-effect and a surface α-effect. Building on the approach described by Jouve *et al.* (2010), who did not include a deep-seated α-effect, the influence of the surface α-effect will be modelled using a time-delayed toroidal field. The use of a time delay is natural in this context: even if flux tubes rise rapidly to the surface, the time taken for the resultant poloidal field to be transported back to the tachocline will, in general, be non-negligible compared to the period of oscillation of the dynamo. Previous studies have investigated systems with competing α-effects (see, for example, Dikpati & Gilman, 2001; Mason *et al.*, 2002; Mann & Proctor, 2009), but it is believed that this is the first study to consider the effects of explicit time delays in a model of this type. The majority of the material contained in this chapter has been published in Astronomy and Astrophysics (Cole & Bushby, 2014).

3.1 Model Setup

Following a similar approach to that adopted by Jouve *et al.* (2010), I consider a simple, illustrative model of the solar dynamo. This model is based upon the standard mean-field dynamo equation (see, e.g., Moffatt, 1978),

$$\frac{\partial \mathbf{B}}{\partial t} = \nabla \times (\alpha \mathbf{B} + \mathbf{U} \times \mathbf{B}) + \eta_T \nabla^2 \mathbf{B},$$

where $\mathbf{U}$ is the large-scale velocity field, α represents the standard mean-field α-effect, η_T is the turbulent magnetic diffusivity (which is assumed to be constant), whilst the mean magnetic field, $\mathbf{B}$, satisfies $\nabla \cdot \mathbf{B} = 0$. Instead of solving this equation in spherical geometry, the simpler problem of dynamo action in a flat Cartesian domain is considered, with the axes oriented so that the y-axis would correspond to the azimuthal direction on a spherical surface. I can then look for dynamo solutions that depend only on a single

spatial variable x (which can be regarded as being analogous to the co-latitude) and time t meaning that the model is constructed to represent a dynamo operating at the base of the tachocline. The solenoidal constraint upon $\mathbf{B}$ can then be satisfied by writing the magnetic field in the following form:

$$\mathbf{B}(x,t) = B(x,t)\hat{\mathbf{y}} + \nabla \times [A(x,t)\hat{\mathbf{y}}]\,,$$

where $B(x,t)$ is the toroidal field component, whilst $A(x,t)$ corresponds to the poloidal potential. For simplicity, it is assumed that α, which represents a deep-seated α-effect, is constant, i.e. $\alpha = \alpha_0$. Furthermore, a fixed velocity profile is adopted of the form $\mathbf{U} = v_0\hat{\mathbf{x}} + \Omega_0 z\hat{\mathbf{y}}$, where v_0 and Ω_0 are both assumed to be constant in this illustrative model. This velocity field gives a constant meridional flow and a differential rotation profile (i.e. $\partial\mathbf{U}/\partial z$) that is independent of x. The well known $\alpha\Omega$ approximation is used, which assumes that differential rotation is the dominant mechanism for toroidal field regeneration. Following Jouve *et al.* (2010), a delayed toroidal field $Q(x,t)$ is also introduced, which lags behind the normal toroidal field with a time delay denoted by τ. The delayed toroidal field is coupled to the other equations via the inclusion of an additional poloidal source term, $SQ(x,t)$, where S is a constant. This source term can be regarded as being the contribution to the local poloidal field from the non-local surface α-effect (which must, therefore, depend upon the strength of the toroidal field at earlier times). Finally, parameterised quenching nonlinearities are introduced into both of the α-effect terms in the poloidal field equation.

This model is different to the system investigated by Jouve *et al.* (2010) in that there are two mechanisms for poloidal field regeneration, namely the Babcock-Leighton and interface type α-effects. In the model studied by Jouve *et al.* (2010) the only source of poloidal field regeneration was from a Babcock-Leighton surface source term however it is likely that both types of α-effects are present within the Sun. It is therefore justified to adapt the governing equations stated in Jouve *et al.* (2010) to include an additional source of poloidal field regeneration from an interface type α-effect and investigate how these two competing α-effects interact with each other. It is important to note that this is not the only difference in the two models. In my model, the time delay τ is assumed to be constant unlike in Jouve *et al.* (2010) where the time delay was considered to be dependent upon the toroidal magnetic field strength. The motivation behind the B-dependent time delay adopted by Jouve *et al.* (2010) was to model the property that the rise times of the flux tubes from the base of the convection zone to the solar surface are dependent upon the toroidal field strength B. Although this is a valid assumption, this elaborate feature hasn't been incorporated into my model in order to focus more clearly on other features of the dynamical system.

Having made these assumptions, it is now possible to write down the three scalar

partial differential equations (PDEs) for $A(x,t)$, $B(x,t)$ and $Q(x,t)$:

$$\frac{\partial A}{\partial t} + v_0\frac{\partial A}{\partial x} = \frac{SQ}{1+\lambda|Q|^2} + \frac{\alpha_0 B}{1+\lambda|B|^2} + \eta_T\frac{\partial^2 A}{\partial x^2}, \tag{3.1}$$

$$\frac{\partial B}{\partial t} + v_0\frac{\partial B}{\partial x} = \Omega_0\frac{\partial A}{\partial x} + \eta_T\frac{\partial^2 B}{\partial x^2}, \tag{3.2}$$

$$\frac{\partial Q}{\partial t} = \frac{1}{\tau}\left(B - Q\right), \tag{3.3}$$

where λ is a constant that determines the strength of the nonlinear quenching. Here the simplest form of quenching is considered where the relative strengths of the quenching parameters are the same for both types of α-effects and is taken to be 1. The differential equation for $Q(t)$ is derived from considering the Taylor series expansion of $Q(t)$, i.e.

$$\begin{aligned}
& Q(t) = B(t-\tau), \\
\iff & B(t) = Q(t+\tau), \\
\implies & B(t) = Q(t) + \tau\frac{\partial Q}{\partial t}(t) + O(\tau^2), \\
\implies & \frac{\partial Q}{\partial t} = \frac{1}{\tau}[B(t) - Q(t)] + O(\tau^2).
\end{aligned}$$

In order to reduce the number of parameters that control the system, the variables can be rescaled as follows:

$$A = \frac{\alpha_0 B_0 L^2}{\eta_T}A', \qquad B = B_0 B', \qquad Q = B_0 Q', \qquad t = \frac{L^2}{\eta_T}t',$$
$$\tau = \frac{L^2}{\eta_T}\tau', \qquad x = Lx', \qquad S = \alpha_0 S',$$

where L is a characteristic length-scale and B_0 is a representative value of the magnetic field strength (which may be chosen so that the constant coefficient in the quenching terms equals unity in these scaled variables). On dropping the primes, the following set of PDEs are obtained:

$$\frac{\partial A}{\partial t} + Re\frac{\partial A}{\partial x} = \frac{SQ}{1+|Q|^2} + \frac{B}{1+|B|^2} + \frac{\partial^2 A}{\partial x^2}, \tag{3.4}$$

$$\frac{\partial B}{\partial t} + Re\frac{\partial B}{\partial x} = D\frac{\partial A}{\partial x} + \frac{\partial^2 B}{\partial x^2}, \tag{3.5}$$

$$\frac{\partial Q}{\partial t} = \frac{1}{\tau}\left(B - Q\right). \tag{3.6}$$

Thus the only parameters to control the system are the Reynolds number, $Re = v_0 L/\eta_T$, which measures the strength of the meridional flow, the dynamo number, $D = \alpha_0 \Omega_0 L^3/\eta_T^2$, which indicates the strength of the dynamo sources relative to magnetic dissipation, the magnitude of the Babcock-Leighton source term S and the value of the time delay τ.

This system can be further simplified by carrying out a local analysis. Because I have the freedom to choose a convenient characteristic length-scale (due to the fact that there is no characteristic length-scale in the horizontal direction), local wavelike solutions can be assumed to have a unit wavenumber without any loss of generality. I therefore seek solutions of the form $A = \tilde{A}(t)e^{ix}$, $B = \tilde{B}(t)e^{ix}$ and $Q = \tilde{Q}(t)e^{ix}$, where $\tilde{A}(t)$, $\tilde{B}(t)$ and $\tilde{Q}(t)$ are complex functions of time only. Dropping the tildes, the governing equations for these quantities become:

$$\frac{dA}{dt} + iReA = \frac{SQ}{1+|Q|^2} + \frac{B}{1+|B|^2} - A, \tag{3.7}$$

$$\frac{dB}{dt} + iReB = iDA - B, \tag{3.8}$$

$$\frac{dQ}{dt} = \frac{1}{\tau}\left(B - Q\right). \tag{3.9}$$

Equations (3.7) to (3.9) describe the time evolution of the magnetic fields A, B and Q in dimensionless form, with the same quenching mechanisms for both types of α-effects. The remaining work included in this chapter is based upon studying these governing equations both analytically and numerically.

Following the methods used in Jones *et al.* (1985) and Jouve *et al.* (2010) it is also possible to reduce the order of this system by using the following representation:

$$A = \rho y e^{i\theta},$$
$$B = \rho e^{i\theta},$$
$$Q = \rho z e^{i\theta},$$

where ρ and θ are real quantities and y and z are complex numbers. Upon substituting these expressions into the governing equations (3.7) - (3.9), the following set of 5 real ODEs is obtained:

$$\frac{d\rho}{dt} = -D\rho y_2 - \rho, \tag{3.10}$$

$$\frac{dy_1}{dt} = \frac{Sz_1}{1+\rho^2(z_1^2+z_2^2)} + \frac{1}{1+\rho^2} + 2y_1y_2D, \tag{3.11}$$

$$\frac{dy_2}{dt} = \frac{Sz_2}{1+\rho^2(z_1^2+z_2^2)} + Dy_2^2 - Dy_1^2, \tag{3.12}$$

$$\frac{dz_1}{dt} = \frac{1-z_1}{\tau} + Dy_1z_2 + Dy_2z_1 - Rez_2 + z_1, \tag{3.13}$$

$$\frac{dz_2}{dt} = \frac{-z_2}{\tau} - Dy_1z_1 + Dy_2z_2 + Rez_1 + z_2, \tag{3.14}$$

where y_1 and y_2 represent the real and imaginary parts of y respectively and z_1 and z_2 represent the corresponding real and imaginary parts of z. By plotting ρy, ρ and ρz against time, it is possible to determine how the magnitudes of the magnetic fields A, B and Q evolve over time with any change in magnitude corresponding to modulation of the dynamo wave. Through this representation, the magnitude of the poloidal potential A and the delayed field Q is measured relative to the toroidal field B.

3.2 Critical Dynamo Number Calculations

In this section, focus is turned towards the governing equations of the local model that are described by Equations (3.7) – (3.9). To further our understanding of this system, I have carried out a series of calculations to determine the critical value of the dynamo number as the parameters S and τ are varied (at fixed Re). It is also possible to identify the value of τ that leads to quasi-periodic solutions analytically by studying the stability of the periodic solution.

3.2.1 Solution method

The critical dynamo numbers can be calculated by linearising the governing equations (3.7) – (3.9) and writing A, B and Q in the following form: $A = \hat{A}e^{\sigma t}, B = \hat{B}e^{\sigma t}$ and $Q = \hat{Q}e^{\sigma t}$. The following characteristic equation is generated:

$$(\sigma + iRe + 1)^2\left(\sigma + \frac{1}{\tau}\right) - iD\left(\sigma + \frac{1}{\tau}\right) - \frac{iSD}{\tau} = 0. \tag{3.15}$$

Setting the real part of the growth rate to be zero and solving the characteristic equation for the imaginary part of σ will determine the critical value of the dynamo number, D_c, at which the trivial (non-magnetic) solution loses stability to oscillatory dynamo waves. Letting $\sigma = i\omega$ ($\omega \in \mathbb{R}$), the following algebraic equation for the frequency is obtained:

$$\begin{aligned} -i\omega^3 - \frac{\omega^2}{\tau} - 2i\omega^2 Re - \frac{2Re\omega}{\tau} - 2\omega^2 + \frac{2i\omega}{\tau} - iRe^2\omega - \frac{Re^2}{\tau} \\ -2\omega Re + \frac{2iRe}{\tau} + i\omega + \frac{1}{\tau} + D_c\omega - \frac{iD_c}{\tau} - \frac{iSD_c}{\tau} = 0. \end{aligned} \tag{3.16}$$

To proceed further, the real and imaginary parts of Equation (3.16) are separated leading to the following set of simultaneous equations:

$$\frac{\omega^2}{\tau} + \frac{2Re\omega}{\tau} + 2\omega^2 + \frac{Re^2}{\tau} + 2\omega Re - \frac{1}{\tau} - \omega D_c = 0, \tag{3.17a}$$

$$\omega^3 + 2\omega^2 Re + \frac{2\omega}{\tau} + Re^2\omega - \frac{2Re}{\tau} - \omega + \frac{D_c}{\tau} + \frac{SD_c}{\tau} = 0. \tag{3.17b}$$

The equations are solved by rearranging Equation (3.17a) to obtain the critical dynamo number D_c as a function of ω and substituting this form of D_c into Equation (3.17b) to solve for ω. The resulting equation is quartic in ω which is solved using a linear bisection method followed by a Newton-Raphson numerical approach to further enhance the accuracy of the estimate. Solving these coupled characteristic equations determines how the critical value of the dynamo number changes as the time delay τ and the strength of the Babcock-Leighton source term S are varied.

Setting S to be zero means that the governing equations revert to the standard $\alpha\omega$ equations. The critical dynamo number can be calculated analytically from Equation (3.15) since the last term is now zero and the factor of $(\sigma + 1/\tau)$ can be factored out, i.e.

$$(\sigma + iRe + 1)^2 - iD = 0.$$

Rearranging for σ gives:

$$\sigma = -iRe - 1 \pm \frac{1}{\sqrt{2}}(1+i)\sqrt{|D|}.$$

Setting the real part of σ to be zero will determine the critical value of $|D|$ that is needed in order to give non-decaying solutions. Hence:

$$\begin{aligned} 0 &= -1 + \frac{1}{\sqrt{2}}\sqrt{|D_c|} \\ \implies |D_c| &= 2, \\ \implies D_c &= \pm 2. \end{aligned}$$

This value of D_c is independent of ω and the Reynolds number and so it is expected that at all values of Re when $S = 0$, D_c should be ± 2. It is also possible to represent the

frequency of the wave in terms of the Reynolds number and the Dynamo number:

$$\omega = -Re \pm \sqrt{\frac{|D|}{2}}.$$

In the case where $S = 0$ it is evident that the frequency of the wave will still depend upon the dynamo number D and the Reynolds number Re and thus, in conclusion, it is only the real part of the growth rate that remains independent of all the parameters in the system.

Generally, when S is non-zero, the critical dynamo number is dependent upon several parameters and so it is important to consider all possible non-trivial cases separately:

3.2.2 Results - No meridional flow

Initially the system is investigated when there is no flow present, i.e. $Re = 0$. This significantly reduces the complexity of Equations (3.17a) and (3.17b); however the algebra still remains lengthy, making it difficult to formulate an analytical relation between S and τ. The critical dynamo numbers have been evaluated numerically and are displayed in Figures 3.1a, 3.1b and 3.2.

Positive D Since Equation (3.17b) is cubic in ω, there is more than one solution of the equation and the smallest value of $|D_c|$ is displayed from all of the solutions. As S becomes small, the governing equations (3.7) and (3.8) tend towards the typical $\alpha\Omega$ dynamo equations and so it is important to note that for all values of τ the critical dynamo number of the competing alpha system tends towards 2 as S approaches 0, which is consistent with the calculations included above.

The plots show that for all values of τ, and for positive values of S, as the magnitude of the time-delayed source term increases the critical dynamo number decreases, indicating that it is easier to excite the dynamo. However, the results for $S < 0$ show that the relationship between $|S|$ and D_c is non-monotonic. The critical value of D depends upon the frequency of the wave, and there exists a cusp (the location of which is dependent upon τ) which is created due to the matching up of two distinct branches. Figure 3.1b shows the value of the critical dynamo number for $-2 < S < 2$. It is clear that as τ is increased, the cusp is located at more negative values of $-S$.

This behaviour is interesting as it suggests that the sign and magnitude of S both play an important role in determining whether the competing α-effects are working constructively or destructively. For values of S greater than zero, the two competing α effects are acting in the same direction and appear to be working together to help drive the dynamo. However, when $S < 0$, the way in which these two α-effects interact is non-trivial. The key to understanding this behaviour is through studying Equation 3.7. Considering the special case when $S = -1$ and $\tau \ll 1$, the two source terms in Equation 3.7 are of the

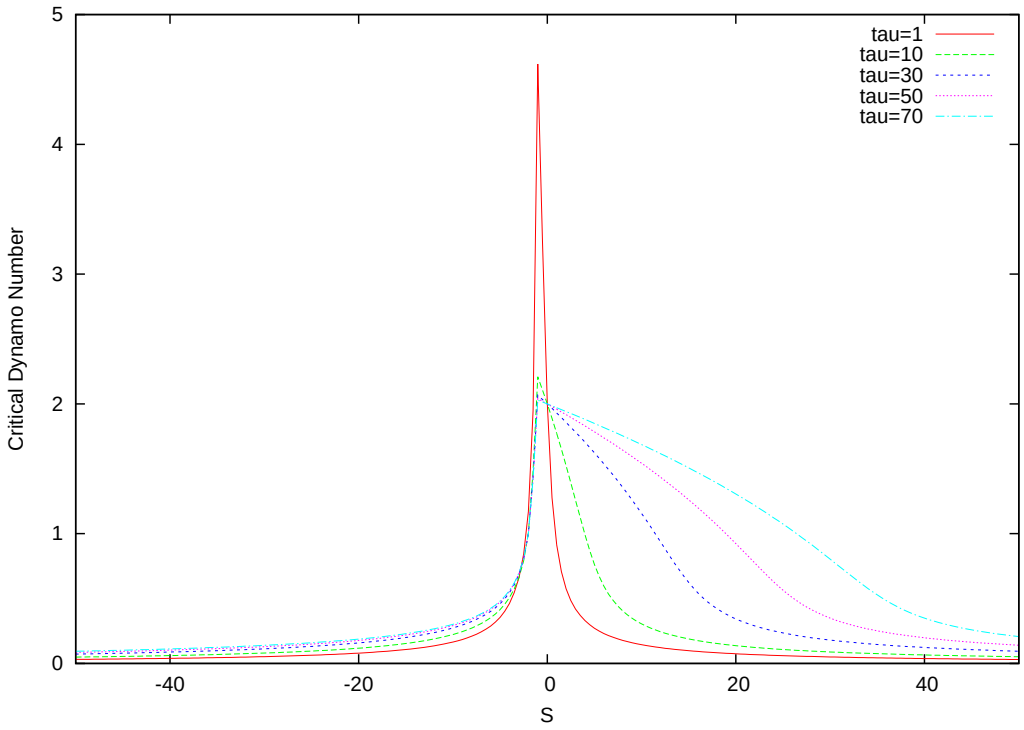

(a)

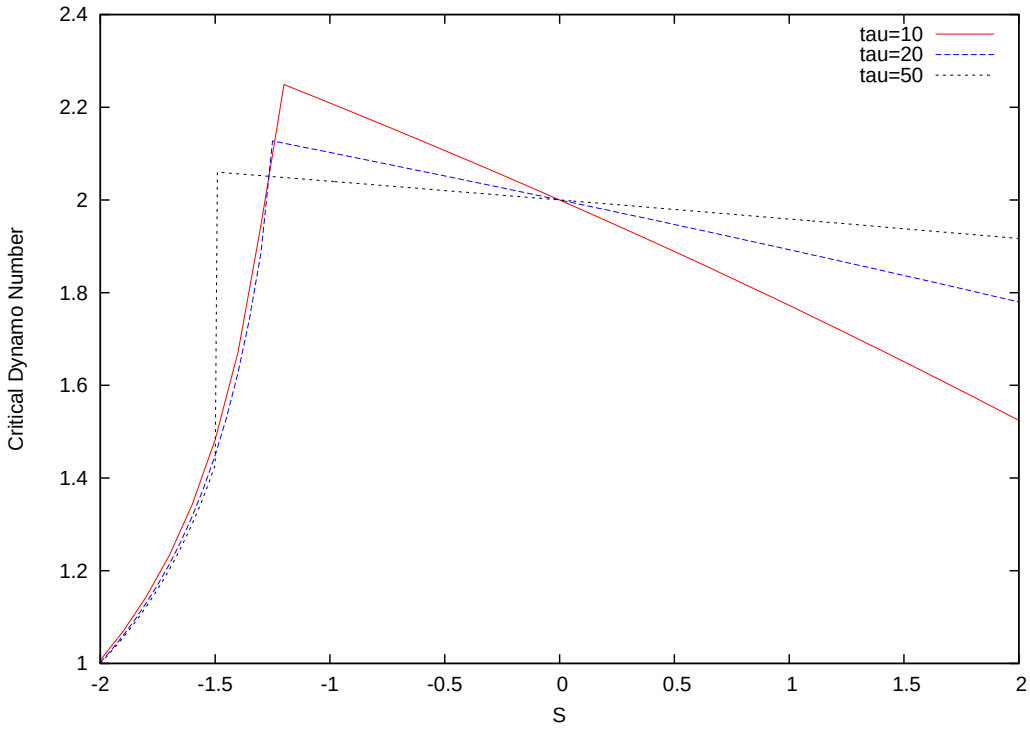

(b)

Figure 3.1: Top: $Re = 0$. Plot of the critical dynamo number D against S for fixed values of τ greater than or equal to 1 when $-50 < S < 50$. Bottom: $Re = 0$. Plot of the critical dynamo number D against S for fixed values of τ greater than 1 when $-2 < S < 2$.

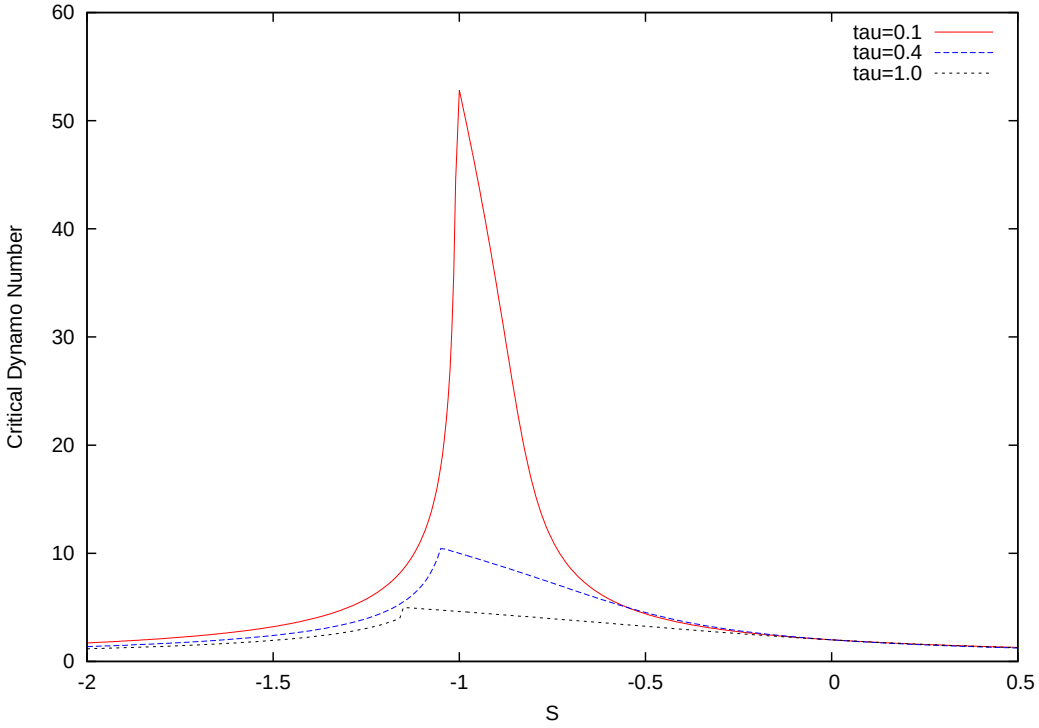

Figure 3.2: $Re = 0$. Plot of the critical dynamo number D against S for fixed values of τ less than or equal to unity.

same order and so the source term in Equation 3.7 becomes rather small. In the limit of vanishing τ, B tends to Q and so there can be no dynamo if $S = -1$. This behaviour can be seen in Figure 3.2 with the value of $\tau = 0.1$ most closely related to this scenario. This is perhaps the region of most interest since the Taylor series expansion of $Q(t)$ that is used to derive the governing equations (3.7) – (3.9) is valid for small values of τ.

As the value of τ increases, Q is of lower amplitude than B requiring $-S$ to be of greater magnitude such that the contribution from the time-delayed source term in Equation 3.7 is of the same order as the interface source term. This is clearly reflected in Figures 3.1b and 3.2 since the cusp is located at a greater value of $|S|$. After this cusp has been reached, as $-S$ increases the two competing α-effects work together again to help drive the dynamo.

Apart from a very narrow range of $-S$ (the size of which is dependent upon τ) it is fair to say that even when S and α work in opposite directions against each other increasing the magnitude of S still helps the to drive the dynamo. In this region, the assumption can be made that it is simply the presence of an additional surface like α-effect, irrespective of the direction of action, that makes it easier to generate non-decaying solutions.

Negative D The same calculations are made for negative values of the critical dynamo number. It is important to consider any symmetries present within the system and through

studying Equations 3.17a and 3.17b it is apparent that letting $D \to -D$, $\omega \to -\omega$ and $Re = 0$, the system is indeed the same. This indicates that the results for the positive D and negative D cases should be a reflection of each other in the S axis. By comparing the numerical results for negative values of the critical dynamo number, it is indeed the case that the two plots are a reflection in the S axis. Due to the similarity of the results to those displayed in Figures 3.1a, 3.1b and 3.2, the corresponding plots have been omitted.

3.2.3 Results - Positive Reynolds number

Thus far, the dependence of the critical dynamo number on S and τ has been investigated without considering the presence of a meridional flow. Concentrating on the effects of a non-zero meridional flow upon the critical dynamo number of the system leads to the following results.

In this study, the Reynolds number is taken to be 10, S varying between -50 and 50 and focusing initially on values of τ greater than unity. Figure 3.3a shows the resulting critical dynamo numbers as a function of S. Firstly, it is important to note that as expected, when S becomes small, the value of D_c tends towards 2 and the system approaches the behaviour displayed by that of a typical $\alpha\Omega$ dynamo model. What is also clear (for $S > 0$) is that as the parameter S is increased at fixed τ, the critical dynamo number increases, indicating that the larger the value of S the harder it is to produce a periodic solution. As the time delay is increased for fixed values of positive S, the critical dynamo number decreases which is the opposite behaviour to what is observed in the system with no flow. The trends observed for negative S exhibit the opposite behaviour to what is seen for critical dynamo number calculations with positive S.

Figure 3.3b shows the critical dynamo number plotted against values of S ranging from -50 to 50 and with values of τ less than 1. Recall that these values of τ appear to be most relevant to the study since the Taylor series expansion of $Q(t)$ that is used to derive the governing equations (3.7) – (3.9) are valid for small values of τ. Coincidently, this is arguably the most interesting result. In this parameter regime it is clear that the interaction between these competing α-effects is non-trivial. As S becomes more positive, the critical dynamo number reaches a maximum at different values of S depending upon the length of the time delay. After this maximum has been reached, the value of D_c decreases as S becomes larger indicating that there is an optimal combination of S and τ that make it easier to generate non decaying solutions. It is interesting to note that this is not the case when considering negative values of S. It is evident that if the time delay is increased at fixed values of negative S it becomes harder to excite the dynamo, which implies that when S is working in the opposite direction to α, the dynamo is easier to excite regardless of the magnitude of S and it is only when S and α are working in the same direction that the interaction between these two sources of poloidal field regeneration

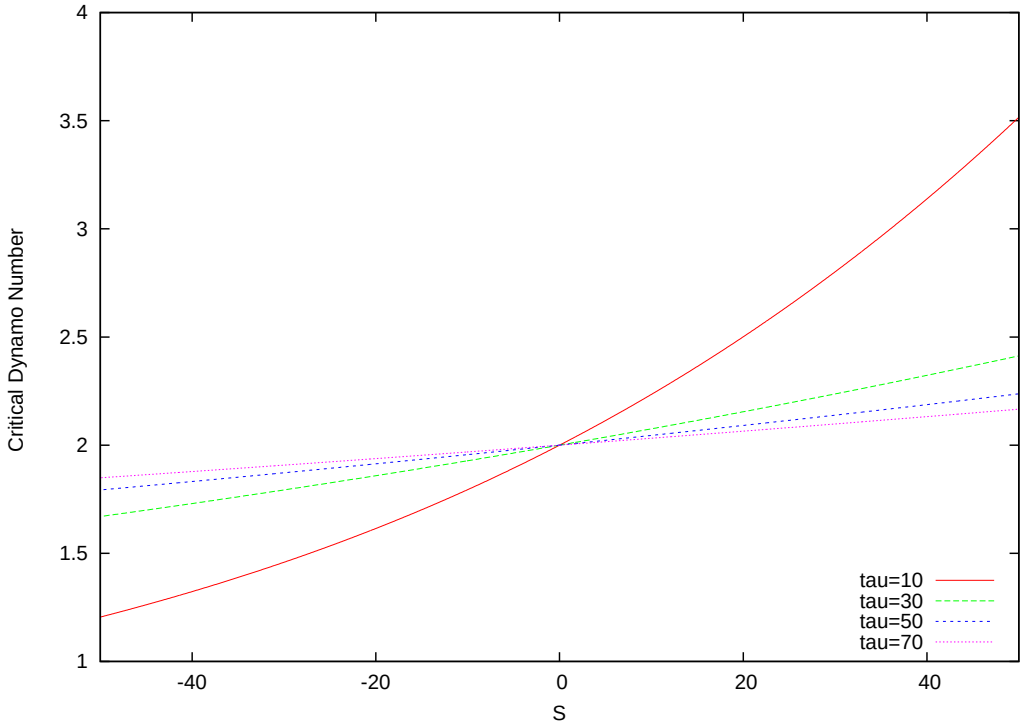

(a)

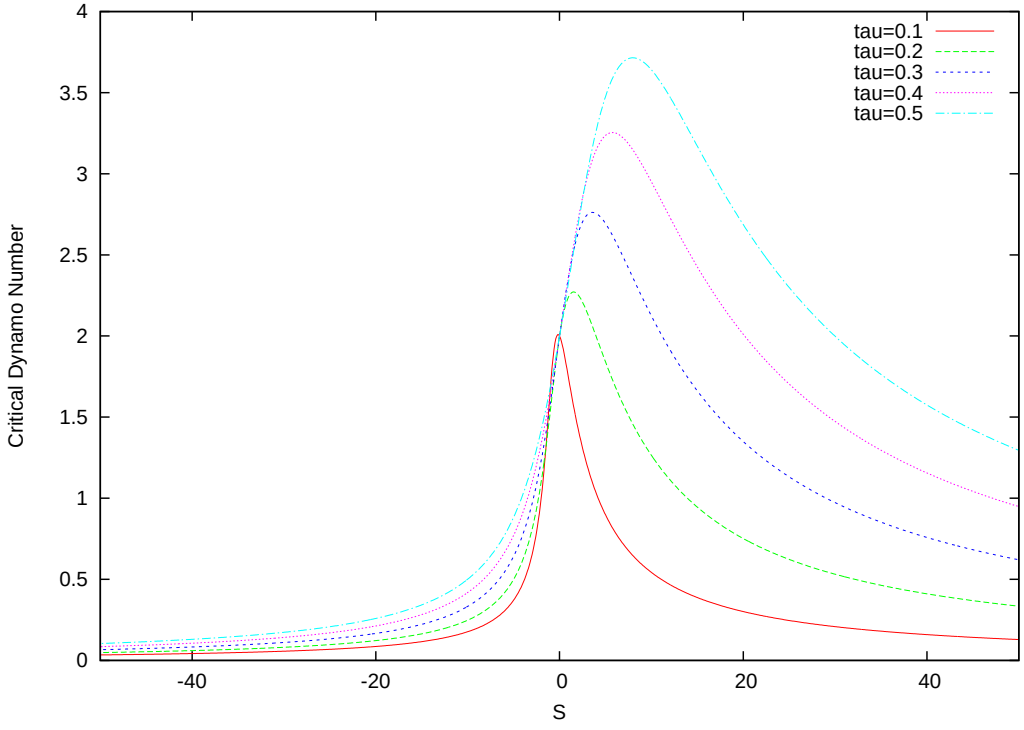

(b)

Figure 3.3: Top: $Re = 10$. Plot of the critical dynamo number D against S for fixed values of τ greater than 1 when $-50 < S < 50$. Bottom: $Re = 10$. Plot of the critical dynamo number D against S for values of τ less than 1 when $-50 < S < 50$.

becomes non-monotonic.

Negative D Keeping the rest of the parameters the same as those previously stated, the analogous calculations are made for negative values of the critical dynamo number, the results of which are shown in Figures 3.4a and 3.4b. For values of τ greater than 1, the behaviour is qualitatively similar to that of positive D although the curves are not a reflection in the S axis. The results are more interesting for values of τ less than 1. For positive values of S and at fixed values of τ, $|D_c|$ decreases as the magnitude of S increases which is comparable to the behaviour seen in the positive $|D_c|$ calculations. For negative values of S, the magnitude of the critical dynamo number reaches a maximum for different values of S as τ is varied however, this maximum is now located at a cusp, which is generated due to matching up two distinct branch points instead of a smooth peak which is seen in the corresponding positive dynamo number calculations in Figure 3.3b.

3.3 The transition from periodic to quasi-periodic behaviour

Restoring the nonlinear terms to the governing equations, finite amplitude oscillations can be found when the modulus of the dynamo number exceeds D_c. The stability of the periodic solution can be analysed by expressing the magnetic fields in the following form:

$$\begin{aligned} A_\omega(t) &= A_0 e^{i\omega t}, \\ B_\omega(t) &= B_0 e^{i\omega t}, \\ Q_\omega(t) &= Q_0 e^{i\omega t}, \end{aligned}$$

where A_0, B_0 and Q_0 are the complex wave amplitudes, ω is the frequency (with the ω subscript denoting the periodic state). The substitution of these expressions into the governing equations (3.7) – (3.9) produce the following set of simultaneous equations:

$$(i\omega + iRe + 1)A_0 = \frac{SQ_0}{1+|Q_0|^2} + \frac{B_0}{1+|B_0|^2}, \tag{3.18a}$$

$$(i\omega + iRe + 1)B_0 = iDA_0, \tag{3.18b}$$

$$\left(i\omega + \frac{1}{\tau}\right) Q_0 = \frac{1}{\tau} B_0. \tag{3.18c}$$

Solving these simultaneous equations it is easy to show that the system has non-trivial solutions when:

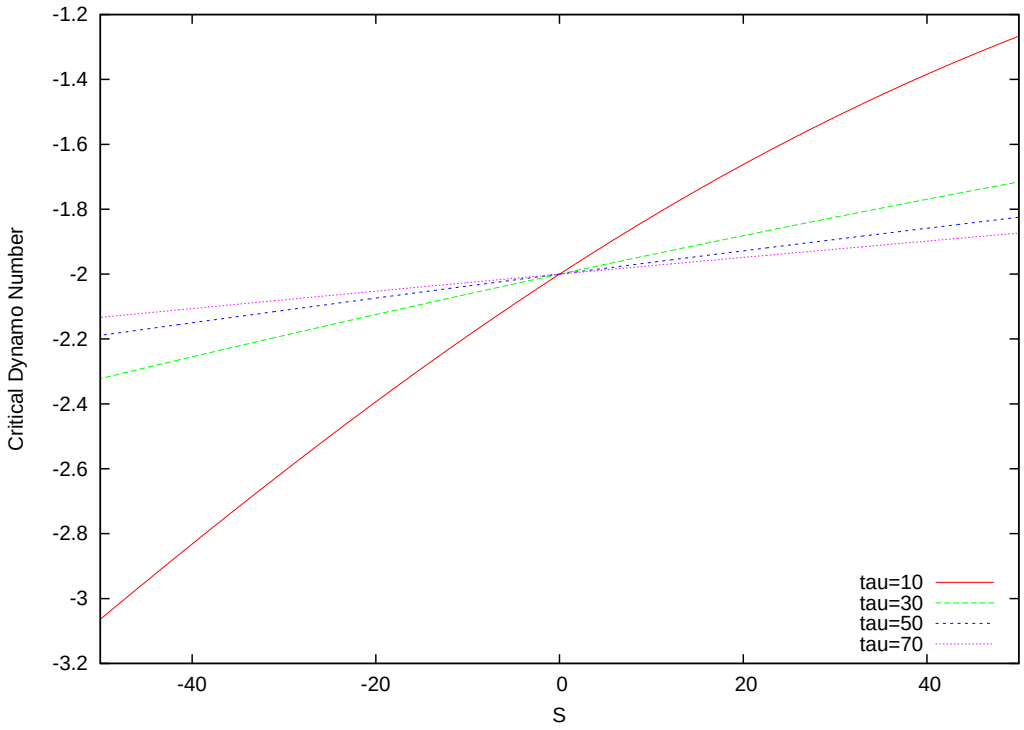

(a)

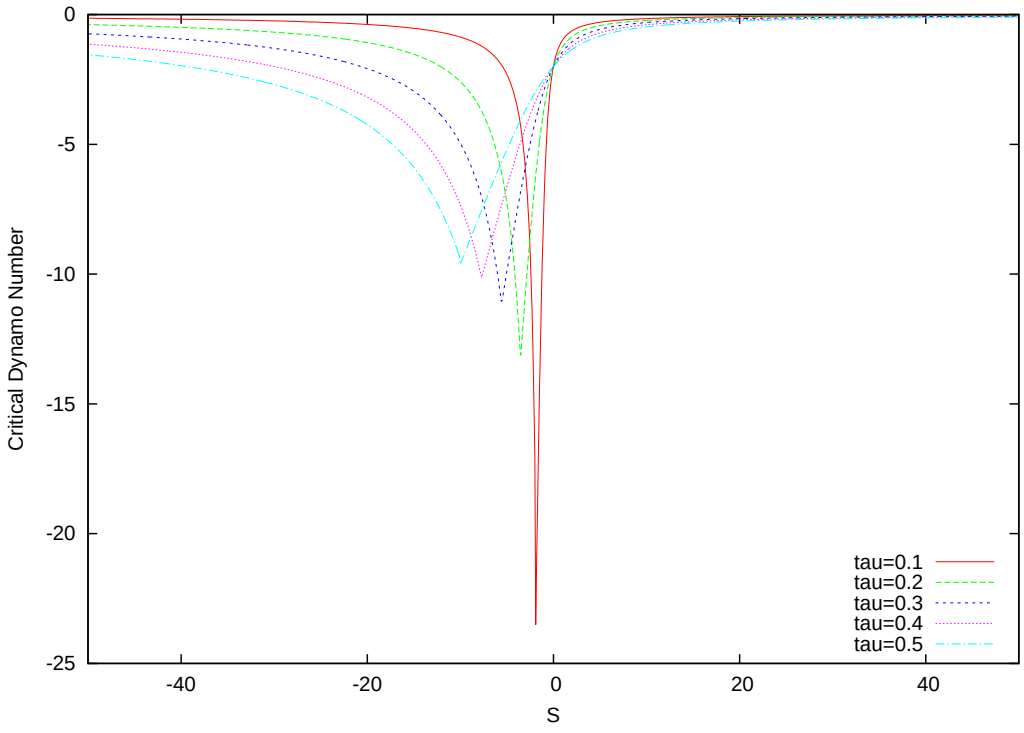

(b)

Figure 3.4: Top: $Re = 10$. Plot for negative values of D when varying S at fixed values of τ greater than 1. Bottom: $Re = 10$. Plot for negative values of D when varying S at fixed values of τ less than 1.

$$(i\omega + iRe + 1)^2 \left(i\omega + \frac{1}{\tau}\right) - \frac{iD}{1+|B_0|^2}\left(i\omega + \frac{1}{\tau}\right) - \frac{SiD}{1+|Q_0|^2}\left(\frac{1}{\tau}\right) = 0. \tag{3.19}$$

Taking the real and imaginary parts of Equation (3.19) gives two coupled equations:

$$\omega^2(1+2\tau) + \omega\left(2Re + 2Re\tau - \frac{D\tau}{1+|B_0|^2}\right) + (Re^2 - 1) = 0, \tag{3.20}$$

$$\omega^3\tau + \omega^2(2\tau Re) + \omega(\tau Re^2 - \tau - 2) + \left(\frac{D}{1+|B_0|^2} + \frac{SD}{1+|Q_0|^2} - 2Re\right) = 0. \tag{3.21}$$

Since there are only two simultaneous equations with three unknown variables, namely ω, B_0 and Q_0, it is necessary to eliminate either $|B_0|$ or $|Q_0|$. The complex conjugate of Equation (3.18c) is:

$$\left(-i\omega + \frac{1}{\tau}\right) Q_0^\star = \frac{1}{\tau} B_0^\star,$$

which can be combined together with Equation (3.18c) to give the following relationship between $|B_0|$ and $|Q_0|$:

$$|Q_0|^2 = \frac{|B_0|^2}{1+\omega^2\tau^2}. \tag{3.22}$$

There is now enough information to solve the system for ω, B_0 and Q_0. By using Equation (3.22) to eliminate $|Q_0|^2$ from the system, it is apparent that Equation (3.21) can be satisfied by 5 values of ω. The resulting system was then solved using Maple by firstly calculating $|B_0|^2$ and then ω. Once the amplitude and frequency of the periodic solution have been determined, it is possible to perturb this solution to study its stability. Following the general method described by Jouve *et al.* (2010), this can be achieved by setting:

$$\begin{aligned} A &= A_\omega \left(1 + \alpha_1 e^{pt} + \alpha_2^\star e^{p^\star t}\right), \\ B &= B_\omega \left(1 + \beta_1 e^{pt} + \beta_2^\star e^{p^\star t}\right), \\ Q &= Q_\omega \left(1 + \gamma_1 e^{pt} + \gamma_2^\star e^{p^\star t}\right), \end{aligned}$$

where $\alpha_1, \alpha_2, \beta_1, \beta_2, \gamma_1$ and γ_2 are the coefficients of the perturbed fields, p is the complex growth rate of the perturbation and the symbol $\star$ represents the complex conjugate. Here, the complex conjugate has been introduced in order to simplify the algebra at a later stage. Substituting these expressions into the governing equations (3.7) - (3.9) results in the following system of 6 coupled equations that relates the coefficients of the perturbed

		Re					
		0	10	20	30	40	50
S	0	-	-	-	-	-	-
	10	-	0.348	0.271	0.259	0.260	0.268
	30	-	0.334	0.255	0.239	0.226	0.208
	50	-	0.332	0.252	0.236	0.221	0.202
	70	-	0.330	0.250	0.234	0.218	0.200

Table 3.1: Critical values of τ for the transition from periodic to quasi-periodic solutions when $D = 1000$. The Reynolds number varies between 0 and 50, with S varying between 0 and 70.

fields to the growth rate p for a given set of parameters.

$$
\begin{aligned}
(1+iRe+i\omega)(\quad 1 \quad & +p+i\omega+iRe)\alpha_1 = \frac{iD}{1+|B_0|^2}\left[\left(1-\frac{|B_0|^2}{1+|B_0|^2}\right)\beta_1 - \frac{|B_0|^2}{1+|B_0|^2}\beta_2\right], \\
+ \quad & \left[(1+iRe+i\omega)^2 - \frac{iD}{1+|B_0|^2}\right]\left[\left(1-\frac{|Q_0|^2}{1+|Q_0|^2}\right)\gamma_1 - \frac{|Q_0|^2}{1+|Q_0|^2}\gamma_2\right], \\
(1-iRe-i\omega)(\quad 1 \quad & +p-i\omega-iRe)\alpha_2 = \frac{-iD}{1+|B_0|^2}\left[\left(1-\frac{|B_0|^2}{1+|B_0|^2}\right)\beta_2 - \frac{|B_0|^2}{1+|B_0|^2}\beta_1\right], \\
+ \quad & \left[(1-iRe-i\omega)^2 + \frac{iD}{1+|B_0|^2}\right]\left[\left(1-\frac{|Q_0|^2}{1+|Q_0|^2}\right)\gamma_2 - \frac{|Q_0|^2}{1+|Q_0|^2}\gamma_1\right],
\end{aligned}
$$

$$
\begin{aligned}
&(1+p+i\omega+iRe)\beta_1 = (1+iRe+i\omega)\alpha_1, \\
&(1+p-i\omega-iRe)\beta_2 = (1-iRe-i\omega)\alpha_2, \\
&\left(p+i\omega+\frac{1}{\tau}\right)\gamma_1 = \left(\frac{1}{\tau}+i\omega\right)\beta_1, \\
&\left(p-i\omega+\frac{1}{\tau}\right)\gamma_2 = \left(\frac{1}{\tau}-i\omega\right)\beta_2,
\end{aligned}
$$

where $|B_0|$ and $|Q_0|$ are related by Equation (3.22). A non-trivial solution only exists when the determinant of the system is zero. Solving the determinant for the growth rate p will indicate the values of the parameters that lead to modulation.

Tables 3.1 and 3.2 illustrate some of the results from this stability analysis. These tables show the parametric dependence of the critical value of τ for the transition from periodic to quasi-periodic solutions. The results in Table 3.1 correspond to $D = 1000$, with $0 \leq Re \leq 50$ and $0 \leq S \leq 70$. In Table 3.2, I have used the same values of Re, but $D = -1000$, whilst $0 \geq S \geq -70$. A dashed line in either table indicates that no transition exists. Unsurprisingly, no modulation is found for $S = 0$. In this case the delayed toroidal field Q decouples from the system and I have a standard $\alpha\Omega$ dynamo

		Re					
		0	10	20	30	40	50
	0	-	-	-	-	-	-
	-10	-	0.310	0.227	0.211	0.206	0.206
S	-30	-	0.321	0.240	0.224	0.219	0.217
	-50	-	0.323	0.243	0.226	0.221	0.219
	-70	-	0.324	0.244	0.227	0.222	0.220

Table 3.2: Critical values of τ for the transition from periodic to quasi-periodic solutions when $D = -1000$. The Reynolds number varies between 0 and 50, with S varying between 0 and -70.

model. More unexpectedly, these results suggest that $Re \neq 0$ is a necessary condition for modulation in this system. So the meridional flow seems to play a crucial role in driving the modulation, perhaps by introducing an additional (advective) time-scale into the problem. If it is simply the presence of an additional time-scale that is the key ingredient here, then it may still be possible to drive modulation in the absence of a flow if some other physical process (such as turbulent pumping) was included in the model. However, it is beyond the scope of this investigation to determine whether or not this is indeed the case. In the case of positive D, no modulation was found for negative S, whilst the same is true for positive values of S in the negative D case. Given the idealised nature of this local model, I should probably not read too much into this result, but (if nothing else) this again illustrates that competing α-effects interact in a rather non-trivial way in this system. Where modulation does occur, some trends can be identified. For example, for fixed Re in the $D = 1000$ case, the critical value of τ decreases with increasing S (whereas it increases with increasing $|S|$ in the $D = -1000$ case). At fixed S, the critical value of τ tends to decrease with increasing values of Re, although this trend appears to reverse at low S and high Re in the $D = 1000$ case. There is no definitive physical explanation for this behaviour but I can speculate that this is somehow related to the non-monotonicity that was observed in the D_c calculations in the previous subsection.

Due to the rescaling of the variables in Section 3.1, the dynamo number D is defined as $\alpha_0 \Omega_0 / \eta_\tau^2$. Changing the sign of D can be interpreted as a change in sign of α and so when considering the behaviour of the system for negative D and negative S, it can be assumed that S and α have the same sign and are working in the same direction.

As with the positive D case, the results for the negative D calculations also show a clear trend. At fixed values of S, the critical value of τ decreases as the Reynolds number increases indicating that the stronger the flow, the easier it becomes to modulate the cycle which is consistent with the corresponding analysis in the case of positive values for both S and D. Once again, there is no modulation found for $S = 0$ or $Re = 0$, indicating that the presence of a flow plays in important role in modulating the cycle.

The results are surprising when examining the trends at increasing values of negative S. When the time-delayed source term S becomes more negative the values of the time delay τ increase indicating that it becomes harder to induce modulation due to this competing α mechanism. This is the opposite behaviour as to what is seen in the case when D is positive.

3.4 Numerical simulations of the local model

As derived in Section 3.1, the equations that govern the evolution of the magnetic fields A, B and Q are given by:

$$\frac{dA}{dt} + iReA = \frac{SQ}{1+|Q|^2} + \frac{B}{1+|B|^2} - A, \tag{3.23}$$

$$\frac{dB}{dt} + iReB = iDA - B, \tag{3.24}$$

$$\frac{dQ}{dt} = \frac{1}{\tau}\left(B - Q\right). \tag{3.25}$$

These equations are solved numerically using a fourth-order Runge-Kutta time-stepping scheme in Fortran, see for example Press *et al.* (2007). However, before applying a numerical approach to the local model that is described by Equations (3.23) – (3.25), it is sensible to verify that I can reproduce the behaviour found by Jouve *et al.* (2010).

3.4.1 Comparison with Jouve *et al.* (2010)

In order to verify that my numerical simulations of the governing equations can reproduce the behaviour described by Jouve *et al.* (2010), I must adapt Equations (3.23) – (3.25) such that the evolution of the magnetic field A no longer includes poloidal field regeneration from a deep-seated α-effect. Also, for consistency with the Jouve *et al.* (2010) paper, the system includes several parameters that have been eliminated from my system due to the rescaling included in Section 3.1. The governing equations are thus given by:

$$\frac{dA}{dt} + ivA = \frac{SQ}{1+\lambda|Q|^2} - \eta A,$$

$$\frac{dB}{dt} + ivB = i\Omega A - \eta B,$$

$$\frac{dQ}{dt} = \frac{1}{\tau}\left(B - Q\right),$$

where $\tau = \tau_0/(1+|B|^2)$ and τ_0 is a constant. Decomposing the system into its real and imaginary parts, I use a fourth-order Runge-Kutta scheme in Fortran to time-step the

governing equations.

Numerical Simulations

In order to reproduce the behaviour seen in Jouve *et al.* (2010), I keep the parameters the same as used in Section 5.1 of their paper, i.e. $\Omega = 100$, $S = 100$, $\eta = 10^{-3}$, $v = 10^{-2}$, $\lambda = 10^{-4}$ and $\tau_0 = 2 \times 10^{-2} B_1^2$ where $B_1 = 3 \times 10^8$ is a normalisation factor. From this point on, and for consistency with Jouve *et al.* (2010), the values of τ_0 will be expressed in terms of multiples of B_1^2.

Solving the system numerically the value of the time delay τ_0 is now varied. Initially, I set the time delay to be small, and for a value of $\tau_0 = 2 \times 10^{-2}$, I am able to reproduce oscillatory behaviour shown here in Figure 3.5. For small values of the time delay, the solution stays periodic. Also visible is a time shift between the two fields which represents the time delay that has been imposed. The delayed field Q is of weaker amplitude than B which is to be expected due to diffusion acting on the toroidal field.

As described in Section 3.1, the system can be reduced to a set of 5 real ODEs given by Equations (3.10) – (3.14). Again, the system implemented in Jouve *et al.* (2010) contains only one source of poloidal field regeneration and thus the governing equations are as follows:

$$\begin{aligned}
\frac{d\rho}{dt} &= -\Omega \rho y_2 - \eta \rho, \\
\frac{dy_1}{dt} &= \frac{S z_1}{1 + \lambda \rho^2 (z_1^2 + z_2^2)} + 2 y_1 y_2 \Omega, \\
\frac{dy_2}{dt} &= \frac{S z_2}{1 + \lambda \rho^2 (z_1^2 + z_2^2)} + \Omega y_2^2 - \Omega y_1^2, \\
\frac{dz_1}{dt} &= \frac{1 - z_1}{\tau} + \Omega y_1 z_2 + \Omega y_2 z_1 - v z_2 + \eta z_1, \\
\frac{dz_2}{dt} &= \frac{-z_2}{\tau} - \Omega y_1 z_1 + \Omega y_2 z_2 + v z_1 + \eta z_2,
\end{aligned}$$

and $\tau = \tau_0/(1 + \rho^2)$. Here y_1 and z_1 are the real components of y and z, and y_2 and z_2 are the imaginary components of y and z respectively.

Figure 3.6 shows how the behaviour of the system depends upon τ_0. For small values of τ_0, the standard periodic solution of the cycle is observed up until the point when $\tau_0 \approx 3.31 \times 10^{-2}$. As τ_0 is increased the system undergoes a series of period doublings. In the case when the time delay has been increased to $\tau_0 = 1.11 \times 10^{-1}$, it is clear that the solution reaches a maximum value after every 2 cycles. Further increasing the value of τ_0 leads to more period doublings until the strongly modulated solution is recovered for $\tau_0 \approx 1.18 \times 10^{-1}$.

Although the results from my code are qualitatively the same as those reproduced in

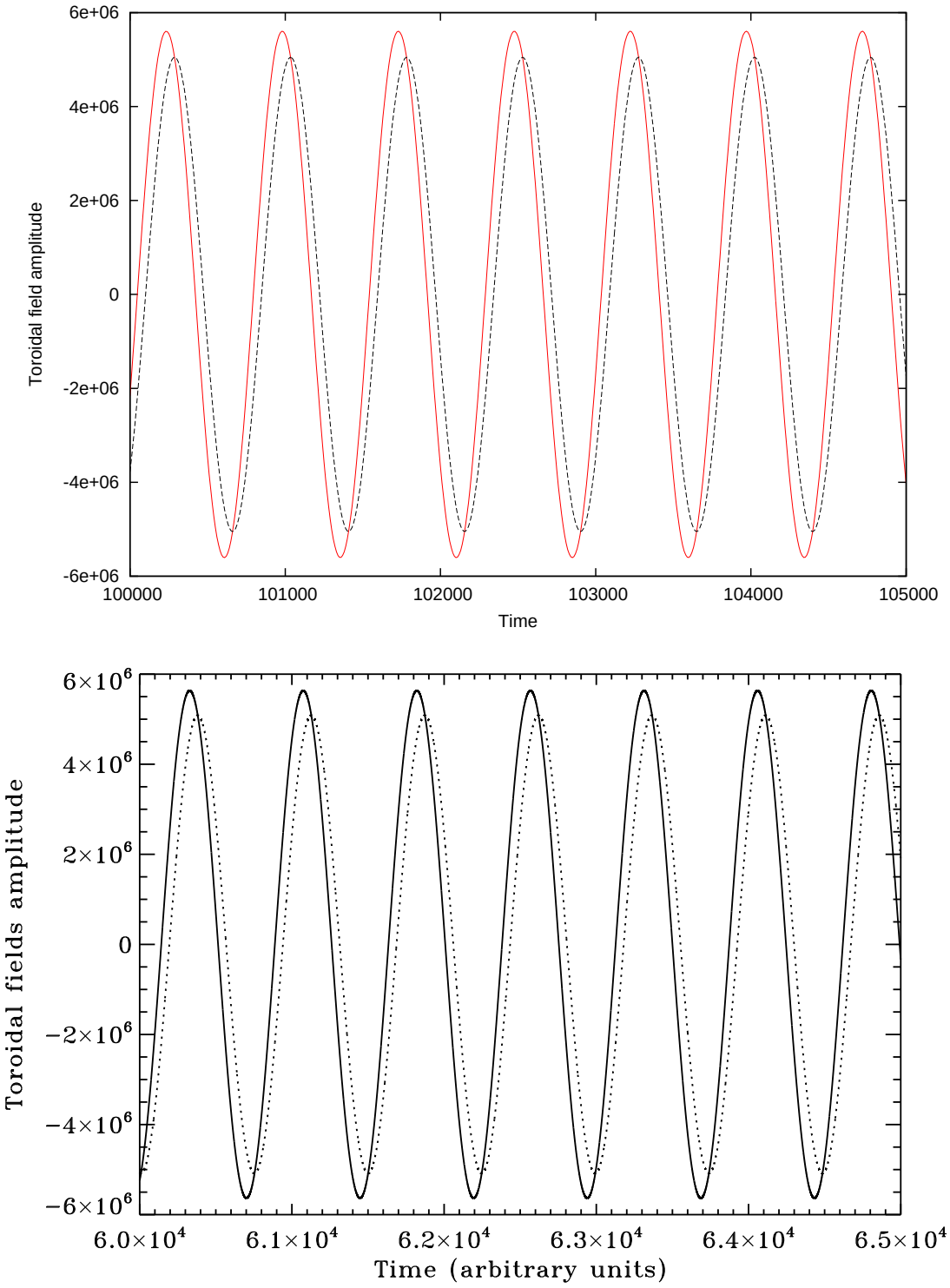

Figure 3.5: Reproducing the behaviour that is seen in Jouve *et al.* (2010) for a value of $\tau_0 = 2 \times 10^{-2}$. The top plot is generated from my code: the red line represents the toroidal field B and black line shows the delayed field Q. The bottom plot is taken from Jouve *et al.* (2010): the solid line represents the toroidal field B and the dotted line represents the delayed field Q.

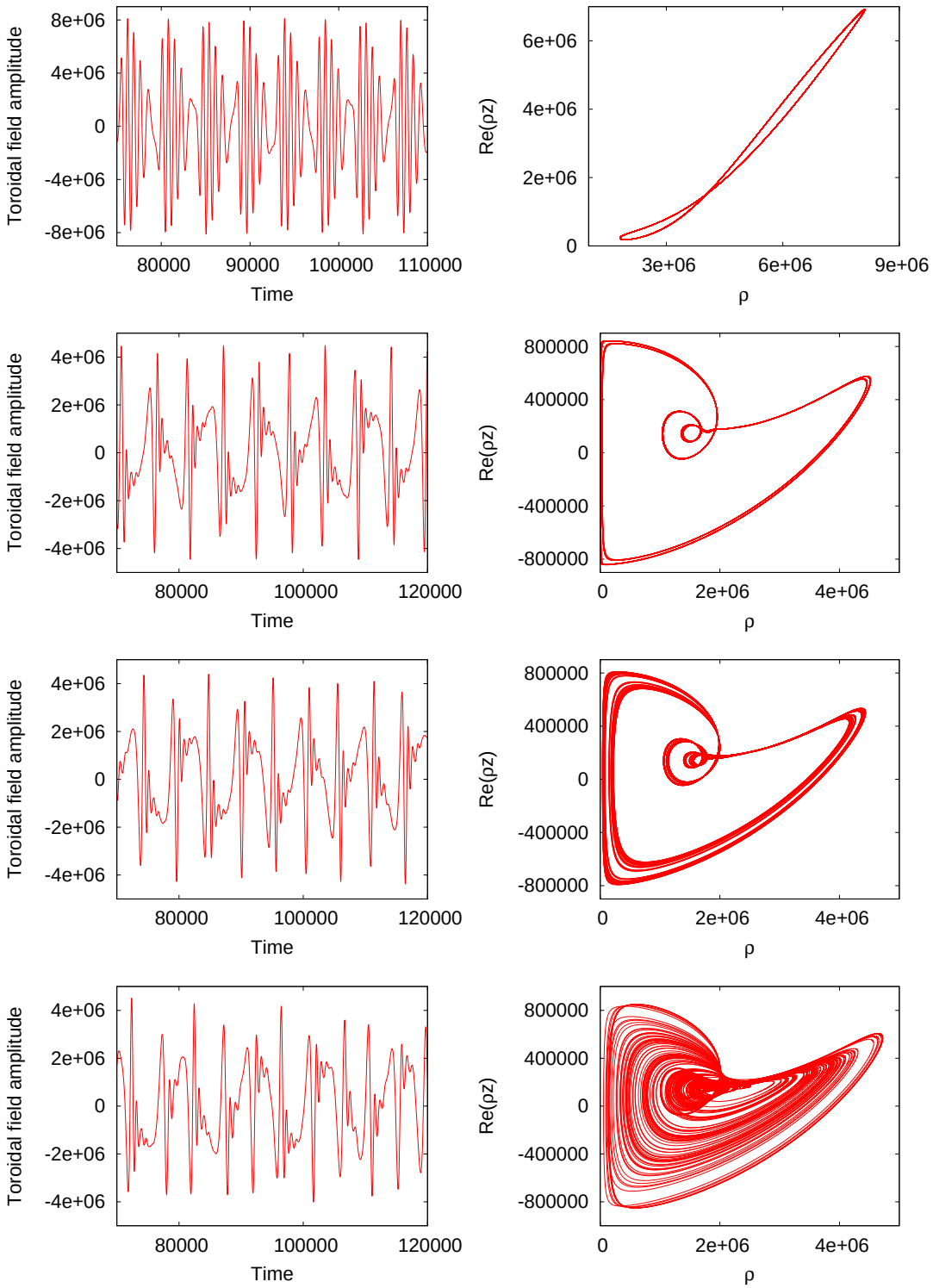

Figure 3.6: The same system that is investigated in Jouve *et al.* (2010) for $\tau_0 = 3.31 \times 10^{-2}$ (first), $\tau_0 = 1.11 \times 10^{-1}$ (second), $\tau_0 = 1.14 \times 10^{-1}$ (third) and $\tau_0 = 1.18 \times 10^{-1}$ (last). The plots on the left show the time-dependence of the toroidal field, whilst the plots on the right show the phase portraits of the amplitudes of ρ against $Re(\rho z)$ which represent $|B(t)|$ and $Re(Q(t))$ respectively (as derived from the 5^{th}-order system).

	$Re = 0$		$Re = 10$		$Re = 20$	
	Analytic Calculation	Numerical Simulation	Analytic Calculation	Numerical Simulation	Analytic Calculation	Numerical Simulation
$\lvert B_0 \rvert$	77.31832	77.31859	52.84574	52.84203	40.59354	40.58328
$\lvert Q_0 \rvert$	76.99327	76.99354	41.20185	41.19928	20.88267	20.87817
ω	0.91987	0.92991	8.03168	8.04248	16.66941	16.67557

Table 3.3: Values of $|B_0|$, $|Q_0|$ and ω from both the analytical calculations and the numerical simulations. Here, $D = 1000$, $S = 10$ and $\tau = 0.1$, whilst the Reynolds number is varied. All results are accurate to at least 1%.

Jouve *et al.* (2010), there were some discrepancies between our results. In Jouve *et al.* (2010), it is stated that the value of τ_0 that is needed to reproduce chaotic behaviour is $\approx 9.0 \times 10^{-2}$. However, using my code, it was found that for this value of τ_0, the solution is still multiply periodic, see Figure 3.7. In fact, with my code, a value of $\tau_0 \approx 1.18 \times 10^{-1}$ was required before strong modulation of the dynamo wave was present. This led to the investigation of the dependence of the solution upon the initial conditions and a vast parameter search was undertaken in order to vary the initial conditions but keep the value of the time delay constant. It was found that this change made very little difference to the solution and so I contacted the author who informed me that they imposed a cap in the form of a maximum value of the time delay. After adding a similar cap to my simulations, I was able to reproduce the same behaviour of the system for the values of τ_0 that are documented in Jouve *et al.* (2010), see Figure 3.7.

3.4.2 Validation of numerical calculations

Now that it has been shown that my numerical code can reproduce the results published by Jouve *et al.* (2010), attention is returned to the proposed system including both sources of poloidal field regeneration and a constant time delay.

It is possible to check that the results of the numerical simulations of Equations (3.23) – (3.25) agree with the critical dynamo numbers that have been calculated in Section 3.2. Fixing the values of $Re = 10$, $S = 20$ and $\tau = 10$, gives a prediction of $D_c = 2.499$. This is consistent with the numerics: I find decaying oscillations for $D = 2.4$, whilst $D = 2.6$ gives a stable periodic solution. I can also compare the amplitude and frequency of the periodic solutions with the corresponding analytical predictions, using a Fourier transform to determine the frequency of oscillation in the numerical case. Table 3.3 shows the results of such a comparison, for variable Re, using $D = 1000$, $S = 10$ and $\tau = 0.1$ (which includes the Case 1 below). All results are accurate to within 1% which clearly validates both the numerical scheme and the analytical calculations. Similarly, fixing $Re = 10$, $D = 1000$ and $S = 10$, I find that the solution exhibits a transition from periodic to quasi-periodic

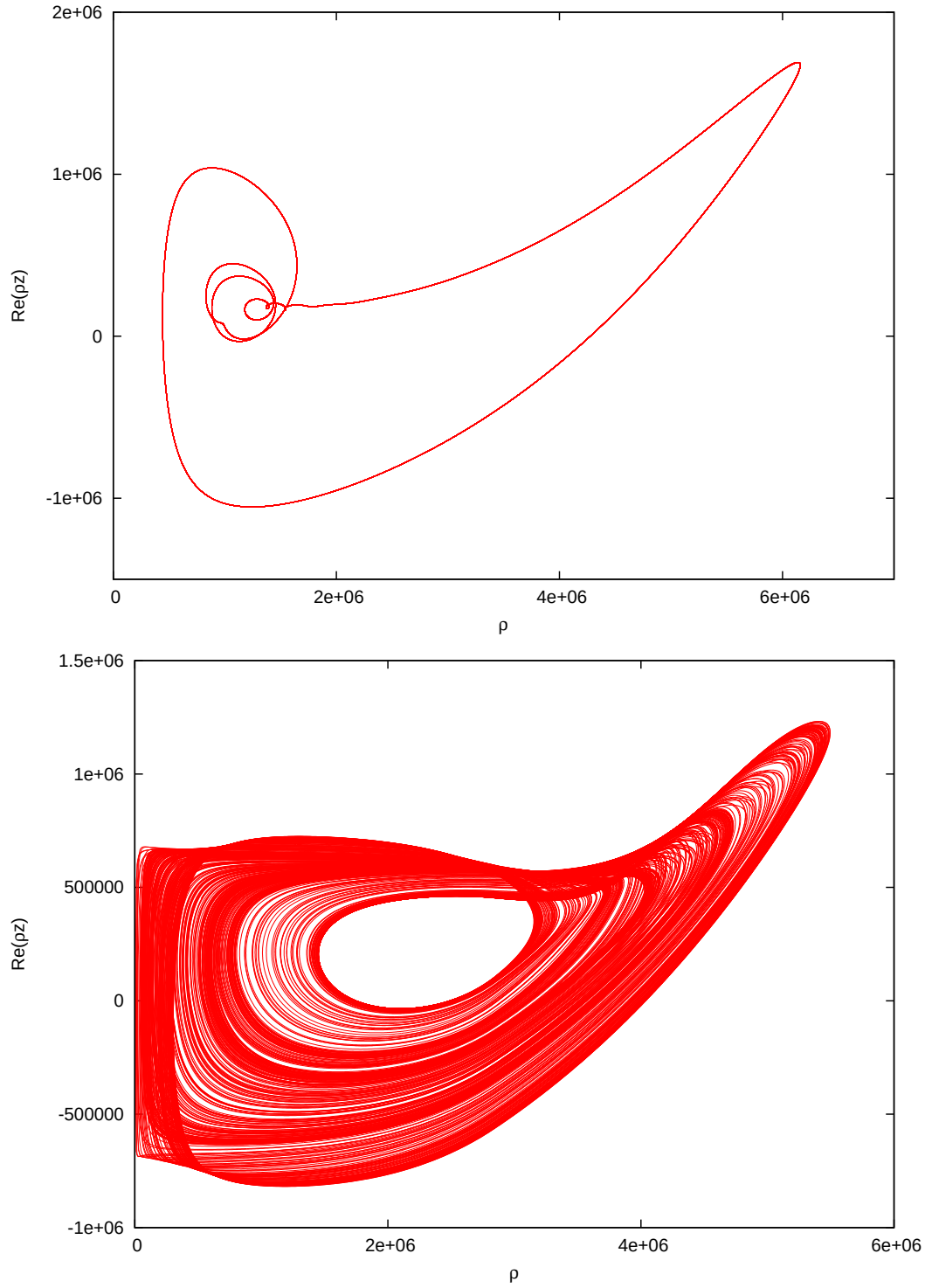

Figure 3.7: Phase portraits of the amplitudes of ρ against ρz which represent $|B(t)|$ and $Re(Q(t))$ respectively. The top plot is the case when no cap is imposed upon the maximum value of the time delay τ. The bottom plot is the same system when a maximum value of the time delay is imposed. Both plots are for a value of $\tau = 9.0 \times 10^{-2}$.

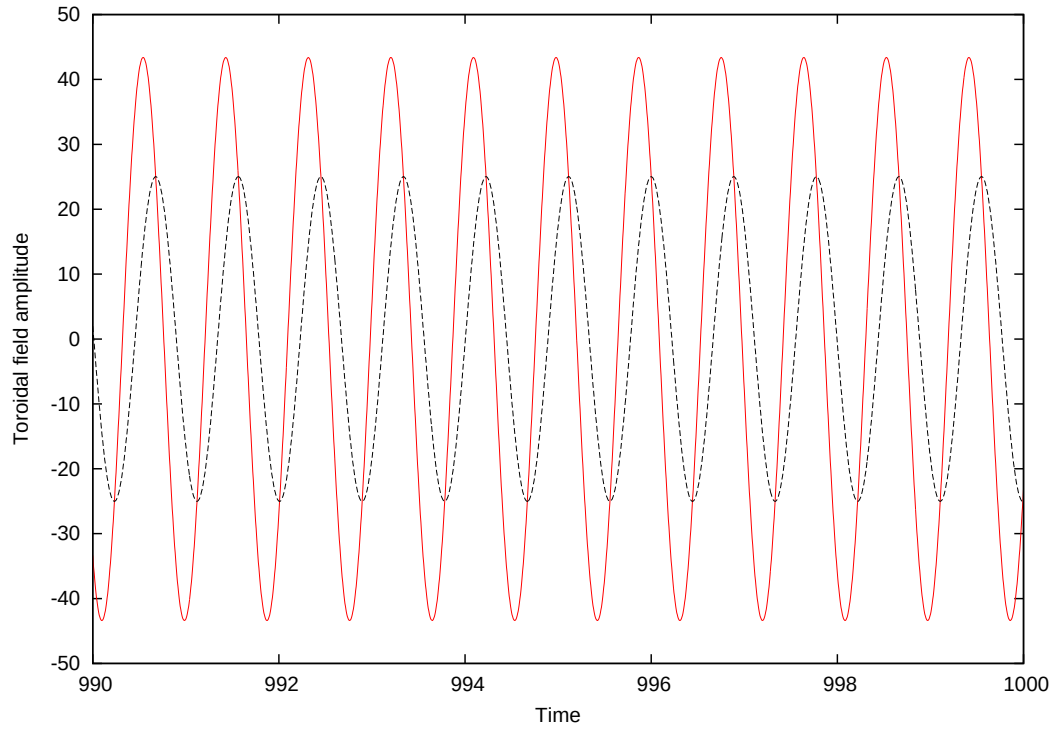

Figure 3.8: Case 1 when $\tau = 0.2$: This shows the toroidal field B (solid line) and the delayed toroidal field Q (dashed line) as a function of time (which is expressed in dimensionless units).

dynamo waves at $\tau = 0.347$, which compares very favourably to the analytic value of $\tau = 0.348$ (see Table 3.1). Other parameter regimes have also been studied and indicate agreement between the numerical simulation and the analytical calculation of the critical dynamo numbers.

3.4.3 Results

As described in the critical dynamo number calculations included in Section 3.2, the interaction between the two competing α-effects is non trivial and is highly sensitive to the parameters of the system. Some results of the numerical simulations of the governing equations have been included in the following section and the details are given here in three separate reference cases.

Case 1 Initially, the parameters are chosen such that $D = 1000$, $Re = 10$, $S = 10$ and τ is varied. This parameter regime may be considered similar to that studied in Jouve *et al.* (2010) since in their study, the dynamo was driven by large values of S and Ω. Figure 3.8 shows that a periodic solution can be found provided that τ is sufficiently small. Both $B(t)$ and $Q(t)$ oscillate with constant amplitude although $Q(t)$ has a smaller amplitude

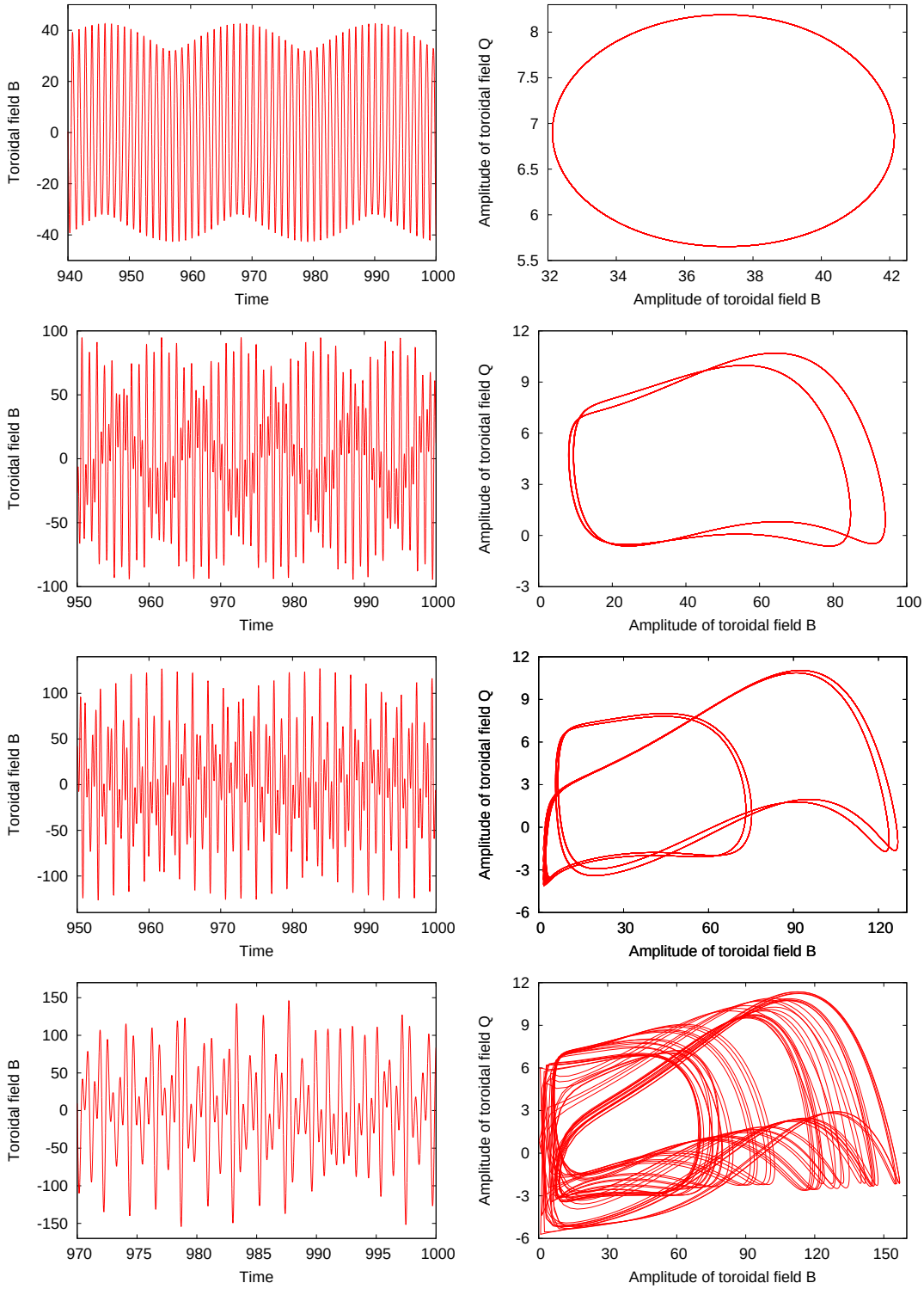

Figure 3.9: Case 1 for $\tau = 0.35$ (first), $\tau = 0.61$ (second), $\tau = 0.75$ (third) and $\tau = 0.86$ (last). The plots on the left show the time-dependence of the toroidal field, whilst the plots on the right show the phase portraits of the amplitudes of $B(t)$ against $Q(t)$ (as derived from the 5^{th}-order system).

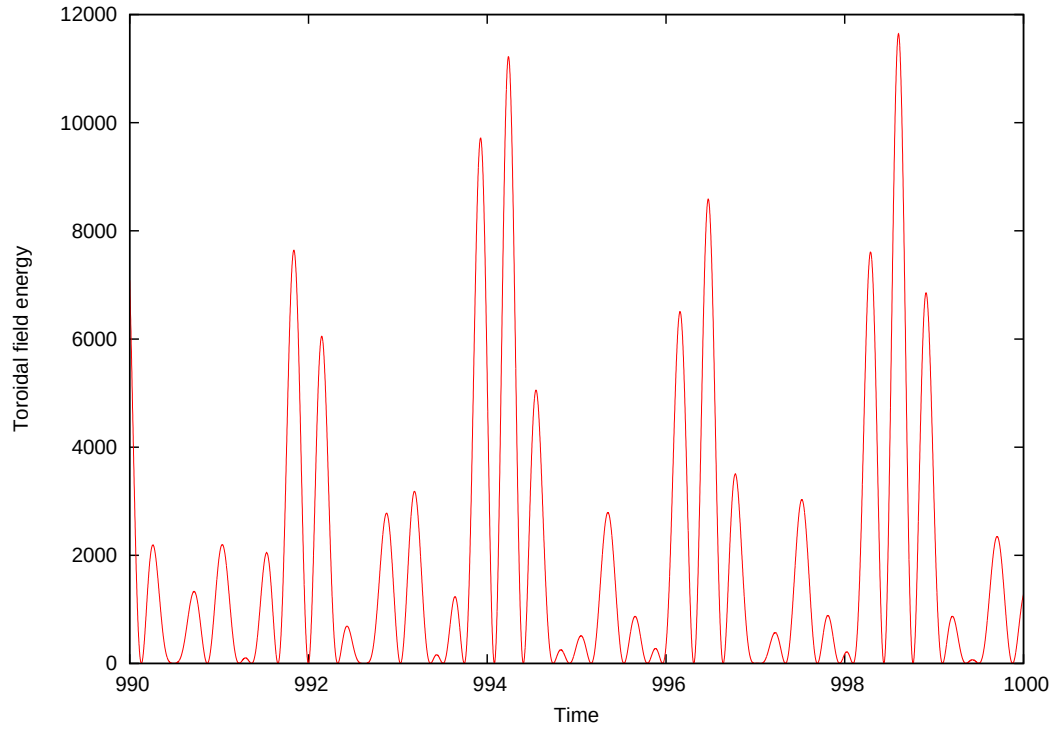

Figure 3.10: Case 1 when $\tau = 0.86$. A plot of B^2 against time, the energy appears to be chaotically modulated.

of oscillation and, as expected, lags behind $B(t)$. The effects of increasing the value of τ are shown in Figure 3.9. As τ is increased through the threshold value of $\tau = 0.347$, the lag between $B(t)$ and $Q(t)$ increases to such an extent that I see a transition to a quasi-periodic state. Further increases in τ lead to further transitions, from multiply periodic to chaotically modulated states. Figure 3.10 shows the time evolution of the toroidal field energy B^2 for $\tau = 0.86$, at which point the solution appears to be chaotically modulated. It is clear that there are several phases of significantly reduced magnetic activity, and it is tempting to compare these to grand minima. The extent to which this behaviour is "solar-like" is a matter of some debate – this is, after all, a highly idealised model. Nevertheless, it is encouraging that this simple model, with competing α-effects, is capable of producing highly modulated dynamo waves when the time delay is sufficiently large.

As indicated by the results in Table 3.1, the analysis of the stability of the periodic solution indicates that it is not possible to find a transition to a quasi-periodic solution for negative values of S, when D is positive. This tendency for the periodic state to be stable (for $S \leq 0$) regardless of the value of τ has been confirmed numerically. However, for positive values of S it always appears to be possible to find a transition to quasi-periodic solutions, provided that the Reynolds number is non-zero, and the transitions that are

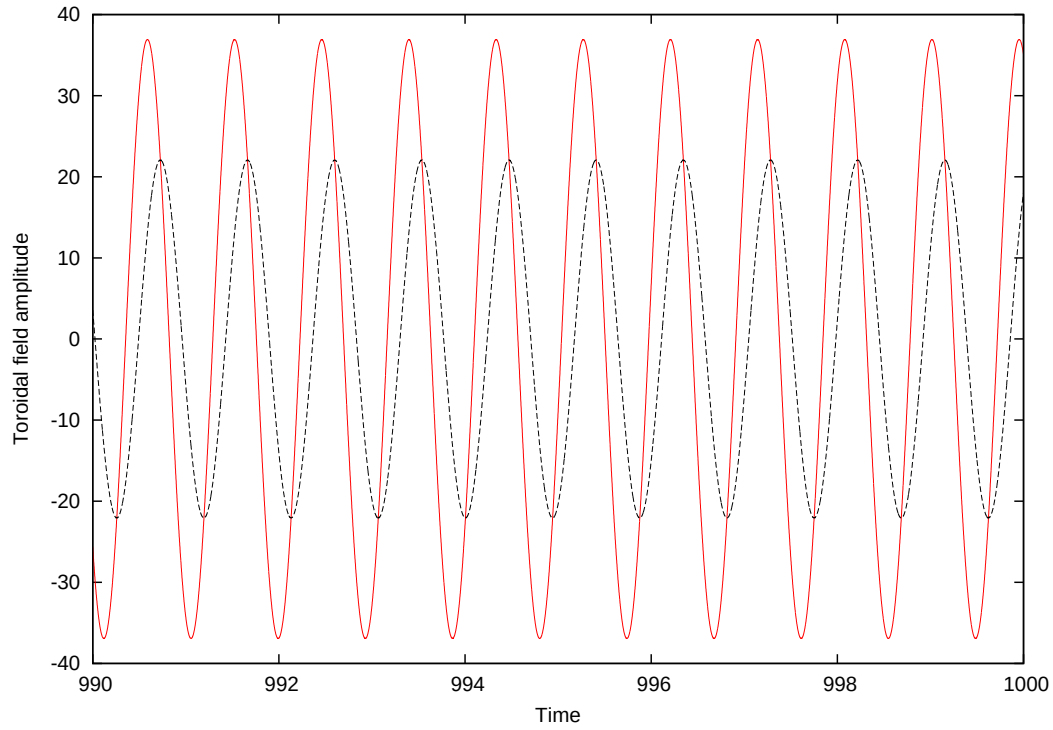

Figure 3.11: Case 2. The plot shows the time evolution of the toroidal field B (solid line) and the delayed toroidal field Q (dashed line) for a periodic solution at $\tau = 0.2$.

found numerically are consistent with those predicted in Table 3.1. Once quasi-periodic solutions have been found it is usually possible to find chaotically-modulated states for sufficiently large values of the time delay.

Case 2 Since it has already been established that modulation is found for positive values of D, the same investigation is carried out for negative values of D. Importantly, it is still possible to show that chaotic modulation of the cycle can be found if the value of τ is large enough. Considering the case when $D = -1000$, $Re = 10$, $S = -10$ and varying τ leads to the following series of bifurcations. Figure 3.11 shows the time evolution of the toroidal fields B and Q when the time delay remains small. As expected the periods of both toroidal fields remain constant and no modulation is found. Again, the period of the delayed field Q is shifted in time with respect to the toroidal field B which represents the effect of the time delay and the magnitude of the delayed field Q is significantly smaller than the magnitude of B.

Figure 3.12 shows the behaviour of the system as τ is increased. The stability analysis included in Section 3.3 predicts that the transition to aperiodic behaviour occurs when the value of $\tau = 0.310$. Numerical results show that at this value of τ the dynamo wave

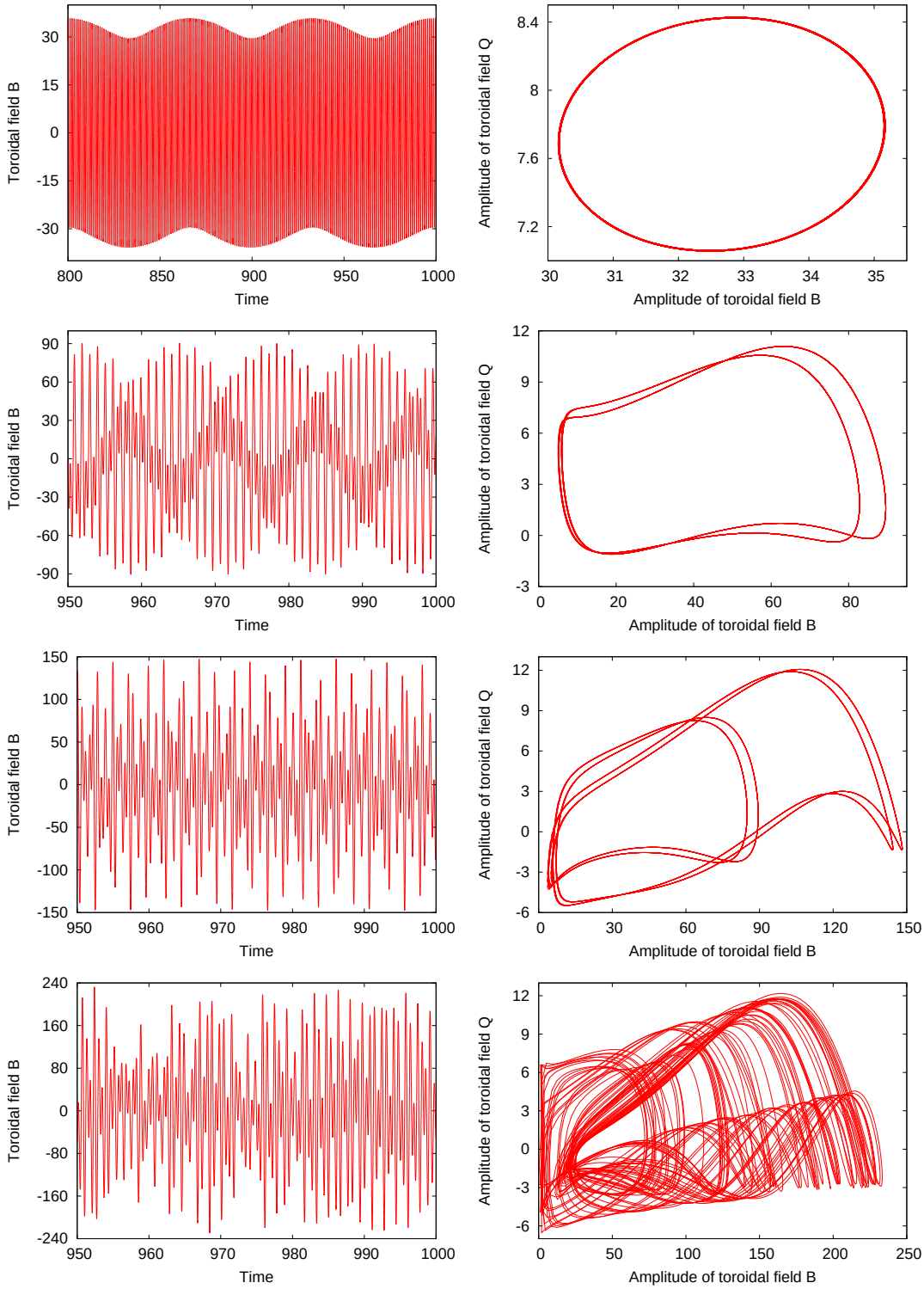

Figure 3.12: Case 2 for $\tau = 0.31$ (first), $\tau = 0.56$ (second), $\tau = 0.75$ (third) and $\tau = 1.08$ (last). The plots on the left show the time-dependence of the toroidal field, whilst the plots on the right show the phase portraits of the amplitudes of $B(t)$ against $Q(t)$ (as derived from the 5^{th}-order system).

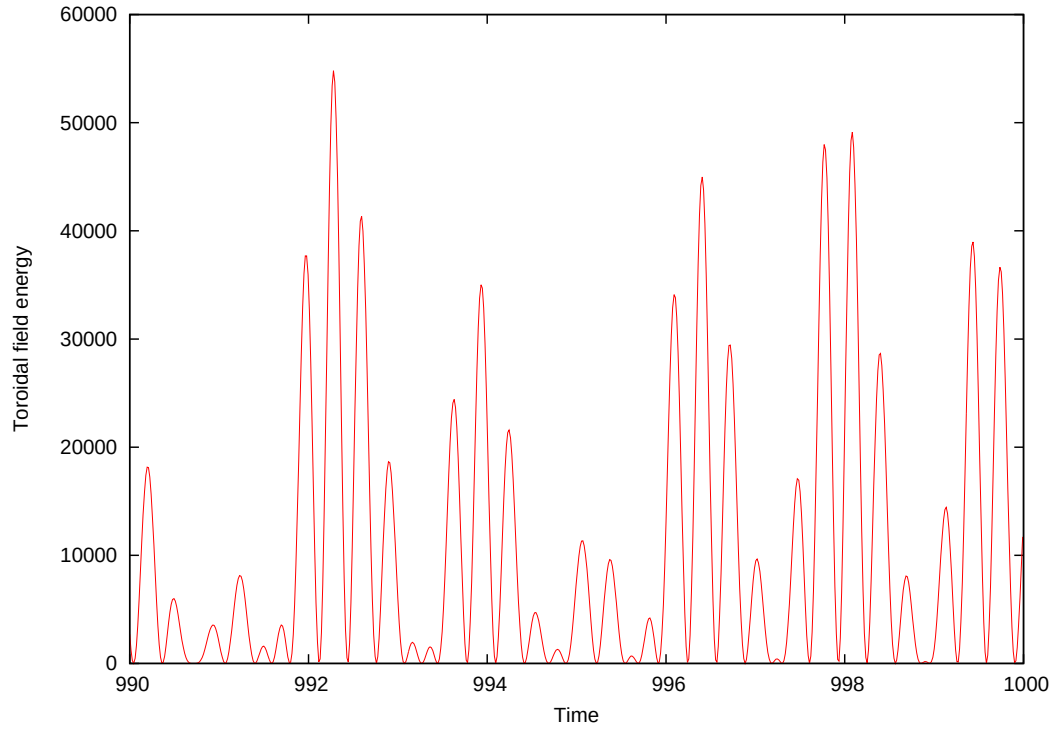

Figure 3.13: Case 2. $D = -1000$, $Re = 10$, $S = -10$ and $\tau = 1.08$: A plot of the toroidal field energy B^2 against time. Periods of low energy are clearly present within the system.

is now quasi periodic and a periodic solution is no longer found such that the magnitudes of B and Q vary on a fixed orbit as the system evolves over time. This is consistent with the aperiodic behaviour seen in the sixth order system. Increasing the time delay τ to 0.56 leads to a doubling of the orbit indicating that the system has undergone a further bifurcation. As τ is increased, period doublings continue to occur until τ reaches 1.08 when a chaotic solution is fully developed. For this value of τ the time evolution of the toroidal field energy is considered and the resulting plot is included in Figure 3.13. The solution contains distinct time intervals of low energy which is consistent with the observed sunspot number, included in Figure 1.9, which shows periods of low sunspot activity.

Again, both positive and negative values of S are considered however modulation is only found for negative values of S. The results of the analytical calculations for $D = -1000$ are included here as Table 3.2. For negative values of the dynamo number, the numerical results are consistent with those predicted analytically. No modulation is found for positive S or for $Re = 0$. For negative S and positive Re, it is possible to find quasi-periodic and chaotically modulated solutions as the time delay is increased.

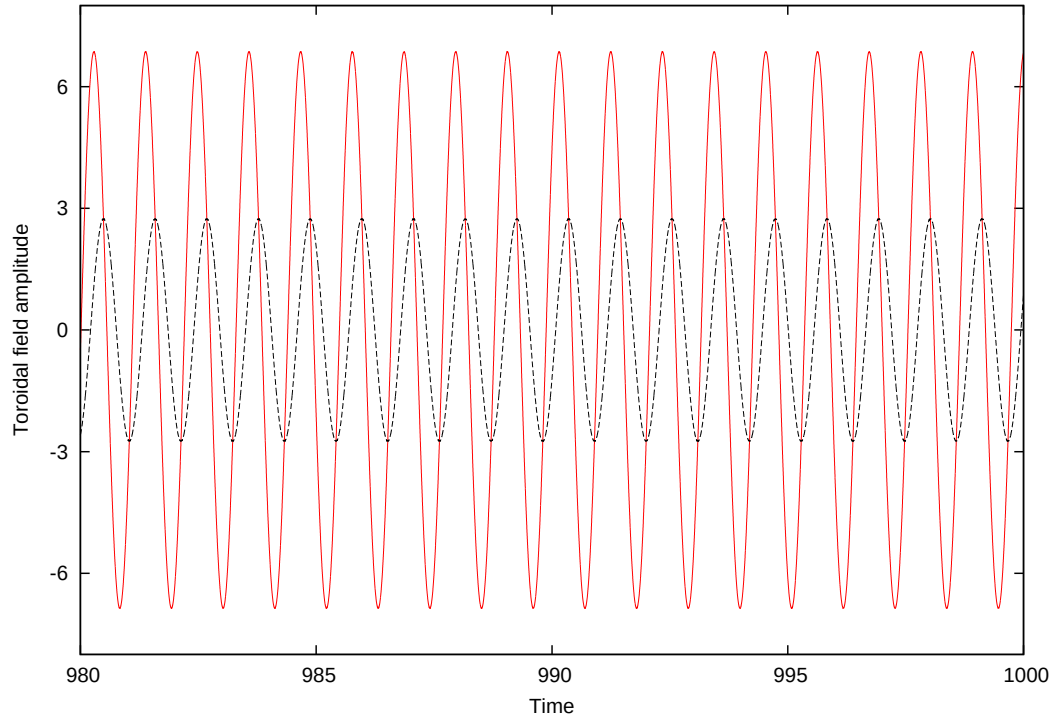

Figure 3.14: Case 3 for $\tau = 0.4$: This shows the toroidal field B (solid line) and the delayed toroidal field Q (dashed line) as a function of time (which is expressed in dimensionless units).

Case 3 Since it has already been shown in Cases 1 and 2 that modulation can be found for large values of D, similar modulation is also searched for at values of D closer to onset. In this scenario, the parameters are chosen such that $D = 50$, $Re = 10$, $S = 8$ and τ is varied, this shall subsequently be referred to as Case 3. Figure 3.14 shows the time evolution of the toroidal field B and delayed field Q when the time delay remains small enough for the solution to remain periodic. As previously seen, under these circumstances, the delayed field Q lags behind the toroidal field B, which represents the time delay, and also the magnitude of Q is significantly smaller than the magnitude of B.

As the time delay is increased, the results are similar to those found in case 1 and 2. Figure 3.15 shows the behaviour of the system for two values of τ. The top plots are generated when $\tau = 0.41$ and it is clear from both the toroidal field evolution and the relative magnitudes of B and Q that the solution is no longer periodic. The bottom plots show the behaviour of the system when the time delay has been increased to 0.57. The solution remains quasi-periodic and the fields B and Q vary on a fixed orbit.

Figure 3.16, shows the behaviour of the system when $\tau = 0.59$ and at this value of τ the solution looks to be chaotic. Although the modulation is less dramatic than the results seen in cases 1 and 2, the phase portraits of the amplitudes of $B(t)$ against $Q(t)$

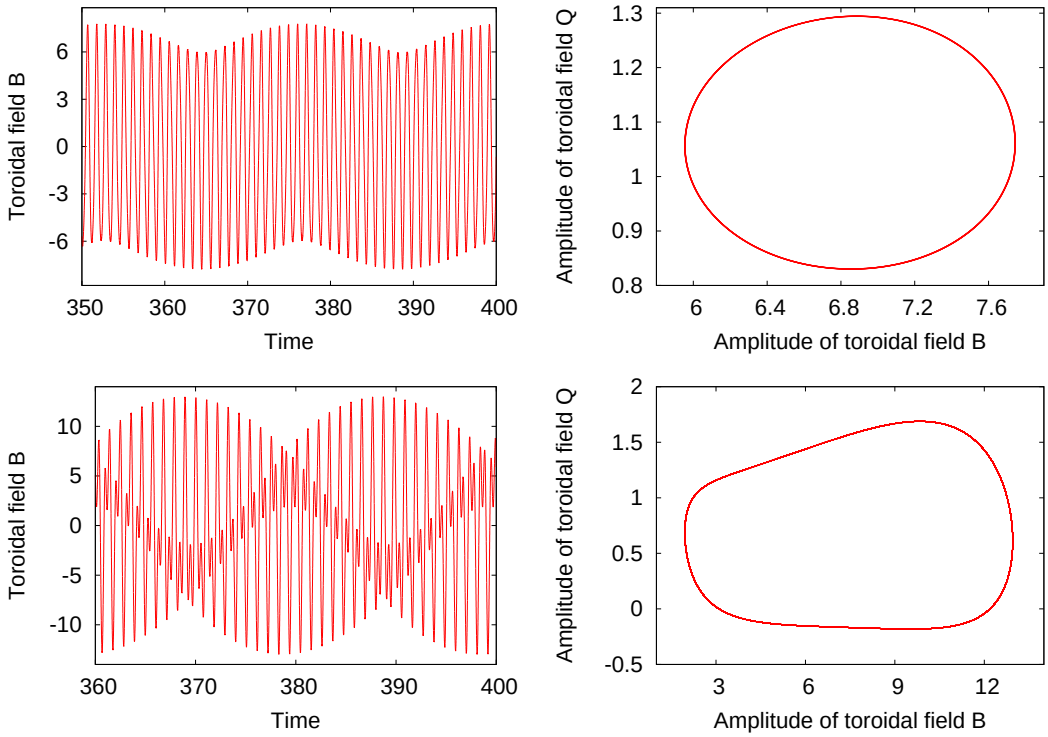

Figure 3.15: Case 3 for two different values of τ. The plots show the Toroidal field B against Time for 2 different values of τ. The top plot is for $\tau = 0.41$, the bottom plot is for $\tau = 0.57$. The plots on the left show the time-dependence of the toroidal field, whilst the plots on the right show the phase portraits of the amplitudes of $B(t)$ against $Q(t)$ (as derived from the 5^{th}-order system).

still show that the system appears to be chaotically modulated. The bottom plot in Figure 3.16 is a time series plot of the toroidal field energy. Although the toroidal field energy is modulated, it cannot be claimed that there are time periods when the energy is significantly reduced. This implies that in order for the solution to exhibit periods of "grand minima", the magnitude of the dynamo number D must be large.

3.5 Solving the PDE system

Recall from Section 3.1 that the original PDE model is governed by the following set of coupled partial differential equations:

$$\begin{aligned}
&\frac{\partial A}{\partial t} + Re\frac{\partial A}{\partial x} = \frac{SQ}{1+|Q|^2} + \frac{B}{1+|B|^2} + \frac{\partial^2 A}{\partial x^2}, \\
&\frac{\partial B}{\partial t} + Re\frac{\partial B}{\partial x} = D\frac{\partial A}{\partial x} + \frac{\partial^2 B}{\partial x^2}, \\
&\frac{\partial Q}{\partial t} = \frac{1}{\tau}\left(B - Q\right).
\end{aligned}$$

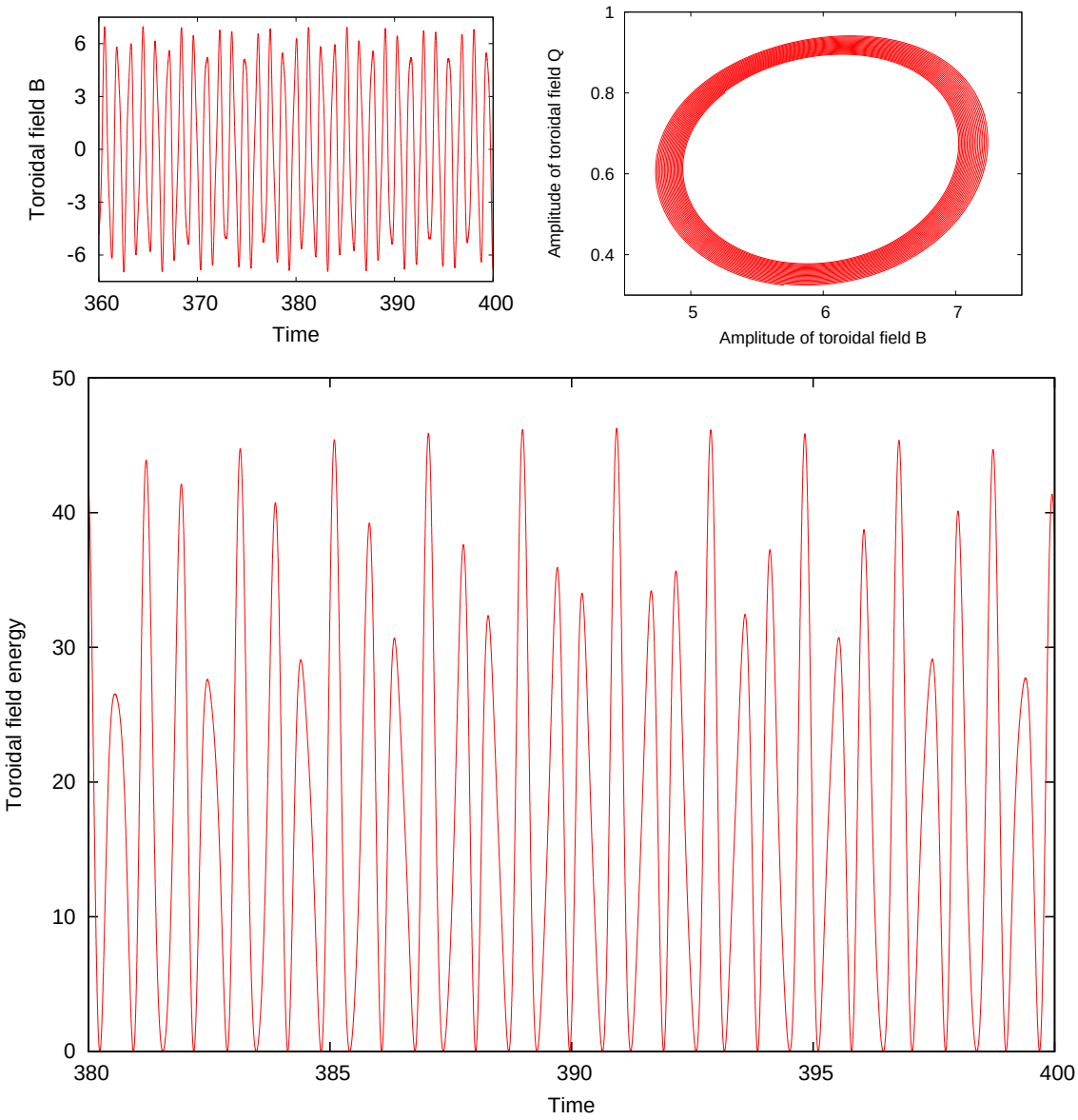

Figure 3.16: Case 3 for $\tau = 0.59$. The top plots show the time-dependence of the toroidal field and the phase portraits of the amplitudes of $B(t)$ against $Q(t)$ (as derived from the 5^{th}-order system). The bottom plot is a plot of the toroidal field energy B^2 against time.

Although the results from the local model are promising, it is important to verify that they are not crucially dependent upon the simplifying assumptions that have been made when deriving the model. In this section, I return to the original model of partial differential equations, as defined by equations (3.4) – (3.6) and are repeated above for reference. In dimensionless units, I assume that $0 \leq x \leq \pi/2$ (recalling that I interpret x as being analogous to the co-latitude on a spherical surface), imposing the boundary conditions that $A = B = Q = 0$ at $x = 0$ (the "North pole") and $B = Q = \partial A/\partial x = 0$ at $x = \pi/2$ (the "Equator"). These boundary conditions correspond to the assumption that the global magnetic field has dipolar symmetry. Having neglected the effects of curvature, and having assumed constant α_0, v_0 and Ω_0, I should stress again that this should still be regarded as an illustrative model. Nevertheless, it contains the key physical ingredient of two competing α-effects with a "surface" α-effect contribution that depends upon a time-delayed toroidal field. In order to obtain dynamo waves that propagate towards the Equator, I focus primarily upon the $D < 0$ parameter regime (which would correspond to a negative deep-seated α-effect in the northern hemisphere). I solve the governing equations numerically, approximating derivatives using second-order finite differences. A 4th-order Runge-Kutta scheme is again used to time-step the governing equations.

Given that I am investigating the $D < 0$ regime, the local model suggests that I should be able to find modulation for negative values of S. However, in this region of parameter space there is an overwhelming tendency for steady modes to be preferred at onset (recall that wavelike solutions were assumed when the local model was derived). It is well known that steady and oscillatory modes can bifurcate from the trivial state at similar values of D in global $\alpha\Omega$ dynamos (see, for example, Jennings & Weiss, 1991), so this behaviour is not entirely unsurprising. However, it is almost certainly rather model specific – experimentation with the inclusion of different nonlinear quenching mechanisms suggests that it is possible to obtain oscillatory solutions in these parameter regimes. Furthermore, oscillatory solutions can be found for positive dynamo numbers and therefore, despite some differences, the results from the local model should not be discarded.

In fact, in the case of this PDE model, interesting solutions can be found for negative values of D and positive values of S. This is illustrated by Figure 3.17 which shows solutions for $D = -6000$, $S = 1$, $Re = 10$ whilst varying τ. A periodic solution can be found at $\tau = 0.01$. This is characterised by an oscillatory magnetic field which propagates towards the Equator (note that these contour plots have been plotted as a function of latitude and time, for ease of comparison with observations). Increasing the time-delay to a value of $\tau = 0.05$ leads to a transition to a quasi-periodic solution. Further increasing τ to 0.09 eventually leads to chaotically modulated oscillations. Figure 3.18 shows the toroidal field energy as a function of time for the quasi periodic solution found when $\tau = 0.05$ and chaotically modulated solution generated when $\tau = 0.09$. From these plots

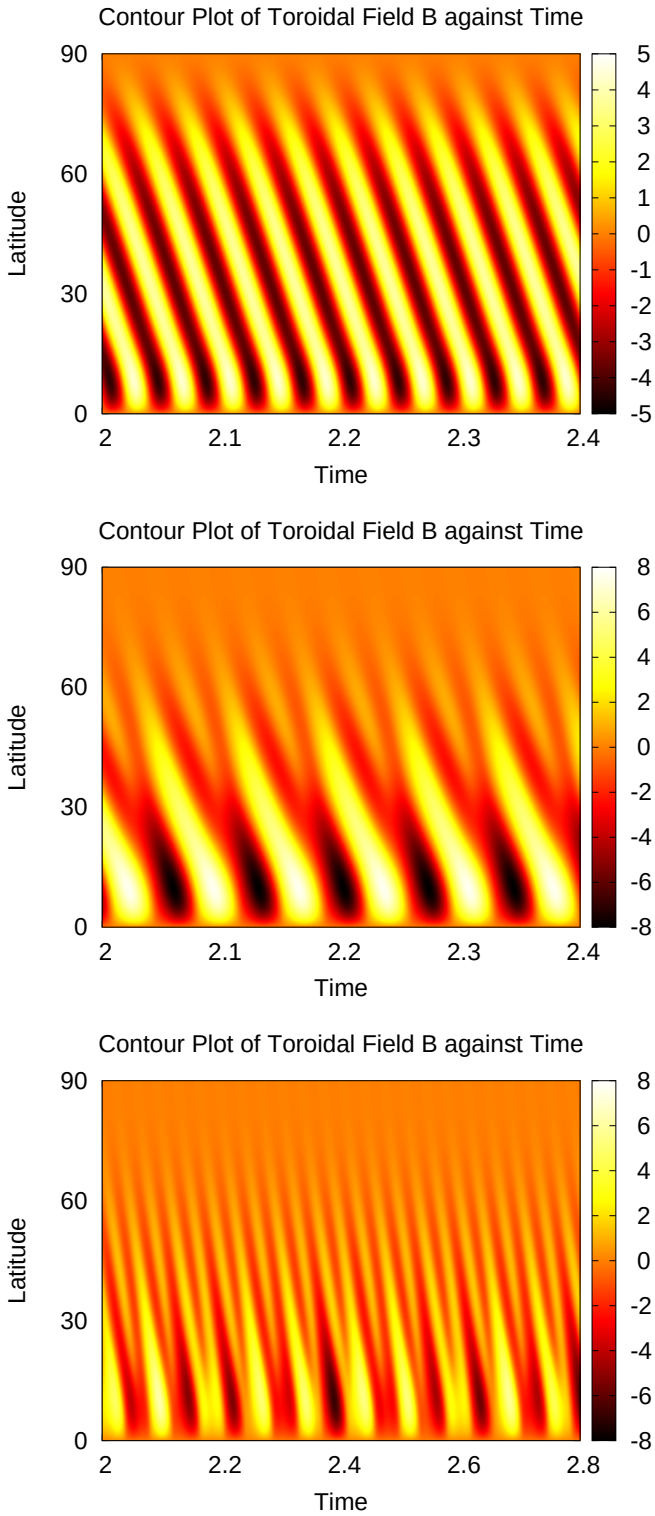

Figure 3.17: Dynamo solutions of the full PDE system ($D = -6000$, $S = 1$ and $Re = 10$). Contours of toroidal field as a function of latitude and time (a latitude of 90° corresponds to the pole, 0° to the equator) for $\tau = 0.01$ (top), $\tau = 0.05$ (middle) and $\tau = 0.09$ (bottom).

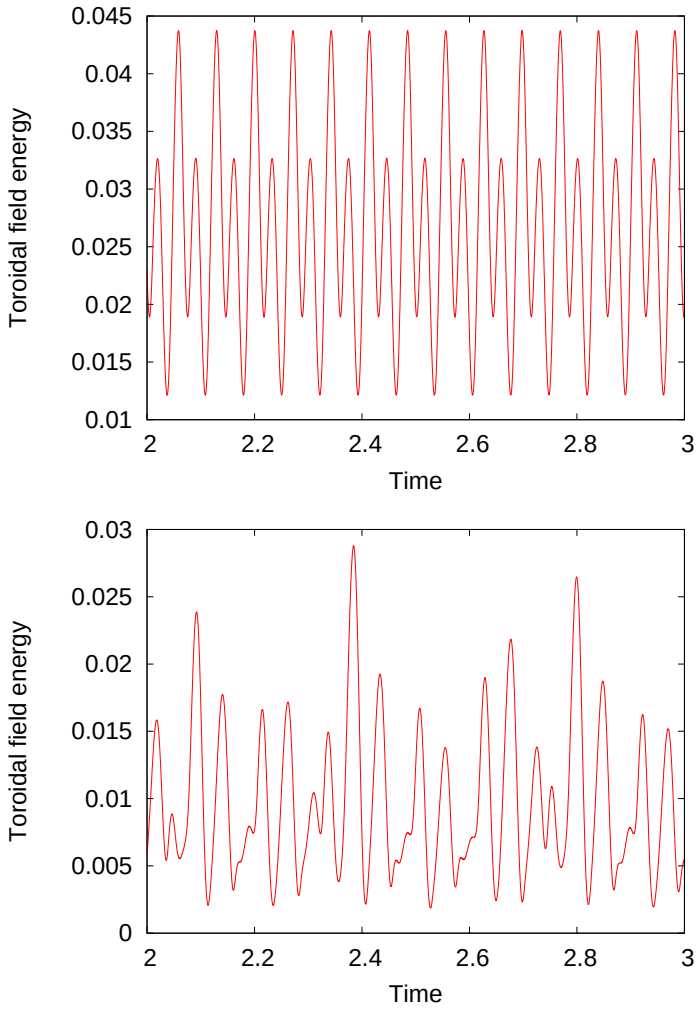

Figure 3.18: Dynamo solutions of the full PDE system ($D = -6000$, $S = 1$ and $Re = 10$). Plots of the energy in the toroidal field as a function of time for the solution that is obtained for $\tau = 0.05$ (top) and $\tau = 0.09$ (bottom).

it is possible to identify cyclic behaviour in the quasi periodic solution whereas when the solution appears to be chaotically modulated it is difficult to identify periodicity in the toroidal field energy. The chaotically modulated solution is rather "solar-like" in many respects, with the dynamo confined to low latitudes, and with strong variations in the amplitudes of successive cycles. Furthermore, the modulation is characterised by periods of reduced magnetic activity.

It is also possible to find modulated behaviour when D is positive. In this regime, it is expected that the dynamo wave propagates polewards and the results given in Figure 3.19 show this feature. Again, the dynamo wave is periodic when τ remains small enough. However modulation is found as τ is increased. The middle plot in Figure 3.19 shows that the dynamo wave is aperiodically modulated and the toroidal field energy, shown in the bottom plot of Figure 3.19 supports this conclusion. Although the toroidal field energy appears to be modulated it is still possible to identify structure within the solution and therefore it is not possible to claim that this solution is chaotically modulated. Nevertheless, this is still a valid example of the modulation that is found within the system.

As previously stated the study of the local model suggest that D and S should both be the same sign in order to find modulated solutions. However the results of the global model suggest that modulation is found when S and D are of opposite signs. Modulation can be found for both positive and negative values of D with S taking the opposite sign so although the modulation due to these competing α-effects is not in the expected parameter regime, it is clearly a robust feature of this system.

3.6 Summary

In this chapter, I have investigated the properties of an illustrative mean-field dynamo model which includes two competing α-effects. The first of these is the standard deep-seated α-effect, the second is due to a surface α-effect. Following the approach described by Jouve *et al.* (2010), who did not consider competing α-effects, the contribution from the surface α-effect was modelled by assuming that it depends upon a time-delayed toroidal field (with a constant parameterised time delay τ). Two different approaches were applied to this model. Initially, a local approximation was made to reduce the governing equations to a system of coupled ordinary differential equations. A linearised version of these equations was used to determine the dependence of the critical dynamo number upon S (the magnitude of the surface α-effect) and τ. Generally, the larger the magnitude of S, the easier it becomes to excite the dynamo. However, there are some regions of parameter space in which the two competing α-effects appear to impede each other, thus inhibiting the dynamo. Moving beyond linear theory, it was found that there are significant regions of parameter space in which the periodic solution becomes unstable with increasing τ,

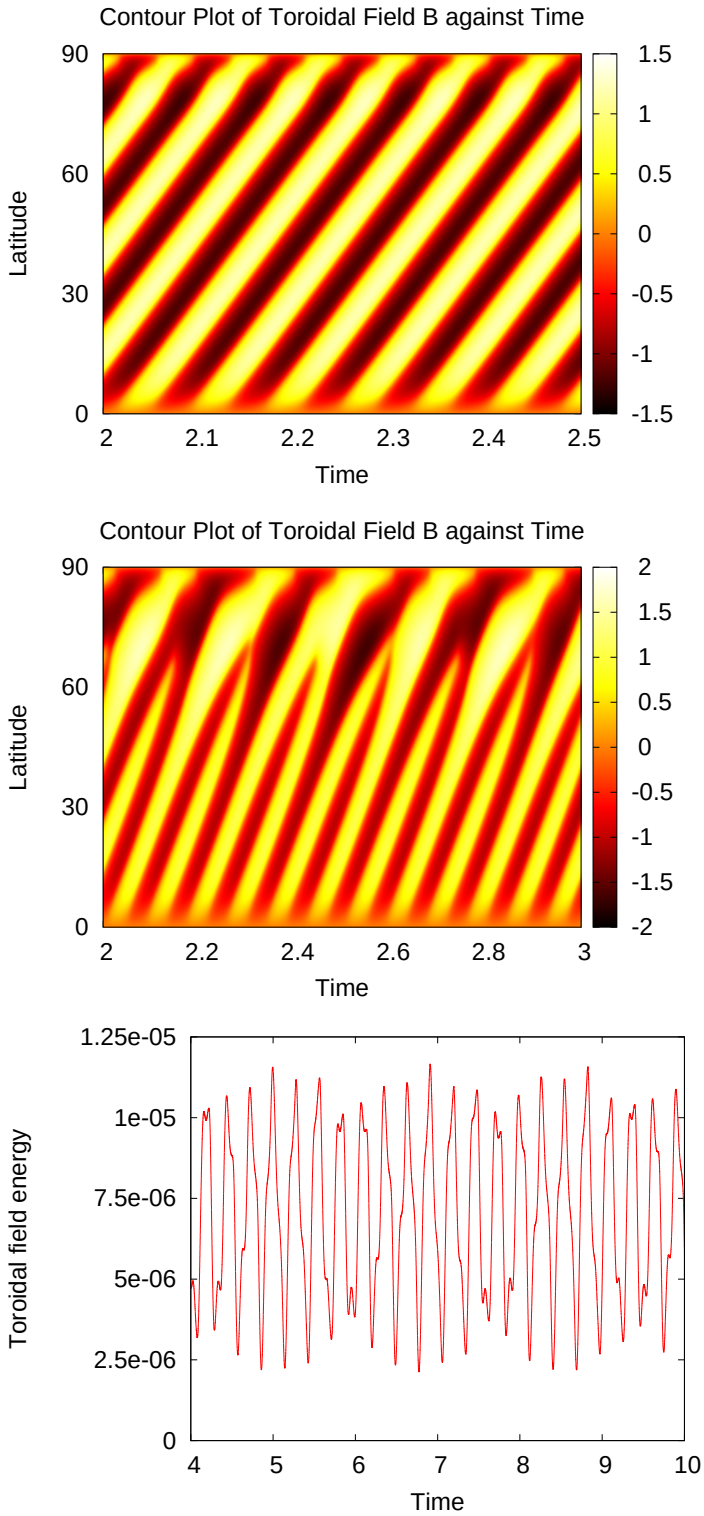

Figure 3.19: Dynamo solutions of the full PDE system ($D = 10000$, $S = 0.7$ and $Re = 1$). Contours of toroidal field as a function of latitude and time for $\tau = 0.005$ (top), $\tau = 0.185$ (middle). The bottom plot is the time evolution of the toroidal field energy when $\tau = 0.185$.

leading to quasi-periodicity. This was verified numerically, where further increases in the time delay were shown to produce chaotically modulated states with phases of significantly reduced activity. The full PDE model was then investigated. Although modulation was found, this occurs in a different parameter regime to that predicted by the ODE model. This discrepancy could be model specific, although I expected to see some differences between the two models due to the fact that significant simplifications were made when deriving the set of coupled ODEs. Nevertheless, it was possible to find chaotically modulated solutions in the PDE model, and these solutions exhibit certain features that are (at least qualitatively) "solar-like".

Chapter 4

Exact ODE Calculations

The previous work in this thesis describes how the delayed field Q can be incorporated in the system by using a Taylor series expansion. Although this is an approximation, it is a valid approximation when τ is small. Nevertheless, it is possible to incorporate the delayed field in an exact way, without having to introduce a differential equation for Q. However, the way that this is implemented is non-trivial. Not only is it challenging to include the delayed field in an exact way but it is also apparent that the results are rather sensitive to the initial conditions used in the numerical simulation. In order to highlight this issue, a similar model is studied in Section 4.2 that can also be solved analytically. After the problem with the initial conditions has been successfully resolved, a comparison is made between the results of this system and the dynamical system studied in Chapter 3.

4.1 Exact system: Model 1

The governing equations are derived in the same way as equations (3.7) to (3.8); the standard $\alpha\Omega$ dynamo equations are taken and both forms of poloidal field regeneration are included, the system is as follows:

$$\begin{aligned} \frac{dA}{dt} + iReA &= \frac{SQ}{1+|Q|^2} + \frac{B}{1+|B|^2} - A, \\ \frac{dB}{dt} + iReB &= iDA - B, \end{aligned} \tag{4.1}$$

where $Q(t)$ is the delayed field.

The challenge with the system lies in how the delayed field is implemented. Essentially, the system is such that there is an $\alpha\Omega$ dynamo operating with the poloidal field regenerated by an interface type α-effect at the base of the convection zone. A delayed field $Q(t)$

(representing the time-delayed source term) is then introduced that is equal to the toroidal field B at the time $t - \tau$, i.e.

$$Q(t) = B(t - \tau). \tag{4.2}$$

The way that this is implemented numerically is to initially simulate a standard $\alpha\Omega$ dynamo model with the only source of poloidal field regeneration due to an interface type α-effect. For the first $-\tau$ time units of the simulation, the value of the toroidal field B is stored in a temporary array. It is only after this time delay has elapsed (i.e. at $t = 0$) that an additional delayed toroidal field $Q(t)$ is introduced that is equal to the toroidal field B at time $t - \tau$ (and is populated by the value of B that is taken from the relevant entry in the temporary array). Simultaneously, as the value of $Q(t)$, or $B(t - \tau)$, is taken from the temporary array, the updated value of $B(t)$ needs to be stored in the temporary array so that it can be used at the time $t + \tau$. A schematic diagram of this mechanism is shown below:

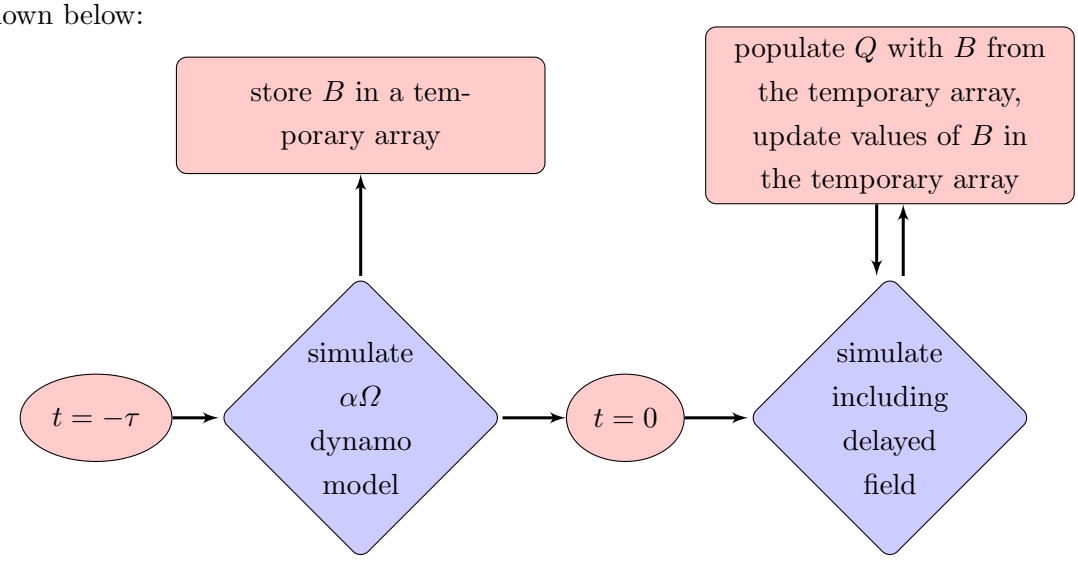

4.2 Validating the numerical scheme

In order to validate the methodology of the numerical simulation, I consider a set of equations that have similar properties to Equations (4.1) but can also be solved analytically. The equations that are considered are as follows:

$$\frac{du}{dt} = \sin(t) + w(t), \tag{4.3a}$$

$$\frac{dv}{dt} = \cos(t), \tag{4.3b}$$

$$w(t) = v(t - \tau). \tag{4.3c}$$

By directly integrating Equations (4.3a) and (4.3b) I can solve them to give analytical functions for u, v and w:

$$\begin{aligned} u(t) &= -\cos(t) - \cos(t-\tau) + c_1 t + c_2, \\ v(t) &= \sin(t) + c_1, \\ w(t) &= \sin(t-\tau) + c_1, \end{aligned} \tag{4.4}$$

where c_1 and c_2 are constants of integration. These equations can then be compared to numerical simulations for given values of τ. Taking advantage of both $\sin(t)$ and $\cos(t)$ being 2π periodic, it is sensible to set $\tau = 2\pi$ and compare the numerical simulations to the analytical calculations. The general solution of the system is shown in Equations (4.5):

$$\begin{aligned} \tau = 2\pi : \qquad u(t) &= -\cos(t) - \cos(t-2\pi) + c_1 t + c_2 = -\cos(t) - \cos(t) + c_1 t + c_2, \\ &= -2\cos(t) + c_1 t + c_2, \\ v(t) &= \sin(t) + c_1, \\ w(t) &= \sin(t-2\pi) + c_1 = \sin(t) + c_1 \end{aligned} \tag{4.5}$$

Imposing the initial conditions $u(0) = v(0) = 0$ leads to the following set of equations that govern u, v and w:

$$\begin{aligned} u(0) = 0 : \qquad u(0) &= -2\cos(0) + c_2 = 0, \\ \implies c_2 &= 2, \\ v(0) = 0 : \qquad v(0) &= \sin(0) + c_1 = 0, \\ \implies c_1 &= 0, \\ \implies u(t) &= -2\cos(t) + 2, \quad v(t) = \sin(t), \quad w(t) = \sin(t) \end{aligned} \tag{4.6}$$

Figure 4.1a shows the numerical simulation of equations (4.3a) - (4.3c) and it is apparent that the numerically calculated value of u agrees with the analytical calculation. The most critical part of this validation is that it proves that the way in which the temporary array is set up and used is correct. At each time step, the temporary array is used to fill w, the new values of v are calculated using an Adams-Bashforth scheme and then the temporary array is overwritten with the new values of v. Figure 4.1b is a time series plot of $v - w$. This clearly shows that during the initial time lag phase, v and w differ since

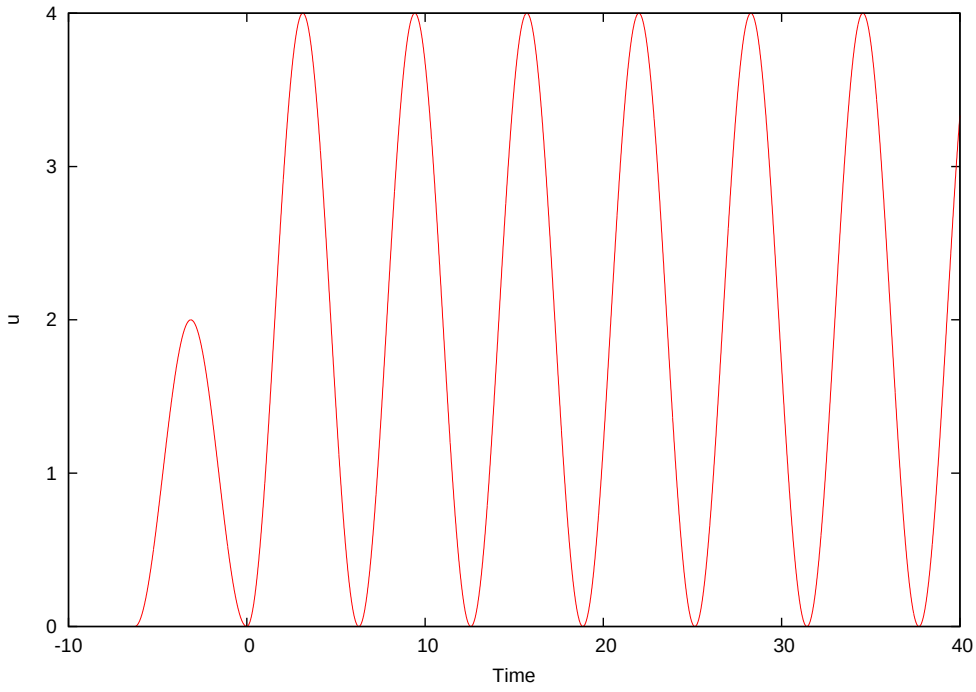

(a)

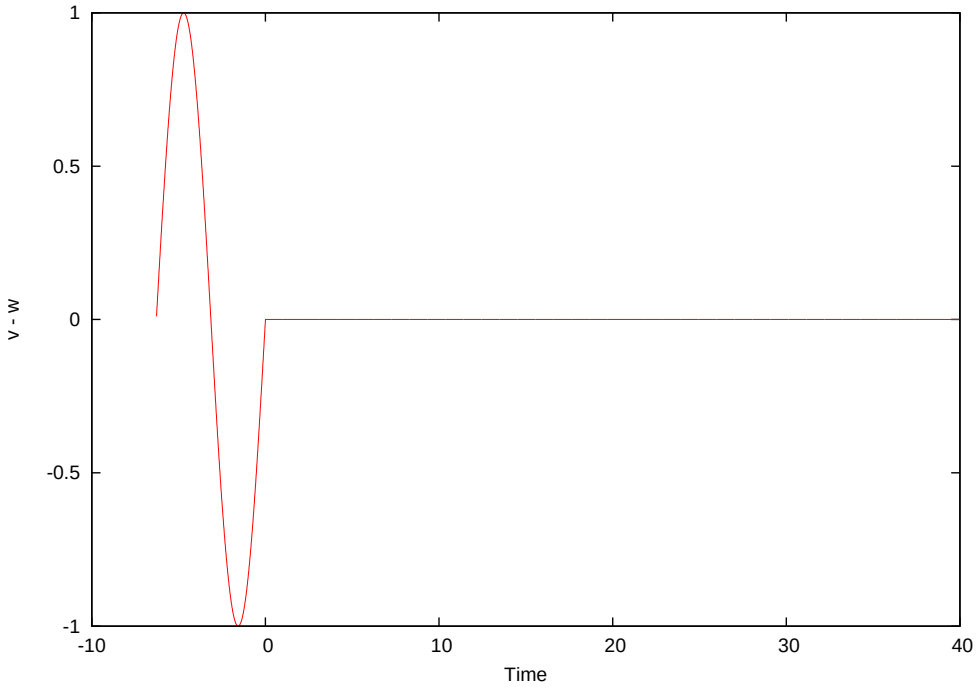

(b)

Figure 4.1: Top: The numerical simulation of u when $\tau = 2\pi$. Bottom: The numerical simulation of $v - w$ when $\tau = 2\pi$. Before $t = 0$, v and w differ since v is $\sin(t)$ and w is zero. After this time lag has elapsed, v and w are identical which means that crucially, the way in which the temporary array is being used is correct. For values of $t > 0$ this is consistent with the analytical solution derived in Equation (4.6), i.e. $u(t) = -2\cos(t) + 2$, $v(t) = \sin(t)$ and $w(t) = \sin(t)$. (For brevity, the individual plots of $v(t)$ and $w(t)$ have not been included).

w is zero however after this time lag has elapsed, v and w are identical, proving that the temporary array is working as expected.

The purpose of working with this similar model is not only to validate that the way in which the temporary array is used is correct but also highlight that careful consideration must be given to the initial conditions. If the incorrect initial conditions are chosen a problem occurs due to the time lag imposed in the simulation and is inherent in the system of equations. For differential equations that can be directly integrated, the corresponding initial conditions can be calculated. However when this is not the case, careful consideration needs to be given as to how to deal with the issue.

The governing equations (4.1), that simulate an $\alpha\Omega$ dynamo with an additional time delayed field Q, cannot be solved analytically and so the way in which the initial conditions are chosen must be carefully considered. If I initially set A to be zero and have a small perturbation for B then, due to the dependence of A upon B, both solutions should grow. It is desirable that A and B are weak during the initial time lag phase (i.e. $-\tau < t < 0$) which means that the subsequent evolution of the magnetic fields will remain independent of the initial conditions.

4.3 Comparison of Model 1 with the 'Approximate' System

The governing equations (3.7) - (3.9), derived in Chapter 3 are restated below for ease of reference and from this point forward will be referred to as the 'approximate' system.

$$\frac{dA}{dt} + iReA = \frac{SQ}{1+|Q|^2} + \frac{B}{1+|B|^2} - A, \tag{4.7}$$

$$\frac{dB}{dt} + iReB = iDA - B, \tag{4.8}$$

$$\frac{dQ}{dt} = \frac{1}{\tau}\left(B - Q\right). \tag{4.9}$$

The derivation of this system requires the use of a Taylor series approximation of Q in order to derive Equation (4.9). This approximation is valid for small values of τ. Since it is now possible to include Q simply as a time delayed version of B, it is sensible to make a comparison between the two systems. Table 4.1 shows the maximum values of the toroidal field B and the frequency of the wave (which has been calculated using a Fourier transform) for given values of τ. The remaining parameters of the system are the same as those used in Case 1 in Section 3.4.3 with $D = 1000$, $Re = 10$ and $S = 10$.

In this case, the results show that when $\tau = 0.01$, the results are (as expected) within very good agreement and the differences in both the maximum values of the toroidal field and the frequency of the wave are less than 0.2%. As τ is increased, it is clear

	$\tau = 0.01$		$\tau = 0.1$		$\tau = 0.2$		$\tau = 0.4$	
	Max B	ω	Max B	ω	Max B	ω	Max B	ω
Model 1	71.08	1.42	42.97	1.24	38.34	1.96	94.02	1.63
approximate	71.20	1.42	52.83	1.28	43.37	1.13	59.91	0.97
% error	0.17%	0.00%	18.82%	3.13%	11.60%	73.45%	56.94%	68.04%

Table 4.1: A comparison between Model 1 and the 'approximate' system (i.e. that considered in Chapter 3). Parameters are the same as those in Case 1 in Chapter 3, i.e. $D = 1000$, $Re = 10$ and $S = 10$ and τ is varied.

that the two systems show a significant difference in results with the percentage errors unacceptably big with the possible exception of the frequency calculated in the case where $\tau = 0.1$. It is worth noting that the solution generated by the 'approximate' system is quasi periodic when $\tau = 0.4$ whereas in the solution generated by Model 1 remains periodic. The discrepancies in the codes may be because the higher order terms that have been neglected in the Taylor series approximation used in the ODE system are now non negligible. In order to speculate if this is the case, other reasons for the systems to disagree need to be ruled out first.

When comparing the codes, the parameters used consider a non-zero Reynolds number, i.e. there is a flow present in the system. When τ is changed, the time delay implemented in the system is increased but there is an additional time scale present due to the non-zero Reynolds number. This may have an effect on the agreement of the two codes. Therefore the codes are again compared, this time without a flow, i.e. $Re = 0$, and Table 4.2 shows the results. Again, as expected, there is very good agreement in the case when $\tau = 0.01$. However as τ is increased the results stay within a very good tolerance of each other, even up to a large value of $\tau = 0.4$. This leads to the conclusion that the effect of the flow on the system is non negligible and that the additional time scale introduced by the Reynolds number greatly affects the behaviour that is observed. The fact that there is good agreement between the codes at a moderate value of $\tau = 0.4$ is somewhat encouraging. The Taylor series approximation that is used in Chapter 3, introduces an error of $O(\tau^2)$ into the differential equation for Q meaning that a time delay of $\tau = 0.4$ introduces an error of ~ 0.16 into the value of Q. At this value of τ, this error term is non negligible and so the agreement between the codes suggests that in this case, the approximation that has been used to generate the dynamical system in Chapter 3, remains valid.

A further comparison is made for finite Reynolds number to show that the codes are within good agreement when the flow remains modest. Table 4.3 shows the results. Again, for small values of τ the codes remain within good agreement and as τ is increased to 0.1 the results differ by an acceptable amount. In this parameter regime, when $\tau = 0.2$, the additional time scale that is introduced by the Reynolds number is comparable to $1/\tau$ and

	$\tau = 0.01$		$\tau = 0.1$		$\tau = 0.2$		$\tau = 0.4$	
	Max B	ω	Max B	ω	Max B	ω	Max B	ω
Model 1	74.49	0.16	77.18	0.145	79.64	0.1373	83.48	0.1221
approximate	74.49	0.16	77.32	0.1431	80.14	0.1335	85.01	0.124
% error	0.00%	0.00%	0.18%	1.33%	0.61%	2.85%	1.80%	1.53%

Table 4.2: No flow: A comparison between Model 1 and the 'approximate' system. Parameters are the same as those in Case 1 in Chapter 3 except $Re = 0$ (i.e. $D = 1000$, $Re = 0$, $S = 10$).

	$\tau = 0.01$		$\tau = 0.1$		$\tau = 0.2$		$\tau = 0.4$	
	Max B	ω	Max B	ω	Max B	ω	Max B	ω
Model 1	7.55	0.63	6.38	0.58	5.22	0.51	3.72	0.39
approximate	7.55	0.63	6.58	0.58	5.84	0.52	4.96	0.44
% error	0.00%	0.00%	3.04%	0.00%	10.62%	1.92%	25.00%	11.36%

Table 4.3: Moderate flow: A comparison between Model 1 and the 'approximate' system. Parameters are $D = 20$, $Re = 5$, $S = 5$ and τ is varied.

so it is unsurprising that the two codes start to differ more significantly from this point as τ is increased.

4.3.1 Results for Model 1

Considering first a periodic case, Figure 4.2 shows the time evolution of the toroidal fields B and Q for two different values of τ. The way in which the delayed field is implemented appears to be correct with Q exhibiting a phase shift with respect to B which is equal to τ time units. By comparing the differences in the plots when $\tau = 0.1$ and $\tau = 0.3$ it is clear that a larger value of the time delay leads to a greater phase shift between B and Q.

This is somewhat consistent with the system that was studied in Chapter 3. However there is an important difference between the two models. It was shown in Chapter 3 that as the time delay is increased, not only does the phase shift between the two fields become greater but this also results in a weaker delayed field, Q, due to the effects of diffusion. This feature is not present within Model 1 due to the way that the delayed field has been implemented: Q is simply a carbon copy of B, τ time units previously, and as such will always be of the same magnitude as B. This feature of Model 1 is clearly displayed in Figure 4.2 since for both values of τ the delayed field Q is of the same magnitude as B.

I have varied the parameters widely to look for modulation, but will focus upon a few illustrative cases:

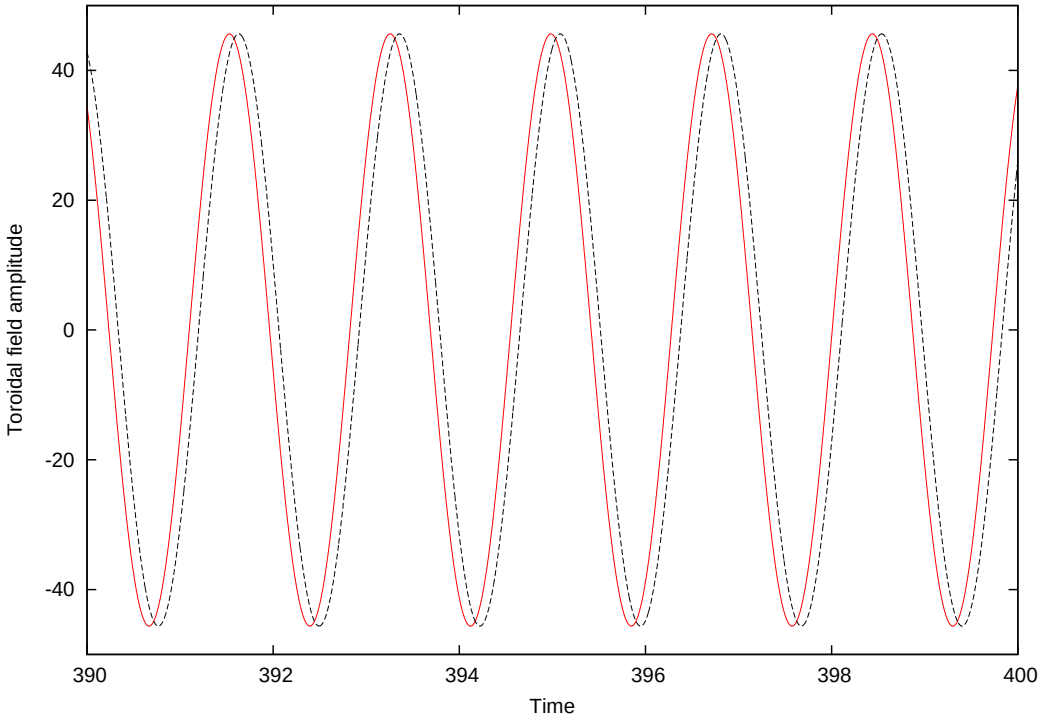

(a) $\tau = 0.1$

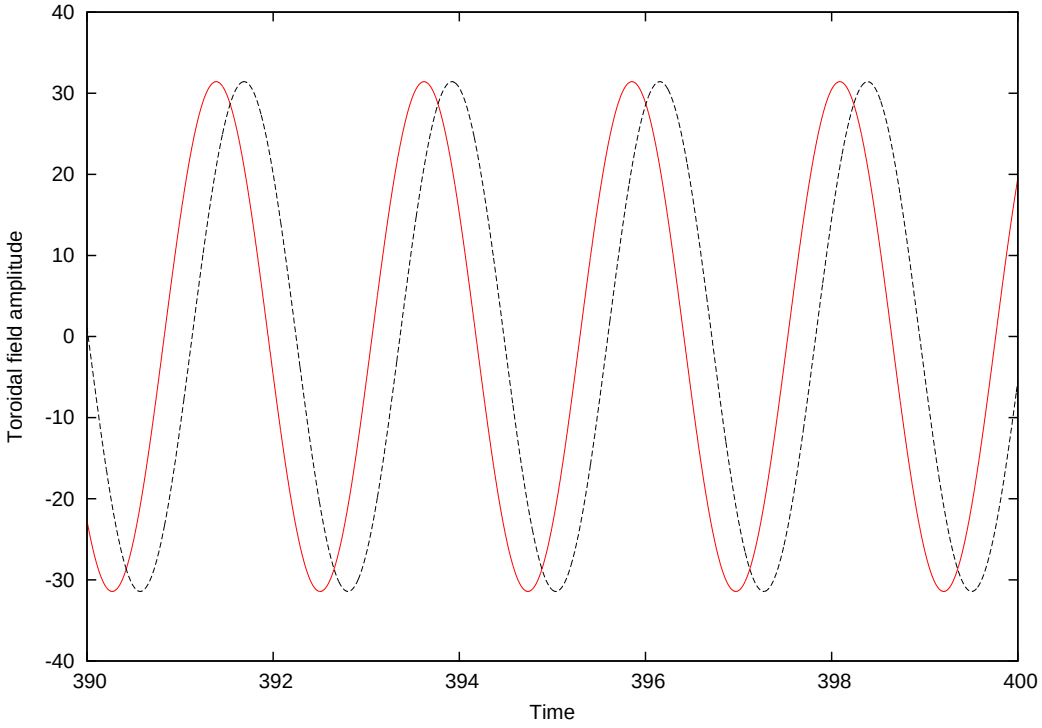

(b) $\tau = 0.3$

Figure 4.2: Periodic solutions for Model 1. The parameters are $D = 20$, $Re = 5$, $S = 9$ with $\tau = 0.1$ (top) and $\tau = 0.3$ (bottom). The red (solid) lines represent the toroidal field B and the black (dashed) lines represent the delayed field Q.

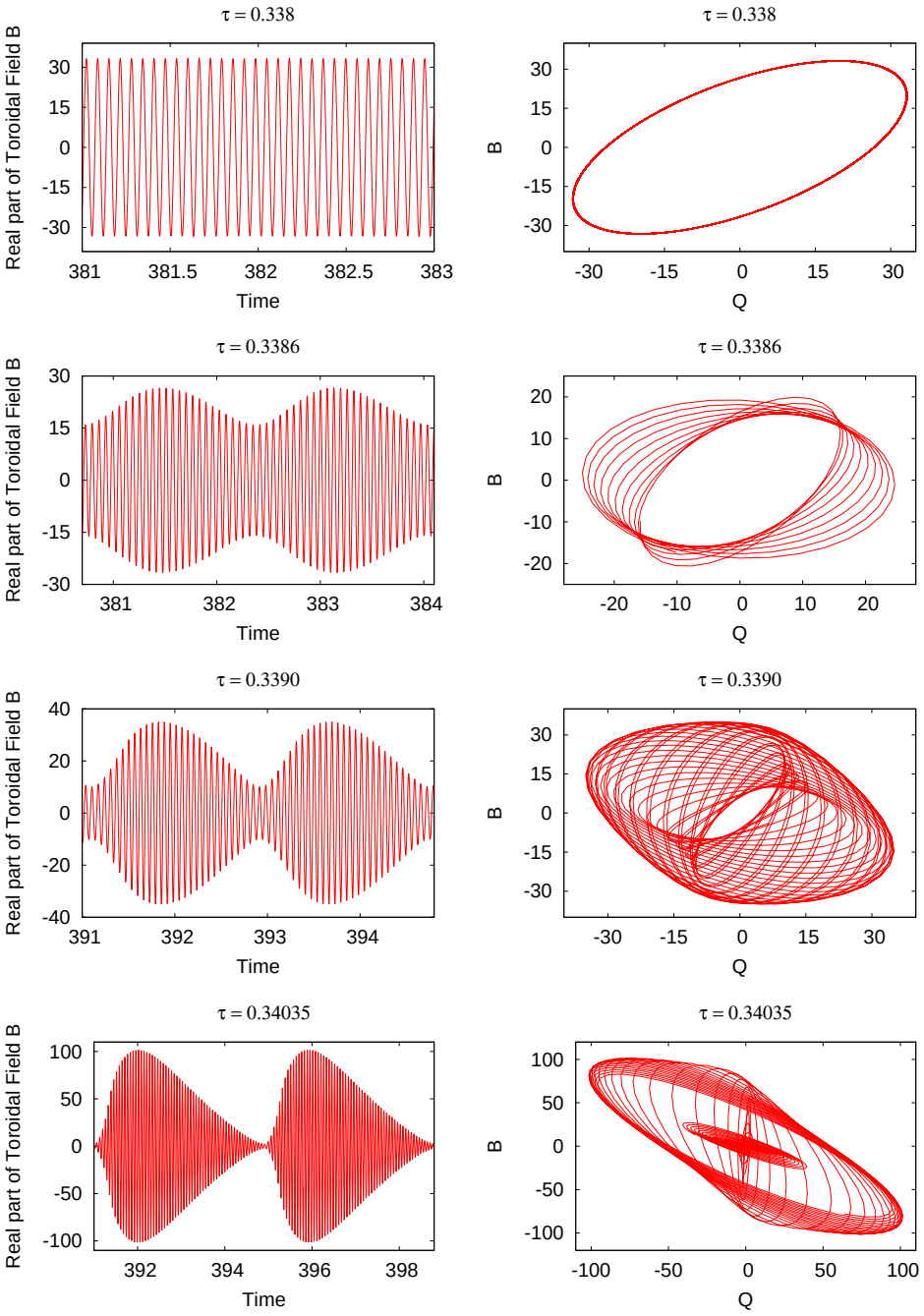

Figure 4.3: Results for Model 1: Here, the parameters are $D = 2000$, $Re = 100$, $S = 2$ and τ is varied. The plots on the left are the time series evolution of the toroidal field B and the plots on the right are the phase portraits of B and Q. When τ is small enough, the solution is periodic and as τ is becomes larger increasingly dramatic modulation is observed.

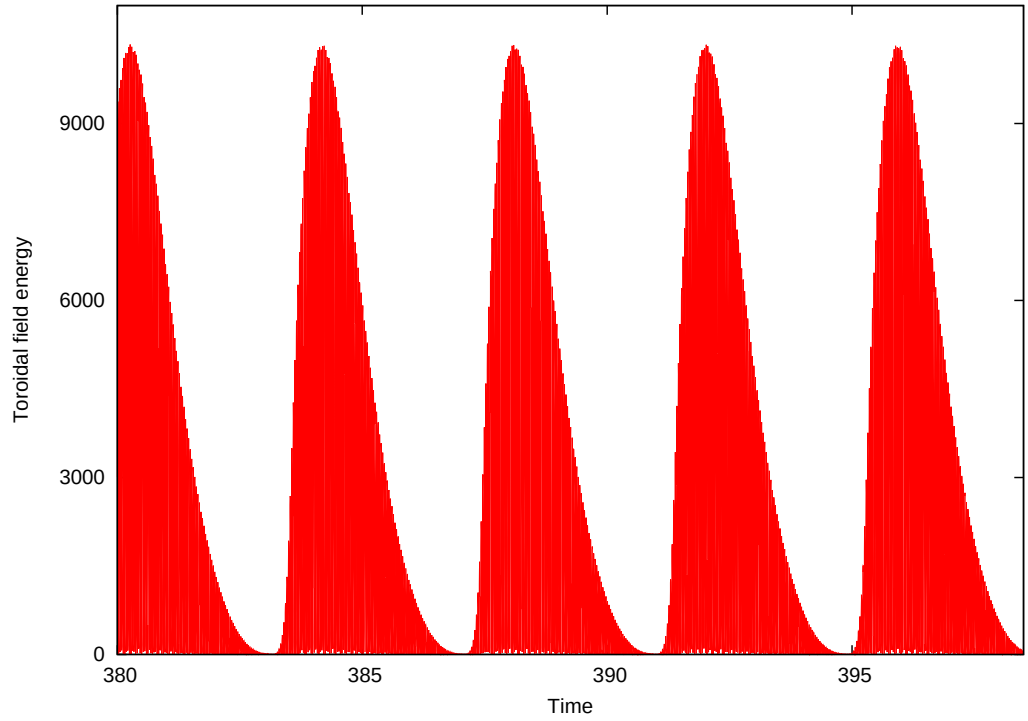

Figure 4.4: Model 1: Toroidal field energy as a function of time for the strongly modulated solution when $D = 2000$, $Re = 100$, $S = 2$ and $\tau = 0.34035$.

Positive D

Figure 4.3 shows an example of the modulation that is found within this system when $D = 2000$, $Re = 100$, $S = 2$ and τ is varied. When τ is less than 0.338, the solution is periodic with the amplitudes of B and Q varying on a fixed orbit and as the time delay is increased, the solution becomes modulated. A Fourier transform of the dynamo wave has been calculated for each value of τ shown and the number of peaks in the signal increases as τ is increased indicating that the solution becomes more strongly modulated as the time delay becomes larger. Once the time delay exceeds 0.35, the periodic solution is again recovered which is consistent with the results from Chapter 3.

The solution when $\tau = 0.34035$ is very attractive when looking for solar like behaviour. Figure 4.4 is the time series evolution of the toroidal field energy for $\tau = 0.34035$ and it shows that there exists periods of low activity which would correspond to grand minima of the Sun's magnetic field. Although this solution is very encouraging, the small window in which this dramatic modulation is found cannot be ignored. Even though the parameter survey was extensive, this particular modulation was difficult to find and therefore it cannot be claimed that this is a typical feature of the system.

Through varying the parameters of the system it is apparent that modulation is easier to find at smaller $|D|$. Figure 4.5 shows another example of the modulation found within

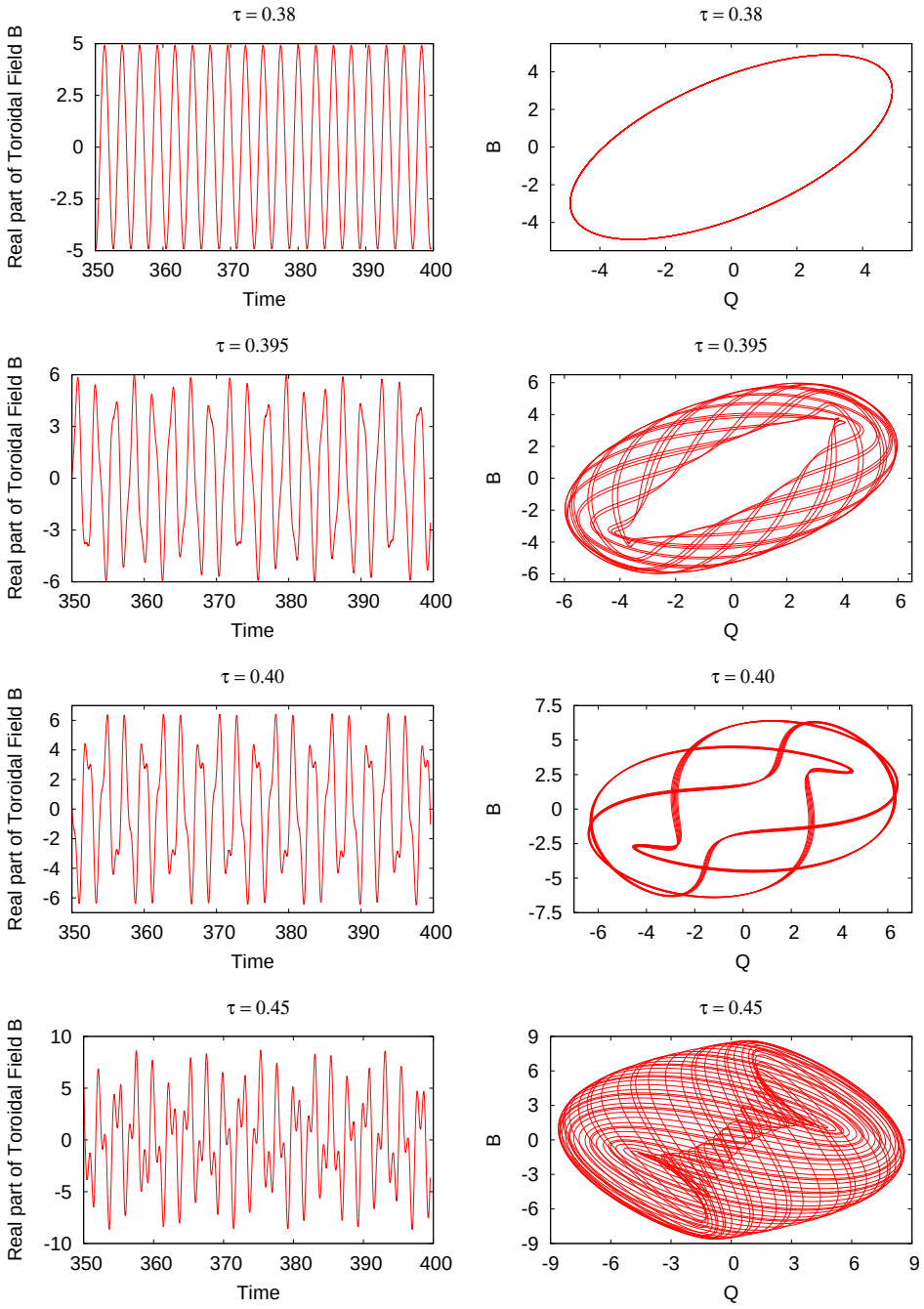

Figure 4.5: Results for Model 1: Here, the parameters are $D = 20$, $Re = 5$, $S = 9$ and τ is varied. The plots on the left are the time series evolution of the toroidal field B and the plots on the right are the phase portraits of B and Q. Modulation of the dynamo wave is observed as τ is increased.

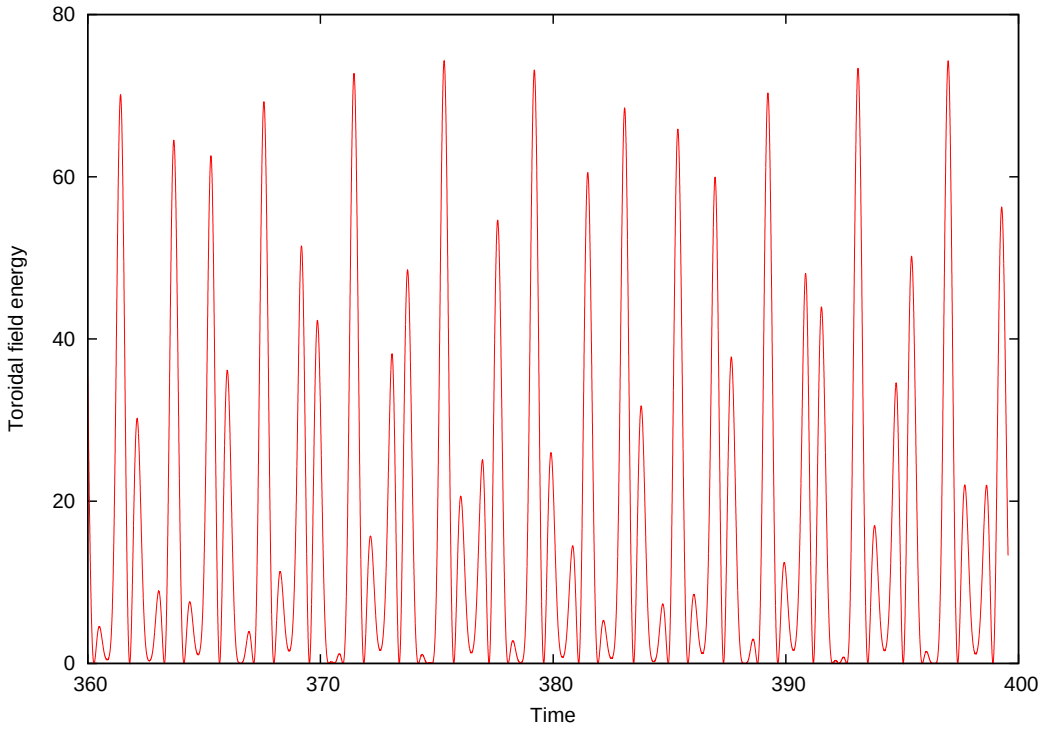

Figure 4.6: Model 1: Toroidal field energy as a function of time for the strongly modulated solution when $D = 20$, $Re = 5$, $S = 9$ and $\tau = 0.45$.

the system when $D = 20$, $Re = 5$, $S = 9$ and τ is varied. This range of parameters is similar to that studied in Case 3 of Chapter 3. The nature of the solution is consistent with the modulation that is shown in Figure 4.3: small values of τ produce periodic solutions and as the time delay is increased the solution becomes more modulated, reaching a strongly modulated state at $\tau = 0.45$. Once the time delay exceeds 0.45, a periodic solution is again recovered. The phase portrait of B against Q when $\tau = 0.40$ is particularly interesting, following a path through phase space that closes in on itself. In this case the frequency of the modulation is an integer multiple of the cycle frequency.

Figure 4.6 shows the toroidal field energy as a function of time when $D = 20$, $Re = 5$, $S = 9$ and $\tau = 0.45$. This (apparently) chaotically modulated solution leads to periods of reduced magnetic activity although it is less pronounced than the modulation found for the other parameter regime that is shown in Figure 4.6. Nevertheless, this is a further example of how varying the time delay can lead to the modulation of the dynamo wave and can result in periods of reduced magnetic activity.

Modulation has also been found for negative values of S. This modulation is similar to that already described in this section and so the plots have been omitted for brevity. However, the trend remains clear. Fixing D, Re and S then increasing τ results in a dynamo wave that becomes more strongly modulated.

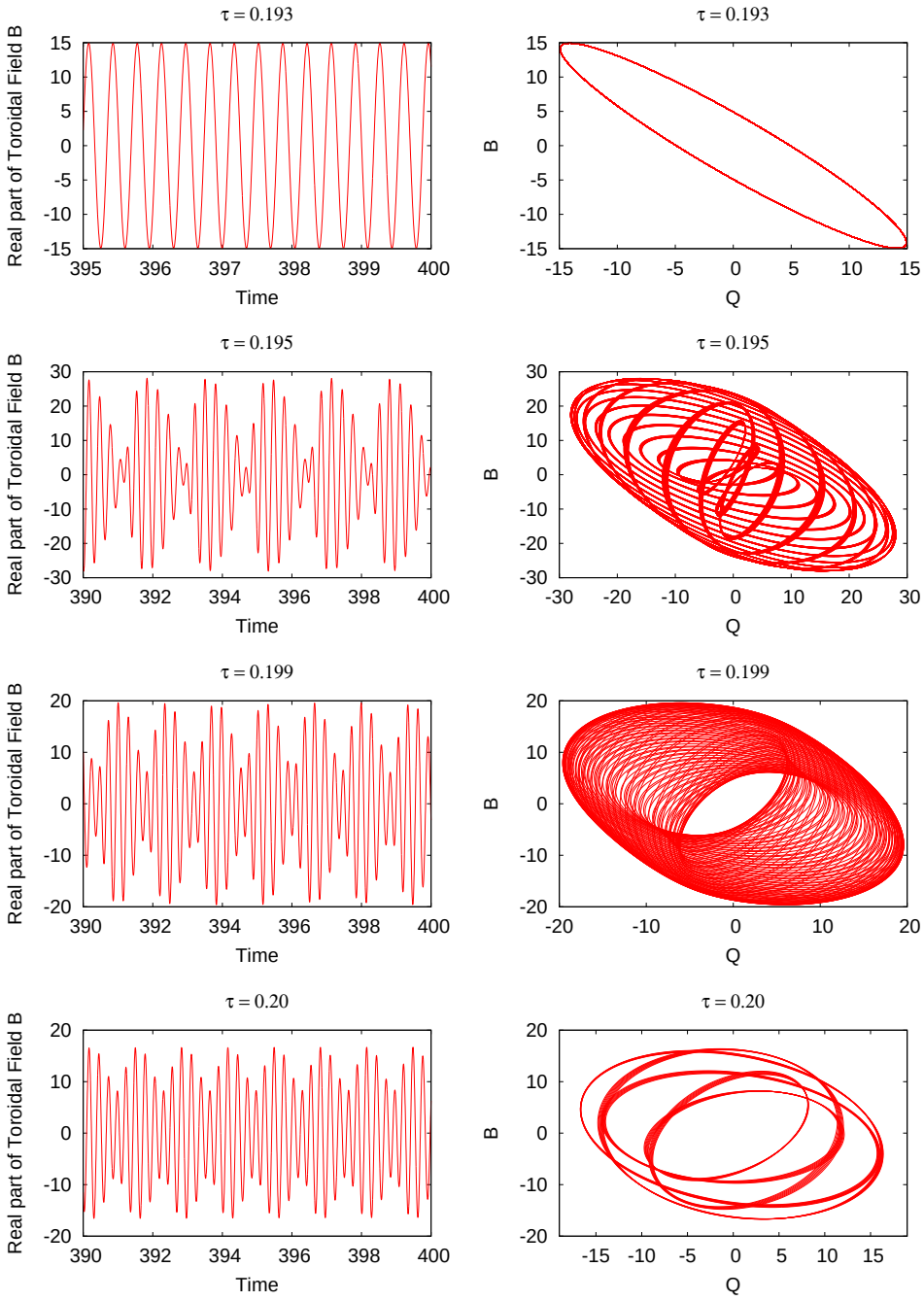

Figure 4.7: Results for Model 1: Here, the parameters are $D = -1000$, $Re = 20$, $S = 2$ and τ is varied. The plots on the left are the time series evolution of the toroidal field B and the plots on the right are the phase portraits of B and Q. Modulation of the dynamo wave is observed as τ is increased.

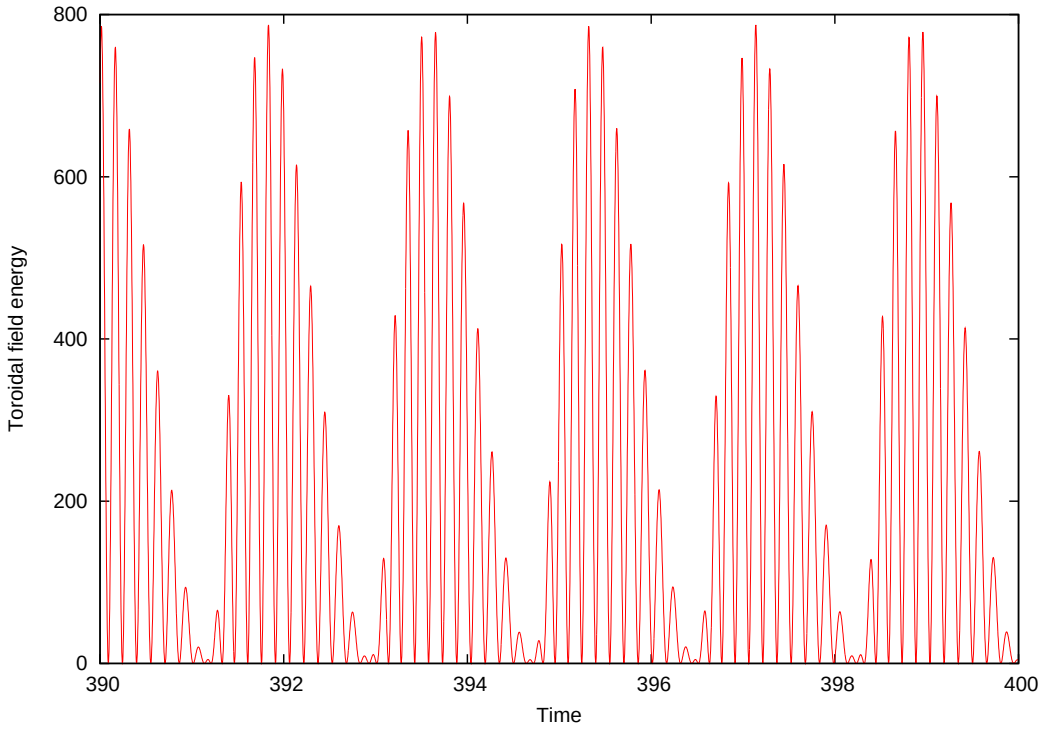

Figure 4.8: Model 1: Toroidal field energy as a function of time for the strongly modulated solution when $D = -1000$, $Re = 20$, $S = 2$ and $\tau = 0.195$.

Negative D

It is important to note that in solar dynamo models, the dynamo number D must be negative in order for the dynamo wave to have the correct direction of propagation when solving a system of PDEs. Although Model 1 consists of a set of coupled ODEs it is encouraging that modulation can also be found in the negative D regime. An example of this is given in Figure 4.7 when $D = -1000$, $Re = 20$, $S = 2$ and τ is varied. When τ is smaller than 0.193, the solution remains periodic and the phase portraits of B and Q show that they vary on a fixed orbit. Once the value of τ has exceeded 0.195, the phase shift between B and Q becomes large enough such that the solution becomes strongly modulated. This modulation is not only shown in the time evolution of the toroidal field B but is also clearly present within the phase portraits of B and Q. When $\tau = 0.195$, the phase portrait is sparsely populated and this indicates that the frequency of the modulation is again an integer multiple of the cycle frequency. Similar behaviour is found when $\tau = 0.2$. Figure 4.8 shows the toroidal field energy as a function of time when $D = -1000$, $Re = 20$, $S = 2$ and $\tau = 0.195$. Periods of significantly reduced activity are present within the system indicating that in this parameter regime, the competing *alpha*-effects are responsible for modulating the total energy within the system.

Although I have only included one example of the modulation for negative values of

D, i.e. $D = -1000$, it is also possible to find modulation when $-D$ is much closer to criticality. It is generally found that modulation is present in a broader window of τ when D becomes closer to criticality and therefore it is easier to find modulation for smaller values of $|D|$. In the examples included, no plots have been shown for negative vales of S but it is also possible to find comparable modulated solutions in this regime.

4.4 Diffusive system: Model 2

The system described thus far in this chapter is constructed such that the delayed field Q is simply a carbon copy of the toroidal field B at a previous point in time corresponding to τ units earlier. This accurately accounts for the time delay imposed in the system; however there is no mechanism through which the delayed field can diffuse. It is reasonable to suppose that this decay should be built into the system because as the magnetic flux rises from the tachocline through the convective zone, the field will decay, resulting in a weaker delayed field returning to the tachocline. This section aims to build this feature into the system.

The governing equations are very similar to those already discussed. The evolution equations for A and B are the same as those stated in Equation 4.1 but the way in which Q is incorporated into the system is now derived from a simple differential equation which includes a diffusive term. In order to derive an expression for $Q(t)$ it is helpful to consider an equivalent differential equation for an auxiliary field $R(t, t')$ that is independent of τ:

$$\begin{aligned} \frac{\partial R}{\partial t'} &= -R(t'), \\ \implies \int \frac{dR}{R} &= -\int dt', \\ \implies R(t, t') &= Ae^{-t'}, \end{aligned}$$

where A is a constant. Equating $R(t, 0)$ to be the toroidal field at the time $t - \tau$, I define, $R(t, 0) = B(t - \tau)$ and so the general general solution is thus

$$R(t, t') = B(t - \tau)e^{-t'}.$$

Note that the variable t' is independent of t. Clearly,

$$R(t, \tau) = B(t - \tau)e^{-\tau}.$$

Having propagated $R(t, 0)$ forward by τ time units, it is natural to equate this function to $Q(t)$. The relationship between $Q(t)$ and $B(t)$ is therefore:

$$Q(t) = B(t - \tau)e^{-\tau}.$$

	$\tau = 0.01$		$\tau = 0.1$		$\tau = 0.2$		$\tau = 0.4$	
	Max B	ω	Max B	ω	Max B	ω	Max B	ω
Model 2	71.40	1.42	42.80	1.24	43.07	1.95	115.49	1.63
approximate	71.20	1.42	52.83	1.28	43.37	1.13	59.91	0.97
% error	0.28%	0.00%	18.99%	3.13%	0.69%	72.57%	92.78%	59.91%

Table 4.4: A comparison between Model 2 and the 'approximate' system. Parameters are the same as those in Case 1 in Chapter 3, i.e. $D = 1000$, $Re = 10$ and $S = 10$ and τ is varied.

	$\tau = 0.01$		$\tau = 0.1$		$\tau = 0.2$		$\tau = 0.4$	
	Max B	ω	Max B	ω	Max B	ω	Max B	ω
Model 2	74.82	0.16	80.81	0.145	87.39	0.1373	100.72	0.1221
approximate	74.49	0.16	77.32	0.1431	80.14	0.1335	85.01	0.124
% error	0.44%	0.00%	4.51%	1.33%	9.05%	2.85%	18.48%	1.53%

Table 4.5: A comparison between Model 2 and the 'approximate' system. Parameters are the same as those in Case 1 in Chapter 3 except $Re = 0$.

This equation for $Q(t)$ is then combined with the evolution equations for A and B that are considered in Chapter 3 (repeated here in equations (4.7) and (4.8)) to give the following set of governing equations for Model 2:

$$\frac{dA}{dt} + iReA = \frac{SQ}{1+|Q|^2} + \frac{B}{1+|B|^2} - A, \tag{4.10}$$

$$\frac{dB}{dt} + iReB = iDA - B, \tag{4.11}$$

$$Q(t) = B(t-\tau)e^{-\tau}. \tag{4.12}$$

The only way in which Model 2 differs from Model 1 is that an exponential decay term is now included in the governing equation for $Q(t)$. In order to allow for more general decay rates, an additional parameter γ could have been introduced and an alternative form for $Q(t)$ would have been $Q(t) = B(t-\tau)e^{-\gamma\tau}$. The effects of varying γ alongside τ is unknown and since Model 2 already contains 4 parameters that govern the system, the dependence of the solution upon γ remains beyond the scope of this thesis.

4.4.1 Comparison with approximate system

As previously done with Model 1, it is appropriate to make a comparison between Model 2 and the approximate model used in Chapter 3. Table 4.4 shows the results for the Model 2 and the 'approximate' system when the Reynolds number is non-zero. Again, the results are in good agreement when τ is very small, i.e. $\tau < 1/Re$. However it is clear that

	$\tau = 0.01$		$\tau = 0.1$		$\tau = 0.2$		$\tau = 0.4$	
	Max B	ω	Max B	ω	Max B	ω	Max B	ω
Model 2	7.58	0.63	6.63	0.58	5.61	0.51	4.28	0.38
approximate	7.55	0.63	6.58	0.58	5.84	0.52	4.96	0.44
% error	0.40%	0.00%	0.76%	0.00%	3.94%	1.92%	13.71%	13.64%

Table 4.6: A comparison between Model 2 and the 'approximate' system. Parameters are $D = 20$, $Re = 5$, $S = 5$ and τ is varied.

as τ is increased, the results start to differ by an unacceptable amount. As previously discovered in Model 1, the difference in values is due to the presence of an additional time scale that is proportional to the inverse Reynolds number. The comparison is done again, this time without a flow and the results are shown in Table 4.5. As expected, the results are very close to each other for small τ. However, as τ is increased there becomes a larger discrepancy in the calculated values of the maximum amplitude of the toroidal field B. This is most likely due to the inclusion of a diffusive term in the governing equation for Q. The difference in the frequency ω remains within a good tolerance of each other as τ is increased. It is interesting to compare the results for Model 1 and Model 2 in this parameter regime. Model 1 consistently underestimates the maximum value of Q whereas Model 2 consistently overestimates the maximum value of Q (as calculated by the "approximate system") . This is because in Model 2 the delayed field will be weaker which will result in a toroidal field B of greater magnitude.

It is also interesting to note that when there is no flow present within the system, and all of the parameters remain fixed, Model 1 and Model 2 both result in a dynamo wave with the same frequency (although this is different to the frequency of the wave calculated in the 'approximate' system). This suggests that the frequency of the dynamo wave is independent of the magnitude of Q. When there is a flow present within the system, this is no longer the case as there is an additional time scale introduced into the solution from the non-zero Reynolds number.

A further comparison is made for finite Reynolds number to show that the codes are within good agreement when the flow remains modest. Table 4.6 shows the results. It is apparent that when τ is small the codes are within good agreement and as τ is increased, the discrepancy between the two codes becomes greater however they remain sufficiently close to each other.

When comparing the maximum values of B and the frequencies of the dynamo waves for Model 1 and Model 2 it is apparent that Model 2 is a closer match to the 'approximate' system when the Reynolds number remains modest. This shows that the decay of the magnetic field included in Model 2 is able to more accurately reproduce the behaviour seen in the 'approximate' system.

4.4.2 Results for Model 2

It is possible to highlight the key difference between Model 1 and Model 2 through studying the periodic solution (which is again found when the time delay remains small enough). Figure 4.9 shows the time evolution of the toroidal fields B and Q when $D = 20$, $Re = 5$, $S = 9$ for two values of τ.

The results show that when the solution remains periodic, not only does there exist a phase shift between B and Q but also the amplitude of Q is smaller than B. This difference in amplitude is expected due to the exponential decay term that is included in the equation for $Q(t)$. By comparing the solutions given in Figure 4.9, it is clear that increasing the time delay leads to a greater phase shift between B and Q, which is consistent with what is seen in Model 1 and also the 'approximate' system studied in Chapter 3. The plots highlight the crucial difference between Model 1 and Model 2: as the time delay is increased, the amplitude of the delayed field Q becomes smaller representing the effects of diffusion upon the delayed toroidal field.

Despite the differences between Model 1 and Model 2, it is still possible to find modulation within the system. As with Model 1, modulation is searched for with the values of D, Re and S remaining fixed and τ is varied.

Positive D

Focusing initially on the $D > 0$ regime, the parameters used to generate the solutions found in Figure 4.10 are $D = 20$, $Re = 5$, $S = 9$ and τ is varied. This modest D regime is similar to that studied in Case 3 of Chapter 3 and the parameters are not dissimilar to those that are used to generate the modulation shown in Figure 4.5 using Model 1. The solutions show many of the features that have been seen before: the dynamo wave remains periodic when τ is small enough and once τ is increased through a threshold value, there exists a transition to a quasi periodic solution. As the time delay is increased, the solution becomes more strongly modulated and it becomes harder to identify periodicity in the time series plot of B. Figure 4.11 shows the time evolution of the toroidal field energy when $D = 20$, $Re = 5$, $S = 9$ and $\tau = 0.44$. The solution contains periods of low energy illustrating that under these circumstances the competing α-effects can lead to periods of reduced magnetic activity. As D is increased it becomes harder to find modulation and no modulated solutions have been found for $D > 1000$.

Negative D

Modulation can also be found for $D < 0$. To illustrate this, Figure 4.12 shows the behaviour of the system when $D = -200$, $Re = 30$, $S = -5$ and τ is varied. The results are consistent with what is observed in other parameter regimes: the solution is periodic when

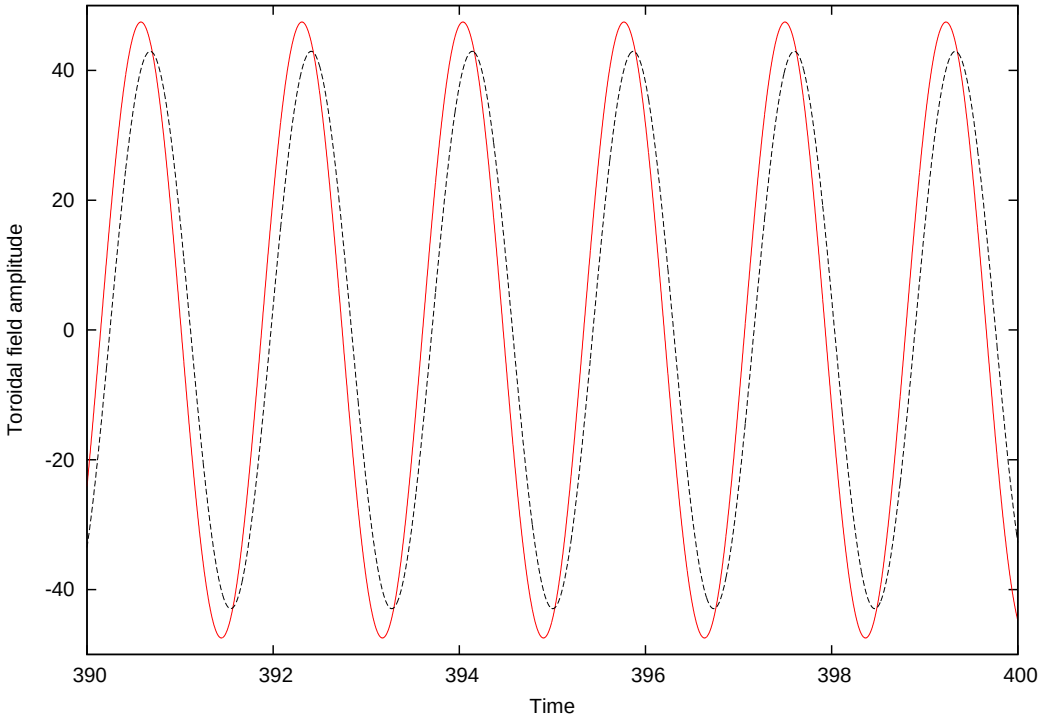

(a) $\tau = 0.1$

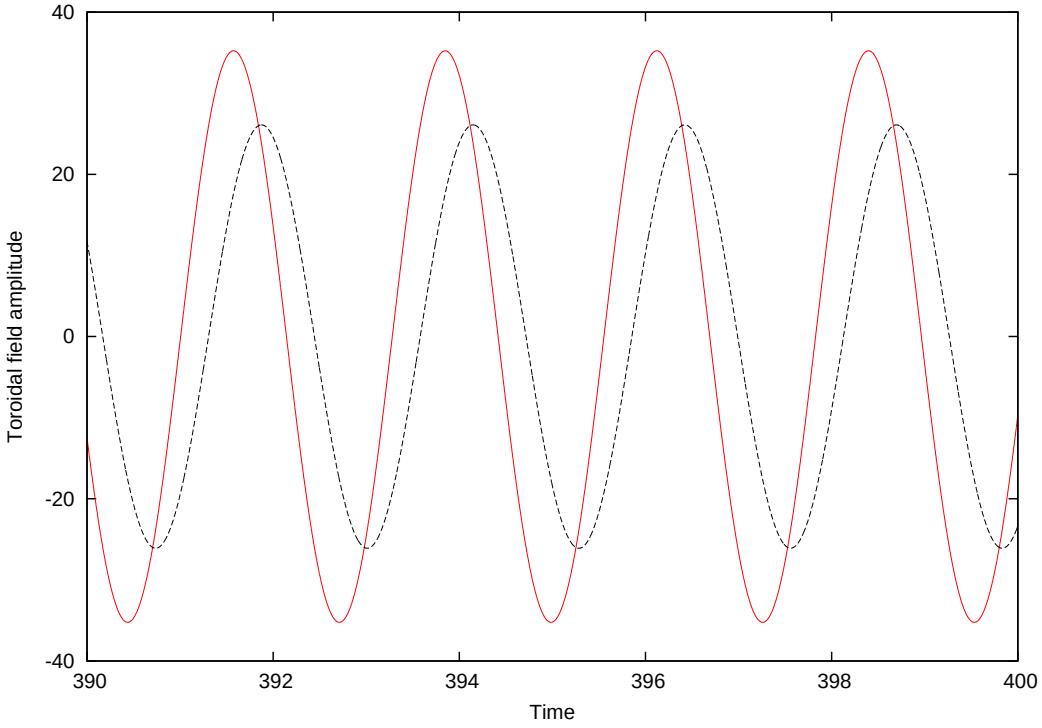

(b) $\tau = 0.3$

Figure 4.9: Periodic solutions for Model 2. The parameters are $D = 20$, $Re = 5$, $S = 9$ with $\tau = 0.1$ (top) and $\tau = 0.3$ (bottom). The red (solid) lines represent the toroidal field B and the black (dashed) lines represent the delayed field Q.

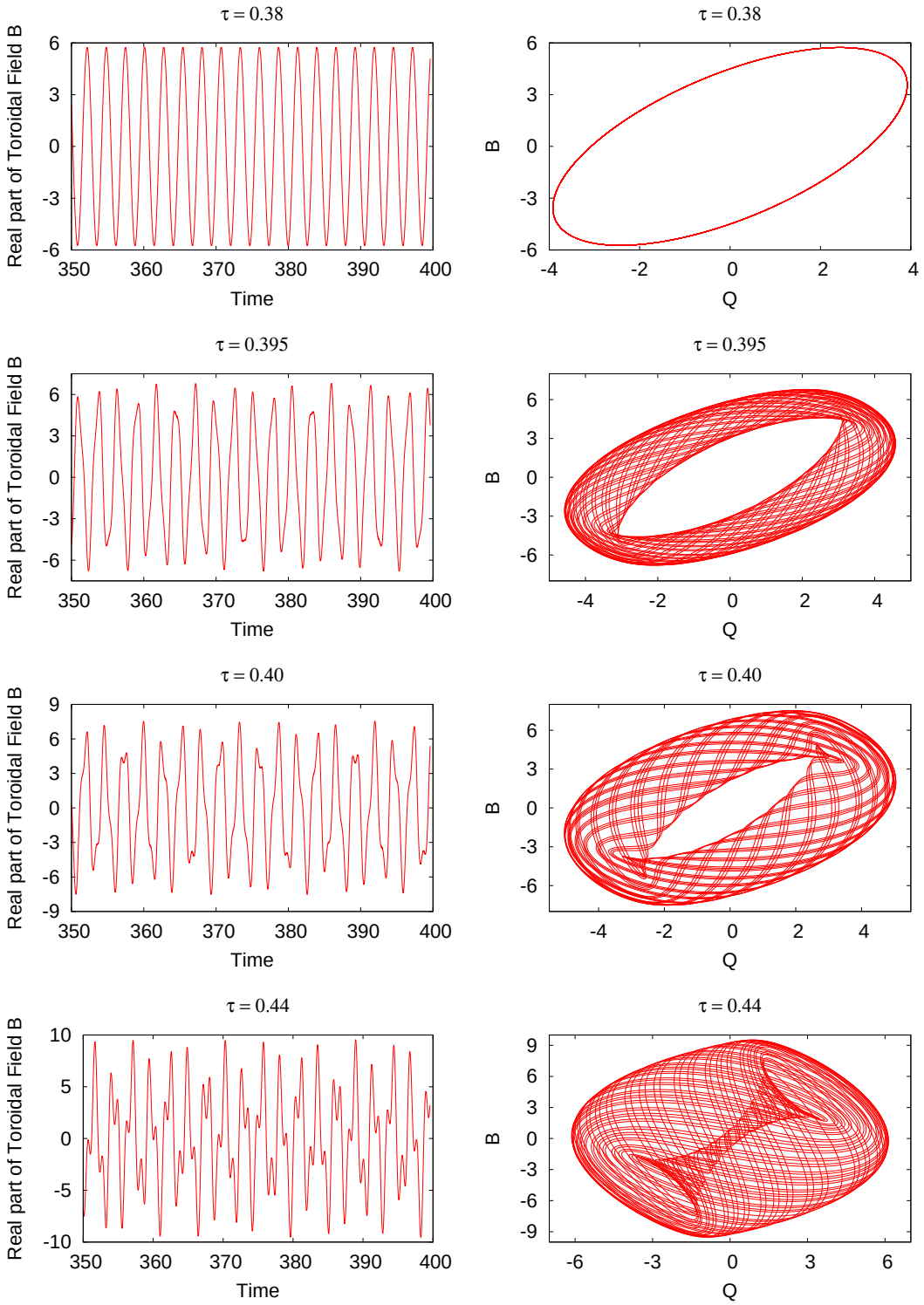

Figure 4.10: Results for Model 2. Here, the parameters are $D = 20$, $Re = 5$, $S = 9$ and τ is varied. When τ is small enough, the solution is periodic and as τ is increased a series of transitions are observed.

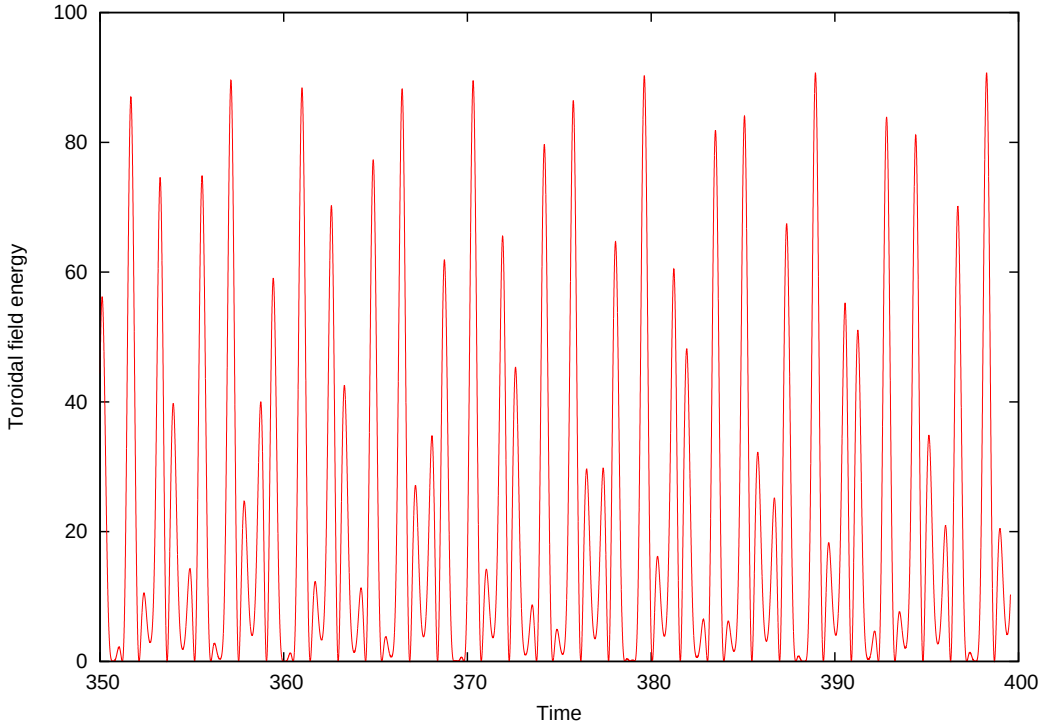

Figure 4.11: Model 2: Toroidal field energy as a function of time for the modulated solution when $D = 20$, $Re = 5$, $S = 9$ and $\tau = 0.44$.

τ remains small enough and once a critical value of τ has been exceeded, the dynamo wave becomes modulated. For this parameter regime, the most dramatic modulation is found when $\tau = 0.248$ and the resulting time evolution of the toroidal field energy is included here in Figure 4.13.

Moving to the more supercritical regime, a final example of the modulation found in Model 2 is given in Figure 4.14. The values of the parameters are $D = -1000$, $Re = 10$, $S = 2$ and τ is varied. The window in which the modulation is found is small, nevertheless this behaviour is still worth documenting. This time, the threshold value that τ must exceed to generate aperiodic solutions is approximately 0.391. For values of τ less than this critical value, the solution remains periodic and the phase portraits of B and Q shows that the solution varies on a fixed orbit. When $\tau = 0.392$, the critical value of τ has been exceeded and the solution appears to be modulated. Once τ becomes too large, the delayed field becomes too weak to have a major affect on B and the modulation is no longer present within the system. Figure 4.15 shows the toroidal field energy as a function of time when $D = -1000$, $Re = 10$, $S = 2$ and $\tau = 0.397$. As expected, the solution contains periods of reduced activity indicating that the competing *alpha*-effects could be responsible for the modulation of the Sun's magnetic field.

As with Model 1, the examples of the modulation that are included in figures 4.10 -

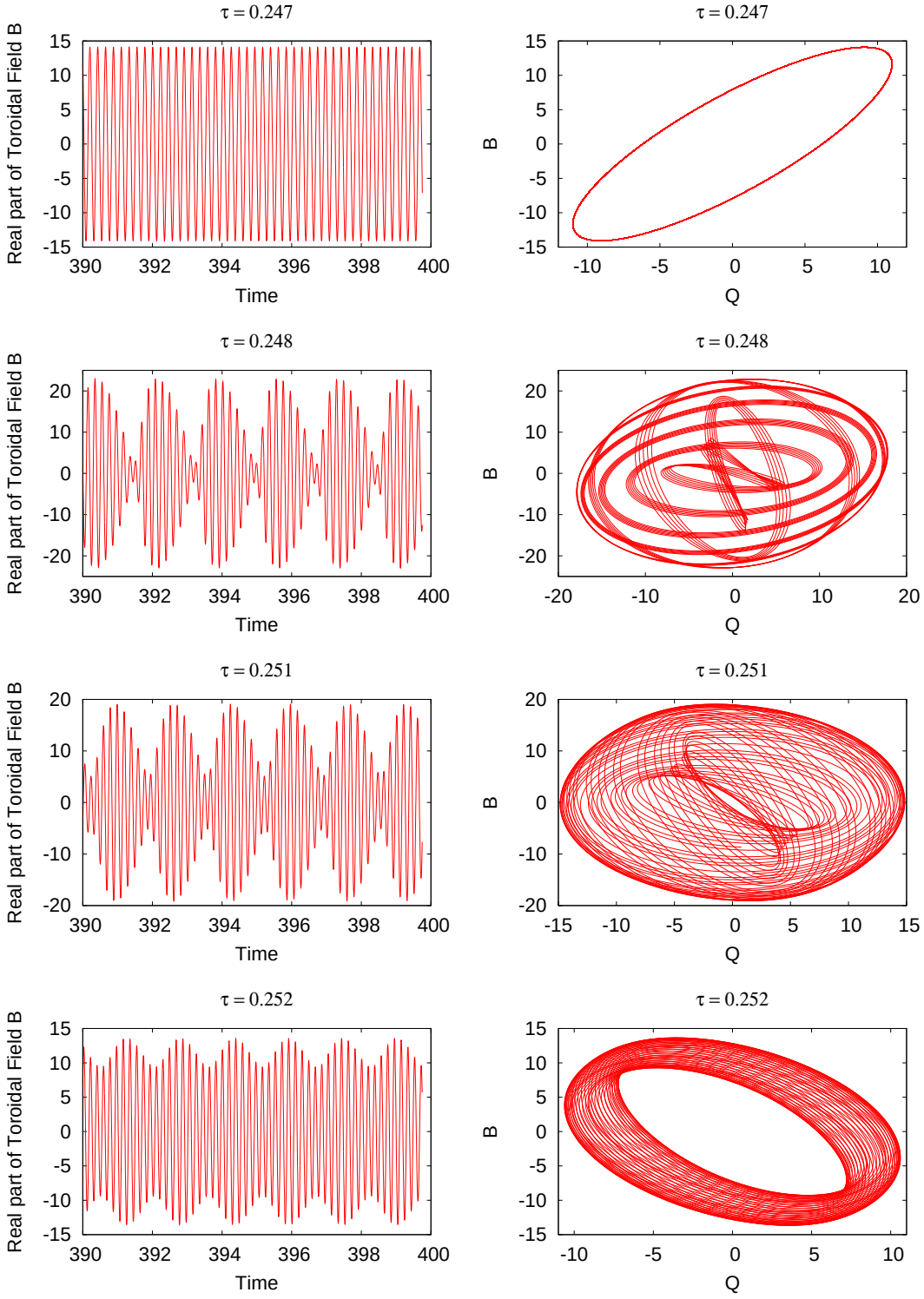

Figure 4.12: Results for Model 2. The parameters are $D = -200$, $Re = 30$, $S = -5$ and τ is varied.

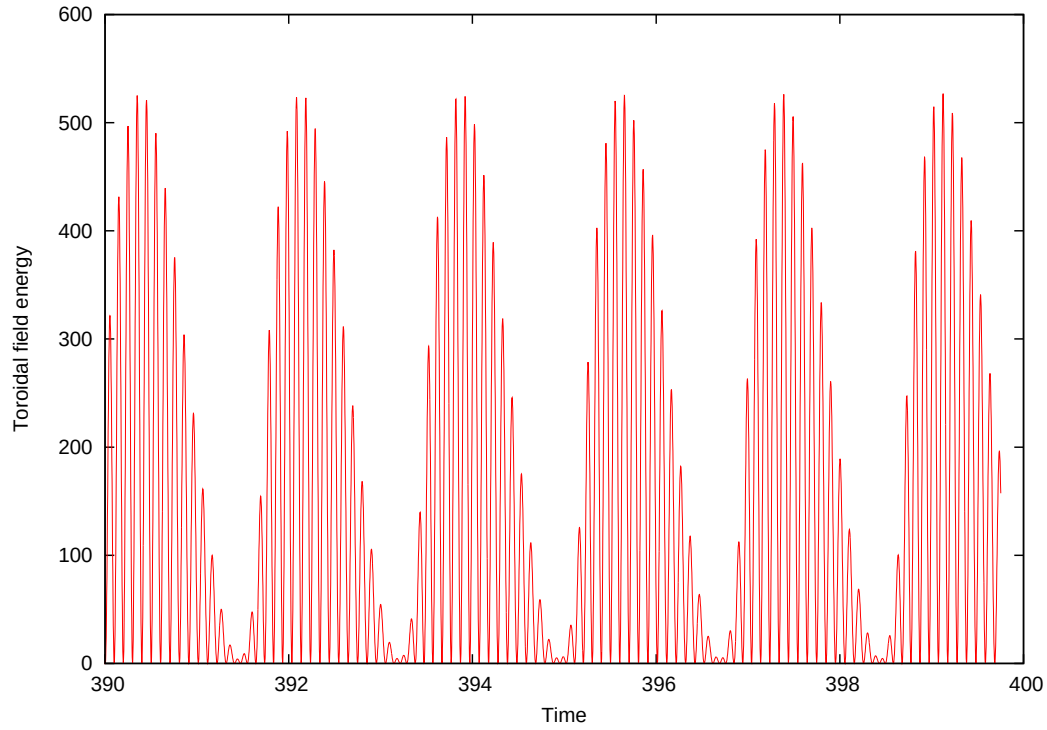

Figure 4.13: Model 2: Toroidal field energy as a function of time for the modulated solution when $D = -200$, $Re = 30$, $S = -5$ and $\tau = 0.248$.

4.15 include a broad range of parameter regimes. Modulation is found for both positive and negative values of D and positive and negative values of S. Again, there appears to be no crucial link between the sign of D and the sign of S when searching for modulated solutions. Modulated solutions are found for values of D that are close to onset as well as supercritical values of D although through varying τ the modulation appears in a broader window closer to onset.

4.5 Summary

This chapter aims to build upon the dynamical system already studied in Chapter 3 through including the delayed toroidal field in a different way. Instead of using a Taylor series approximation when deriving a governing equation for $Q(t)$, two alternative models are considered. The first model (Model 1) assumes that the delayed field Q is simply a carbon copy of the toroidal field B, τ time units previously, and the second model (Model 2) builds upon Model 1 through the introduction of an exponential decay term that is proportional to τ. This should represent the effects of diffusion upon the delayed field Q.

Before the results of the numerical calculations are considered, a comparison is made between both the models and the dynamical system that is considered in Chapter 3. It

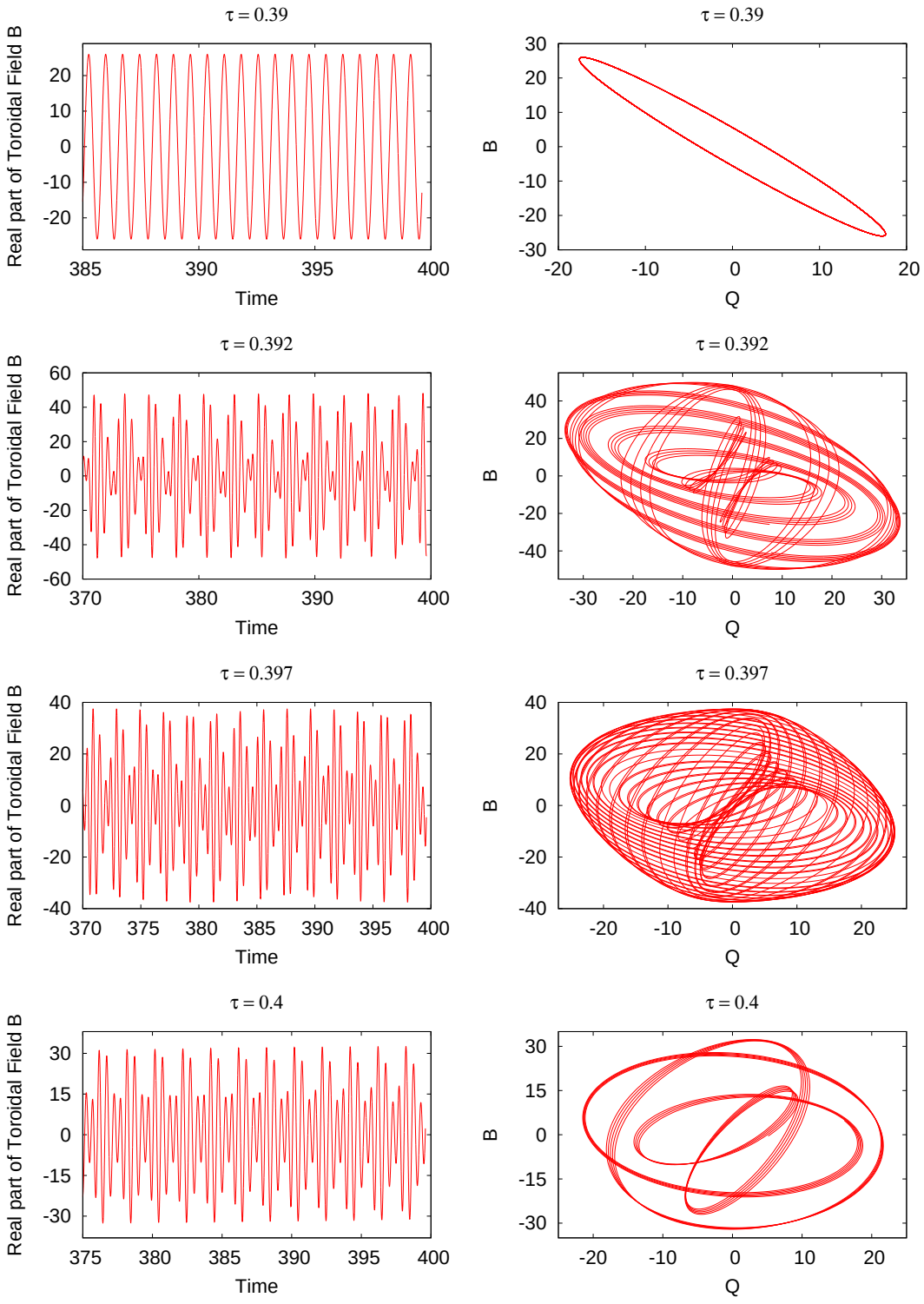

Figure 4.14: Results for Model 2. The parameters are $D = -1000$, $Re = 10$, $S = 2$ and τ is varied.

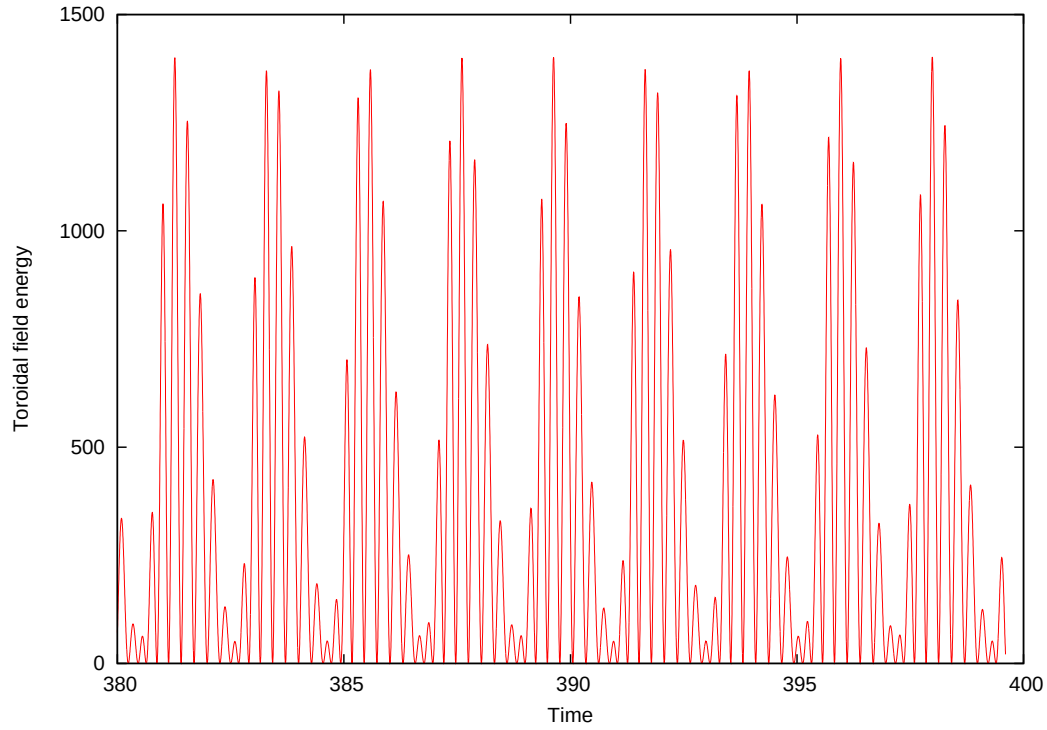

Figure 4.15: Model 2: Toroidal field energy as a function of time for the modulated solution when $D = -1000$, $Re = 10$, $S = 2$ and $\tau = 0.397$.

is found that for both models, when there is a flow present within the system, there is poor agreement to the 'approximate' system studied in Chapter 3. This is due to the effects of the meridional flow which introduces an additional time scale (as illustrated by the fact that agreement between both models and the 'approximate' system ceases to be acceptable when $\tau \sim 1/Re$). When this meridional flow is removed from the system both Model 1 and Model 2 are within good agreement to the 'approximate' system even up to values of τ approaching 0.4.

The key difference between Model 1 and Model 2 is the way in which the delayed field Q is implemented. Numerical results clearly show that the period of Q becomes longer as τ is increased for both models. For Model 2, it is shown that through varying τ the effects of diffusion upon the delayed field results in a lower amplitude of Q when τ is increased. This result is as expected when studying the governing equation for Q.

Encouragingly, modulation is found in both systems, which supports the conclusions that have previously been made in Chapter 3: the time delay τ has to exceed a threshold value before modulation is induced. If this delay becomes too big, Q fails to significantly influence B and the solution returns to a periodic state. Modulation is found in several parameter regimes and it is not critical that D and S have the same or indeed opposite signs to generate modulated solutions. In both models, modulation is found for values of

$|D|$ close to onset as well as supercritical values of $|D|$ however it is generally easier to find modulation for smaller values of $|D|$. This is because the window (in τ) in which the modulation appears becomes narrower as $|D|$ is increased. Since modulation is found in both Model 1 and Model 2, the diffusion of the delayed field Q does not appear to be vital when searching for modulation of the dynamo wave and indeed the most crucial feature of all the models is that the nature of the modulation is dependent upon the time delay τ.

The system studied in Chapter 3 introduced an error term into the governing equation for Q through the use of a Taylor series approximation. Models 1 and 2 in this chapter indicate that modulation comparable to that found in the 'approximate' system can still be found when the time delay is included in an exact way. This leads to the conclusion that the 'approximate' system is a valid representation of the governing equations when the time delay τ remains relatively small.

Part III

Competing alpha effects in Spherical Geometry

Chapter 5

The $\alpha\omega$ dynamo in Spherical Geometry

Thus far, the work contained in this thesis considers the $\alpha\omega$ dynamo equations in cartesian geometry. The logical progression is to show that the modulation found in previous chapters can also be found when solving the competing alpha system in spherical geometry. The transition to spherical geometry is non-trivial: not only does the differential operator ∇ introduce additional multiplicative factors in the governing equations but the boundary conditions also require careful consideration.

After the governing equations and boundary conditions have been derived, it is important to check the validity of the numerical code. This chapter contains details of the derivation of both the governing equations and boundary conditions and also the stringent checks that the code has passed.

5.1 Model Setup

I start from the (axisymmetric) mean field dynamo equation:

$$\frac{\partial \mathbf{B}}{\partial t} = \nabla \times (\mathbf{U} \times \mathbf{B}) + \nabla \times (\alpha \mathbf{B}) + \eta_\tau \nabla^2 \mathbf{B},$$

where the velocity field is given by $\mathbf{U} = r\Omega(r,\theta)\sin\theta \mathbf{e}_\phi + \mathbf{U}_p(r,\theta)$, with functions $\eta_\tau = \eta_\tau(r,\theta)$ and $\alpha = \alpha(r,\theta)$. Here $\Omega(r,\theta)$ represents the differential rotation and $\mathbf{U}_p(r,\theta)$ represents the meridional flow. This leads to the following set of equations for the r, θ and ϕ components of $\mathbf{B}$:

$$
\begin{aligned}
\frac{\partial B_r}{\partial t} &= \frac{1}{r^2\sin^2\theta}\frac{\partial}{\partial\theta}\left[\alpha r\sin\theta B_\phi\right] + \frac{1}{r\sin\theta}\frac{\partial}{\partial\theta}\left[\sin\theta\left(u_r B_\theta - B_r u_\theta\right)\right] \\
&\quad + \eta\left(\nabla^2 B_r - \frac{2B_r}{r^2} - \frac{2}{r^2\sin\theta}\frac{\partial}{\partial\theta}\left[\sin\theta\left(u_r B_\theta - B_r u_\theta\right)\right]\right), \\
\frac{\partial B_\theta}{\partial t} &= \frac{-1}{r\sin\theta}\frac{\partial}{\partial r}\left[\alpha r\sin\theta B_\phi\right] + \frac{1}{r}\frac{\partial}{\partial r}\left[r\left(B_r u_\theta - u_r B_\theta\right)\right] \\
&\quad + \eta\left(\nabla^2 B_\theta - \frac{B_\theta}{r^2\sin^2\theta} + \frac{2}{r^2}\frac{\partial B_r}{\partial\theta}\right) + \frac{1}{r}\frac{\partial\eta}{\partial r}\left(\frac{\partial}{\partial r}\left[rB_\theta\right] - \frac{\partial B_r}{\partial\theta}\right), \\
\frac{\partial B_\phi}{\partial t} &= \frac{1}{r}\left(\frac{\partial}{\partial r}\left[ru_\phi B_r - ru_r B_\phi + \alpha r B_\theta\right] + \frac{\partial}{\partial\theta}\left[u_\phi B_\theta - u_\theta B_\phi - \alpha B_r\right]\right) \\
&\quad + \eta\left(\nabla^2 B_\phi - \frac{B_\phi}{r^2\sin^2\theta}\right) + \frac{\partial\eta}{\partial r}\left(\frac{1}{r}\frac{\partial}{\partial r}\left[rB_\phi\right]\right) \\
&\quad + \frac{1}{r^2\sin^2\theta}\frac{\partial\eta}{\partial\theta}\left(\frac{\partial}{\partial\theta}\left[B_\phi\sin\theta\right]\right).
\end{aligned}
$$

Taking the mean-field equation and decomposing the magnetic field $\mathbf{B}$ into its toroidal and poloidal components, i.e. $\mathbf{B} = B\mathbf{e}_\phi + \nabla\times A\mathbf{e}_\phi$, leads to the following equations for the evolution of the toroidal field B and the poloidal potential A:

$$
\begin{aligned}
\frac{\partial A}{\partial t} &= \eta\left(\nabla^2 - \frac{1}{\varpi^2}\right)A - \frac{\mathbf{U}_p}{\varpi}\cdot\nabla\left(\varpi A\right) + \alpha B, \\
\frac{\partial B}{\partial t} &= \eta\left(\nabla^2 - \frac{1}{\varpi^2}\right)B + \frac{1}{\varpi}\frac{\partial}{\partial r}\left(\varpi B\right)\frac{\partial\eta}{\partial r} + \frac{1}{\varpi}\frac{\partial\eta}{\partial\theta}\frac{\partial}{\partial\theta}\left(\frac{B\varpi}{r}\right) - \varpi\mathbf{U}_p\cdot\nabla\left(\frac{B}{\varpi}\right) \\
&\quad - B\nabla\cdot\mathbf{U_p} + \varpi\left(\nabla\times A\mathbf{e}_\phi\right)\cdot\nabla\Omega + \left[\nabla\times\left(\alpha\nabla\times A\mathbf{e}_\phi\right)\right]_\phi,
\end{aligned}
$$

where $\varpi = r\sin\theta$. Rescaling the variables as follows, it is possible to reduce the number of parameters in the system:

$$
\begin{aligned}
A &= R_0 B_0 A', \qquad B = B_0 B', \qquad t = \frac{R_0^2}{\eta_{T0}}t', \\
r &= R_0 r', \qquad \alpha = \alpha_0\alpha', \qquad \Omega = \Omega_0\Omega', \\
\eta_T &= \eta_{T0}\eta_T', \qquad \mathbf{U}_p = U_0\mathbf{U}_p',
\end{aligned}
$$

where the subscript 0 denotes representative values of the corresponding components and after dropping the primes the governing equations become:

$$\frac{\partial A}{\partial t} = \eta\left(\nabla^2 - \frac{1}{\varpi^2}\right)A - Re\frac{\mathbf{U}_p}{\varpi}\cdot\nabla\left(\varpi A\right) + R_\alpha\alpha B,$$
$$\frac{\partial B}{\partial t} = \eta\left(\nabla^2 - \frac{1}{\varpi^2}\right)B + \frac{1}{\varpi}\frac{\partial}{\partial r}\left(\varpi B\right)\frac{\partial \eta}{\partial r} + \frac{1}{\varpi}\frac{\partial \eta}{\partial \theta}\frac{\partial}{\partial \theta}\left(\frac{B\varpi}{r}\right) - Re\varpi\mathbf{U}_p\cdot\nabla\left(\frac{B}{\varpi}\right)$$
$$- ReB\nabla\cdot\mathbf{U_p} + R_\omega\varpi\left(\nabla\times A\mathbf{e}_\phi\right)\cdot\nabla\Omega + R_\alpha\nabla\times\left(\alpha\nabla\times A\mathbf{e}_\phi\right)_\phi,$$

where $Re = U_0R_0/\eta_{T0}$, $R_\alpha = \alpha_0R_0/\eta_{T0}$ and $R_\omega = \Omega_0R_0^2/\eta_{T0}$. Letting $A = R_\alpha A'$, it is possible to combine the dimensionless constants R_α and R_ω into the familiar dynamo number $D = \alpha_0\Omega_0R_0^3/\eta_{T0}^2$. Making the well known $\alpha\Omega$ approximation, i.e. $|\nabla\Omega| \gg \alpha$, the final term in the $\partial B/\partial t$ equation may be ignored and hence the governing equations are:

$$\frac{\partial A}{\partial t} = \eta\left(\nabla^2 - \frac{1}{\varpi^2}\right)A - Re\frac{\mathbf{U}_p}{\varpi}\cdot\nabla\left(\varpi A\right) + \alpha B, \tag{5.1a}$$
$$\frac{\partial B}{\partial t} = \eta\left(\nabla^2 - \frac{1}{\varpi^2}\right)B + \frac{1}{\varpi}\frac{\partial}{\partial r}\left(\varpi B\right)\frac{\partial \eta}{\partial r} + \frac{1}{\varpi}\frac{\partial \eta}{\partial \theta}\frac{\partial}{\partial \theta}\left(\frac{B\varpi}{r}\right)$$
$$-Re\varpi\mathbf{U}_p\cdot\nabla\left(\frac{B}{\varpi}\right) - ReB\nabla\cdot\mathbf{U_p} + D\varpi\left(\nabla\times A\mathbf{e}_\phi\right)\cdot\nabla\Omega. \tag{5.1b}$$

It is possible to make these equations nonlinear by replacing α with $\alpha/(1+B^2)$. This α-quenching term limits the magnitude of the large-scale solar magnetic field, ensuring that it does not become too large. This is the simplest form of non-linearity that can be used and is consistent with previous work included in Chapters 3 and 4.

5.1.1 Numerical Considerations

The following discussion focuses upon the poloidal potential A but the same statements are also valid for the toroidal field B.

The computational domain is discretzed into a uniform mesh parameterised by lines of constant r represented by the index i and lines of constant θ represented by the index j with the grid spacing denoted by the constants Δr and $\Delta\theta$ respectively. The indices i and j are both integers ranging from 1 to N_r and 1 to N_θ respectively, where N_r and N_θ are given by the maximum values of the grid resolution. The quantity A_i^j represents the value of A at the i^{th} co-ordinate of r and the j^{th} co-ordinate of θ. The governing equations are solved numerically using a centered finite difference representation of the spatial derivatives of A given by:

$$\frac{\partial A}{\partial r} = \frac{A^j_{i+1} - A^j_{i-1}}{2\Delta r}, \tag{5.2a}$$

$$\frac{\partial^2 A}{\partial r^2} = \frac{A^j_{i+1} - 2A^j_i + A^j_{i-1}}{(\Delta r)^2}. \tag{5.2b}$$

with similar expressions for the θ derivatives. In order to minimise the likelihood of numerical instabilities, upwinding derivatives are used for the finite difference representation of the spatial derivatives in the advective terms. These derivatives are dependent upon the direction of the flow $\mathbf{U}$ and ensure that the information used to calculate the value of the spatial derivative always lies upstream. Therefore, the finite difference representation is as follows:

$$\frac{\partial A}{\partial r} = \frac{3A^j_i - 4A^j_{i-1} + A^j_{i-2}}{2\Delta r} \quad \text{for } u_r > 0, \tag{5.3a}$$

$$\frac{\partial A}{\partial r} = \frac{-A^j_{i+2} + 4A^j_{i+1} - 3A^j_i}{2\Delta r} \quad \text{for } u_r < 0. \tag{5.3b}$$

with the corresponding values of the spatial derivatives that lie near the boundaries calculated by using a centred finite difference representation that are analogous to Equations (5.2a) and (5.2b).

An Adams-Bashforth time-stepping scheme, see for example Iserles (1996), is used to evolve the governing equations which calculates the updated value of A by using values from the previous two time steps i.e.:

$$A^j_i(t) = A^j_i(t-h) + \frac{h}{2}\left[3f^j_i(t-h) - f^j_i(t-2h)\right].$$

where h is the time step and $f(t)$ is the numerically calculated value of the right hand side of equation 5.1a.

5.2 Geometry and Boundary Conditions

The computational domain is constructed such that there is a spherical shell with $r_{in} \leq r \leq 1$ and $0 \leq \theta \leq \pi$. It is important to capture within the system the critical layer of the tachocline located around the base of the convection zone. In the Sun, the base of the convection zone is located at around $0.7R_\odot$ and so taking $r_{in} = 0.6$ ensures that this region, as well as the upper part of the radiative zone, is located within the computational domain, see Figure 5.1.

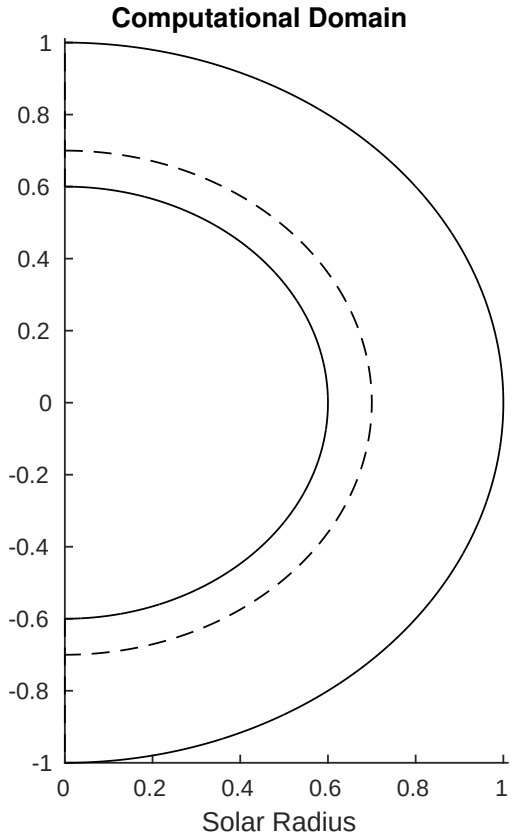

Figure 5.1: The computational domain for $0.6 \leq r \leq 1$ and $0 \leq \theta \leq \pi$. The dashed line represents the base of the convection zone at $r = 0.7$

The boundary conditions are a crucial component of the model and I must carefully consider the requirements that they must satisfy. At $\theta = 0$ and $\theta = \pi$ it is required that the radial component of both the current and the magnetic field remains finite which leads me to take $A = B = 0$. I also set $A = B = 0$ at $r = r_{in}$, which is consistent with the assumption that the dynamo is localised around the base of the convection zone. At the solar surface, I set $B = 0$ and also implement a potential field boundary condition, which corresponds to an insulating exterior.

For the potential field, I need to satisfy $\frac{1}{\mu_0}\nabla \times \mathbf{B} = \mathbf{0}$ in $r \geq 1$, which, after decomposing $\mathbf{B}$ into its toroidal and poloidal components, leads to the following equation in spherical coordinates:

$$\frac{\partial}{\partial r}\left(r^2 \frac{\partial A}{\partial r}\right) + \frac{1}{\sin\theta}\frac{\partial}{\partial \theta}\left(\sin\theta \frac{\partial A}{\partial \theta}\right) - \frac{A}{\sin^2\theta} = 0. \tag{5.4}$$

This equation can be solved by using separation of variables. I must ensure that the

magnetic field vanishes at infinity and so the general solution to Equation (5.4) is

$$A(r,\theta) = \sum_{l=0}^{\infty} \psi_l r^{-(l+1)} P_l^1(\cos\theta), \qquad \text{for } r \geq 1. \tag{5.5}$$

Here, l is the index to be summed over, ψ_l are constant coefficients and $P_l^1(\cos\theta)$ are the associated Legendre functions. Through the use of the standard orthogonality relationship for these functions, see for example Abramowitz & Stegun (1968), Equation 5.5 can be rewritten as:

$$\int_0^{\pi} P_l^1(\cos\theta) P_n^1(\cos\theta) \sin\theta d\theta = \frac{2l(l+1)}{2l+1}\delta_{ln}.$$

I can make use of this relationship by multiplying Equation (5.5) by $P_n^1(\cos\theta)\sin\theta$ and integrating from 0 to π, i.e.

$$\begin{aligned}
\int_0^{\pi} A(r,\theta) P_n^1(\cos\theta)\sin\theta d\theta &= \sum_{l=0}^{\infty} \psi_l r^{-(l+1)} \int_0^{\pi} P_l^1(\cos\theta) P_n^1(\cos\theta)\sin\theta d\theta \\
&= \sum_{l=0}^{\infty} \psi_l r^{-(l+1)} \times \frac{2l(l+1)}{2l+1}\delta_{ln} \\
&= \psi_n r^{-(n+1)} \times \frac{2n(n+1)}{2n+1},
\end{aligned}$$

since δ_{ln} is only non zero when $l = n$. Solving this equation for ψ_n leads to:

$$\psi_n = \frac{2n+1}{2n(n+1)} r^{n+1} \int_0^{\pi} A(r,\theta) P_n^1(\cos\theta)\sin\theta d\theta. \tag{5.6}$$

I have now specified all the requirements that $A(r,\theta)$ must satisfy for $r \geq 1$. However it is required that A is a continuous field therefore I need to ensure that both A and the radial derivative of A must be continuous at the solar surface. Differentiating Equation (5.5) with respect to r gives the radial derivative of A:

$$\frac{\partial A}{\partial r} = -\sum_{l=0}^{\infty} (l+1)\psi_l r_{out}^{-(l+2)} P_l^1(\cos\theta) \qquad \text{at } r = 1. \tag{5.7}$$

For $r < 1$, a finite difference representation of the radial derivative of A is given by:

$$\frac{\partial A}{\partial r} = \frac{3A_i^j - 4A_{i-1}^j + A_{i-2}^j}{2\Delta r}, \tag{5.8}$$

where $A_i^j = A(i\Delta r, j\Delta\theta)$. In order to satisfy that the radial derivative of A at the boundary is continuous, I have two equations (5.7) and (5.8) that can be matched up. This is done by implementing an iterative scheme, the algorithm for which is as follows:

		Stix	Markiel	Bushby	My code LR	My code HR
D<0	D_c	-95.74	-94.55 ± 0.05	-93.51 ± 0.03	-92.71 ± 0.03	-93.84 ± 0.03
	Frequency	79.18	75.5 ± 0.3	74.27 ± 0.4	73.34	74.78
D>0	D_c	83.00	82.35 ± 0.05	83.99 ± 0.03	83.52 ± 0.03	83.55 ± 0.03
	Frequency	81.48	79.6 ± 0.1	82.47 ± 0.5	81.97	81.49

Table 5.1: Critical dynamo numbers and the frequencies of oscillation for the comparison with Stix (2002). The low resolution case has 22 grid points radially and 65 grid points latitudinally. The high resolution case has 64 grid points radially and 65 grid points latitudinally. The results show that my code is within good agreement to previously published results.

- For each time step, the values of A_i^j from the previous time step are used as an initial estimate to the true values of A_i^j and the ψ_l are calculated
- The ψ_l are then fed into Equation (5.7) and the radial derivative of A is calculated
- This value of the radial derivative of A is then substituted into the finite difference representation for $\partial A/\partial r$ i.e. Equation (5.8)
- Equation (5.8) is then rearranged and solved to give A_i^j and the process starts again

This iterative process is repeated until the solution has converged and the desired accuracy is achieved. Due to the time step being small, the values of A_i^j at the previous time step are a good estimate for the current time step and the solution converges very quickly. Although it is clear that the solution converges within a few iterations, the algorithm was programmed to complete 10 iterations in order to ensure that a suitably accurate value has been obtained.

5.3 Code Validation

Before the code is used to carry out new work, it is important to check that the code can accurately reproduce results already published. The following section describes how quantities such as the critical dynamo numbers, period of oscillation, peak toroidal field at the base of the convection zone and peak radial field at the solar surface are compared to those already published and subsequently ensures the validity of my numerical code.

5.3.1 Comparison with Stix (1976)

The $\alpha\omega$ dynamo equations have already been solved as an eigenvalue problem by Stix (1976). In Stix's "model 4", the equations are solved in a spherical shell with $0.5R_\odot < r < R_\odot$. The boundary conditions that are implemented are the same as those in Section 5.2 with one exception; Stix treated the core as a perfectly conducting sphere and so the

condition on B at the inner radius is $\partial(rB)/\partial r = 0$ instead of $B = 0$. The initial conditions used set A to be zero at all points in the computational domain, B to be a small linear combination of $P_1^1(\cos\theta)$ and $P_2^1(\cos\theta)$ at a region around the base of the convection zone and zero everywhere else.

The profiles for the differential rotation, α-effect and the magnetic diffusivity are as follows:

$$\begin{aligned} \Omega(r,\theta) &= r^2 \sin^2\theta, \\ \alpha(r,\theta) &= \cos\theta, \\ \eta &= 1. \end{aligned} \tag{5.9}$$

After removing the α-quenching term the solutions will either grow or decay exponentially, depending upon the strength of D. By varying the magnitude of D it is possible to determine by using interval bisection the critical value, D_c, that will allow for non decaying solutions. Using the above profiles, Stix calculated the critical dynamo numbers. This calculation has been used to validate several other codes in the past. Markiel (1999) and Bushby (2003) have published values obtained from their codes which are included here in Table 5.1 alongside the corresponding entries obtained from my code. It is important to note that both Markiel and Stix used a different definition of the dynamo number than I have and so I must take the square root of the critical dynamo numbers that I have calculated in order to compare the results. Both Markiel and Bushby use a staggered non-uniform mesh in their simulation whereas I have implemented a standard uniform grid. The results are nonetheless promising. Because of the differences in the mesh setup, I have calculated critical dynamo numbers using both a low resolution (22 $\times$65) and high resolution (64 $\times$ 65) case. The low resolution critical dynamo numbers from my code are within 3.2% of that calculated by Stix. Increasing the resolution, the critical dynamo numbers are now within 2% of that calculated by Stix which has improved upon the accuracy given by the low resolution simulation as expected. It is worth noting that Stix only used a small number of modes when doing the calculations and so it should be assumed that the results from that paper will include a substantial numerical error and therefore will be significantly different from the true values.

Once the critical dynamo numbers have been calculated, the α-quenching term is reinstated and a butterfly diagram can be produced. The frequency of the resulting dynamo wave can be calculated using a Fourier transform and the results are also included in Table 5.1. It is clear that in all cases the frequencies that I have calculated are in good agreement with previously published results. In particular, in both the low and high resolution cases for both positive and negative dynamo numbers the results are within 2% of Bushby's.

	Bushby	Markiel	My code
Peak toroidal field	3.14	3.20	3.28
Period of oscillation	0.0097	0.0094	0.0109

Table 5.2: Values of the peak toroidal field and the period of oscillation for the comparison included in 5.3.2. All calculations are done at a resolution of 64 grid points radially and 65 grid points latitudinally.

	Bushby	My code
Peak toroidal field	2.74	2.80
Period of oscillation	0.0076	0.0078

Table 5.3: Values of the peak toroidal field and the period of oscillation for the comparison included in 5.3.2. All calculations are done at a resolution of 101 grid points radially and 193 grid points latitudinally.

5.3.2 Comparison with Markiel (1999)

After the critical dynamo numbers have been successfully reproduced, the next step in the validation of my numerical code is to reinstate the α quenching term such that a butterfly diagram is able to be reproduced and comparisons can be made with the work published in Markiel (1999). Quantities of particular interest include the values of the peak toroidal field at the base of the convection zone and the period of oscillation of the dynamo wave. Returning to the original boundary conditions detailed in Section 5.2, the profiles that are used for the α-effect, differential rotation and magnetic diffusivity are given in Equation (5.10)

$$\begin{aligned} \alpha(r,\theta) &= \cos\theta \exp\left[-\left(\frac{r-0.71}{0.025}\right)^2\right], \\ \Omega(r,\theta) &= \Omega_c + \frac{1}{2}\left[1+\Phi\left(\frac{r-0.685}{0.025}\right)\right]\left(P - Q\cos^2\theta - R\cos^4\theta\right), \\ \eta(r) &= \left(\frac{1-\eta_c}{2}\right)\left[1+\Phi\left(\frac{r-0.685}{0.025}\right)\right] + \eta_c, \end{aligned} \tag{5.10}$$

where Φ represents the error function, $\eta_c = 0.01$, $P = 0.0571$, $Q = 0.123$, $R = 0.155$ and $\Omega_c = 0.915$. The simulation used a grid mesh that has 64 radial grid points and 65 latitudinal grid points. The value of the dynamo number D is -1×10^6.

The α profile that is chosen represents a tachocline based α-effect and the differential rotation profile is chosen such that there is a narrow transition region at 0.7 representing the tachocline where the rigidly rotating core is coupled to the convection zone, these profiles are included here in Figure 5.2.

Figure 5.4 shows contour plots of the toroidal field B at a fixed radius of $r = 0.68$

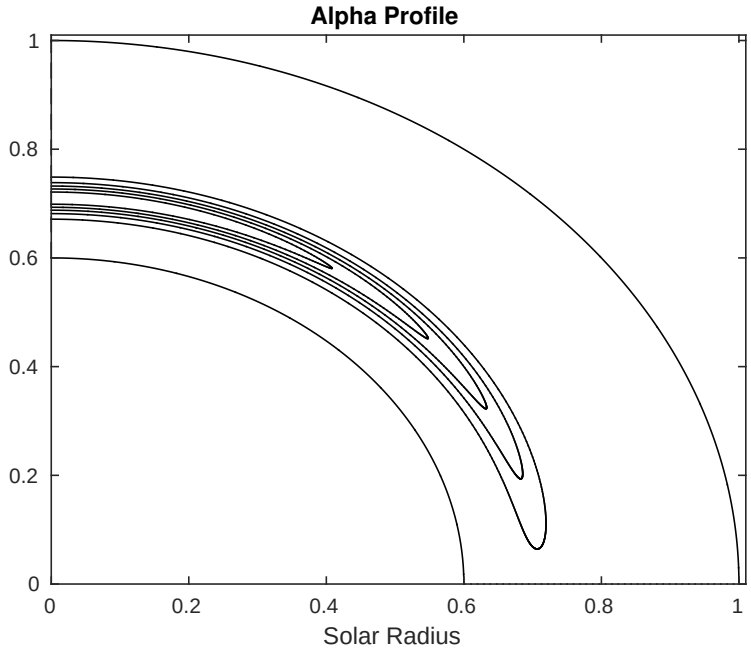

(a)

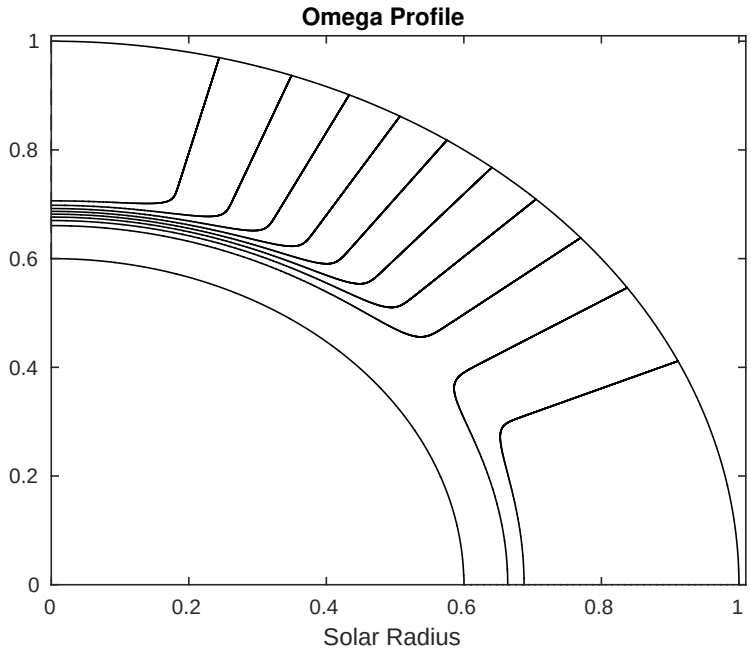

(b)

Figure 5.2: The alpha and omega profile for the Markiel comparison. Here the upper hemisphere is shown, alpha is antisymmetric about the equator and omega is symmetric about the equator. The alpha profile is active at a region based near the tachocline.

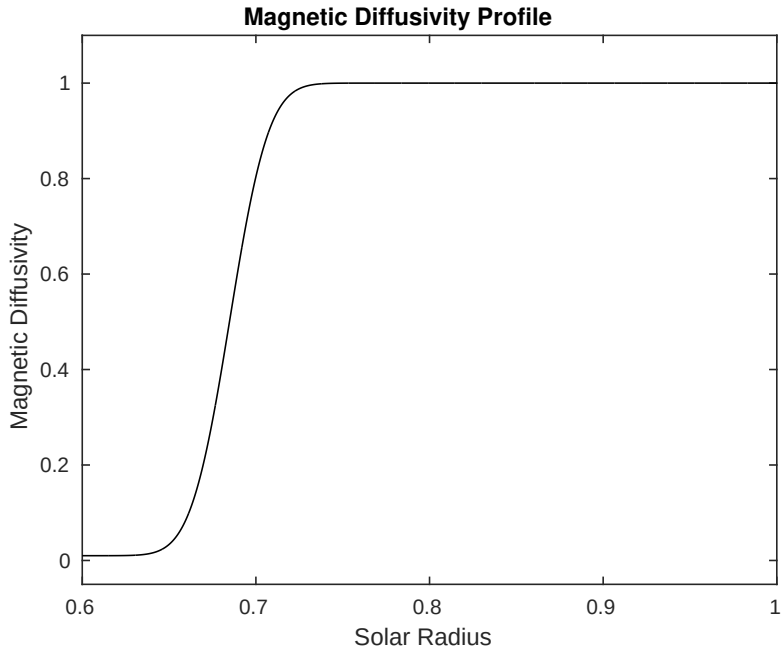

Figure 5.3: The magnetic diffusivity profile for the Markiel comparison.

and at a resolution of 64×65. The top plot is from my code and the bottom plot is from Bushby (2003). The results are qualitatively similar; both simulations show that the dynamo wave migrates polewards and is confined to latitudes of greater than $\pm 40°$.

Both Markiel and Bushby have published the values of the peak toroidal fields at a given (dimensionless) radius that is 0.68 units and at a resolution of 64×65. The value of the peak toroidal field that I have calculated is within 2.5% of Markiel's result and within 4.46% of Bushby's result, however the period of oscillation that I have determined from my code is 12.37% different from that of Markiel's work and 4.46% different from that stated by Bushby. The results of this comparison are included in Table 5.2. These discrepancies could be because I have too few radial grid points and thus the resolution is insufficient. The results are then repeated for a resolution of 101 points radially and 193 points latitudinally and the peak toroidal field and period of oscillation are calculated again. These values are shown here in Table 5.3 together with the relevant values from my code, however there is not an equivalent comparison that can be made with Markiel (1999) at this resolution. This time, the peak toroidal field is 2.78 and the period of oscillation is 0.00775, the equivalent values from Bushby's code are 2.74 and 0.0076 respectively. These results are within 2% of those calculated by Bushby and so these results are acceptable considering the differences in the mesh setup.

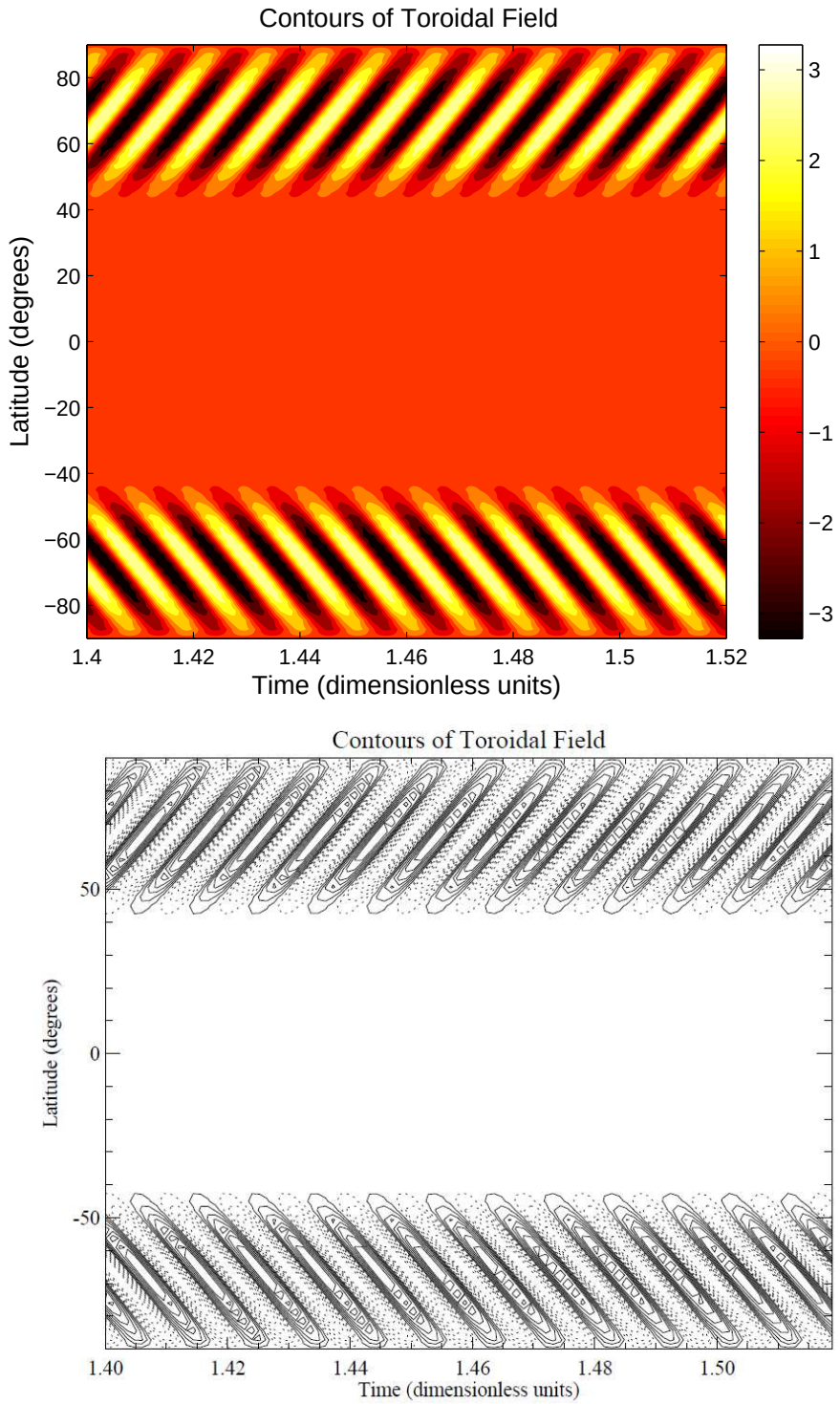

Figure 5.4: $D = -1 \times 10^6$, resolution is 64×65. Contour plots of the toroidal field B as a function of latitude against time at fixed $r = 0.68$. The top plot is from my code and the bottom plot is from Bushby (2003). In my plot, regions that are light represent positive values and regions that are dark represent negative values. The behaviour is confined to high latitudes and the waves migrate polewards.

5.3.3 Comparison with Jouve *et al.* (2008)

Thus far, the checks that have been carried out on my code have not implemented a meridional flow. Since the work included in this thesis relies upon correctly implementing such a flow into the dynamo model, it is important that this is checked in detail before new work is carried out. In the paper by Jouve *et al.* (2008) a detailed comparison between several codes is carried out with the critical dynamo numbers and period of the resulting wave included which I can use as a benchmark to test my code against.

The computational domain is slightly different to that used in previous checks with $0.65 < r < 1$ and $0 < \theta < \pi$ which still includes the tachocline, however the overshoot region now stops at $r = 0.65$. The boundary conditions imposed are the same as those used in the Stix (2002) comparison: at $\theta = 0$ and $\theta = \pi$, $A = B = 0$; and at the inner radius, the core is treated as a perfectly conducting sphere meaning that $A = 0$ and $\partial(rB)/\partial r = 0$ at $r = 0.65$. The initial conditions are chosen such that the large scale field can be confined to a dipolar field, i.e.

$$A = \frac{\sin(\theta)}{r^2} \quad \text{for} \quad r \geq 0.7 \quad \text{and} \quad A = 0 \quad \text{otherwise} \quad \text{and} \quad B = 0.$$

In this setup, there is no α-effect based at the tachocline. Instead a new source term ψ is introduced into Equation (5.1a) which represents poloidal field regeneration from a Babcock-Leighton mechanism that is proportional to the toroidal field at the base of the convection zone. The initial profiles for the differential rotation and magnetic diffusivity are shown here in Equation (5.11) alongside the poloidal field source term ψ;

$$\begin{aligned}
\alpha(r,\theta) &= 0, \\
\psi(r,\theta,t) &= \frac{1}{2}\left[1+\Phi\left(\frac{r-r_1}{d_1}\right)\right]\left[1-\Phi\left(\frac{r-1}{d_1}\right)\right]\cos\theta\sin\theta B(r_c,\theta,t), \\
\Omega(r,\theta) &= \Omega_c + \frac{1}{2}\left[1+\Phi\left(\frac{r-r_c}{d}\right)\right]\left(1-\Omega_c - c_2\cos^2\theta\right), \\
\eta(r) &= \eta_c + \frac{1}{2}\left(1-\eta_c\right)\left[1+\Phi\left(\frac{r-r_c}{d}\right)\right],
\end{aligned} \tag{5.11}$$

where Φ represents the error function, $r_c = 0.7, r_1 = 0.95, d = 0.02, d_1 = 0.01, \Omega_c = 0.92$ and $c_2 = 0.2$. The ψ profile is shown in Figure 5.5 and the Ω and η profiles are qualitatively similar to those implemented in the Markiel comparison, shown in Figures 5.2 and 5.3.

Here the poloidal field is regenerated due to a Babcock-Leighton type source term at the solar surface. For effective coupling between the solar surface and tachocline we need a meridional circulation which is used to transport poloidal flux from the surface to the base of the convection zone. In this profile, a single cell circulation is imposed with the flow moving polewards at the surface and closing off at the inner radius of $r = 0.65$ which

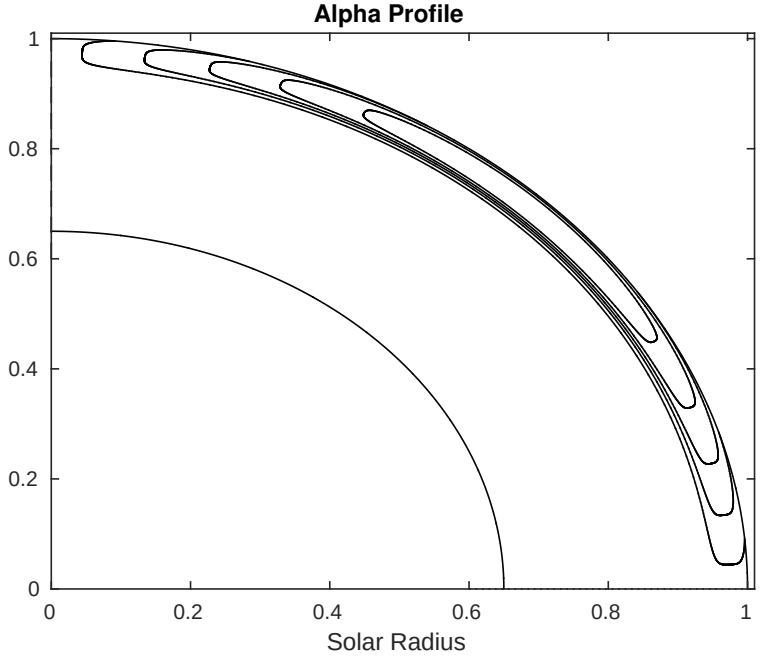

Figure 5.5: The ψ profile for the Jouve comparison. Here the upper hemisphere is shown and ψ is antisymmetric about the equator. This source term is generated through the decay of active regions at the solar surface.

penetrates slightly below the tachocline. Helioseismology has determined that the Sun's meridional flow is polewards at the surface however the exact location of the corresponding equatorward flow remains unknown. Taking this to occur at $r = 0.65$ is by no means conclusive but would agree with observations and thus is suitable to impose in this model. Therefore, the stream function is given as follows:

$$\xi(r,\theta) = -\frac{2}{\pi}\frac{(r-r_b)^2}{(1-r_b)}\sin\left(\pi\frac{r-r_b}{1-r_b}\right)\cos\theta\sin\theta.$$

The r and θ components of the meridional flow can be calculated by using the relation $\mathbf{u}_p = \nabla\times(\xi\hat{\mathbf{e}}_\phi)$ and are as follows:

$$\begin{aligned} u_r(r,\theta) =& -\frac{2(1-r_b)}{\pi r}\frac{(r-r_b)^2}{(1-r_b)^2}\sin\left(\pi\frac{r-r_b}{1-r_b}\right)(3\cos^2\theta-1), \\ u_\theta(r,\theta) =& \left[\frac{3r-r_b}{1-r_b}\sin\left(\pi\frac{r-r_b}{1-r_b}\right)+\frac{r\pi}{(1-r_b)}\frac{(r-r_b)}{(1-r_b)}\cos\left(\pi\frac{r-r_b}{1-r_b}\right)\right] \\ &\times\frac{2(1-r_b)}{\pi r}\frac{(r-r_b)}{(1-r_b)}\cos\theta\sin\theta, \end{aligned} \tag{5.12}$$

with $r_b = 0.65$. A plot of the resulting velocity field is included here as Figure 5.6. It is

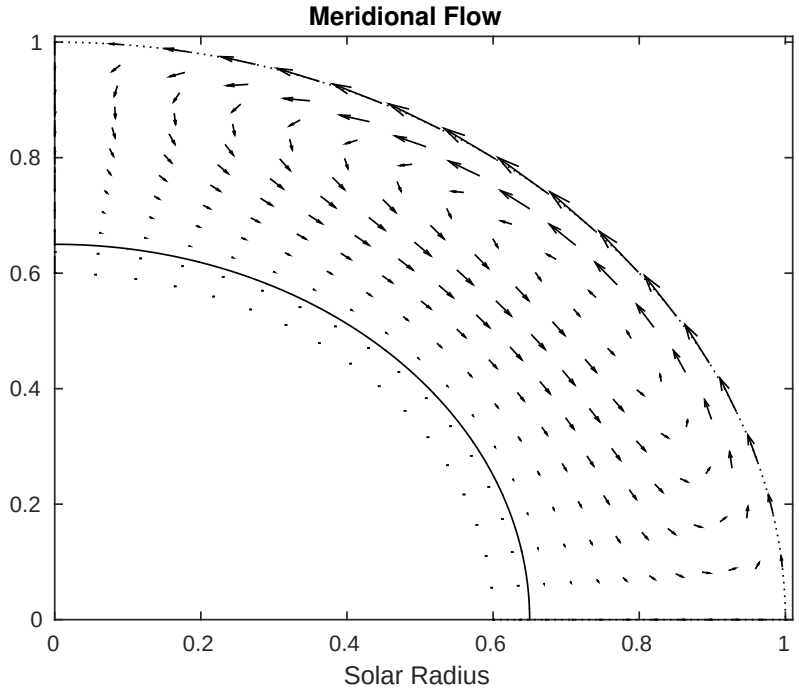

Figure 5.6: The meridional flow profile for the comparison with Jouve *et al.* (2008). The flow consists of a single cell and closes at $r = 0.65$.

useful to note that an estimate of the circulation time of this prescribed meridional flow is approximately 1.57 diffusion times.

The first check is to calculate the critical dynamo number of the system. The profiles for the differential rotation, magnetic diffusivity and α-effect are identical to those included in Equation (5.11). Note that there is no alpha quenching present. By studying the total energy in the system, it is possible to identify the critical dynamo number above which the solutions grow exponentially. The results from the paper by Jouve *et al.* (2008) are included here in Table 5.4 which shows the critical dynamo numbers for five different codes alongside the equivalent value from my code. It is clear from the table that the value of D_c that I have calculated compares favourably to those calculated in the Jouve paper. In fact, removing the entry from the Hollerbach code means that the mean critical dynamo number calculated in the Jouve paper increases to 352800. This moves the critical dynamo number that I have calculated to within 0.4% of the mean value calculated in the Jouve paper.

After the critical dynamo number of the system has been determined, alpha quenching is introduced in order to promote oscillatory solutions. The dynamo number is taken to be $1.03D_c$, just above onset and the frequency of the resulting wave is calculated using a Fourier Transform. The frequency that is calculated from my code is within 0.12% of the

Code	Resolution	Δt	D_c	ω
STELEM	129×129	10^{-6}	352800	542
NDYND	81×81	10^{-6}	351820	525
HAO2	101×101	10^{-5}	352100	546
MBRK	151×151	10^{-6}	355600	532
HOLLER	100×100	5×10^{-8}	329700	538
Mean			348460	536.6
COLE	128×193	10^{-6}	354200	537

Table 5.4: A comparison between the codes from Jouve *et al.* (2008).

mean frequency calculated in the Jouve paper. Since both the critical dynamo number and frequency match up very well to results published by Jouve *et al.* (2008), the next check is to carry out more checks on my code to study the behaviour of the system well above onset.

5.3.4 Comparison with Bushby (2003)

This final check is done by running parallel simulations of my code with the code implemented in Bushby (2003). Similar to the comparison with Jouve *et al.* (2008), a poloidal field source term is chosen to represent the Babcock-Leighton mechanism at the solar surface. The initial profiles for the differential rotation and magnetic diffusivity are shown here in Equation (5.13) alongside the poloidal field source term ψ.

$$\begin{aligned}
\alpha(r,\theta) &= 0, \\
\psi(r,\theta,t) &= \frac{1}{2}\left[1+\Phi\left(\frac{r-0.95}{0.01}\right)\right]\left[1-\Phi\left(\frac{r-1}{0.01}\right)\right]\cos\theta\sin\theta \times \frac{B(r_c,\theta,t)}{1+B(r_c,\theta,t)^2}, \\
\Omega(r,\theta) &= \Omega_c + \frac{1}{2}\left[1+\Phi\left(\frac{r-0.7}{0.025}\right)\right]\left(P - Q\cos^2\theta - R\cos^4\theta\right), \\
\eta(r) &= \left(\frac{1-\eta_c}{2}\right)\left[1+\Phi\left(\frac{r-0.7}{0.025}\right)\right] + \eta_c,
\end{aligned} \tag{5.13}$$

where Φ represents the error function, $r_c = 0.7$, $P = 0.0606$, $Q = 0.136$ and $R = 0.146$. The ψ, Ω and η profiles are qualitatively similar to those shown in Figures 5.5, 5.2 and 5.3.

The r and θ components of the meridional flow are given by:

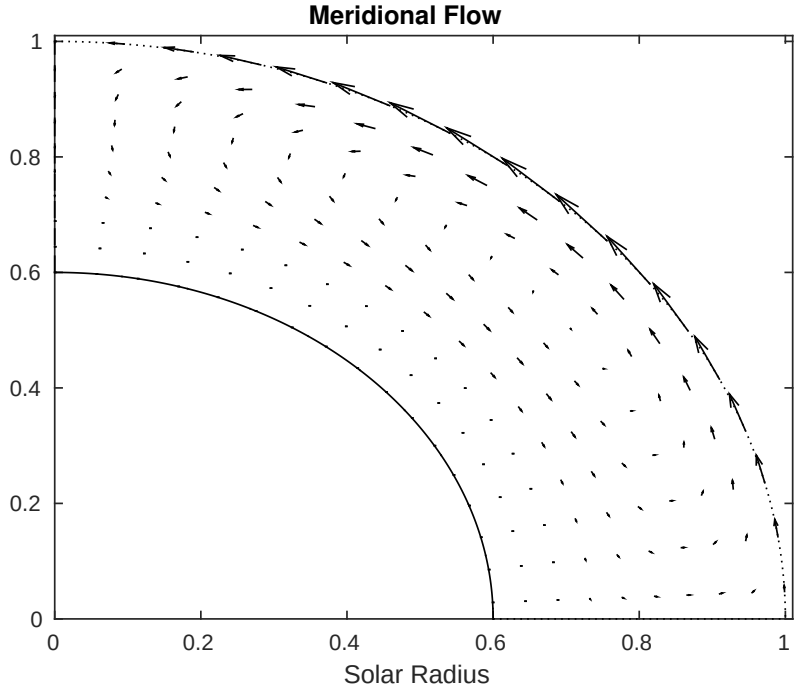

Figure 5.7: The meridional flow profile for the comparison with Bushby (2003). The flow consists of a single cell and closes at $r = 0.7$.

$$u_r(r,\theta) = \left(\frac{2}{r^2}\right)\left[-\frac{2}{3}\left(\frac{1}{r}-1\right) + \frac{c_1}{2}\left(\frac{1}{r}-1\right)^{1.5} - \frac{4c_2}{9}\left(\frac{1}{r}-1\right)^{1.75}\right](2\cos^2\theta - \sin^2\theta),$$
$$u_\theta(r,\theta) = \left(\frac{2}{r^3}\right)\left[-1 + c_1\left(\frac{1}{r}-1\right)^{0.5} - c_2\left(\frac{1}{r}-1\right)^{0.75}\right]\sin(\theta)\cos(\theta),$$

where $c_1 =$ and c_2 are defined as:

$$c_1 = 4\left(\frac{1}{r_b}-1\right)^{-0.5} \quad \text{and} \quad c_2 = 3\left(\frac{1}{r_b}-1\right)^{-0.75}$$

and $r_b = 0.7$. This meridional flow consists of a single cell in both the northern and southern hemisphere which is polewards at the surface with the corresponding equatorward flow is taken to be at the base of the convection zone, see Figure 5.7.

Figures 5.8 and 5.9 show the behaviour of the toroidal field at the base of the convection zone and the poloidal field at the solar surface respectively. The top plot is produced from my code and the bottom plot from Bushby's. A comparison of these plots suggests that the codes are producing very similar results and are in good agreement with each other. A quantitative comparison can be made of some global quantities, namely the value of

	Bushby's code	My code	Percentage difference
Period of oscillation (years)	47.24	46.63	0.31%
Peak toroidal field at $r = 0.7(KG)$	44.45	44.59	1.3%
Peak radial field at $r = 1.0(KG)$	15.90	15.44	2.98%

Table 5.5: A comparison between the codes. Here the quantities have been scaled in terms of physical values. The non dimensional value of B_ϕ has been multiplied by 5×10^3, the non dimensional value of B_r has been multiplied by 1.39×10^5 and the non dimensional value of the period of oscillation has been multiplied by 3.07×10^3.

the toroidal field at the base of the convection zone, the poloidal field at the solar surface and the period of oscillation. The results are given in Table 5.5 and show that both codes agree with each other to within 3% for all quantities. The percentage errors in the codes when comparing both the period of oscillation and peak toroidal field at the base of the convection zone are particularly small; however the remaining comparison of the peak radial field at $r = 1.0$ is significantly higher but is still within acceptable limits. This discrepancy is most likely due to the different way that the boundary condition at the solar surface is implemented. Bushby used an additional grid point just outside of the solar surface (due to the use of a staggered mesh) in order to satisfy the boundary condition on A at this fixed radius; however in my work, I have satisfied the boundary condition on A without the need to introduce an additional grid point outside of the computational domain.

Since the validity of my code has been stringently checked I am confident that it can be used to investigate similar models of the solar dynamo. The forthcoming chapters contain results that have been produced using modifications to this code and I am confident that the results are accurate given the stringent checks that have been detailed in this chapter.

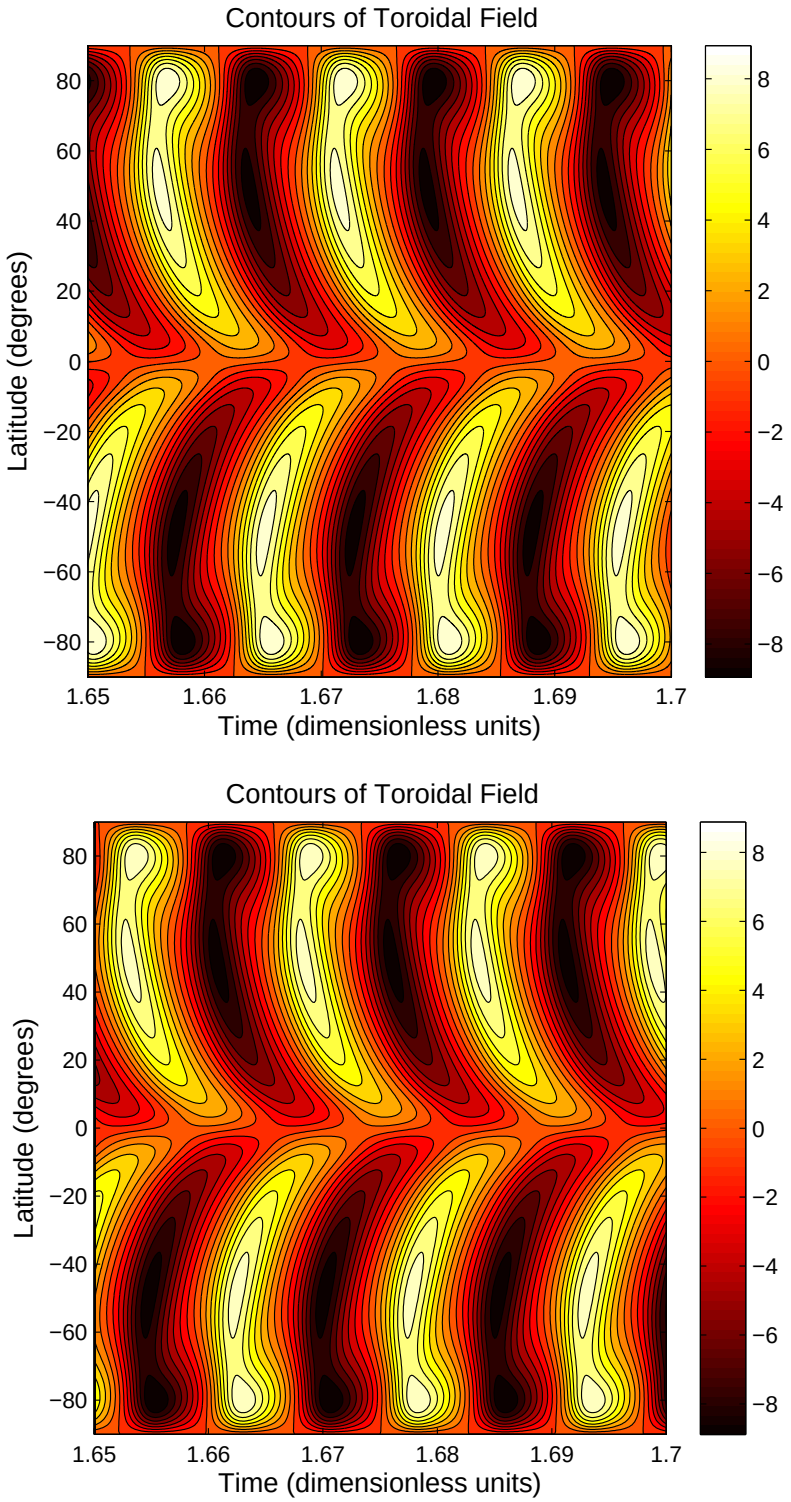

Figure 5.8: Parameter values: $D = 7 \times 10^6$ and $Re = 1.4 \times 10^3$. Contour plots of toroidal field B as a function of latitude against time at fixed $r = 0.7$. The top plot is from my code and the bottom plot is from Bushby's code.

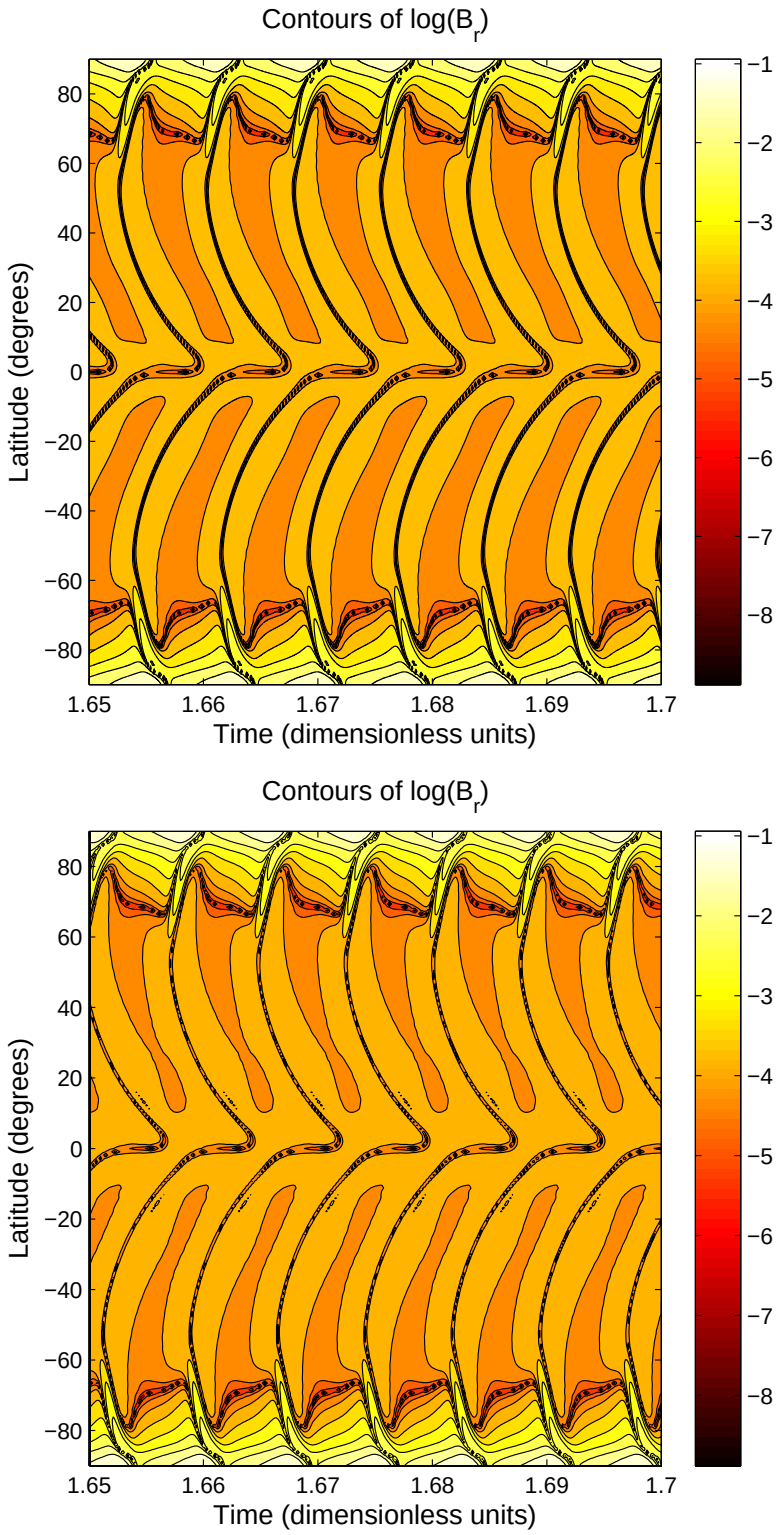

Figure 5.9: Parameter values: $D = 7 \times 10^6$ and $Re = 1.4 \times 10^3$. Contour plots of $\log(B_r)$ at the solar surface as a function of latitude against time. The top plot is from my code and the bottom plot is from Bushby's code.

Chapter 6

Competing α-effects in axisymmetric spherical geometry

This chapter builds upon the models described in earlier chapters by explicitly incorporating a surface α-effect into an interface-like $\alpha\omega$ dynamo model, without the need for the inclusion of an additional delayed field. This is done by including two sources of poloidal field regeneration: one from an interface dynamo with an α-effect localised at the base of the convection zone and another from a Babcock-Leighton α-effect located at the solar surface. Babcock-Leighton models typically include a deep meridional flow, coupling surface layers to the region around the base of the convection zone (where the ω-effect is operating). However the details of this flow are poorly constrained by observations. Motivated by the recent work of Hathaway (2012), who suggested a shallow return (i.e. equatorward) flow, I consider a model in which the meridional flow is closed at a radius of $r = 0.85R_{\odot}$. This implies that the model essentially represents an interface type dynamo with a perturbation from a surface source term. To the best of my knowledge, this is the first time that this sort of shallow flow has been implemented in models of this type.

6.1 Babcock-Leighton dynamos - open questions

Before giving the details of my model, it is important to understand the properties of some of the existing models in more detail, focusing particularly upon open questions that exist in solar dynamo modelling.

As discussed in Chapter 1, the details of the meridional flows in the solar interior are not well constrained by observations. However, such flows play a crucial role in many models. Choudhuri *et al.* (1995) show that the meridional circulation plays a crucial role when looking for dynamo solutions that are "solar-like" in Babcock-Leighton dynamo models. Working in 2D spherical geometry they assume axisymmetry and couple a localised sur-

face α-effect to the ω-effect located at the base of the convection zone. The spherical shell is chosen such that only the northern hemisphere is simulated and the boundary conditions are selected such that dipolar solutions are preferred. When there is no meridional circulation imposed, the only way that the α and ω effects are coupled is through diffusion, and the results show that the dynamo wave propagates polewards with the period of oscillation set by the diffusion time. When the meridional circulation is turned on, the results are strikingly different. The dynamo wave now propagates equatorwards and the magnitude of the toroidal field at low latitudes is greater due to the additional coupling between the surface α-effect and the deep-lying shear that helps to promote the dynamo. Other features that should be noted is that the period of the dynamo wave decreases as the Reynolds number is increased and that the toroidal field near the poles appears to be of the opposite polarity to the toroidal field near the equator. In models of this type, it is clear that the inclusion of the meridional circulation is the key component when looking for dynamo solutions that propagate equatorwards and it also appears to set the period of the wave.

This model was expanded upon by Dikpati & Charbonneau (1999). A key new feature of the model is that the strength of the surface α-effect is proportional to the magnitude of the toroidal field at the base of the convection zone so is now a non-local quantity. A "solar-like" butterfly diagram is produced: a strong equatorward branch of the toroidal field is present; a radial field at the solar surface originates at mid-latitudes with the flux migrating polewards; and a phase shift of $\pi/2$ exists between the radial field at the solar surface and the toroidal field at the base of the convection zone. The paper describes how the amplitude of the meridional flow plays a key part in setting the cycle period. This is intuitive, since increasing the strength of the meridional flow will result in the flux at the solar surface, that has been generated through the decay of active regions, being transported more quickly to the base of the convection zone. It is also apparent that increasing the strength of the Babcock-Leighton surface α-effect leads to an increase in magnitude of the toroidal field at the base of the convection zone.

Of particular relevance to the present study is the work of Dikpati & Gilman (2001). They compare two distinct dynamo models, one that imposes an interface type α-effect and another that makes use of a Babcock-Leighton type α-effect. The interface dynamo model is solved in the northern hemisphere with $0 \leq \theta \leq \pi/2$ and is only able to reproduce solar like solutions with the inclusion of a single cell meridional flow. The authors then introduce a surface α-effect (that is the same magnitude as the deep-seated α-effect) into this model and an oscillatory mode is found with toroidal flux migrating equatorward at low latitudes. The model is extended to include the full spherical shell (i.e. $0 \leq \theta \leq \pi$) such that equator is no longer a boundary condition of the problem and therefore the dynamo is free to choose the parity of the solution. Butterfly diagrams which show the

time evolution of the toroidal field at the base of the convection zone are shown here in Figure 6.1. If the only source of poloidal field regeneration is through an interface type α-effect, the solution is of odd (dipolar) parity, i.e. the toroidal field is antisymmetric about the equator. Whereas if the only source of poloidal field regeneration is from a surface α-effect, the solution is of even (quadrupolar) parity. The polarity of the solar cycle is unknown before the year 1600 and it is unclear if the Sun exhibited odd or even polarity before this time. However, it is known that after this period, the Sun has chosen an odd parity solution. It is fair to say that most Babcock-Leighton dynamo models produce predominantly quadrupolar solutions. This (so called) "parity problem" is highlighted in Dikpati & Gilman (2001) and still remains a defining feature of Babcock-Leighton dynamo models in more recent work, (see, for example, Chatterjee *et al.*, 2004; Dikpati *et al.*, 2005).

One important point that should be noted is that Babcock-Leighton dynamos are not able to restart after a grand minimum period since there is no magnetic flux deposited at the solar surface through the decay of active regions. Regardless of the efficiency of any surface α-effect that is present, this leads to the assumption that a deep-seated interface type α-effect must be present within the Sun, such that the dynamo action can be restarted. The relative strengths of the two α-effects are not known and Dikpati & Gilman (2001) suggest that the interface type α-effect must be the predominant source of poloidal field regeneration since this is the model that exhibits odd parity solutions which is consistent with current observations of the Sun. The paper found evidence to suggest that when the relative magnitudes of the α-effects were varied, the solution was governed by the α-effect of greater magnitude. However the survey was by no means extensive; only two examples were stated which considered the scenario when each α-effect was 5 times the strength of the other. There was also some evidence to suggest that these α-effects could interact destructively to kill the dynamo action. This conclusion is supported in Chapter 3 of this thesis through studying the dependence of the critical dynamo number on the relative strengths of the two source terms. Dikpati & Gilman (2001) provide further evidence to suggest that inducing modulation in Babcock-Leighton dynamo models becomes easier when an interface type α-effect is also included. This means that the deep-seated α-effect could not only be responsible for restarting the dynamo after a period of grand minima but the interactions between these two competing α-effects could be a viable mechanism that leads to periods of reduced magnetic activity within the Sun.

There are several interesting/open questions that remain about Babcock-Leighton dynamo models:

- Can the "parity problem" be fully addressed? Under what circumstances are dipolar solutions preferred and are these assumptions reasonable when applied to the Sun?
- What role does the meridional flow play in the dynamo model? To what extent can

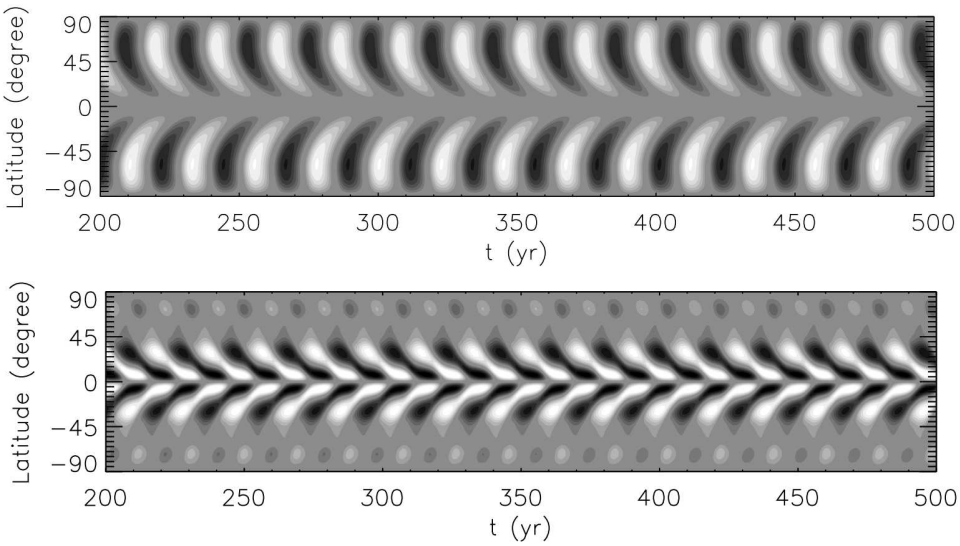

Figure 6.1: The evolution of the toroidal field at the base of the convection zone for a Babcock-Leighton dynamo (top) and an interface type dynamo (bottom). The polarity of the solution is dependent upon the mechanism for poloidal field regeneration. These figures are taken from Dikpati & Gilman (2001).

a "solar-like" butterfly diagram be produced without the inclusion of a meridional flow? Is there any other mechanism that can set the period of the dynamo wave?

- There is uncertainty as to the structure of the meridional flow: Does it penetrate into the convection zone or does it close at a shallow depth? Does it have a single or double cell structure?
- What mechanisms are able to modulate the dynamo wave? Under what circumstances can competing α-effects interact in such a way to disrupt the periodicity of the magnetic cycle?

6.2 Model Setup

6.2.1 Governing Equations

The $\alpha\omega$ dynamo model that is described in Chapter 5 is now adapted to include an additional source of poloidal flux from a Babcock-Leighton α-effect located at the solar surface. The governing equations are the same as those described in equations (5.1a) - (5.1b) with the addition of an extra source term in the governing equation for A which represents a non-local Babcock-Leighton α-effect that is proportional to the strength of the magnetic field at the base of the convection zone. Also, quenching parameters are introduced into both source terms to enable the generation of finite amplitude nonlinear

solutions. The governing equations are thus:

$$\frac{\partial A}{\partial t} = \eta\left(\nabla^2 - \frac{1}{\varpi^2}\right)A - Re\frac{\mathbf{U}_p}{\varpi}\cdot\nabla(\varpi A) + \frac{\alpha B}{1+|B|^2} + S_0\psi, \tag{6.1a}$$

$$\frac{\partial B}{\partial t} = \eta\left(\nabla^2 - \frac{1}{\varpi^2}\right)B + \frac{1}{\varpi}\frac{\partial}{\partial r}(\varpi B)\frac{\partial \eta}{\partial r} + \frac{1}{\varpi}\frac{\partial \eta}{\partial \theta}\frac{\partial}{\partial \theta}\left(\frac{B\varpi}{r}\right) - Re\varpi\mathbf{U}_p\cdot\nabla\left(\frac{B}{\varpi}\right) - ReB\nabla\cdot\mathbf{U_p} + D\varpi(\nabla\times A\mathbf{e}_\phi)\cdot\nabla\Omega, \tag{6.1b}$$

where $\varpi = r\sin\theta$ and ψ represents the structure of the Babcock-Leighton source term. The system is governed by 3 parameters: the Dynamo Number D, the Reynolds number Re and the strength (relative to the magnitude of the interface α-effect) of the Babcock-Leighton source term S_0.

The same computational domain is used that is represented in Figure 5.1 and is constructed such that $0.6 \leq r \leq 1$ and $0 \leq \theta \leq \pi$. Since the governing equations are solved in both hemispheres, the equator is not a boundary of the computational domain and the dynamo is free to choose the parity of the solution. The boundary conditions are also the same as those implemented in Chapter 5 with $A = B = 0$ when $\theta = 0$ and $\theta = \pi$. At the inner boundary, I take $A = B = 0$ which is consistent with the assumption that the dynamo is localised around the base of the convection zone. A potential field boundary condition is implemented at the solar surface and I also set $B = 0$ at this outer radius.

6.2.2 Parameter Profiles

The same meridional flow profile that is given in Equation 5.12 is imposed. However the flow is now closed at a radius of $r_b = 0.85$. This is a reasonable assumption since there is no definitive conclusion as to where the returning equatorward meridional flow is located. As mentioned earlier, it is this shallow flow that gives this model some degree of novelty. The velocity field of this flow is shown in Figure 6.2. Under these assumptions, the model represents an interface type dynamo with a perturbation from a Babcock-Leighton surface source term. This shallow flow transports magnetic flux at the solar surface polewards and then down into the solar interior without penetrating below a radius of $r = 0.85$. The flux can then be transported to the tachocline through the effects of diffusion.

The profiles for α, ψ, Ω and η remain fixed for the results that are contained within this chapter and are given by:

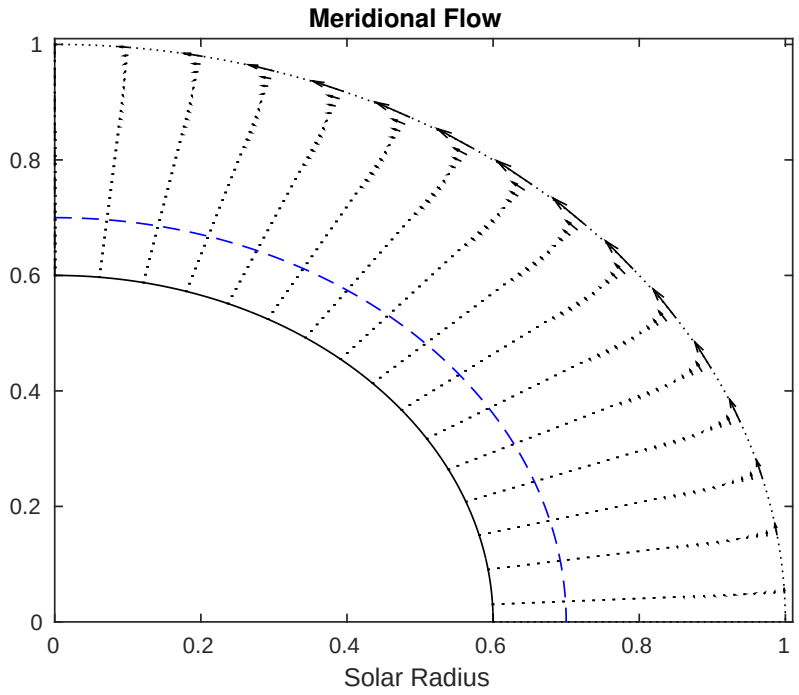

Figure 6.2: Meridional flow profile: The flow consists of a single cell and closes at $r = 0.85$. The blue(dashed) line represents the base of the convection zone at $r = 0.7$.

$$
\begin{aligned}
\alpha(r,\theta) &= \exp\left[-\left(\frac{r-0.71}{0.025}\right)^2\right]\cos\theta\sin^4\theta,\\
\psi(r,\theta) &= \frac{1}{2}\left[1+\Phi\left(\frac{r-0.95}{0.01}\right)\right]\left[1-\Phi\left(\frac{r-1}{0.01}\right)\right]\cos\theta\sin\theta\times\frac{B(0.7,\theta,t)}{1+B(0.7,\theta,t)^2},\\
\Omega(r,\theta) &= \Omega_c+\frac{1}{2}\left[1+\Phi\left(\frac{r-0.7}{0.025}\right)\right]\left(P-Q\cos^2\theta-R\cos^4\theta\right),\\
\eta(r) &= \left(\frac{1-\eta_c}{2}\right)\left[1+\Phi\left(\frac{r-0.7}{0.025}\right)\right]+\eta_c,
\end{aligned}
\tag{6.2}
$$

with $P = 0.0571$, $Q = 0.123$, $R = 0.155$, $\Omega_c = 0.915$ and $\eta_c = 0.01$. Figure 6.3 shows that the interface α-effect is confined to a region close to the tachocline meaning that the preferred mode of dynamo action (in absence of other sources) is restricted to low latitudes at the base of the convection zone. The contour plots of ψ and Ω have already been included previously in this thesis and are given in figures 5.5 and 5.2b respectively. The source term ψ is chosen such that the Babcock-Leighton α-effect is confined to active latitudes near the solar surface with a magnitude that is proportional to the toroidal field at the base of the convection zone. This represents the idea that magnetic flux that is

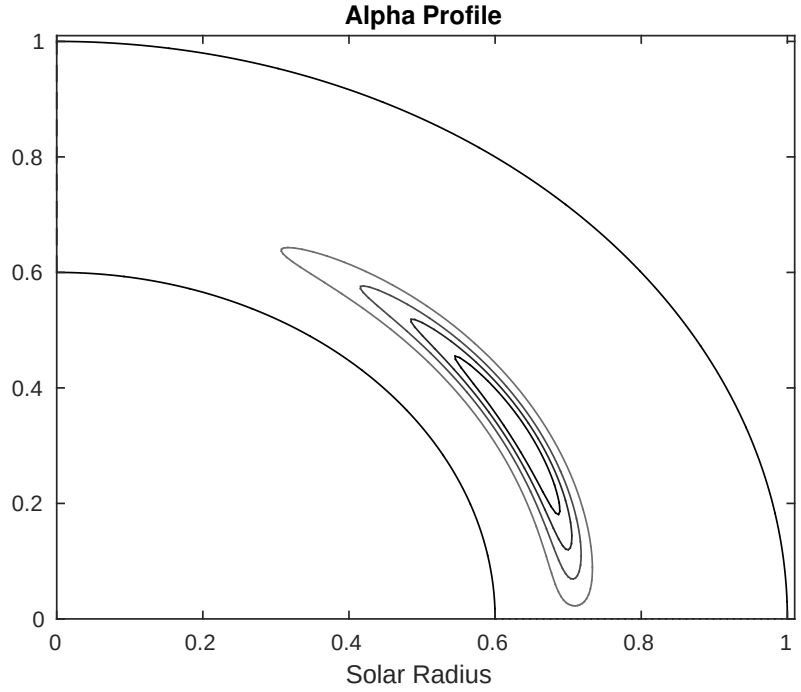

Figure 6.3: The alpha profile. Here the upper hemisphere is shown, alpha is antisymmetric about the equator. The mechanism is active at a region based near the tachocline.

deposited at the solar surface in the form of sunspots is proportional to the strength of rising flux tubes at the base of the convection zone. The source term is also multiplied by a non-local quenching term for the same reason. The η profile represents a magnetic diffusivity that is enhanced by the turbulence in the convection zone and the form of Ω is taken to be consistent with observations of the Sun.

6.3 Results

A substantial parameter survey has been carried out which considers how the behaviour of the system depends upon the values of the Dynamo number D, the Reynolds number Re and the strength of the Babcock-Leighton source term S_0. The results offer several interesting features that are explained in this section.

Before these results are explained, it is important to verify that the code can reproduce the "solar-like" solution given in Chapter 5 which is consistent with the work contained in Bushby (2003). For this check, the parameters of the system are $D = -2 \times 10^6$, $Re = 0$ and $S_0 = 0$. This means that the system reverts to an interface dynamo model (with no additional source of poloidal field) without a meridional flow. The resulting contour plot is shown in Figure 6.4 and displays many of the features of the Sun's magnetic field. The

magnetic activity is confined to low latitudes, the field is of predominantly dipolar parity and the dynamo wave propagates towards the equator.

It is clear from the contour plot that the magnetic field is periodic in time. One way to measure this computationally is to calculate the magnetic energy of the system which is proportional to

$$E = \int \left(B^2 + \frac{1}{r^2} \left[\frac{\partial (Ar)}{\partial r} \right]^2 + \frac{1}{r^2 \sin^2 \theta} \left[\frac{\partial (A \sin \theta)}{\partial \theta} \right]^2 \right) r^2 \sin(\theta) dr d\theta. \tag{6.3}$$

The resulting time series of the energy integral not only provides useful information about the numerical convergence of the solution but it is a convenient way to show the modulation of the system. Another useful tool when studying the nature of the solutions is to calculate the parity of the solution which is given by:

$$P = \frac{E_q - E_d}{E_q + E_d} \tag{6.4}$$

where E_d is the energy associated with the dipolar component of the magnetic field and is comprised of the symmetric part of the poloidal potential A and the antisymmetric part of the toroidal field B. E_q is the energy associated with the quadrupolar magnetic field and is comprised of the antisymmetric part of the poloidal potential A and the symmetric part of the toroidal field B. By this definition, $P = 1$ corresponds to a solution that is fully quadrupolar and $P = -1$ corresponds to a solution that is fully dipolar. For the "solar-like" solution included in Figure 6.4, the time series of the energy shows that the magnetic field is periodic. The parity of the solution has also been calculated to be -0.5 indicating that the solution is predominantly dipolar in nature.

6.3.1 Dependence on S_0

The following results intend to investigate the effects of the surface α-effect on the interface dynamo when S_0 remains small. Initially, the system is investigated when there is no flow present and $|S_0|$ is chosen to be small (i.e. $|S_0| \ll 1$) such that it acts as a perturbation to the deep-seated α-effect. Figures 6.5, 6.6 and 6.7 show the resulting butterfly diagrams.

When S_0 is positive, there is an overwhelming tendency for the system to generate steady modes. Figure 6.5 is produced when $S_0 = 0.1$ and the resulting contour plot shows that the dipolar magnetic field is not oscillatory. The time evolution of the energy also shows that the solution is a steady mode. For large values of S_0, steady modes are preferred and it has not been possible to find an oscillatory magnetic field in this regime. When $S_0 = 0.01$, the strength of the Babcock-Leighton source term is not strong enough to influence the behaviour of the dynamo and a butterfly diagram is produced that is quantitatively similar to Figure 6.4.

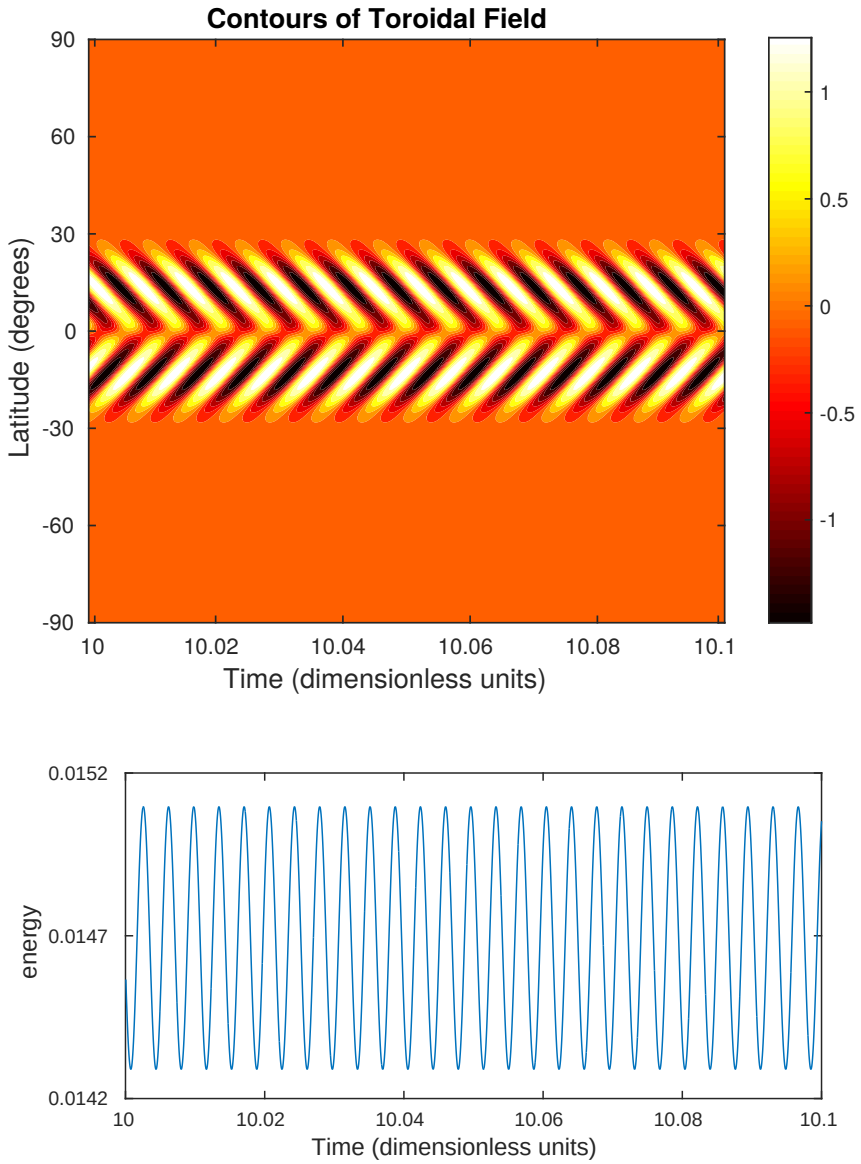

Figure 6.4: A periodic solution. Here $D = -2 \times 10^6$, $Re = 0$ and $S = 0$. Top: Contours of toroidal field B at the base of the convection zone. Bottom: Time series of the energy.

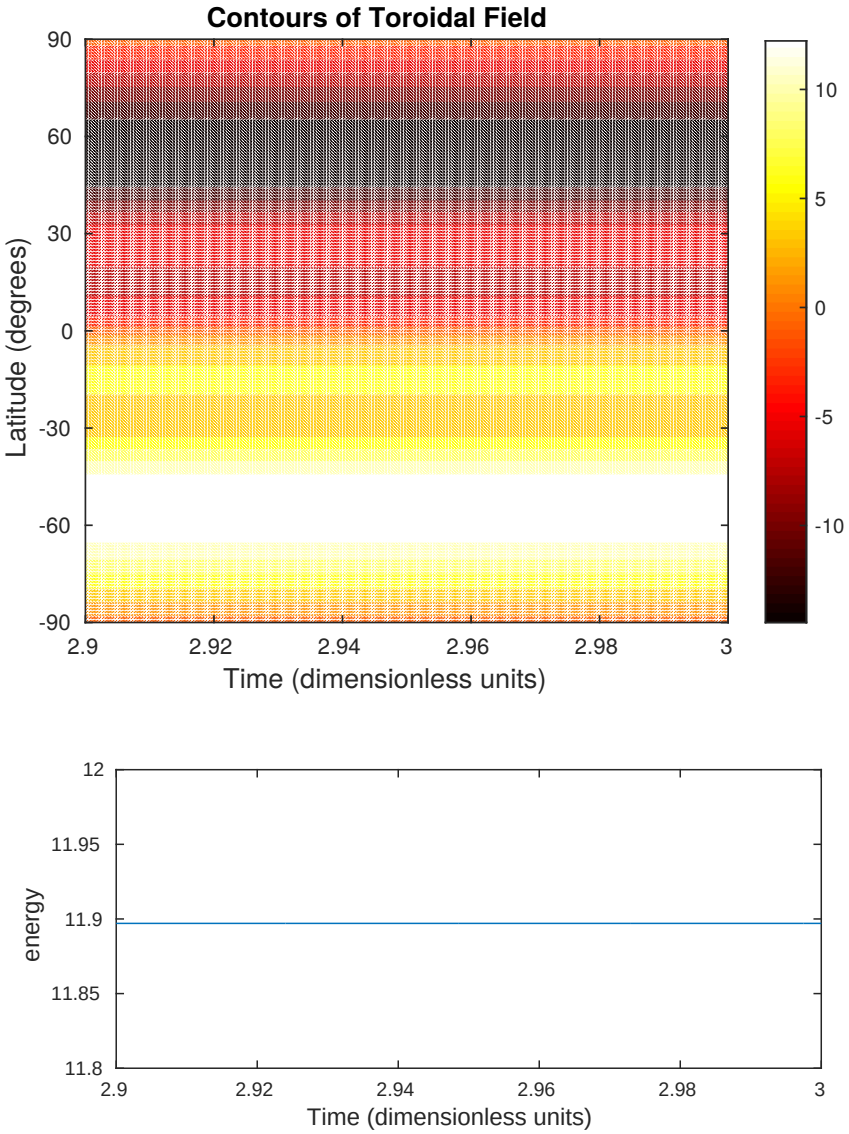

Figure 6.5: The dependence of the solution on S_0. Here $D = -2 \times 10^6$, $Re = 0$ and $S = 0.1$. Top: Contours of toroidal field B at the base of the convection zone. Bottom: Time series of the energy.

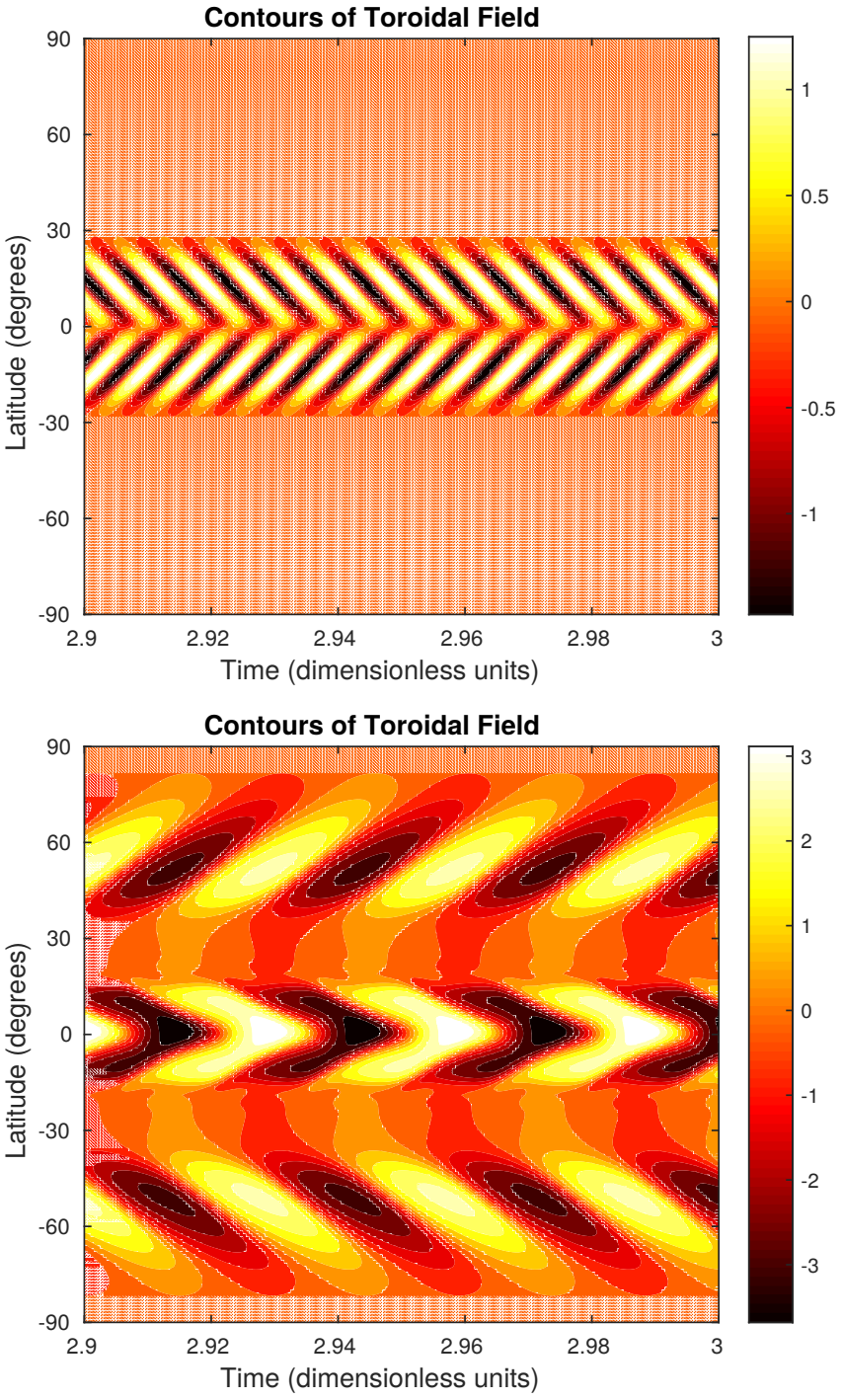

Figure 6.6: The dependence of the solution on S_0. Contour plots of toroidal field at a fixed radius of $r = 0.7$. For both plots, $D = -2 \times 10^6$ and $Re = 0$. For the top plot $S_0 = -0.1$ and for the bottom plot $S_0 = -0.15$.

For negative values of S_0, oscillatory solutions are preferred. Figure 6.6 shows the behaviour of the system for two values of S_0 namely $S_0 = -0.1$ and $S_0 = -0.15$. When $S_0 = -0.1$, the butterfly diagram indicates that the magnitude of the Babcock-Leighton source term is not yet large enough to affect the behaviour of the system. As $|S_0|$ is increased to -0.15 the contour plot is strikingly different to what is found for smaller values of $|S_0|$ with the addition of a poleward migrating branch originating at mid latitudes. This is not the only difference to be noted. Firstly, the parity of the solution has now changed to being predominantly quadrupolar and also the period of the wave has become significantly longer. This illustrates that even though $|S_0|$ is small the dynamo now appears to be significantly influenced by the surface α-effect.

Figure 6.7 shows two more butterfly diagrams for values of $S_0 = -0.5$ and $S_0 = -1.0$. When $S_0 = -0.5$ the solution is no longer confined to low latitudes with the toroidal field maximum occurring at around $\pm 50^\circ$. The solution is no longer of dipolar symmetry, in fact it is a mixed parity mode with a strong quadrupolar component. The solution is not "solar-like". Although the magnetic field migrates equatorwards at low magnitudes, there is a strong poleward migrating branch. In addition, the solution is not of dipolar parity and the toroidal field maximum occurs at a latitude that is much higher than desired. When S_0 is further increased to -1.0, the behaviour is similar to what is seen in Babcock-Leighton dynamo models (see, for example, Dikpati & Gilman, 2001; Dikpati & Charbonneau, 1999). The toroidal field has the correct direction of propagation at low latitudes and is of dipolar parity however it is not confined to a region $\pm 30^\circ$ above the equator. Also the toroidal field maximum occurs at a higher latitude than desired when comparing to sunspot observations. The behaviour is very similar to what is shown in Figure 4(c) of Dikpati & Charbonneau (1999), which is produced using a Babcock-Leighton dynamo with no flow. However, with my model, the toroidal field maximum occurs at a slightly lower latitude. Given that this result is obtained when the relative magnitudes of source terms are comparable, this is evidence to suggest that when there is no meridional flow present within the system, the more dominant source of poloidal field regeneration in my model is from the Babcock-Leighton α-effect. Another feature of these plots is that they show that the period of the dynamo wave is determined by the magnitude of S_0. As S_0 is increased, the period of the wave also increases showing that the meridional flow is not the only mechanism that could be responsible for setting the cycle period.

The same investigation is undertaken when the meridional flow has been turned on and the results are included in Figures 6.8, 6.9 and 6.10. When S_0 is positive, the system again favours steady modes and even for a value of $S_0 = 0.01$ it is not possible to find an oscillatory solution. This is evidence to support the conclusion that the inclusion of a meridional flow enhances the potency of the surface source term, which is consistent with

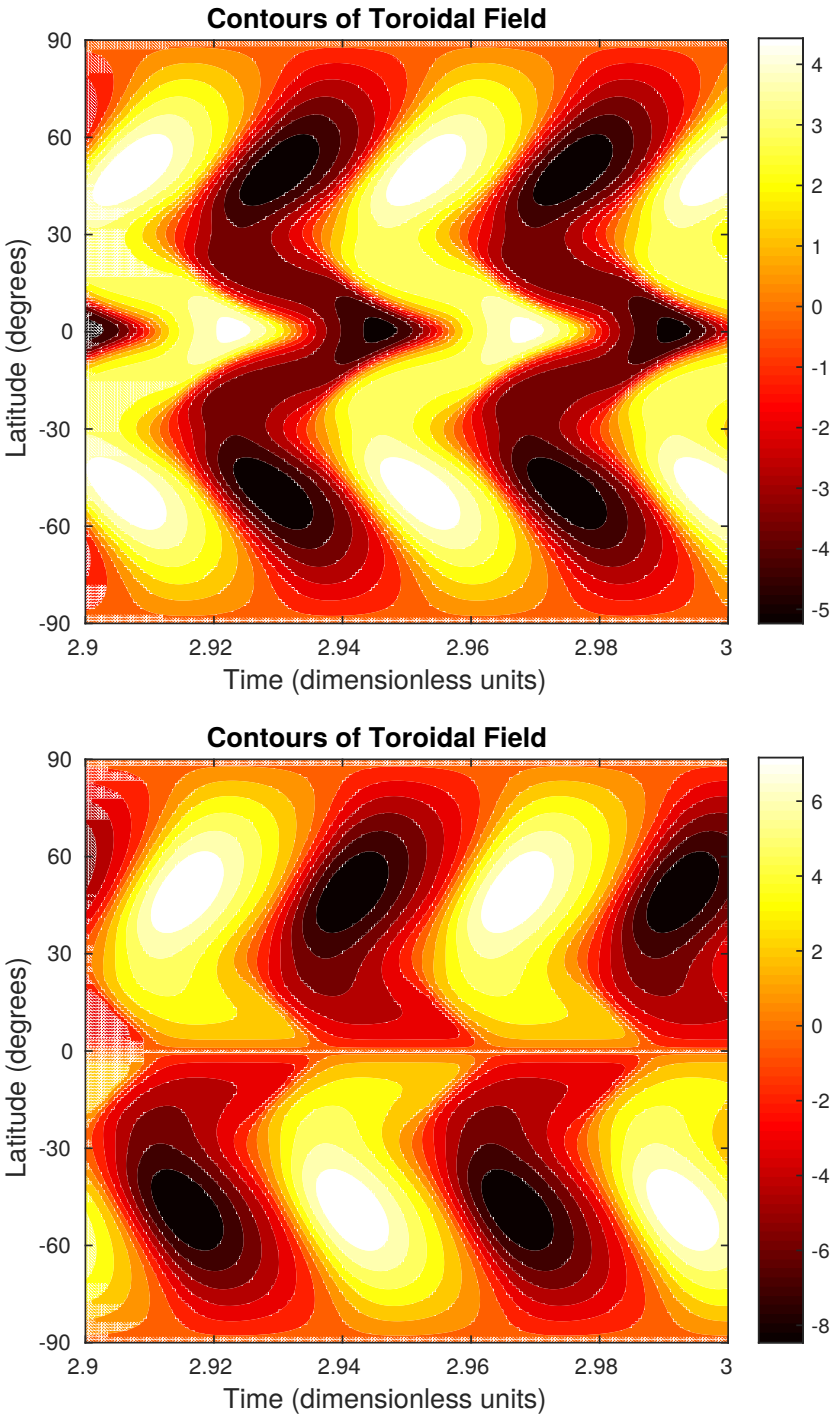

Figure 6.7: The dependence of the solution on S_0. Contour plots of toroidal field at a fixed radius of $r = 0.7$. For both plots, $D = -2 \times 10^6$ and $Re = 0$. For the top plot $S_0 = -0.5$ and for the bottom plot $S_0 = -1.0$.

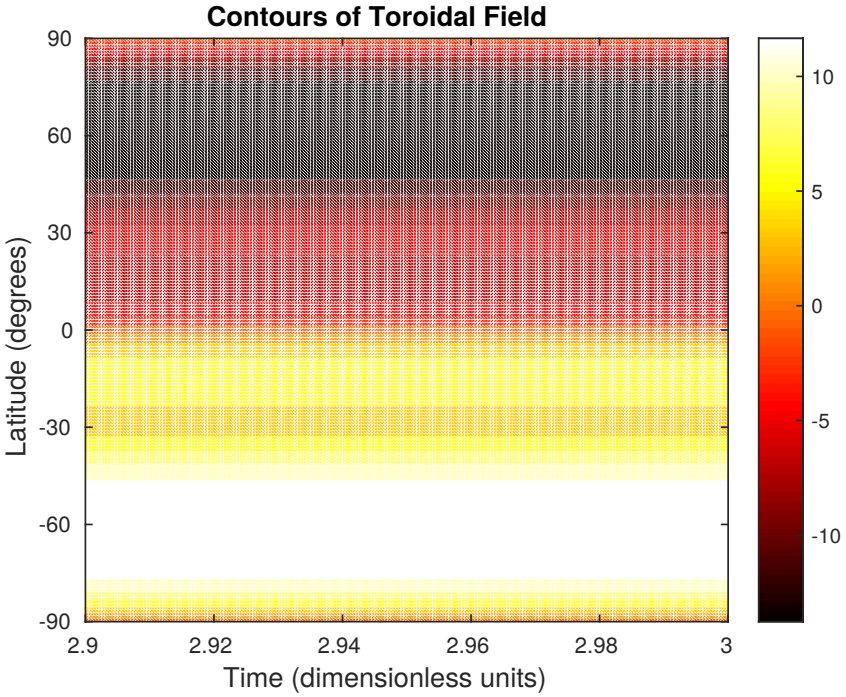

Figure 6.8: The dependence of the solution on S_0. Contour plot of toroidal field at a fixed radius of $r = 0.7$. Here, $D = -2 \times 10^6$, $Re = 5 \times 10^3$ and $S_0 = -0.01$.

the findings of Mann & Proctor (2009).

When $D = -2 \times 10^6$, $Re = 5 \times 10^3$ and $S_0 = 0.0$, the solution is a steady mode. Figure 6.8 is a contour plot of the toroidal field at the base of the convection zone when $S_0 = -0.01$. Here, the strength of the Babcock-Leighton source term is not strong enough to influence the dynamo such that steady modes continue to be generated. When $|S_0|$ is increased to -0.1, shown here in Figure 6.9, the solution now becomes periodic with the generation of a weak poleward migrating branch at mid to high latitudes. The solution is "solar-like" – the equatorward migrating branch has the correct direction of propagation and is confined to a region that is $\pm 30^\circ$ above the equator with the solution being predominantly dipolar in nature.

When $|S_0|$ is increased to -0.25, the parity of the solution has now changed to being predominantly quadrupolar. The magnitude of the peak toroidal field has increased nearly twofold and the period of the dynamo wave is significantly longer. The poleward migrating branch now originates at a lower latitude (although still $\pm 30^\circ$ above the equator) and the equatorward branch is now confined to a region approximately $\pm 15^\circ$ above the equator. As $|S_0|$ continues to be increased, quadrupolar solutions remain preferred. Figure 6.10 shows the behaviour of the system for two more values of S_0. When $S_0 = -0.5$, both the poleward and equatorward migrating branches have begun to merge and they are fully

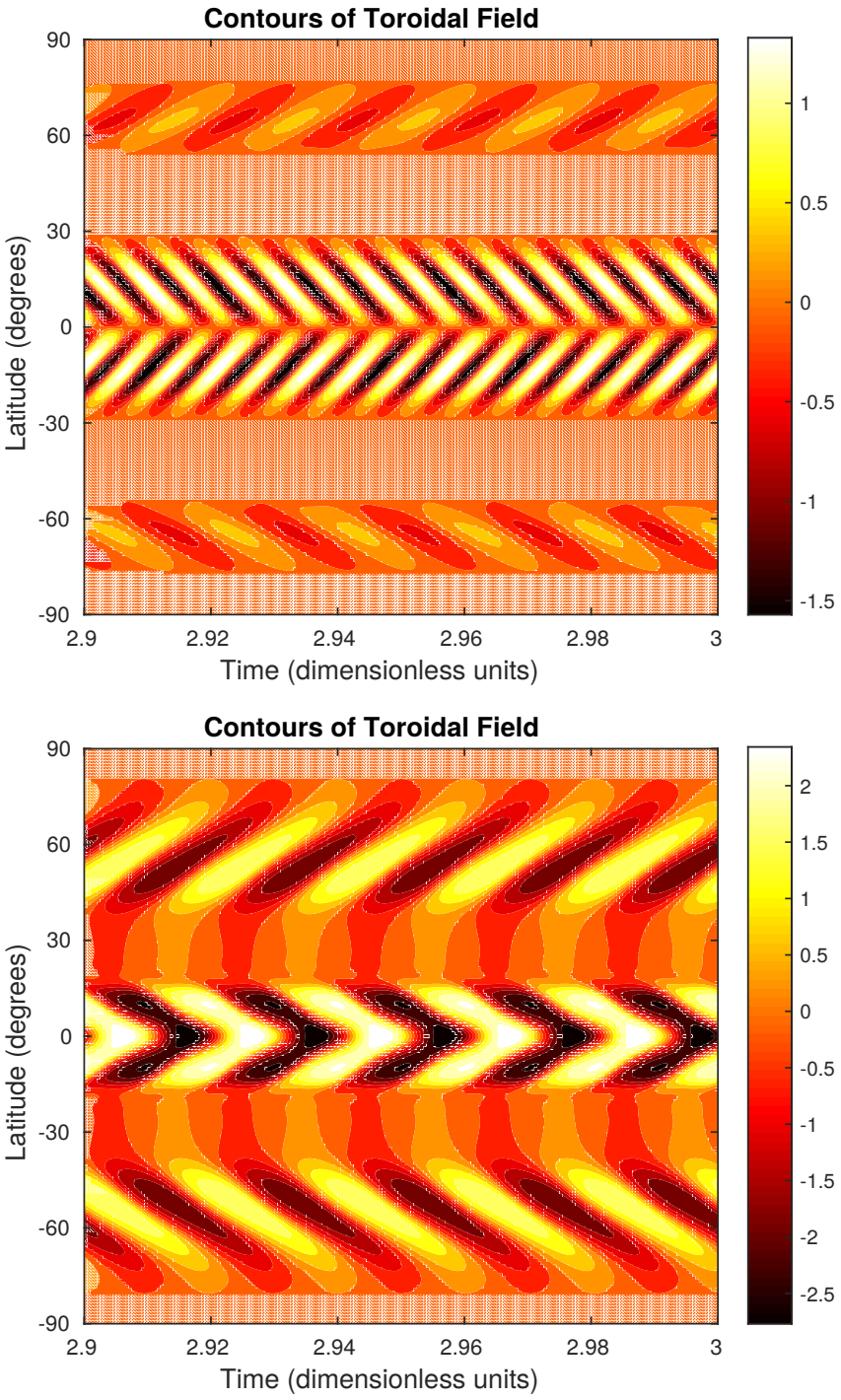

Figure 6.9: The dependence of the solution on S_0. Contour plots of toroidal field at a fixed radius of $r = 0.7$. For both plots, $D = -2 \times 10^6$ and $Re = 5 \times 10^3$. For the top plot $S_0 = -0.1$ and for the bottom plot $S_0 = -0.25$.

coupled when $S_0 = -1.0$. The butterfly diagram for $S_0 = -1.0$ features strong toroidal fields at high latitudes and the solution is not "solar-like"; it is not dipolar in nature and is not confined to a region $\pm 30^\circ$ above the equator. Also, the toroidal field maximum is located at a higher latitude than desired. In this case, the introduction of a meridional flow appears to have enhanced the potency of the Babcock-Leighton source term and has hindered the generation of "solar-like" solutions since the magnetic field is of quadrupolar parity.

For all of the oscillatory plots included in Figures 6.4 to 6.10, both the energy and the parity of the solutions are strictly periodic with no modulation observed in the system.

6.3.2 Parity Dependence

A striking conclusion from the parameter survey is that the parity of the solution is dependent upon the value of Re at fixed S_0. Figures 6.11 and 6.12 show contour plots of the toroidal field at the base of the convection zone when $D = -2 \times 10^6$ and $S_0 = -0.25$. The four plots are generated when $Re = 0$, $Re = 3 \times 10^3$, $Re = 4 \times 10^3$ and $Re = 6 \times 10^3$. When there is no flow (included here as the top plot of Figure 6.11), the resulting dynamo wave is of predominantly quadrupolar symmetry with a strong poleward migrating branch originating at mid latitudes. When the Reynolds number is increased to $Re = 3 \times 10^3$ (bottom plot of Figure 6.11), the solution is still predominantly quadrupolar however the poleward migrating branch has been suppressed by the flow and is now slightly weaker. Increasing the meridional flow tends to concentrate the magnetic activity at lower latitudes and this is precisely what is observed when Re is increased to 4×10^3. The solution is still predominantly quadrupolar however the equatorward branch of the toroidal field is now more concentrated around the solar equator with the peak toroidal field having been slightly reduced in magnitude. These quadrupolar solutions remain preferred until a Reynolds number of 6×10^3, which generates a solution that is of predominantly dipolar symmetry, with the toroidal field at the solar equator confined to a region of approximately $\pm 15^\circ$. Although the parity of the solution is dipolar (which is desired) the magnetic activity is too concentrated around the equator and should extend to a region of approximately $\pm 30^\circ$. The toroidal field also exhibits a polewards migrating branch at mid latitudes. Through this example, it is clear that the strength of the meridional flow is a crucial component in selecting the parity of the solution.

Table 6.1 shows how the parity (and period) of the dynamo wave is dependent upon the Reynolds number Re and the strength of the Babcock-Leighton source term S_0 for values of $-0.35 < S_0 < -0.10$ and $1 \times 10^3 < Re < 8 \times 10^3$. The results show that in general, at fixed S_0 when the Reynolds number remains small (3×10^3) quadrupolar solutions are preferred and as Re is increased, dipolar solutions can be found. If S_0 is small (i.e. $|S_0| < 0.20$), modulated solutions are present with a strong dipolar component.

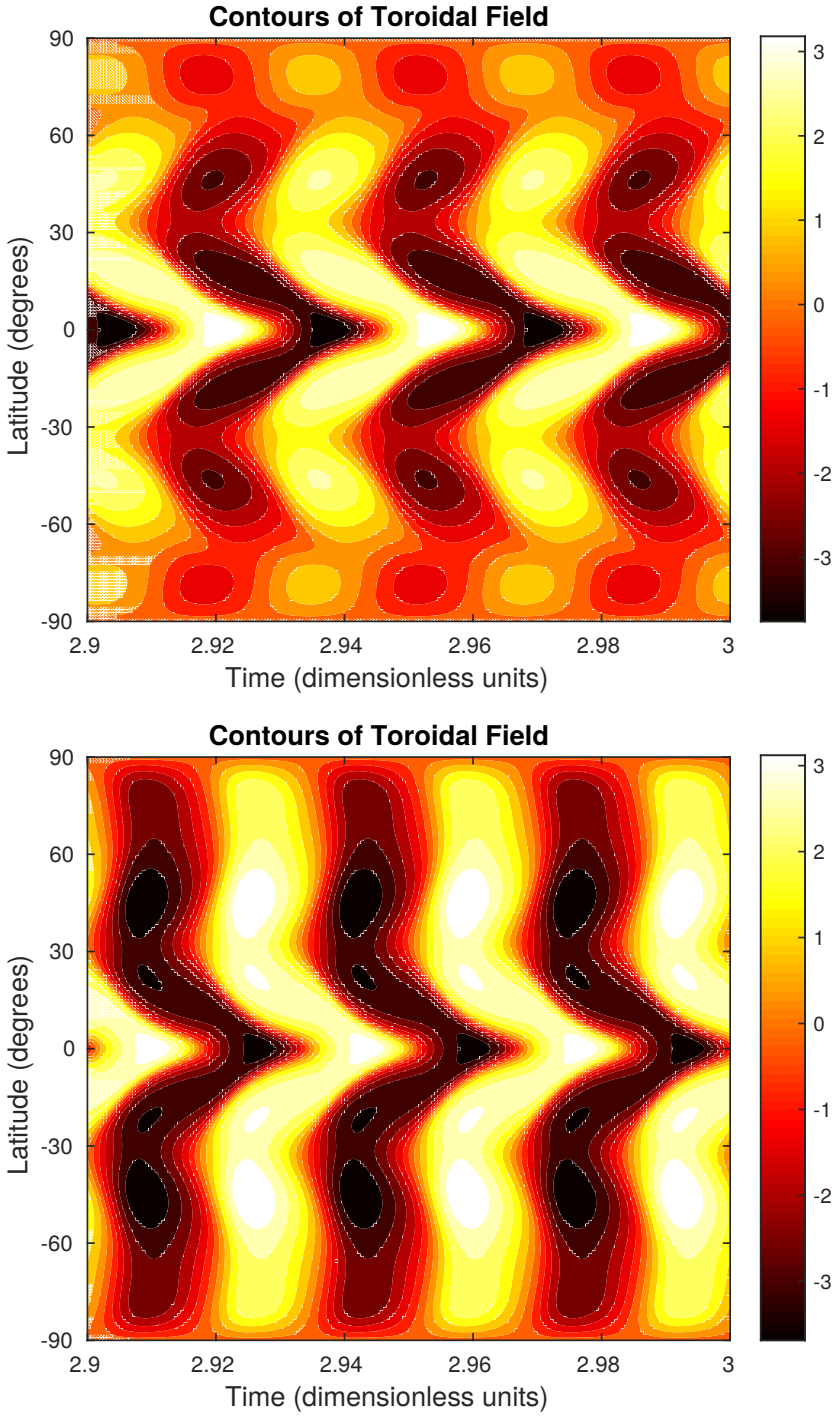

Figure 6.10: Contour plots of toroidal field at a fixed radius of $r = 0.7$. For both plots, $D = -2\times10^6$ and $Re = 5 \times 10^3$. For the top plot $S_0 = -0.5$ and for the bottom plot $S_0 = -1.0$.

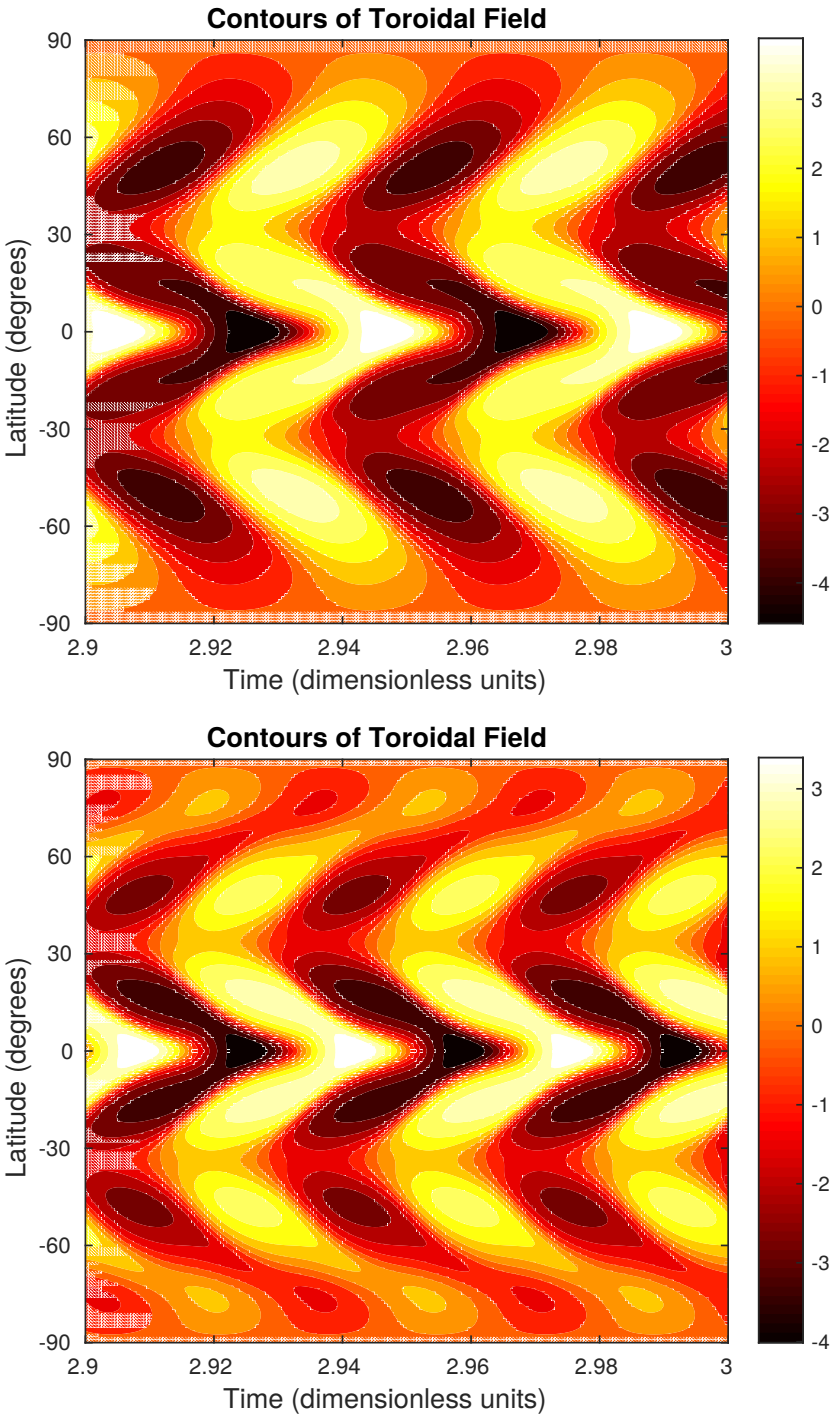

Figure 6.11: Parity dependence. Contour plots of toroidal field at a fixed radius of $r = 0.7$. For both plots, $D = -2 \times 0^6$ and $S_0 = -0.25$. For the top plot $Re = 0$ and for the bottom plot $Re = 3 \times 10^3$.

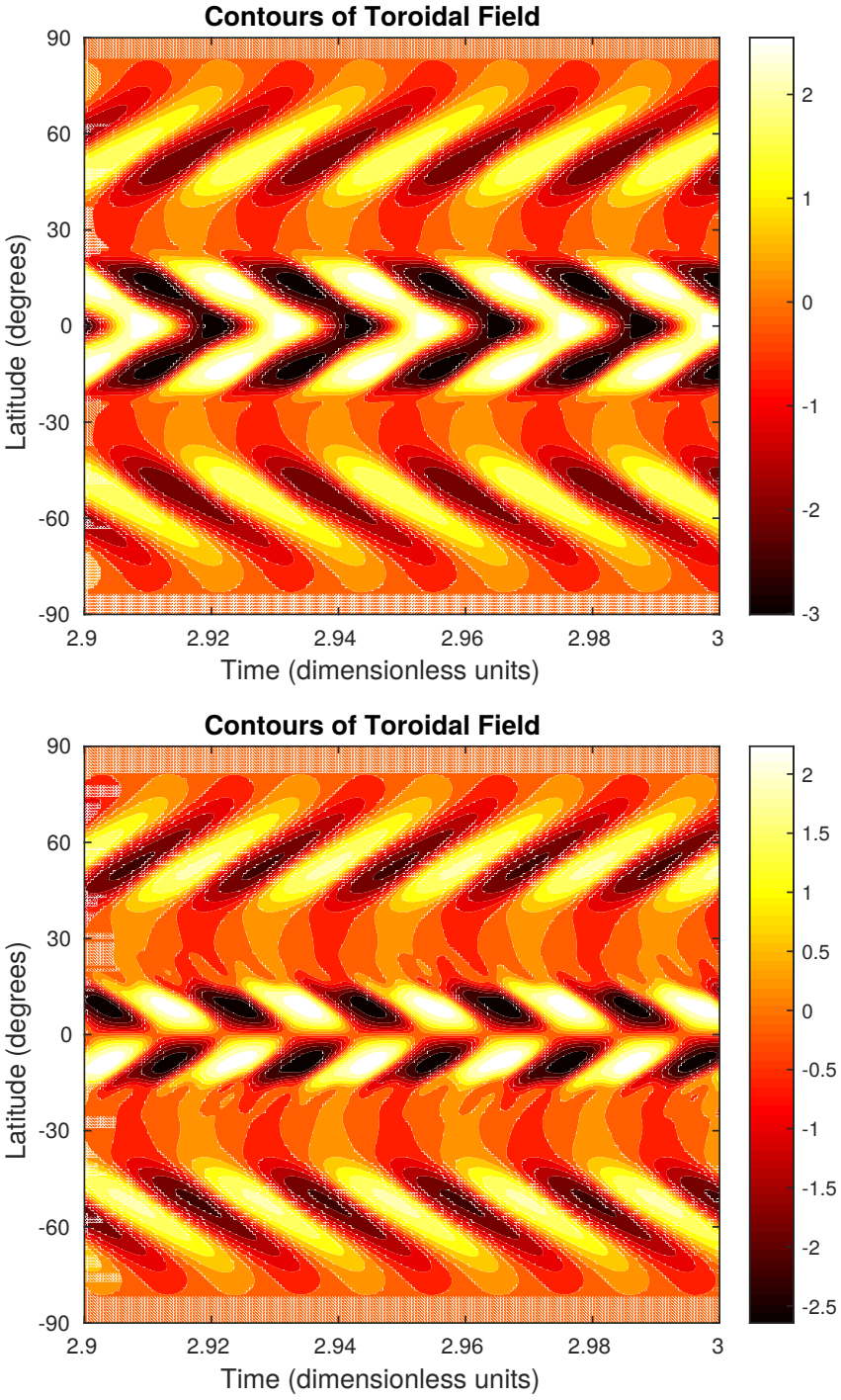

Figure 6.12: Contour plots of toroidal field at a fixed radius of $r = 0.7$. For both plots, $D = -2\times10^6$ and $S_0 = -0.25$. For the top plot $Re = 4 \times 10^3$ and for the bottom plot $Re = 6 \times 10^3$.

		S_0					
		-0.10	-0.15	-0.20	-0.25	-0.30	-0.35
	1×10^3	0.0073 (d)	0.0213 (q)	0.0233 (q)	0.0320 (q)	0.0365 (q)	0.0365 (q)
	2×10^3	(mod d)	0.0213 (q)	0.0233 (q)	0.0320 (q)	0.0365 (q)	0.0365 (q)
	3×10^3	(mod mi)	0.0213 (q)	0.0233 (q)	0.0320 (q)	0.0365 (q)	0.0365 (q)
Re	4×10^3	(mod d)	(mod d)	0.0213 (q)	0.0233 (q)	0.0320 (q)	0.0320 (q)
	5×10^3	(mod d)	(mod d)	0.0197 (q)	0.0197 (q)	0.0213 (q)	0.0320 (q)
	6×10^3	0.0073 (d)	(mod d)	(mod d)	0.0213 (d)	0.0197 (q)	0.0213 (q)
	7×10^3	0.0073 (d)	(mod d)	(mod d)	0.0197 (d)	0.0197 (mi)	0.0197 (q)
	8×10^3	0.0073 (d)	(mod d)	(mod d)	0.0197 (d)	0.0213 (d)	0.0197 (q)

Table 6.1: The period of the dynamo wave (in diffusion times). (q) represents a solution of quadrupolar symmetry, (d) represents a solution of dipolar symmetry, (mi) represents a mixed parity solution and (mod) represents a modulated solution (to be discussed later in this chapter). In the case of a modulated solution, no cycle period has been calculated.

These will be discussed in more detail in the next section. For values of $|S_0| > 0.20$ only periodic dipolar solutions have been found. This indicates that if both sources of poloidal field regeneration are present within the Sun, there exists an optimal combination of the Reynolds number and S_0 if dipolar "solar-like" solutions are to be generated. As $|S_0|$ is increased through to $S_0 = -0.35$, it is found that the Reynolds number must also be larger to generate dipolar solutions. There are a few anomalies to these trends. Firstly, a mixed solution is found for $S_0 = -0.30$ when $Re = 7 \times 10^3$. The most likely explanation for this is that it is located in a transitional region through which the dynamo wave moves from being quadrupolar to dipolar. Similar mixed parity solutions are likely to be present within the parameter space. However this was the only solution to have been simulated. There is another mixed mode found for $S_0 = -0.1$ and $Re = 3 \times 10^3$ however this is now a modulated solution. It is difficult to speculate why this is the case since dipolar solutions are found for values of the Reynolds number immediately above and below this point. However the mixed mode may arise due to the modulation of the dynamo wave and is therefore not a result of the combination of the Reynolds number and S_0. These features are represented in a schematic diagram included in Figure 6.13.

It is also interesting to study how the period of the solution is dependent upon the parameters of the system. The results clearly show that at fixed Reynolds number as $|S_0|$ is increased, the period of the dynamo wave also increases. Conversely, at fixed S_0 as the Reynolds number is increased, the period of the wave decreases. This is intuitive since a quicker flow will transport magnetic flux from the solar surface to the base of the convection zone more rapidly and hence lead to a decrease in the period of the dynamo wave.

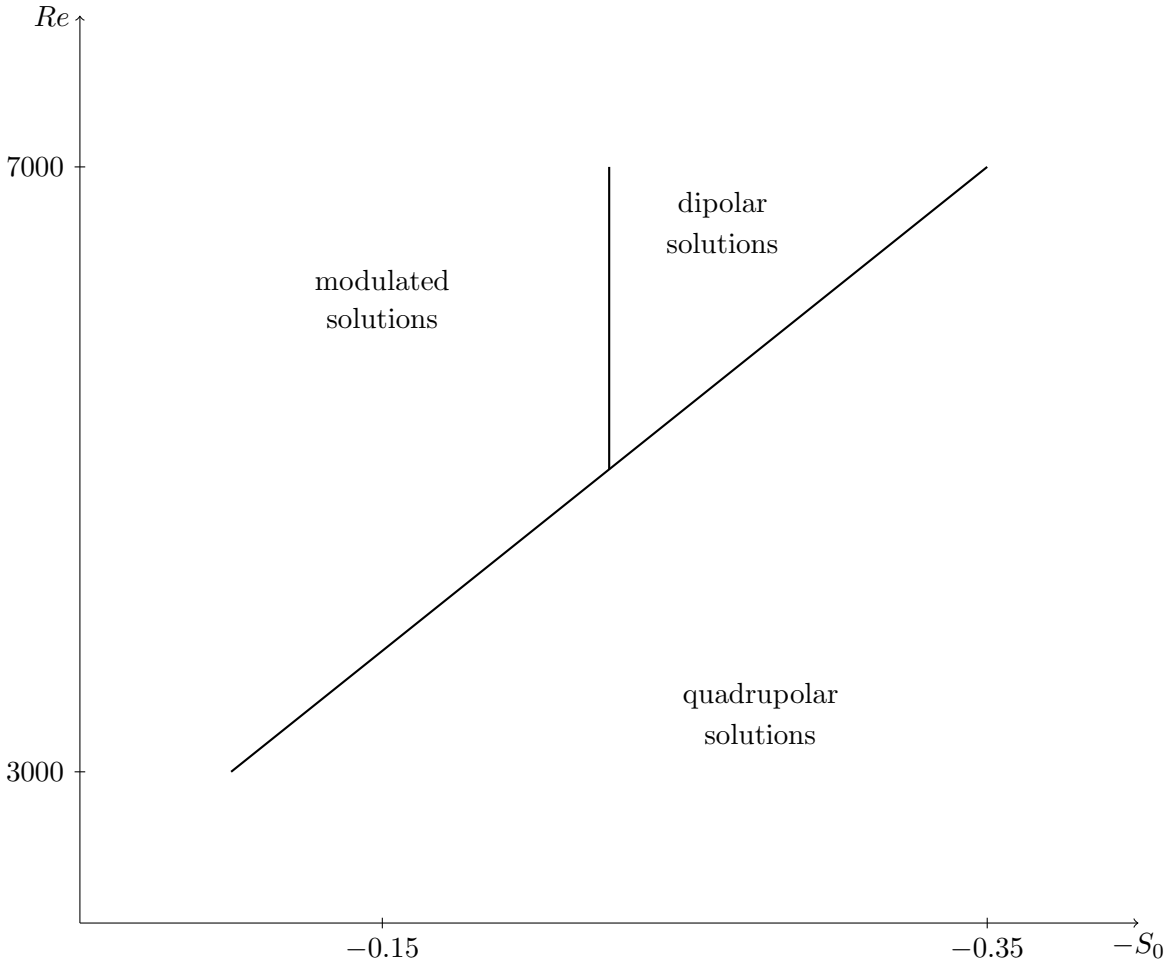

Figure 6.13: Schematic diagram showing how the parity of the solution is dependent upon the Reynolds number and the strength of the Babcock-Leighton source term S_0.

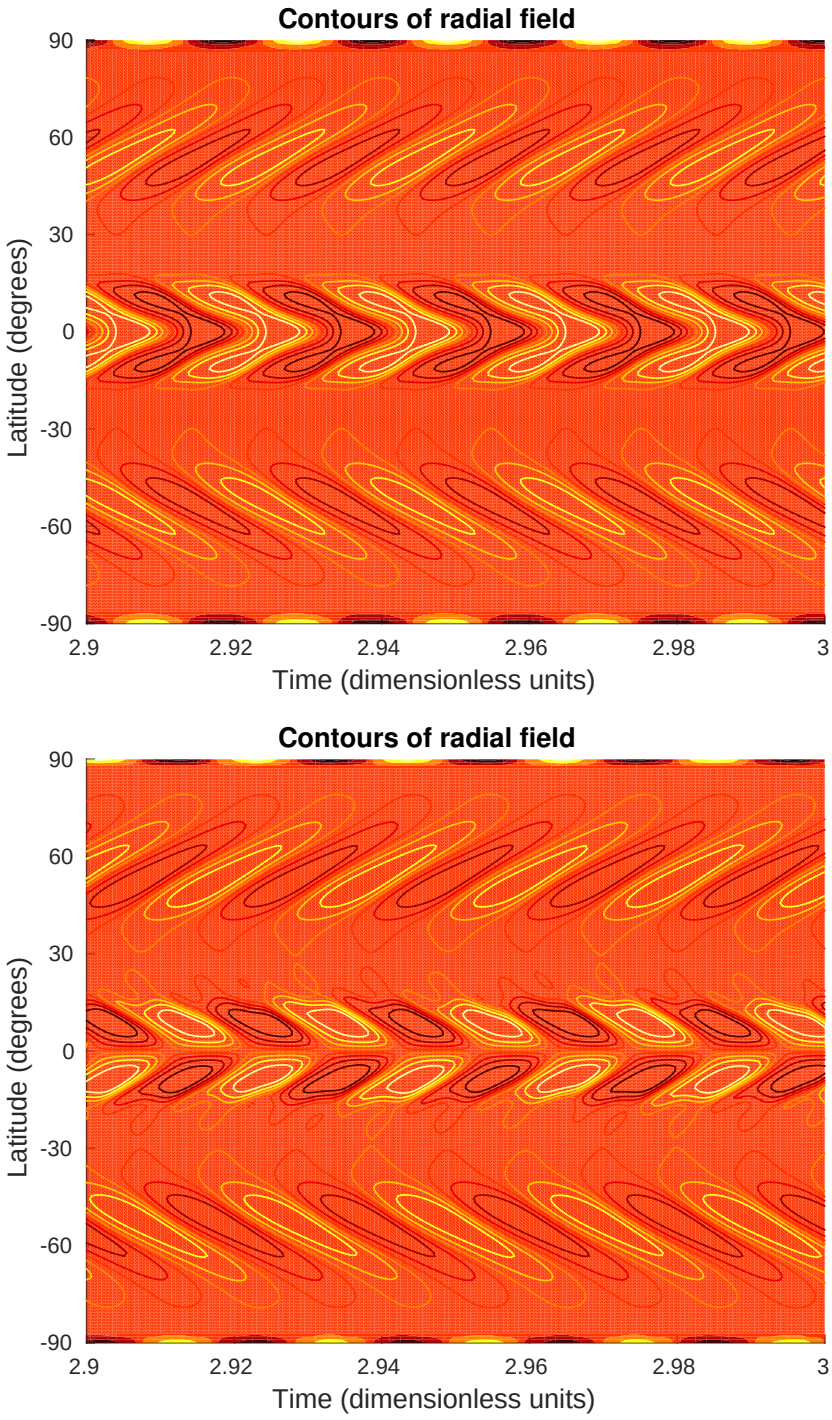

Figure 6.14: The radial field at the solar surface. Contour plot of the radial field at the solar surface (filled contours) with contours of toroidal field at $r = 0.7$ superimposed. Here, $D = -2 \times 10^6$ and $S_0 = -0.25$ for both plots. For the top plot $Re = 5 \times 10^3$ and for the bottom plot $Re = 6 \times 10^3$.

6.3.3 Radial Field

As with the previous models that have been detailed in this thesis, the motivation behind introducing these competing α-effects is to determine whether they can interact in such a way that can lead to modulation of the Sun's magnetic field. Substantial evidence for modulation is found within the system. However before these results are described, it is important to show that the model can reproduce the observed phase shift between the maximum value of the toroidal field at the base of the convection zone and the polarity reversal of the radial field at the solar surface.

Figure 6.14 shows two contour plots of the radial field at the solar surface with contours of toroidal field at the base of the convection zone ($r = 0.7$) superimposed. For both plots, $D = -2 \times 10^6$ and $S_0 = -0.25$. The top plot shows that the toroidal field is of predominantly dipolar parity and is generated when $Re = 5 \times 10^3$ and the bottom plot is for a predominantly quadrupolar solution which is generated when $Re = 6 \times 10^3$. It is difficult to determine precisely when the radial field changes because contours of B_r are extremely localised around the poles. However, for both solutions, the radial field at the solar surface (at a latitude of $\pm 90^\circ$) changes polarity some time after the toroidal field maximum. The phase shift remains constant and the fields remain phase locked as the solution propagates forward in time.

6.3.4 Modulation

Now that it has been shown that the results are consistent with previous numerical work, it is possible to describe the modulation that is found within the system. The numerical simulations have been carried out for two different values of the dynamo number D and the remaining plots within this chapter are spilt into these two categories.

$\mathbf{D = -2 \times 10^6}$

The following plots are generated through fixing the values of $D = -2 \times 10^6$ and $S_0 = -0.15$ whilst varying Re. Information about the period and parity of these solutions can be found in the second column of Table 6.1. Figure 6.15 shows the nature of the solution when $Re = 2 \times 10^3$. For this set of parameters, the solution remains periodic and is of quadrupolar parity which is clearly indicated in the time series evolution of the energy and parity. The butterfly diagram indicates that the equatorward branch is confined to a region that is $\pm 15^\circ$ either side of the equator and there is also a strong poleward branch originating at mid latitudes.

When Re is increased to 4×10^3, the solution is no longer periodic. The behaviour of the system is shown in Figure 6.16 and the butterfly diagram shows a modulated (predominantly) dipolar equatorward branch (confined to $\pm 30^\circ$ in latitude) with varying

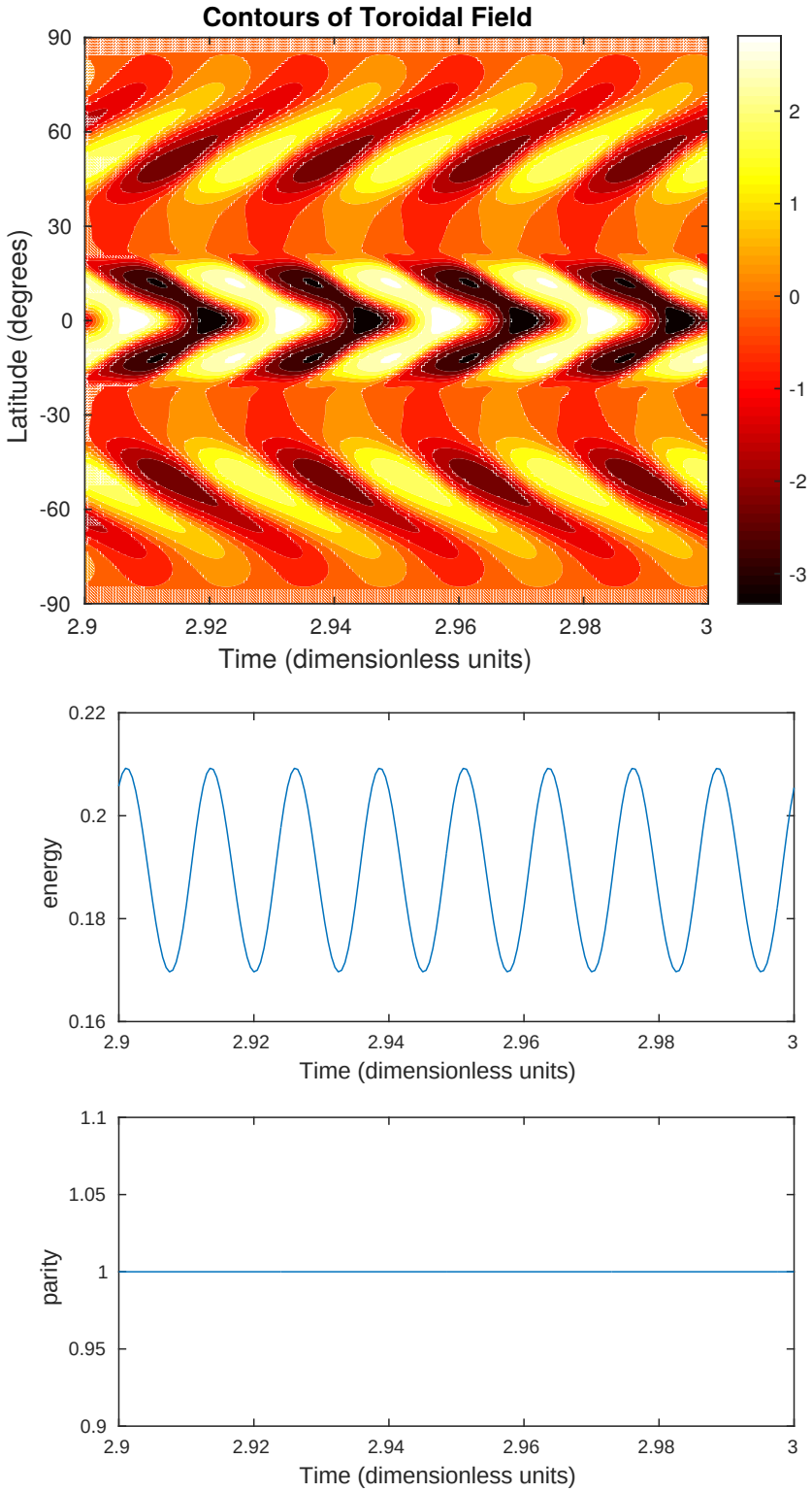

Figure 6.15: Here, $D = -2 \times 10^6$, $S_0 = -0.15$ and $Re = 2 \times 10^3$. The top plot is a contour plot of the toroidal field at $r = 0.7$, the middle plot is a time series of the magnetic energy and the bottom plot is the parity of the solution.

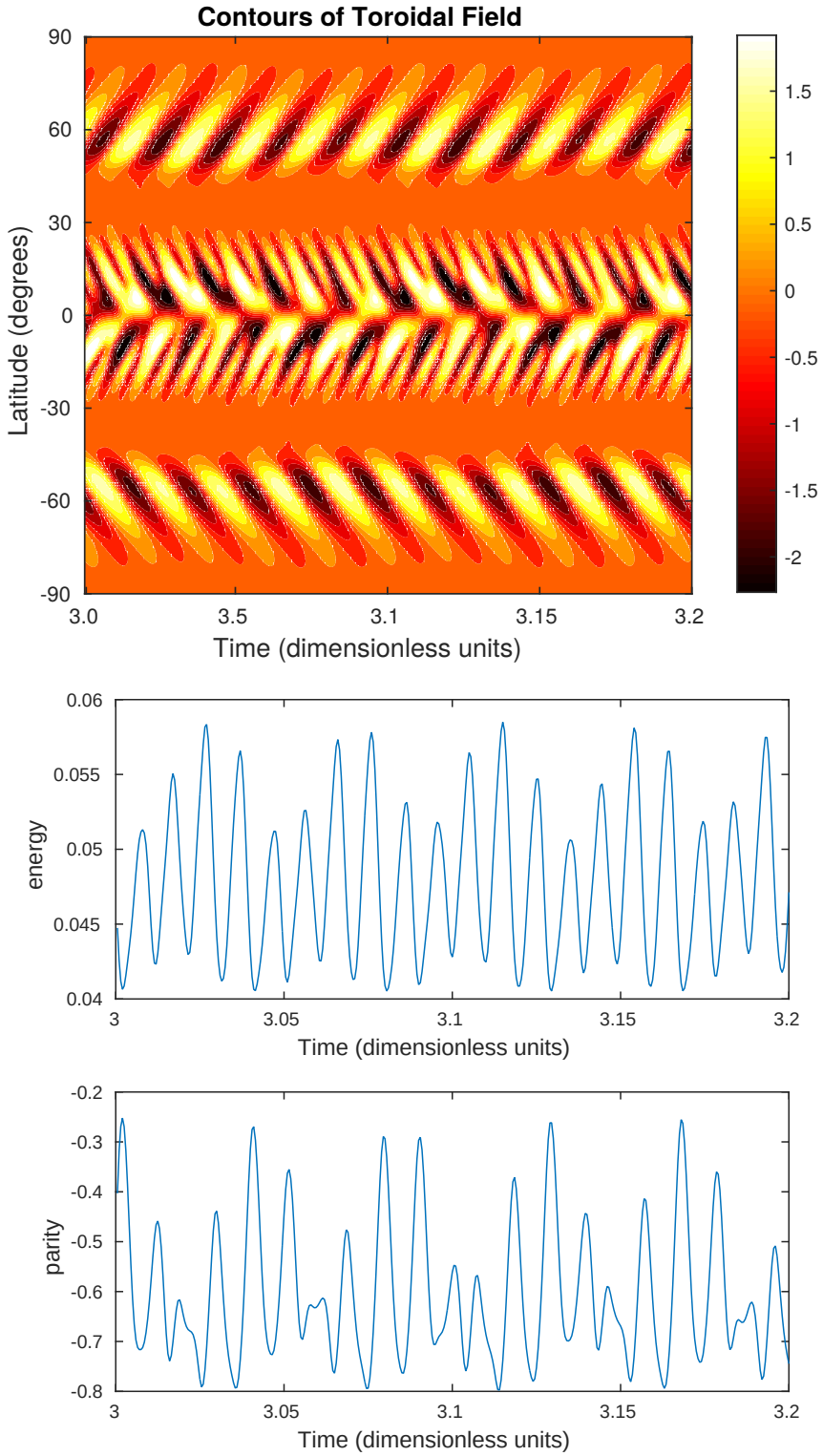

Figure 6.16: Here, $D = -2 \times 10^6$, $S_0 = -0.15$ and $Re = 4 \times 10^3$. The top plot is a contour plot of the toroidal field at $r = 0.7$, the middle plot is a time series of the magnetic energy and the bottom plot is the parity of the solution.

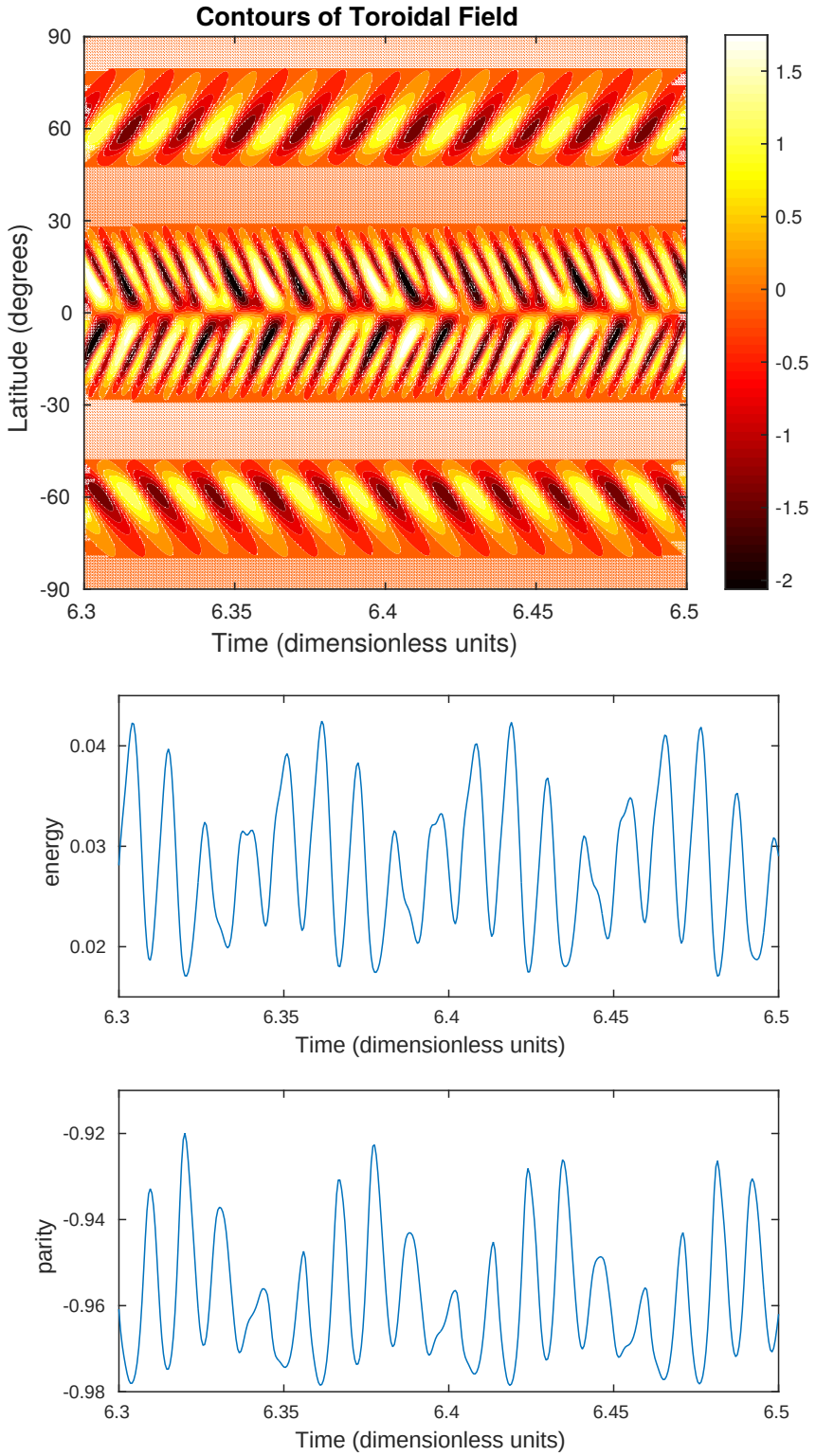

Figure 6.17: Here, $D = -2 \times 10^6$, $S_0 = -0.15$ and $Re = 7 \times 10^3$. The top plot is a contour plot of the toroidal field at $r = 0.7$, the middle plot is a time series of the magnetic energy and the bottom plot is the parity of the solution.

magnitudes of successive cycles. There is very little modulation present within the poleward migrating branch and the magnitude of the peak toroidal field has now decreased in comparison with the solution for $Re = 2 \times 10^3$. Time series of both the energy and parity are modulated with the parity of the solution remaining predominantly dipolar throughout.

Increasing the Reynolds number to $Re = 7 \times 10^3$ leads to further modulation of the equatorward branch, shown here in Figure 6.17. For this combination of parameters the magnitude of successive cycles is more variable with very strong cycles immediately followed by very weak cycles. Another interesting feature is the parity of the solution. Here, the time series of the parity remains strictly below -0.9 indicating a very strong dipolar component. In the previous solution (when $Re = 4 \times 10^3$), the parity ranges from -0.2 to -0.8 indicating that at times there is a mixed mode that is generated. It is clear that the Sun's magnetic field is dipolar in nature and the solution for $Re = 7 \times 10^3$ is a reasonable representation of the Sun's magnetic activity at low latitudes.

$\mathbf{D = -2 \times 10^7}$ (Case 1)

Modulation is also found for a larger value of $D = -2 \times 10^7$ which is as expected since this value of D is more supercritical. An example of this is included here when D remains fixed at -2×10^7, Re is fixed at 7×10^3 and S_0 is varied. Figure 6.18 shows the behaviour of the system when $S_0 = -0.15$. For this combination of parameters, the solution is quasi periodic mainly due to the evolution of the magnetic field between $\pm 10^\circ - 50^\circ$. Between these latitudes, the period of the wave is ≈ 3 times smaller than the period of the wave at the equator and high latitudes.

Increasing the value of $|S_0|$ to $S_0 = -0.20$ leads to the strongly modulated solution shown in Figure 6.19. In this case, the solution is clearly not periodic or doubly periodic and appears to be chaotically modulated. The parity is generally a mixed mode with instances of strong dipolar fields which can be seen at around $t = 10.695$. The amplitude of the equatorward branch varies greatly between cycles with strong (longer) cycles followed by weaker (shorter) cycles. This feature is particularly evident at around $t = 10.7$. Once the value of S_0 has reached -0.30, the solution returns to being periodic with the dynamo selecting a dipolar parity.

$\mathbf{D = -2 \times 10^7}$ (Case 2)

A further example of the modulation within the system is given when $D = -2 \times 10^7$, $Re = 5 \times 10^3$ and S_0 is varied. When $S_0 = -0.20$ the dynamo wave remains periodic at all latitudes. Figure 6.20 is generated after $|S_0|$ has increased to -0.30 and the magnetic energy is now multiply periodic due to the behaviour of the dynamo wave in the region approximately $\pm 20^\circ - 40^\circ$ above the equator. In this region, the dynamo wave is now

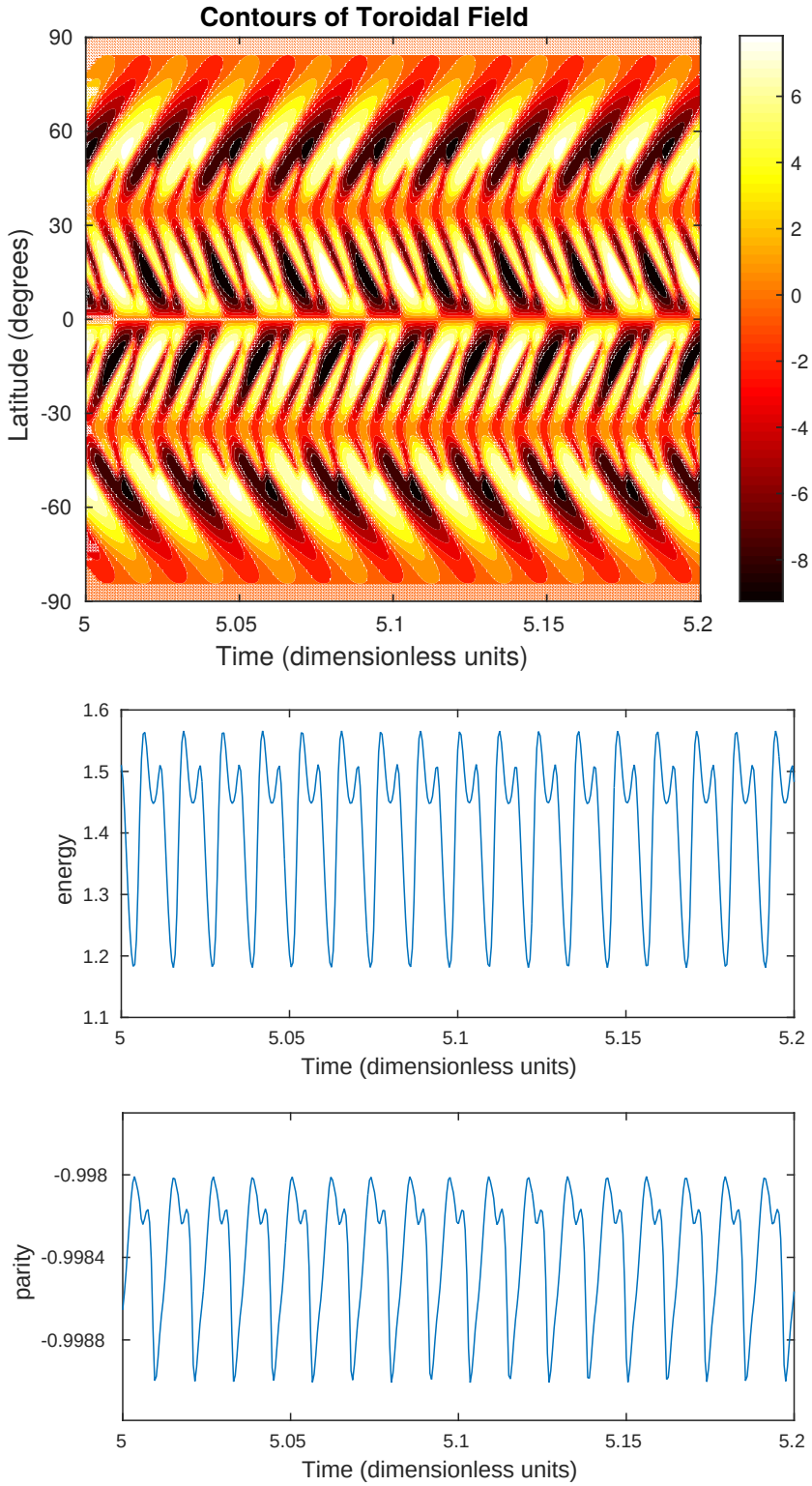

Figure 6.18: Case 1: Here, $D = -2 \times 10^7$, $Re = 7 \times 10^3$ and $S_0 = -0.15$. The top plot is a contour plot of the toroidal field at $r = 0.7$, the middle plot is a time series of the magnetic energy and the bottom plot is the parity of the solution.

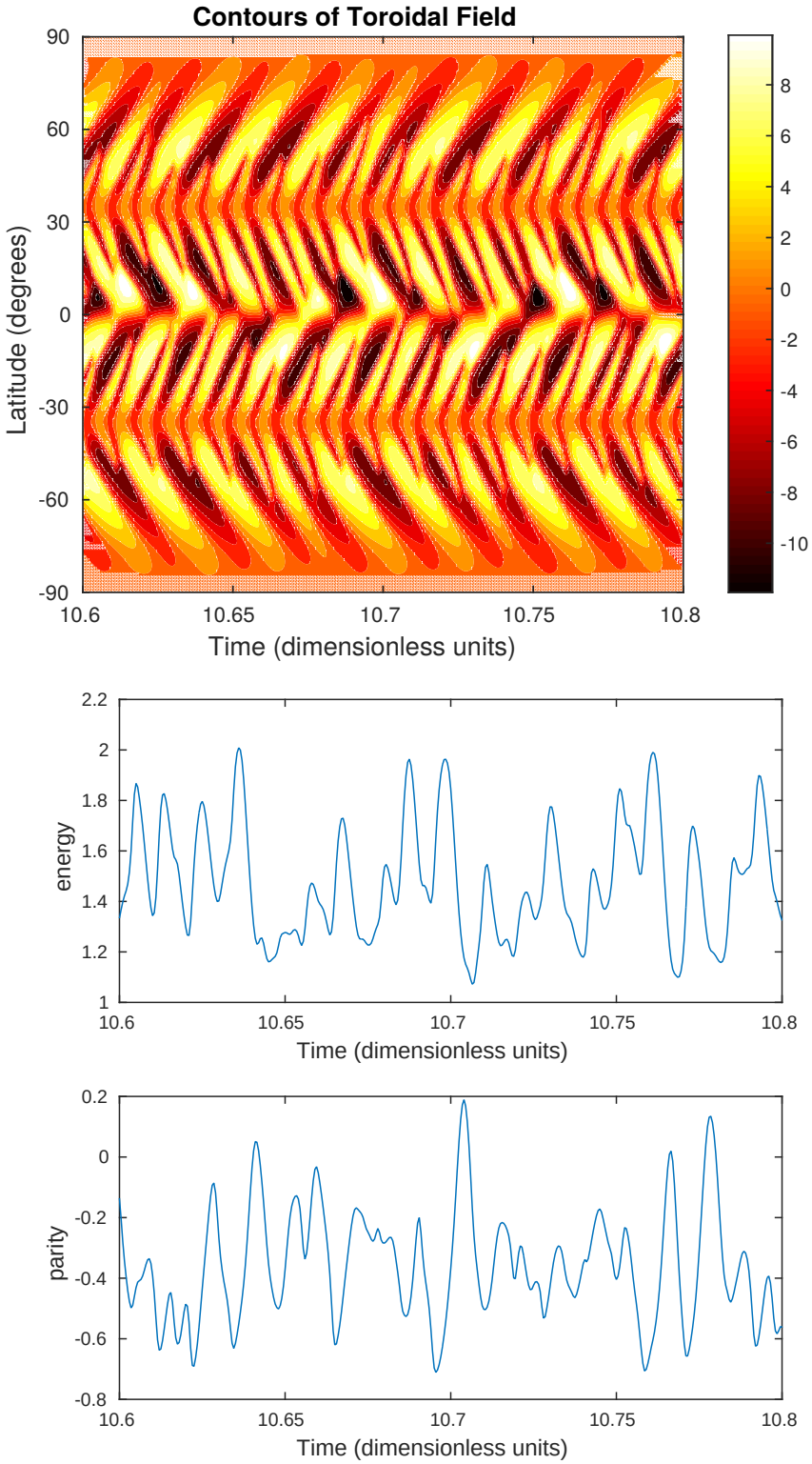

Figure 6.19: Case 1: Here, $D = -2 \times 10^7$, $Re = 7 \times 10^3$ and $S_0 = -0.20$. The top plot is a contour plot of the toroidal field at $r = 0.7$, the middle plot is a time series of the magnetic energy and the bottom plot is the parity of the solution.

multiply periodic with strong (longer) cycles followed by short (weaker) cycles. Figure 6.21 shows the behaviour of the system after $|S_0|$ has been increased to -0.35 and modulation is now present in both the equatorward and poleward migrating branches. Not only is the amplitude of the dynamo wave modulated but the parity of the solution ranges from being predominantly dipolar at around $t = 11.5$ to almost wholly quadrupolar at around $t = 11.7$. Although the Sun's magnetic field has been known to be of dipolar parity from around 1600, unfortunately there are no records of the parity of the Sun's magnetic field before this date. This means that it is certainly feasible that the field was quadrupolar in nature and then went through a transition to dipolar parity before 1600. If this is the case, there is no reason to suspect that this change in parity could not occur again in the future. The solution shown in Figure 6.21 shows that the competing alpha mechanism with a shallow meridional flow can represent parity modulation of this nature.

6.4 Summary

Building upon the models previously described in this thesis, this chapter has successfully demonstrated that an interface type dynamo with a perturbation from a surface source term can lead to "solar-like" behaviour as well as significant modulation in both energy and parity. Based upon recent observations by Hathaway (2012), a shallow meridional flow is used to transport toroidal flux generated from a Babcock-Leighton source term from the solar surface down to a radius of $r = 0.85$. To the best of my knowledge this is the first study of this type to include such a shallow meridional flow.

At the beginning of this chapter several key/open questions were introduced:

The "parity problem" Although there is no knowledge of the parity of the Sun's magnetic field before 1600, after this time it is known to be of dipolar parity. Babcock-Leighton dynamo models predominantly produce solutions of quadrupolar parity and one criticism of these models is that it is difficult for these models to produce solutions that are dipolar in nature. Through varying the magnitude of the Babcock-Leighton source term and the strength of the Reynolds number, I have shown that my model can produce dipolar solutions for an optimal combination of these parameters. Numerical simulations suggest that quadrupolar solutions become increasingly prominent as the strength of the Babcock-Leighton source term is increased which is as expected. However, if the magnitude of the Babcock-Leighton source term remains fixed and the strength of the Reynolds number is increased, it is possible for the model to produce the favoured dipolar solutions.

What role does the meridional flow play? It is clear that the meridional flow can set the period of the dynamo wave. This is consistent with previous work and is a well

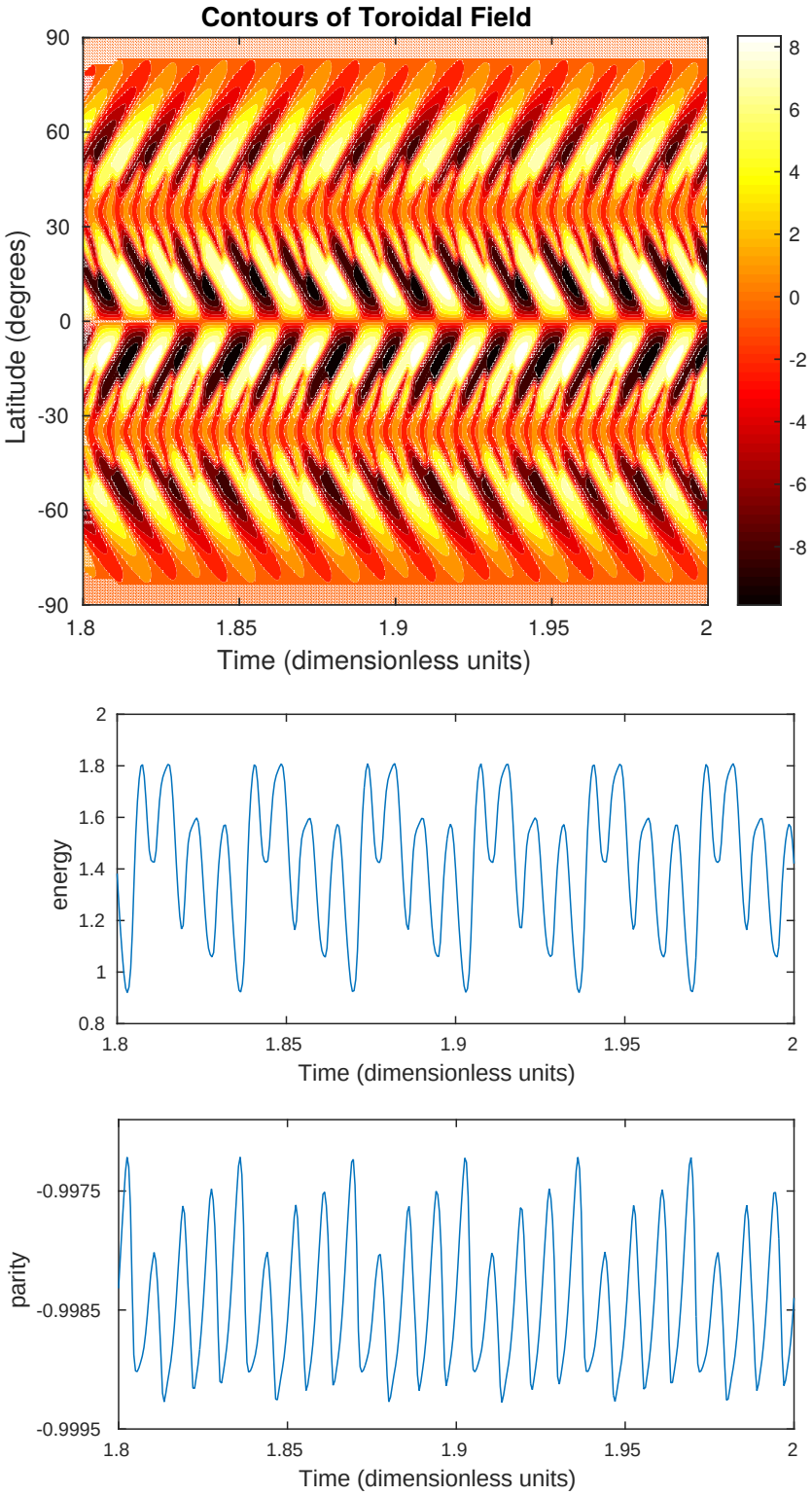

Figure 6.20: Case 2: The solution when $D = -2 \times 10^7$, $Re = 5 \times 10^3$ and $S_0 = -0.30$.
Case 2: Here, $D = -2 \times 10^7$, $Re = 5 \times 10^3$ and $S_0 = -0.30$. The top plot is a contour plot of the toroidal field at $r = 0.7$, the middle plot is a time series of the magnetic energy and the bottom plot is the parity of the solution.

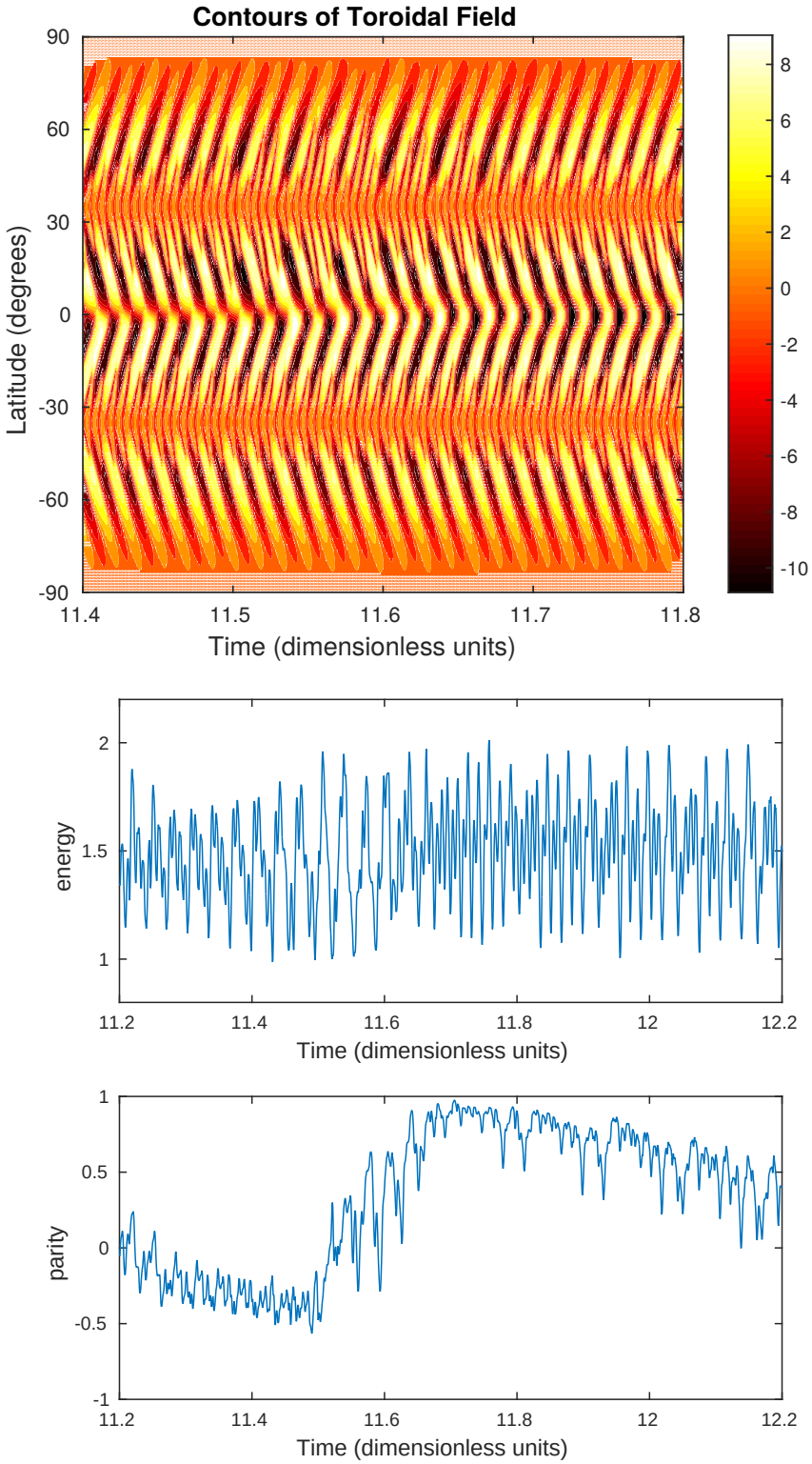

Figure 6.21: Case 2: Here, $D = -2 \times 10^7$, $Re = 5 \times 10^3$ and $S_0 = -0.35$. The top plot is a contour plot of the toroidal field at $r = 0.7$, the middle plot is a time series of the magnetic energy and the bottom plot is the parity of the solution.

known feature of flux transport dynamo models. However, this is not the only feature of my model that is able to set the period of the dynamo wave. It is found that when the strength of the Babcock-Leighton source term is increased, the period of the dynamo wave also increases. This could be because there is more poloidal flux at the solar surface that needs to be transported by the meridional flow. My model is able to produce a reasonable "solar-like" solution without a meridional flow. This means that both diffusion and advection are responsible for coupling the source region at the solar surface to the base of the convection zone. The top plot in Figure 6.6 is generated when $Re = 0$ and the strength of the Babcock-Leighton source term is -0.1. For this solution, the dynamo wave has the correct direction of propagation, the magnetic field is confined to a region $\pm 30^{\circ}$ above the equator and it is of predominantly dipolar parity. In this case, the surface α-effect plays a passive role and the model definitely represents an interface dynamo with a perturbation from a surface source term.

What form can the meridional flow take? Traditionally, Babcock-Leighton dynamo models incorporate a meridional flow that penetrates deep into the convection zone. In this model, it has been shown than a shallow meridional flow (with a returning equatorward flow located at a radius of $0.85R_{\odot}$) can help transport poloidal field regenerated at the solar surface to the base of the convection zone. Of course, this is not the only mechanism through which the source layers are coupled: diffusion and advection can also play a role however, through numerical simulations, it is apparent that the strength of the meridional flow can significantly influence the properties of the dynamo wave. Since the model was constructed to represent an interface dynamo with a perturbation from a surface source term no other representations of the meridional flow were considered.

What mechanisms are able to modulate the dynamo wave? Modulation is a robust feature of my model. For two different values of the dynamo number modulation was found in both regimes alongside periodic and quasiperiodic solutions. In the lower D regime, (for the modulated solutions) no interaction was found between the equatorward and poleward migrating branches with the poleward branch remaining sufficiently periodic throughout the parameter survey. Substantial modulation of the equatorward branch was found through varying Re and S_0 with the amplitude of successive cycles varying between strong (longer) cycles and short (weaker) cycles. In the higher D regime, interaction was found between the poleward and equatorward migrating branches. This is the regime in which the most dramatic modulation was present. Not only was it possible to find strongly modulated time series of the magnetic energy but parity modulation was also found within the system. The Sun's magnetic field could have been quadrupolar before 1600 and it is possible for the parity to change again in the future. If this is indeed the

case, these competing α-effects with a shallow meridional flow could be responsible for parity modulation of this nature.

It is clear that my model is able to reproduce several features of the solar cycle. One thing that is missing from my solutions are periods of grand minima. In theory, using the model that I have described the dynamo should be able to restart after these periods. However, this has not yet been demonstrated in the numerical simulations.

Part IV

Summary

Chapter 7

Conclusions

7.1 Summary

Much is known about the Sun's magnetic field. It is oscillatory with a full period of approximately 22 years and is confined to a region that is approximately $\pm 30^{\circ}$ above the equator. The large-scale magnetic field is dipolar in nature and reverses sign at the end of each 11 year sunspot cycle. The appearance of sunspots are modulated in time and there have been instances of grand minima where the Sun's magnetic activity has been significantly reduced.

Mean field dynamo theory has been successful in reproducing many of the observations of the Sun's magnetic field. These models require mechanisms that are able to generate poloidal field from toroidal field and vice versa. Differential rotation (known as the ω-effect) can be measured throughout most of the solar interior and is widely accepted to be the process that is responsible for converting poloidal field into toroidal field. Due to the strong toroidal field at the base of the convection zone (and also because of strong turbulent pumping in this region) the tachocline is the preferred location for flux storage. Although there is widespread agreement that the ω-effect is responsible for toroidal field regeneration, the converse process (α-effect) which is responsible for converting toroidal field back into poloidal field remains a topic of some debate. A heuristic picture of this process was first introduced by Parker (1955*a*). His α-effect relied upon cyclonic turbulence to twist the toroidal field lines into the poloidal direction. This interface type α-effect is conjectured to be located at a region just above the base of the convection zone where the toroidal field is not deemed strong enough to suppress cyclonic turbulence. The two source regions are then coupled through magnetic diffusion and turbulent pumping. Another mechanism for poloidal field regeneration was introduced by Babcock (1961) and Leighton (1964) who suggested that poloidal flux could be produced by the decay of active regions at the solar surface (which tend to emerge with a systematic tilt with respect to the azimuthal

direction due to Joy's law). The transportation of the magnetic flux from the solar surface to the tachocline could be achieved by diffusion or by pumping, but meridional flows could also play an important role in this respect.

A polewards meridional flow of approximately $20ms^{-1}$ is observed at the solar surface and, due to the conservation of mass, a returning equatorward flow must be located somewhere within the solar interior. Due to the limitations of heliosisemology and partly due to the much smaller magnitude of the meridional flow compared to other flows within the Sun's interior, there is no consensus as to where this returning equatorward flow is located. A recent study by Hathaway (2012) has suggested that the poleward meridional flow is confined to a shallow region in the surface shear layer and the Sun's returning equatorward flow is located at a depth very close to this.

One of the challenges when describing a model that is able to successfully reproduce observations of the Sun lies in describing a viable mechanism through which the dynamo wave can be modulated. The Sun's convection zone is highly turbulent, and stochastic fluctuations in the interface α-effect, surface α-effect and meridional flow have proven successful in reproducing modulated solutions. Fully deterministic models which make use of the back reaction of the Lorentz force upon the magnetic field have also been able to produce modulated dynamo waves. Deterministic time delays in dynamo models have also been studied and represent another mechanism through which the dynamo wave can be modulated.

Based upon solar observations and working within the framework of mean field dynamo theory, in Chapter 3 I introduced a model that was adapted from Jouve *et al.* (2010) which investigates the effects of time delays in a simple cartesian model. My model (which solves the governing equations as a set of ODEs) differs from that of Jouve *et al.* (2010) through the inclusion of both sources of poloidal field regeneration, i.e. a deep-seated α-effect and an additional surface source term. A delayed field is introduced which represents the time lag generated by the time taken to transport magnetic flux between surface layers and the base of the convection zone. This process is not instantaneous and the time taken for this magnetic flux to be recaptured into the system is non-negligible. Investigating the dependence of the critical dynamo number upon the relative magnitudes of the deep-seated (α) and surface (S) source terms indicates that the way in which these two competing α-effects interact is non trivial. In the most interesting regime, there exists a threshold which the sum of α and S must exceed before these two competing α-effects can work together to help drive the dynamo. The model is also highly successful in reproducing modulated solutions through varying the magnitude of S and the length of the time delay τ. Transitions can be described which show that at fixed values of S, as τ is increased, the system goes through a series of bifurcations until a strongly modulated solution is found. Shortly after τ is increased through this point, the delayed field Q is unable to

significantly affect B and a periodic solution is recovered. The most strongly modulated solutions contain periods of low magnetic energy which would correspond to periods of grand minima in the solar cycle. The analogous PDE model is also investigated and similar strongly modulated solutions are found within the system which exhibit some features that are (at least qualitatively) "solar-like".

The model described in Chapter 3 makes use of a Taylor series approximation to derive a governing equation for Q. Although this approximation is valid for small vales of τ it was important to investigate if the error term that was introduced had a significant effect on the behaviour of the system. Chapter 4 described two different models that incorporated the delayed field explicitly into the system. The first model assumed that the delayed field Q was simply a carbon copy of the toroidal field B, τ time units previously. This model was able to reproduce similar behaviour to what was seen in Chapter 3: as the time delay τ is increased, the system goes through a series of bifurcations until a strongly modulated solution is found. After τ has exceeded this value, a periodic solution is again recovered. A second model is also derived that includes a mechanism through which the delayed field can diffuse. Again, as τ is increased at fixed values of S, a series of transitions is observed until the solution appears to be strongly modulated with periods of significantly reduced activity. In both of these models, it is generally found that modulation is easier to find for smaller values of $|D|$.

Motivated by the recent work of Hathaway (2012), who suggested that the meridional flow was confined to the Sun's shallow interior, a new type of dynamo model was described in Chapter 6. The numerical code that was used to carry out the simulations was adapted from the $\alpha\omega$ dynamo model that was written in Chapter 5. Two sources of poloidal field regeneration were included: one from an interface dynamo with an alpha-effect localised at the base of the convection zone and another from a Babcock-Leighton alpha effect located at the solar surface. Due to the inclusion of a shallow meridional flow this model essentially represents an interface type dynamo with a perturbation from a surface source term. To the best of my knowledge, this is the first time a model of this type (characterised by the inclusion of a shallow meridional flow) has been studied. Several interesting features are found within the model. Firstly, the parity of the solution appears to be strongly dependent upon the combination of the strength of the Babcock-Leighton source term S_0 and the magnitude of the Reynolds number Re. It is known that the Sun's magnetic field has been of dipolar parity since 1600 and my model is able to produce solutions that are dipolar for an optimal combination of Re and S_0. Secondly, the strength of the Babcock-Leighton source term is able to set the period of the dynamo wave. It is widely reported that in flux transport dynamo models, the period of the dynamo wave can be controlled by varying the Reynolds number and this is still true for my model. However, through the introduction of these two competing α-effects, I have introduced an additional mechanism

which can alter the period of the dynamo wave. Finally, substantial modulation can also be found within the system. A parameter survey was carried out for two different values of D. For $D = -2 \times 10^6$, it is possible to fix S_0 and vary Re such that a periodic solution is initially found with the dynamo wave becoming more strongly modulated as Re is increased. In this example, the solution is of dipolar parity and the equatorward branch of the dynamo wave is confined to a region $\pm 30^\circ$ above the equator. Modulation is also found when $D = -2 \times 10^7$. For this value of D, the solutions range from exhibiting periodic, quasiperiodic and strongly modulated behaviour; however a strong example of parity modulation has also been identified.

7.2 Future Work

The models described in this thesis have successfully introduced ways in which the dynamo wave can be modulated. One thing that is absent from the modulated solutions are periods of grand minima. This means that it is not possible to say whether the dynamo could successfully restart after these events. In theory, it should be possible, since a deep-seated interface dynamo relies upon cyclonic turbulence to regenerate poloidal field. The generation of grand minima could be induced through stochastic fluctuations of the source terms or meridional flow which can essentially temporarily "turn off" the required dynamo components. However, since this thesis has concentrated upon deterministic features that could modulate the dynamo wave it would not be sensible to include such stochastic fluctuations. One way that grand minima can be induced in deterministic models is through the inclusion of a Malkus-Proctor effect (Malkus & Proctor, 1975) which considers the consequences of including a large-scale Lorentz-force $\mathbf{J} \times \mathbf{B}$. This means that the flow field will be significantly influenced by the magnetic field such that it is no longer statistically steady. Models of this type have successfully produced grand minima and there is no reason to suspect that this would not be the case in the competing α model described in chapter 6.

Another possible area for future work would be to take the 2D code in spherical geometry and try the direct analogue of the cartesian model that is described in Chapter 3. This model would be an interface dynamo with an explicit time delayed toroidal field Q. Some preliminary calculations have been carried out, but I have not yet found convincing regions of modulation in a realistic set up. One thing that could be investigated is changing the form of the two competing α-effects. In my preliminary calculations, both sources of poloidal field regeneration were assumed to be of the same form, and were located at a region near the tachocline. A more realistic form for S would be to implement a surface source term which would mimic the Babcock-Leighton setup. With this parameter profile, it is possible that modulation would be more readily produced.

Bibliography

Abramowitz, M. & Stegun, I. A. 1968 *Handbook of Mathematical Functions*. New York: Dover publications.

Alfvén, H. 1942 Existence of Electromagnetic-Hydrodynamic Waves. *Nature* **150**, 405–406.

Babcock, H. D. 1959 The Sun's Polar Magnetic Field. *The Astrophysical Journal* **130**, 364.

Babcock, H. W. 1961 The Topology of the Sun's Magnetic Field and the 22-YEAR Cycle. *The Astrophysical Journal* **133**, 572.

Balogh, A. & Thompson, M. 2009 *Introduction to Solar Magnetism: The Early Years*. New York: Springer-Verlag.

Beer, J., Raisbeck, G. M. & Yiou, F. 1991 Time variations of Be-10 and solar activity. In *The Sun in Time* (ed. C. P. Sonett, M. S. Giampapa & M. S. Matthews), pp. 343–359.

Beer, J., Siegenthaler, U. & Blinov, A. 1988 Temporal ^{10}Be variations in ice: information on solar activity and geomagnetic field intensity. In *Secular Solar and Geomagnetic Variations in the Last 10,000 Years,* (ed. F. R. Stephenson & A. W. Wolfendale), pp. 297–313.

Beer, J., Tobias, S. & Weiss, N. 1998 An Active Sun Throughout the Maunder Minimum. *Solar Physics* **181**, 237–249.

Bhatnagar, A. & Livingston, W. C. 2005 *Fundamentals of Solar Astronomy*. Hackensack, NJ: World Scientific.

Bogart, R. S. & Basu, S. 2004 Zonally Averaged Meridional Flows Determined from Long-Term "RING-DIAGRAM" Analysis. In *SOHO 14 Helio- and Asteroseismology: Towards a Golden Future* (ed. D. Danesy), *ESA Special Publication*, vol. 559, p. 329.

Brandenburg, A., Krause, F., Meinel, R., Moss, D. & Tuominen, I. 1989 The stability of nonlinear dynamos and the limited role of kinematic growth rates. *Astronomy and Astrophysics* **213**, 411–422.

Brandenburg, A., Sokoloff, D. & Subramanian, K. 2012 Current Status of Turbulent Dynamo Theory. From Large-Scale to Small-Scale Dynamos. *Space Science Reviews* **169**, 123–157.

Braun, D. C. & Fan, Y. 1998 Helioseismic Measurements of the Subsurface Meridional Flow. *The Astrophysical Journal* **508**, L105–L108.

Brooke, J., Moss, D. & Phillips, A. 2002 Deep minima in stellar dynamos. *Astronomy and Astrophysics* **395**, 1013–1022.

Bullard, E. & Gellman, H. 1954 Homogeneous Dynamos and Terrestrial Magnetism. *Philosophical Transactions of the Royal Society of London Series A* **247**, 213–278.

Bumba, V. & Howard, R. 1965 Large-Scale Distribution of Solar Magnetic Fields. *The Astrophysical Journal* **141**, 1502.

Bushby, P. J. 2003 Nonlinear Dynamos in Stars. PhD thesis, University of Cambridge.

Bushby, P. J. 2006 Zonal flows and grand minima in a solar dynamo model. *Monthly Notices of the Royal Astronomical Society* **371**, 772–780.

Bushby, P. J. & Tobias, S. M. 2007 On Predicting the Solar Cycle Using Mean-Field Models. *The Astrophysical Journal* **661**, 1289–1296.

Caligari, P., Moreno-Insertis, F. & Schussler, M. 1995 Emerging flux tubes in the solar convection zone. 1: Asymmetry, tilt, and emergence latitude. *The Astrophysical Journal* **441**, 886–902.

Carbonell, M., Oliver, R. & Ballester, J. L. 1993 On the asymmetry of solar activity. *Astronomy and Astrophysics* **274**, 497.

Caspar, M. & Hellman, C. D. 1993 *Kepler*. New York: Dover Publications.

Cattaneo, F. & Hughes, D. W. 2009 Problems with kinematic mean field electrodynamics at high magnetic Reynolds numbers. *Monthly Notices of the Royal Astronomical Society* **395**, L48–L51.

Charbonneau, P. 2005 Dynamo models of the solar cycle. *Living Reviews in Solar Physics* **2** (2).

Charbonneau, P., Blais-Laurier, G. & St-Jean, C. 2004 Intermittency and Phase Persistence in a Babcock-Leighton Model of the Solar Cycle. *The Astrophysical Journal* **616**, L183–L186.

Charbonneau, P. & Dikpati, M. 2000 Stochastic Fluctuations in a Babcock-Leighton Model of the Solar Cycle. *The Astrophysical Journal* **543**, 1027–1043.

Charbonneau, P. & MacGregor, K. B. 1996 On the Generation of Equipartition-Strength Magnetic Fields by Turbulent Hydromagnetic Dynamos. *The Astrophysical Journal* **473**, L59.

Charbonneau, P., St-Jean, C. & Zacharias, P. 2005 Fluctuations in Babcock-Leighton Dynamos. I. Period Doubling and Transition to Chaos. *The Astrophysical Journal* **619**, 613–622.

Chatterjee, P., Nandy, D. & Choudhuri, A. R. 2004 Full-sphere simulations of a circulation-dominated solar dynamo: Exploring the parity issue. *Astronomy and Astrophysics* **427**, 1019–1030.

Choudhuri, A. R. 1998 *The Physics of Fluids and Plasmas: An Introduction for Astrophysicists*. Cambridge: Cambridge University Press.

Choudhuri, A. R., Schussler, M. & Dikpati, M. 1995 The solar dynamo with meridional circulation. *Astronomy and Astrophysics* **303**, L29.

Cole, L. C. & Bushby, P. J. 2014 Modulated cycles in an illustrative solar dynamo model with competing α-effects. *Astronomy and Astrophysics* **563**, A116.

Cowling, T. G. 1934 The magnetic field of sunspots. *Monthly Notices of the Royal Astronomical Society* **94**, 39–48.

Delaygue, G. & Bard, E. 2011 An Antarctic view of Beryllium-10 and solar activity for the past millennium. *Climate Dynamics* **36**, 2201–2218.

Dikpati, M. & Charbonneau, P. 1999 A Babcock-Leighton Flux Transport Dynamo with Solar-like Differential Rotation. *The Astrophysical Journal* **518**, 508–520.

Dikpati, M. & Choudhuri, A. R. 1994 The evolution of the Sun's poloidal field. *Astronomy and Astrophysics* **291**, 975–989.

Dikpati, M. & Choudhuri, A. R. 1995 On the Large-Scale Diffuse Magnetic Field of the Sun. *Solar Physics* **161**, 9–27.

Dikpati, M. & Gilman, P. A. 2001 Flux-Transport Dynamos with α-Effect from Global Instability of Tachocline Differential Rotation: A Solution for Magnetic Parity Selection in the Sun. *The Astrophysical Journal* **559**, 428–442.

Dikpati, M. & Gilman, P. A. 2009 Flux-Transport Solar Dynamos. *Space Science Reviews* **144**, 67–75.

Dikpati, M., Rempel, M., Gilman, P. A. & MacGregor, K. B. 2005 Comments on "Full-sphere simulations of circulation-dominated solar dynamo: Exploring the parity issue". *Astronomy and Astrophysics* **437**, 699–702.

D'Silva, S. 1993 Can equipartition fields produce the tilts of bipolar magnetic regions? *The Astrophysical Journal* **407**, 385–397.

D'Silva, S. & Choudhuri, A. R. 1993 A theoretical model for tilts of bipolar magnetic regions. *Astronomy and Astrophysics* **272**, 621.

Durney, B. R. 1995 On a Babcock-Leighton dynamo model with a deep-seated generating layer for the toroidal magnetic field. *Solar Physics* **160**, 213–235.

Durney, B. R. 1996 On a Babcock-Leighton Dynamo Model with a Deep-Seated Generating Layer for the Toroidal Magnetic Field, II. *Solar Physics* **166**, 231–260.

Durney, B. R. 1997 On a Babcock-Leighton Solar Dynamo Model with a Deep-seated Generating Layer for the Toroidal Magnetic Field. IV. *The Astrophysical Journal* **486**, 1065–1077.

Duvall, Jr., T. L. 1979 Large-scale solar velocity fields. *Solar Physics* **63**, 3–15.

Dziembowski, W. A., Goode, P. R. & Libbrecht, K. G. 1989 The radial gradient in the sun's rotation. *The Astrophysical Journal* **337**, L53–L57.

Eddy, J. A. 1976 The Maunder Minimum. *Science* **192**, 1189–1202.

Fan, Y., Fisher, G. H. & McClymont, A. N. 1994 Dynamics of emerging active region flux loops. *The Astrophysical Journal* **436**, 907–928.

Fisher, G. H., Fan, Y. & Howard, R. F. 1995 Comparisons between theory and observation of active region tilts. *The Astrophysical Journal* **438**, 463–471.

Giles, P. M. 1999 Time-Distance Measurements of Large-Scale Flows in the Solar Convection Zone. PhD thesis, Stanford University.

Giles, P. M., Duvall, T. L., Scherrer, P. H. & Bogart, R. S. 1997 A subsurface flow of material from the Sun's equator to its poles. *Nature* **390**, 52–54.

Giovanelli, R. G. 1984 *Secrets of the Sun*. Cambridge: Cambridge University Press.

Gizon, L., Duvall, Jr., T. L. & Larsen, R. M. 2001 Probing Surface Flows and Magnetic Activity with Time-Distance Helioseismology. In *Recent Insights into the Physics of the Sun and Heliosphere: Highlights from SOHO and Other Space Missions* (ed. P. Brekke, B. Fleck & J. B. Gurman), *IAU Symposium*, vol. 203, p. 189.

Gleissberg, W. 1939 A long-periodic fluctuation of the sun-spot numbers. *The Observatory* **62**, 158–159.

Gleissberg, W. 1971 The Probable Behaviour of Sunspot Cycle 21. *Solar Physics* **21**, 240–245.

Goedbloed, J. P. & Poedts, S. 2004 *Principles of magnetohydrodynamics : with applications to laboratory and astrophysical plasmas*. Cambridge: Cambridge University Press.

Haber, D. A., Hindman, B. W., Toomre, J., Bogart, R. S., Larsen, R. M. & Hill, F. 2002*a* Evolving Submerged Meridional Circulation Cells within the Upper Convection Zone Revealed by Ring-Diagram Analysis. *The Astrophysical Journal* **570**, 855–864.

Haber, D. A., Hindman, B. W., Toomre, J., Bogart, R. S., Larsen, R. M. & Hill, F. 2002*b* Evolving Submerged Meridional Circulation Cells within the Upper Convection Zone Revealed by Ring-Diagram Analysis. *The Astrophysical Journal* **570**, 855–864.

Hale, G. E., Ellerman, F., Nicholson, S. B. & Joy, A. H. 1919 The Magnetic Polarity of Sun-Spots. *The Astrophysical Journal* **49**, 153.

Hanslmeier, A. 2002 *The Sun and Space Weather*. London: Kluwer Academic Publishers.

Hartmann, R. 1971 A New Representation of the 80-Year Cycle in Sunspot Frequency. *Solar Physics* **21**, 246–248.

Harvey, J. W., Duvall, Jr., T. L. & Pomerantz, M. A. 1986 Helioseismology Results from South Pole Observations. In *Bulletin of the American Astronomical Society*, *Bulletin of the American Astronomical Society*, vol. 18, p. 1011.

Hathaway, D. 2015*a* The butterfly diagram. `http://solarscience.msfc.nasa.gov/SunspotCycle.shtml`.

Hathaway, D. 2015*b* The magnetic butterfly diagram. `http://solarscience.msfc.nasa.gov/dynamo.shtml`.

Hathaway, D. 2015*c* The sunspot cycle. `http://solarscience.msfc.nasa.gov/SunspotCycle.shtml`.

Hathaway, D. 2016 The omega effect. `http://solarscience.msfc.nasa.gov/images/omega.gif`.

Hathaway, D. H. 2012 Supergranules as Probes of the Sun's Meridional Circulation. *The Astrophysical Journal* **760**, 84.

Hathaway, D. H., Gilman, P. A., Jones, H. P., Kasher, J., Simon, G. W., GONG Nearly Steady Flows Team & GONG Magnetic Fields Team 1996 GONG Observations of Solar Surface Flows. In *American Astronomical Society Meeting Abstracts #188*, *Bulletin of the American Astronomical Society*, vol. 28, p. 903.

Hathaway, D. H., Nandy, D., Wilson, R. M. & Reichmann, E. J. 2003 Evidence That a Deep Meridional Flow Sets the Sunspot Cycle Period. *The Astrophysical Journal* **589**, 665–670.

Hathaway, D. H. & Rightmire, L. 2010 Variations in the Sun's Meridional Flow over a Solar Cycle. *Science* **327**, 1350–.

Henkel, R. 1972 Evidence for an Ultra-Long Cycle of Solar Activity. *Solar Physics* **25**, 498–499.

Howard, R. & Labonte, B. J. 1980 The sun is observed to be a torsional oscillator with a period of 11 years. *The Astrophysical Journal* **239**, L33–L36.

Howard, R. & Labonte, B. J. 1981 Surface magnetic fields during the solar activity cycle. *Solar Physics* **74**, 131–145.

Howe, R., Christensen-Dalsgaard, J., Hill, F., Komm, R. W., Larsen, R. M., Schou, J., Thompson, M. J. & Toomre, J. 2000 Deeply Penetrating Banded Zonal Flows in the Solar Convection Zone. *The Astrophysical Journal* **533**, L163–L166.

Hoyng, P. 1993 Helicity fluctuations in mean field theory: an explanation for the variability of the solar cycle? *Astronomy and Astrophysics* **272**, 321.

Hoyt, D. V. & Schatten, K. H. 1996 *The Role of the Sun in Climate Change*. New York: Oxford University Press.

Hughes, D. W., Rosner, R. & Weiss, N. O. 1998 *The Solar Tachocline*. Cambridge: Cambridge University Press.

Iserles, A. 1996 *A First Course in the Numerical Analysis of Differential Equations*. Cambridge University Press.

Ivanova, T. S. & Ruzmaikin, A. A. 1976 A Magnetohydrodynamic dynamo model of the solar cycle. *Soviet Astronomy* **20**, 227.

Jennings, R. L. & Weiss, N. O. 1991 Symmetry breaking in stellar dynamos. *Monthly Notices of the Royal Astronomical Society* **252**, 249–260.

Jones, C. A., Thompson, M. J. & Tobias, S. M. 2010 The Solar Dynamo. *Space Science Reviews* **152**, 591–616.

Jones, C. A., Weiss, N. O. & Cattaneo, F. 1985 Nonlinear dynamos: A complex generalization of the Lorenz equations. *Physica D Nonlinear Phenomena* **14**, 161–176.

Jouve, L. & Brun, A. S. 2009 Three-Dimensional Nonlinear Evolution of a Magnetic Flux Tube in a Spherical Shell: Influence of Turbulent Convection and Associated Mean Flows. *The Astrophysical Journal* **701**, 1300–1322.

Jouve, L., Brun, A. S., Arlt, R., Brandenburg, A., Dikpati, M., Bonanno, A., Käpylä, P. J., Moss, D., Rempel, M., Gilman, P., Korpi, M. J. & Kosovichev, A. G. 2008 A solar mean field dynamo benchmark. *Astronomy and Astrophysics* **483**, 949–960.

Jouve, L., Proctor, M. R. E. & Lesur, G. 2010 Buoyancy-induced time delays in Babcock-Leighton flux-transport dynamo models. *Astronomy and Astrophysics* **519**, A68.

Karak, B. B. & Choudhuri, A. R. 2010 The Waldmeier Effect in Sunspot Cycles. *Astrophysics and Space Science Proceedings* **19**, 402–404.

Kitchatinov, L. L., Ruediger, G. & Kueker, M. 1994 Lambda-quenching as the nonlinearity in stellar-turbulence dynamos. *Astronomy and Astrophysics* **292**, 125–132.

Layzer, D., Rosner, R. & Doyle, H. T. 1979 On the origin of solar magnetic fields. *The Astrophysical Journal* **229**, 1126–1137.

Leighton, R. 1969 A magneto-kinematic model of the solar cycle. *The Astrophysical Journal* **156**, 1–26.

Leighton, R. B. 1964 Transport of Magnetic Fields on the Sun. *The Astrophysical Journal* **140**, 1547.

Makarov, V. I., Fatianov, M. P. & Sivaraman, K. R. 1983 Poleward migration of the magnetic neutral line and the reversal of the polar fields on the sun. I - Period 1945-1981. *Solar Physics* **85**, 215–226.

Makarov, V. I. & Sivaraman, K. R. 1989 Evolution of latitude zonal structure of the large-scale magnetic field in solar cycles. *Solar Physics* **119**, 35–44.

Malkus, W. V. R. & Proctor, M. R. E. 1975 The macrodynamics of alpha-effect dynamos in rotating fluids. *Journal of Fluid Mechanics* **67**, 417–443.

Mann, P. D. & Proctor, M. R. E. 2009 Competing local and non-local α-effects for a simplified flux transport dynamo model. *Monthly Notices of the Royal Astronomical Society* **399**, L99–L102.

Markiel, J. A. 1999 Solar and Stellar Dynamo Models. PhD thesis, University of Rochester.

Mason, J., Hughes, D. W. & Tobias, S. M. 2002 The Competition in the Solar Dynamo between Surface and Deep-seated α-Effects. *The Astrophysical Journal* **580**, L89–L92.

Maunder, E. 1904 1904 butterfly diagram. `http://datavis.ca/milestones//admin/uploads/images/Maunder1904.jpg`.

Moffatt, H. K. 1978 *Magnetic Field Generation in Electrically Conducting Fluids*. Cambridge: Cambridge University Press.

Moss, D., Brandenburg, A., Tavakol, R. & Tuominen, I. 1992 Stochastic effects in mean-field dynamos. *Astronomy and Astrophysics* **265**, 843–849.

Muscheler, R., Joos, F., Beer, J., Müller, S. A., Vonmoos, M. & Snowball, I. 2007 Solar activity during the last 1000 yr inferred from radionuclide records. *Quaternary Science Reviews* **26**, 82–97.

Nandy, D. & Choudhuri, A. R. 2001 Toward a Mean Field Formulation of the Babcock-Leighton Type Solar Dynamo. I. α-Coefficient versus Durney's Double-Ring Approach. *The Astrophysical Journal* **551**, 576–585.

Nandy, D. & Choudhuri, A. R. 2002 Explaining the Latitudinal Distribution of Sunspots with Deep Meridional Flow. *Science* **296**, 1671–1673.

North, J. 1974 *Thomas Harriot and the First Telescopic Observations of Sunspots*, pp. 144–161. Oxford: Clarendon Press.

Ossendrijver, A. J. H., Hoyng, P. & Schmitt, D. 1996 Stochastic excitation and memory of the solar dynamo. *Astronomy and Astrophysics* **313**, 938–948.

Ossendrijver, M. A. J. H. 2000 Grand minima in a buoyancy-driven solar dynamo. *Astronomy and Astrophysics* **359**, 364–372.

Parker, E. N. 1955*a* Hydromagnetic Dynamo Models. *The Astrophysical Journal* **122**, 293.

Parker, E. N. 1955*b* The Formation of Sunspots from the Solar Toroidal Field. *The Astrophysical Journal* **121**, 491.

Parker, E. N. 1993 A solar dynamo surface wave at the interface between convection and nonuniform rotation. *The Astrophysical Journal* **408**, 707–719.

Press, W. H., Teukolsky, S. A., Vetterling, W. T. & Flannery, B. P. 2007 *Numerical Recipes 3rd Edition: The Art of Scientific Computing*, 3rd edn. New York, NY, USA: Cambridge University Press.

Raisbeck, G. M. & Yiou, F. 1988 ^{10}Be as a proxy indicator of variations in solar activity and geomagnetic field intensity during the last 10,000 years. In *Secular Solar and Geomagnetic Variations in the Last 10,000 Years,* (ed. F. R. Stephenson & A. W. Wolfendale), pp. 287–296.

Ribes, J. C. & Nesme-Ribes, E. 1993 The solar sunspot cycle in the Maunder minimum AD1645 to AD1715. *Astronomy and Astrophysics* **276**, 549.

Schou, J., Antia, H. M., Basu, S., Bogart, R. S., Bush, R. I., Chitre, S. M., Christensen-Dalsgaard, J., di Mauro, M. P., Dziembowski, W. A., Eff-Darwich, A., Gough, D. O., Haber, D. A., Hoeksema, J. T., Howe, R., Korzennik, S. G., Kosovichev, A. G., Larsen, R. M., Pijpers, F. P., Scherrer, P. H., Sekii, T., Tarbell, T. D., Title, A. M., Thompson, M. J. & Toomre, J. 1998 Helioseismic Studies of Differential Rotation in the Solar Envelope by the Solar Oscillations Investigation Using the Michelson Doppler Imager. *The Astrophysical Journal* **505**, 390–417.

Sheeley, Jr., N. R., Nash, A. G. & Wang, Y.-M. 1987 The origin of rigidly rotating magnetic field patterns on the sun. *The Astrophysical Journal* **319**, 481–502.

Sivaraman, K. R., Sivaraman, H., Gupta, S. S. & Howard, R. F. 2010 Return Meridional Flow in the Convection Zone from Latitudinal Motions of Umbrae of Sunspot Groups. *Solar Physics* **266**, 247–259.

Snodgrass, H. B. & Howard, R. 1985 Torsional oscillations of the sun. *Science* **228**, 945–952.

Spiegel, E. A. & Zahn, J.-P. 1992 The solar tachocline. *Astronomy and Astrophysics* **265**, 106–114.

Steenbeck, M., Krause, F. & Rädler, K.-H. 1966 A calculation of the mean electromotive force of an electrically conducting fluid in turbulent motion under the influence of Coriolis forces. *Naturforsch* **21**, 369.

Stix, M. 1976 Differential rotation and the solar dynamo. *Astronomy and Astrophysics* **47**, 243.

Stix, M. 2002 *The Sun: An Introduction*. Berlin: Springer-Verlag.

Stuiver, M. & Braziunas, T. F. 1988 The solar component of the atmospheric ^{14}C record. In *Secular Solar and Geomagnetic Variations in the Last 10,000 Years,* (ed. F. R. Stephenson & A. W. Wolfendale), pp. 245–266.

Thomas, J. H. & Weiss, N. O. 1992 *Sunspots: Theory and Observations*. Berlin: Springer-Verlag Berlin Heidelberg.

Thompson, M. J., Toomre, J., Anderson, E. R., Antia, H. M., Berthomieu, G., Burtonclay, D., Chitre, S. M., Christensen-Dalsgaard, J., Corbard, T., De Rosa, M., Genovese, C. R., Gough, D. O., Haber, D. A., Harvey, J. W., Hill, F., Howe, R., Korzennik, S. G., Kosovichev, A. G., Leibacher, J. W., Pijpers, F. P., Provost, J., Rhodes, Jr., E. J., Schou, J., Sekii, T., Stark, P. B. & Wilson, P. R. 1996 Differential Rotation and Dynamics of the Solar Interior. *Science* **272**, 1300–1305.

Tobias, S. M. 1996 Grand minimia in nonlinear dynamos. *Astronomy and Astrophysics* **307**, L21.

Tobias, S. M. 1997 The solar cycle: parity interactions and amplitude modulation. *Astronomy and Astrophysics* **322**, 1007–1017.

Tobias, S. M. 2005 The solar tachocline: Formation, stability and its role in the solar dynamo. In *Fluid Dynamics and Dynamos in Astrophysics and Geophysics* (ed. A. M. Soward, C. A. Jones, D. W. Hughes & N. O. Weiss), p. 193.

Tobias, S. M., Brummell, N. H., Clune, T. L. & Toomre, J. 2001 Transport and Storage of Magnetic Field by Overshooting Turbulent Compressible Convection. *The Astrophysical Journal* **549**, 1183–1203.

Ulrich, R. K., Boyden, J. E., Webster, L., Padilla, S. P. & Snodgrass, H. B. 1988 Solar rotation measurements at Mount Wilson. V - Reanalysis of 21 years of data. *Solar Physics* **117**, 291–328.

Vizoso, G. & Ballester, J. L. 1990 The north-south asymmetry of sunspots. *Astronomy and Astrophysics* **229**, 540–546.

Vorontsov, S. V., Christensen-Dalsgaard, J., Schou, J., Strakhov, V. N. & Thompson, M. J. 2002 Solar internal rotation as seen from SOHO MIDI data. In *From Solar Min to Max: Half a Solar Cycle with SOHO* (ed. A. Wilson), *ESA Special Publication*, vol. 508, pp. 111–114.

Wang, Y.-M., Nash, A. G. & Sheeley, Jr., N. R. 1989*a* Evolution of the sun's polar fields during sunspot cycle 21 - Poleward surges and long-term behavior. *The Astrophysical Journal* **347**, 529–539.

Wang, Y.-M., Nash, A. G. & Sheeley, Jr., N. R. 1989*b* Magnetic flux transport on the sun. *Science* **245**, 712–718.

Wang, Y.-M. & Sheeley, Jr., N. R. 1991 Magnetic flux transport and the sun's dipole moment - New twists to the Babcock-Leighton model. *The Astrophysical Journal* **375**, 761–770.

Wang, Y.-M., Sheeley, Jr., N. R. & Nash, A. G. 1991 A new solar cycle model including meridional circulation. *The Astrophysical Journal* **383**, 431–442.

Weiss, N. O., Cattaneo, F. & Jones, C. A. 1984 Periodic and aperiodic dynamo waves. *Geophysical and Astrophysical Fluid Dynamics* **30**, 305–341.

Weiss, N. O. & Tobias, S. M. 2000 Physical Causes of Solar Activity. *Space Science Reviews* **94**, 99–112.

Wilmot-Smith, A. L., Nandy, D., Hornig, G. & Martens, P. C. H. 2006 A Time Delay Model for Solar and Stellar Dynamos. *The Astrophysical Journal* **652**, 696–708.

Yoshimura, H. 1978 Nonlinear astrophysical dynamos - Multiple-period dynamo wave oscillations and long-term modulations of the 22 year solar cycle. *The Astrophysical Journal* **226**, 706–719.

Zel'dovich , Y. B. 1957 . *Soviet Physics JETP* **4**, 460.

Zhao, J., Bogart, R. S., Kosovichev, A. G., Duvall, Jr., T. L. & Hartlep, T. 2013 Detection of Equatorward Meridional Flow and Evidence of Double-cell Meridional Circulation inside the Sun. *The Astrophysical Journal* **774**, L29.

Zhao, J., Couvidat, S., Bogart, R. S., Parchevsky, K. V., Birch, A. C., Duvall, T. L., Beck, J. G., Kosovichev, A. G. & Scherrer, P. H. 2012 Time-Distance Helioseismology Data-Analysis Pipeline for Helioseismic and Magnetic Imager Onboard Solar Dynamics Observatory (SDO/HMI) and Its Initial Results. *Solar Physics* **275**, 375–390.

Zhao, J., Hartlep, T., Kosovichev, A. G. & Mansour, N. N. 2009 Imaging the Solar Tachocline by Time-Distance Helioseismology. *The Astrophysical Journal* **702**, 1150–1156.

Zhao, J. & Kosovichev, A. G. 2004 Torsional Oscillation, Meridional Flows, and Vorticity Inferred in the Upper Convection Zone of the Sun by Time-Distance Helioseismology. *The Astrophysical Journal* **603**, 776–784.